Trace element and sulphur isotope variations of sulphides in the Koperberg Suite, O'okiep Copper District, Namaqualand, South Africa: implications for formation of sulphides and the role of crustal sulphur assimilation

Edmore Marima

ORCID iD: 0000-0002-3420-6950

January 2022

Thesis submitted in fulfilment of the requirements for Master of Science degree in Geology in the Department of Geology, Rhodes University.

Supervisors: Prof. Steffen H. Büttner and Prof. Stephen A. Prevec

Declaration

I declare that this thesis is my own work, and information from other publications is adequately referenced. It is being submitted in fulfilment for the Master of Science degree in the Department of Geology, Rhodes University.

Edmore Marima

21 January 2022

Date

Acknowledgements

First, I thank God who gives us life and has made everything possible.

My sincere gratitude goes to my supervisors Prof. Steffen Büttner and Prof. Steve Prevec for their guidance throughout this research project.

Mr. Koos Beukes is thanked for his assistance with the conceptualisation of the project and acquisition of samples.

This work is based on the research supported in part by the National Research Foundation of South Africa (Grant Number: 122972) through the DST-NRF Innovation Master's Scholarship.

This study was partly funded by the Rhodes University through the Henderson Scholarship. I am grateful to Prof. Tony Booth and Mr. John Gillam for facilitating the funding.

The support of the DSI-NRF Centre of Excellence (CoE) for Integrated Mineral and Energy Resource Analysis (DSI-NRF CIMERA) towards this research is hereby acknowledged. Opinions expressed and conclusions arrived at, are those of the author and are not necessarily to be attributed to the CoE.

Dr. Laure Martin and Dr. Malcom Roberts are thanked for conducting SIMS analytical work.

Mr. Paul Middlestead and Mrs. Riana Rossouw are thanked for conducting bulk sulphur isotope and trace element analytical work.

Dr. Deon van Niekerk and Mr. Marvin Randall are thanked for their assistance with EPMA and EDS-SEM calibration and data extraction. I would like to thank Rhodes University for access to the Electron Microprobe Analyser (the purchase of which was partially funded by NRF National Equipment Program grant UID 74464).

Ms. Andrea King and Mr. Andile 'Chris' Pikoli are thanked for their assistance with sample preparation.

Lastly, I thank my parents, family and friends for the encouragement and believing in me.

Abstract

The major economic copper sulphide deposits hosted in the late Mesoproterozoic intrusions of the Koperberg Suite in the O'okiep Copper District immediately overlie sulphur-bearing paragneisses of the Khurisberg Subgroup in an otherwise low-sulphur granitic basement. The dominant sulphide assemblage (chalcopyrite and bornite) hosted in the Koperberg Suite is also atypical of the intermediate solid solution (*iss*) assemblage (chalcopyrite and pyrrhotite) observed in most Cu-Ni magmatic sulphide deposits. This study presents sulphur isotope and *in-situ* trace element analysis of sulphides from the Koperberg Suite and the Khurisberg Subgroup with the view of placing constraints on the role of sulphide-bearing supracrustal metasedimentary of the Khurisberg Subgroup as a source of additional sulphur in the genesis of these deposits, and ore-forming (sulphide formation) processes which result in trace element variations registered by sulphides hosted in the Koperberg Suite.

The high concentrations (up to 2100 ppm) of monosulphide solid solution (*mss*)-incompatible trace elements (e.g., Te, Se, Bi, Ag, Pb), and the depletion in Ni and Co (<40 ppm) of sulphides hosted in the Koperberg Suite are instead consistent with the derivation of such sulphides from a Cu-rich sulphide melt which segregated from a Ni-rich sulphide melt prior to magma emplacement in the middle crust, in agreement with one of the petrogenetic models for the Koperberg Suite proposed in the existing literature.

The low S/Se ratios (~650-10300) of sulphides hosted in the Koperberg Suite and the high S/Se ratios (~18800-56000) registered by the main sulphide phase (pyrite) in the Khurisberg Subgroup argues against crustal contamination of the Koperberg Suite magmas by the Khurisberg Subgroup. The S/Se and Cu/S ratios of coexisting bornite and chalcopyrite hosted in the Koperberg Suite are positively correlated with the bornite modal abundance in the Koperberg Suite. Such trends are interpreted to be consistent with progressive oxidation of sulphide melt, a process which results in the crystallisation of *iss*-bornite assemblage and/or replacement of *iss* with bornite due to the enrichment of Cu and depletion in S of the sulphide melt. The oxidation of sulphide melt is likely to have been effectuated by the fractional crystallisation of *mss* in a prior sulphide melt segregation event and/or the fractional crystallisation of Fe^{2+}-dominated silicate phases. Fractionation of the Cu-rich melt sulphide melt (segregated from *mss*) also tends to enrich the residual sulphide melts in Se. Thus, the chalcopyrite-dominated assemblage with S/Se ratios of ~1300-10200 observed in the less basic rocks in the Koperberg Suite (leucodiorites and leuconorites) is interpreted to have formed from the least evolved sulphide melt, whereas the bornite-dominated assemblage with S/Se ratios of ~650-5500 observed in the more mafic members of the Koperberg Suite (orthopyroxenites and norites) is interpreted to have formed from the most evolved sulphide melt.

The $\delta^{34}S$ isotopic signatures in sulphides of the Koperberg Suite (-1.4 to +1.91‰) and the proposed contaminant, the Khurisberg Subgroup (-1.2 to +3.5‰), overlap with the those of the Koperberg Suite below the Khurisberg Subgroup (+0.74‰) and typical mantle-derived magmatic rocks (0 ±

2‰). Hence, the sulphur isotope variations are inconclusive as an indicator of possible crustal sulphur assimilation into the intruding mantle magma. However, considering the trace element systematics and the sulphur isotope data, the Koperberg magmas likely attained sulphur saturation at deeper crustal levels.

Table of Contents

Declaration i

Acknowledgements ii

Abstract iii

List of Figures viii

List of Tables xiv

1 Introduction 1

1.1 Background 1

1.2 Key principles of magmatic sulphide deposit formation 3

1.3 Sulphur isotope and trace element systematics in magmatic sulphide deposits 4

1.4 Previous stable isotope and trace element work 5

1.5 Research problem and research approach 7

1.6 Aims and objectives 10

2 Geological setting 11

2.1 Regional geology 11

2.1.1 The Namaqua Sector of the Namaqua-Natal Metamorphic Province 11

2.1.2 The Bushmanland Domain 12

2.2 Geology of the O'okiep Copper District 14

2.2.1 Lithostratigraphy and geochronology 14

2.2.2 Structure and metamorphism 18

2.2.3 Koperberg Suite 22

2.2.3.1 Petrology 22

2.2.3.2 Distribution, field relationships, and emplacement models 23

2.2.3.3 Proposed petrogenetic models for the Koperberg Suite 26

3 Methods 32

3.1 Sampling and sample preparation 32

3.2 Petrography 32

3.3 Analytical techniques and data processing 33

3.3.1 Energy Dispersive Spectroscopy (EDS) 33

3.3.2 Electron Probe Micro-analysis (EPMA) 33

3.3.3 Laser Ablation Inductively Coupled Plasma Mass Spectrometry (LA-ICP-MS) 34
3.3.4 Secondary Ion Mass Spectrometry (SIMS) 35
3.3.5 Isotope Ratio Mass Spectrometry (IRMS) 36
4 Petrographic descriptions 36
4.1 Khurisberg Subgroup 37
4.1.1 Sample 039T-1A (Garnet-biotite-sillimanite gneiss, Khurisberg Subgroup, Nababeep Mine) 37
4.1.2 Sample 039T-1B (Garnet-biotite-sillimanite gneiss, Khurisberg Subgroup, Nababeep Mine) 40
4.2 Koperberg Suite 42
4.2.1 Sample 039T-4 (Diorite, Nababeep Mine) 42
4.2.2 Sample 016T-3 (Leucodiorite, Nababeep Mine) 43
4.2.3 Sample KNU 477 (Norite, Nigramoep Mine) 45
4.2.4 Sample CD 01 (Orthopyroxenite, Carolusberg Mine) 47
4.3 Koperberg Suite below the Khurisberg Subgroup (Sugarloaf Quarry) 49
4.3.1 Sample DSQ (Leuconorite, Sugarloaf Quarry) 49
5 Mineral chemistry 52
5.1 Major element chemistry 52
5.1.1 Silicates 52
5.1.1.1 Garnet 52
5.1.1.2 K-feldspar 52
5.1.1.3 Plagioclase 52
5.1.1.4 Biotite 52
5.1.1.5 Muscovite 53
5.1.1.6 Orthopyroxene 53
5.1.2 Oxides 53
5.1.2.1 Ilmenite 53
5.1.2.2 Spinel 53
5.1.3 Sulphides 54
5.1.3.1 Pyrite 54
5.1.3.2 Pyrrhotite 54

5.1.3.3 Chalcopyrite 59
5.1.3.4 Bornite and chalcocite 59
5.2 Trace element chemistry 66
5.3 Sulphur Isotopes 78
5.3.1 Sulphur isotope results 78
5.3.2 Synthesis 82
6 Discussion 82
6.1 The bornite problem 82
6.2 Trace element chemistry 85
6.2.1 General trace element trends 85
6.2.2 S/Se ratios 86
6.2.3 Implications of S/Se ratios trends for Koperberg Suite petrogenetic model 90
6.3 Sulphur isotopes 92
6.3.1 Constraints of S-isotope signatures based on a mantle source 92
6.3.2 Constraints of S-isotope signatures based on a lower crustal sulphur source 93
6.3.3 Synthesis 94
7 Conclusion 95
8 Recommendations for future research 96
References 97
Appendix 109
Appendix 1: EDS analyses for silicates, oxides, and phosphates 109
Appendix 2: EPMA detection limits for sulphides 120

List of Figures

Figure 1. 1 Regional geological setting and the tectonostratigraphic subdivisions of the Namaqua Sector, Namaqua-Natal Metamorphic Province (NNMP). Areal extent of the O'okiep Copper District (OCD) demarcated in red. Insert shows the areal extent of the NNMP. BSZ: Boven Rugzeer Shear Zone, DT: Dabep Thrust, GT: Groothoek Thrust, HRT: Hartbees River Thrust, NSZ: Neusberg Shear Zone, PSZ: Pofadder Shear Zone, MRPSZ: Marshall Rocks-Pofadder Shear Zone, TSZ: Trooilapspan Shear Zone, BF: Brakbosh Fault, DF: Doornberg Fault, GeT: Gemsbokvlei Thrust (GeT) (modified after Macey et al., 2018; Schorn et al., 2020). 2

Figure 1. 2 $\delta^{18}O$ values of the granite-gneiss country rocks and the Koperberg Suite in comparison with typical mantle values. [1]Boer et al. (1994), [2]Kyser et al. (1982). 5

Figure 1. 3 $\delta^{34}S$ values of mantle-derived rocks, Narrap- and Carolusberg-type ores. References: [1] Boer et al. (1994), [2] von Gehlen et al. (1990), [3]Dechow and Jensen (1965), [4]von Gehlen et al. (1983), [5]Ohmoto and Rye (1979), Sakai et al. (1984), Peters et al. (2010). 6

Figure 1. 4 A stratigraphic column showing the spatial relations of the Khurisberg Subgroup and the Koperberg ore bodies, and past production and orebodies as of 1996. Mixed Zone=Intercalated Nababeep and Concordia Granites. *Subeconomic ore bodies, **uneconomic ore bodies; LNS: Little Namaqualand Suite (modified after Potgieter, 1996). 9

Figure 1. 5 Cross-section showing pinch-and-swell geometries developed in the Koperberg Suite bodies at Koperberg-Carolusberg Mine (modified after Lombaard et al., 1986; Kisters et al., 1994; Maier, 2000). 10

Figure 2. 1 Geological map and cross-section of the O'okiep Copper District. Lithostratigraphic positions of the Khurisberg Subgroup subunits (the Springbok Formation, Wolfram Schist, and Ratelpoort Formation) shown in the cross-section. Locations of historical and operational copper mines depicted as black squares. The location of Sugarloaf Quarry is depicted as red square. Sample localities are highlighted in yellow (modified after Lombaard et al., 1986; Clifford and Barton, 2012). 17

Figure 2. 2 The timing of the main magmatic, metamorphic, deformation and related orogenic events in the Bushmanland Domain and the OCD in the Mesoproterozoic. These episodes overprint the Palaeoproterozoic basement and form new Mesoproterozoic crust. STZ: Skelmfontein Thrust Zone, UHT: Ultra-high temperature, NG: Nababeep Granite, MG: Modderfontein Granite, KG: Kweekfontein Granite, CG: Concordia Granite, RG: Rietberg Granite. Reinterpretation by Macey et al. (2018) depicted in red. References: [1] Joubert, (1986) [2]Clifford et al. (1981), [3] Blignault et al., (1983), [4]Barton (1983), [5]Waters (1989), [6]Kisters et al. (1996), [7]Gibson et al. (1996), [8]Raith and Harley (1998), [9]Clifford et al., (2004), [11]Cornell et al., (2006), [12]Dewey et al., (2006), [13]Clifford and Barton

(2012), [14]Macey et al., (2017), [15]Macey et al. (2018), [16]Clifford et al. (2004), [17]Robb et al. (1999), [18]Doggart (2019). 19

Figure 2. 3 The Klondike East steep structure located ~5 km north of Okiep showing a Koperberg Suite dyke in the central parts of the steep structure (red dashed lines). Note the dragging or the rotation of the subhorizontal foliation of the Nababeep Granite Gneiss (black dashed lines) to subvertical attitude with increasing proximity to the Koperberg Suite dyke in the centre of the steep structure. 25

Figure 2. 4 The distribution of steep structures within the O'okiep Copper District (modified after Clifford and Barton, 2012). 26

Figure 2. 5 Schematic model of stages leading to the emplacement of the Koperberg Suite according to Duchesne et al. (2007). (a) Incorporation of the oceanic crust with Cu-Fe sulphides into the lower crust at ~1900 Ma. (b) Metamorphism of oceanic crust at granulite facies conditions and the generation of voluminous granitoids related to post-orogenic magmatism between ~1240 and 1180 Ma. (c) Partial melting of crust producing granitoids of the Spektakel Suite and partial melting of the mafic granulites to produce the Koperberg magmas between ~1070 and 1030 Ma. Heat input during the partial melting event related to detachment of subcontinental lithosphere along a major shear zone and asthenosphere inflow or thermal plume beneath the Bushmanland Domain. VMS: volcanogenic massive sulphide, LM: lithospheric mantle, LNS: Little Namaqualand Suite. Not to scale. 29

Figure 2. 6 IOCG model for the formation of Hondekloof (Fig. 1.1), Eezelsfontein and O'okiep deposits (Fig. 2.1) according to Maier et al. (2012). (a) Segregation of sulphide liquid from basaltic magma, and fractionation of the sulphide liquid to form a Ni-rich sulphide residue (forming the Hondekloof Ni deposits) and a Cu-rich iss sulphide liquid at deeper crustal levels. (b) Entrainment of the Cu-rich sulphide liquid by magma and redeposition at relatively shallower crustal levels, followed by the fractionation of the sulphide liquid producing a Ni-rich sulphide liquid and a Cu-rich iss sulphide liquid (forming the Eezelsfontein deposits). (c) Entrainment of the Cu-rich iss sulphide liquid by magma to the shallowest crustal levels producing the O'okiep Cu deposits. 31

Figure 4. 1 Specimen of sample 039T-1A (Nababeep Mine) exhibiting banding defined garnet-biotite-sillimanite domains and quartz-feldspar domains. 37

Figure 4. 2 Photomicrographs of typical parts of thin sections from sample 039T-1A (Nababeep Mine) under reflected light (a,d) and cross-polarised (b) and in backscattered electron (BSE) mode (c). (a) Photomicrograph showing close association of pyrite to the garnet-biotite-sillimanite domain and the difference in the size of pyrite crystals in the garnet-biotite-sillimanite and quartz-feldspar domains. (b) Sillimanite and biotite forming along quartz and K-feldspar grain boundaries.

(c) Quartz, biotite, pyrite and pyrrhotite inclusions in garnet. (d) Pyrite-chalcopyrite intergrowth hosted in garnet. 39

Figure 4. 3 Specimen of sample 039T-1B (Khurisberg Subgroup, Nababeep Mine) exhibiting banding defined garnet-biotite-sillimanite domains and quartz-feldspar domains. 40

Figure 4. 4 Photomicrographs of typical parts of sample 039T-1B (Nababeep Mine) in cross-polarised light (a) and under reflected light (b-d). Photomicrograph (b) is the corresponding reflected light image for (a). (a) Quartz, K-feldspar, sillimanite, biotite and opaque phases inclusions in garnet. (b-d) Sulphide phases occurring as independent grains or in close association with oxide phases; biotite forms around some of the sulphide grains. (d) Pyrrhotite-chalcopyrite intergrowth in garnet. 41

Figure 4. 5 Specimen of mesocratic diorite sample 039T-4 (Nababeep Mine) showing clusters consisting of biotite and orthopyroxene in a plagioclase-quartz matrix. Larger chalcopyrite grains are spatially associated with biotite-orthopyroxene clusters. 42

Figure 4. 6 Photomicrographs of typical parts of diorite sample 039T-4 (Nababeep Mine) in cross polarised light (a,c), reflected light (b) and backscattered electron mode (d). Image (b) shows the corresponding area shown in (a) in reflected light. (a) Opaque phases (oxides and sulphides) occur along or close to the grain boundaries of plagioclase. (a-b,d) Sulphide phases are characterised by feathered margins, whereas oxide phases have smooth and rounded grain boundaries. (c) Opaque phases occur along or close to the grain boundaries of plagioclase and along biotite grain boundaries. The position of image (d) is demarcated in red. (d) Chalcopyrite in close spatial association with magnetite and magnetite-ilmenite intergrowths. 43

Figure 4. 7 Hand specimen for leucodiorite sample 016T-3 (Nababeep Mine) showing clusters consisting of biotite and/or magnetite in a plagioclase-quartz matrix. 44

Figure 4. 8 Photomicrographs of typical parts of sample 016-3 (Nababeep Mine) in cross polarised light (a), in plane polarised light (b), under reflected light (c,d) and backscattered electron mode (e). (a,c,e) Opaque phases (oxide and sulphide phases) form along plagioclase grain boundaries or as chadacrysts to plagioclase. (b) Biotite associated with orthopyroxene. (c) Chalcopyrite-bornite intergrowth abuts biotite grain boundaries. (d-e) Chalcopyrite-bornite intergrowth in close association with magnetite. Muscovite commonly forms around bornite. 45

Figure 4. 9 Hand specimen for norite sample KNU 477 (Nigramoep Mine) showing plagioclase within orthopyroxene-biotite rich parts. Dashed white lines demarcate boundaries of some of the plagioclase or clusters of plagioclase grains. Chalcopyrite and magnetite grains are spatially associated with the orthopyroxene-biotite rich parts. 46

Figure 4. 10 Photomicrographs of typical parts of norite sample KNU 477 (Nigramoep Mine) in cross polarised light (a) and reflected light (b,c). (a) Opaque phases forming within or on grain boundaries of orthopyroxene and biotite. Plagioclase forms chadacrysts to these orthopyroxene-

biotite-oxide rich zones. The positions of (b) and (c) are demarcated in red. (b-c) Oxide and sulphide phases showing a close spatial relationship. 47

Figure 4. 11 Hand specimen for orthopyroxenite sample CD 01 (Carolusberg Mine) showing bornite and magnetite within an orthopyroxene matrix..... 48

Figure 4. 12 Photomicrographs in plane polarised light (a) and in reflected light (b,c) for the representative parts of orthopyroxenite sample CD 01 (Carolusberg Mine). The corresponding area in (a) is shown in (b). (a-c) Bornite and magnetite coexisting interstitially to orthopyroxene. (c) Chalcocite exsolutions in bornite. Note the inverse or negative grain shapes of bornite (i.e., interstitial) relative to magnetite. 49

Figure 4. 13 Typical hand specimen for leuconorite sample DSQ 3 (Sugarloaf Quarry) showing orthopyroxene evenly disseminated in an equigranular plagioclase-rich matrix..... 50

Figure 4. 14 Photomicrographs of leuconorite DSQ 3 (Sugarloaf Quarry) in plane polarised light (a), cross polarised light (c) and reflected light (b,d). The corresponding reflected light images for (a) and (c) are (b) and (d), respectively. (a-d) Sulphide and oxide phases commonly occur within orthopyroxene-biotite clusters, along grain boundaries of mafic silicate phases (biotite and orthopyroxene) and plagioclase. Sulphides exhibit feathered grain boundaries whereas oxides have smooth grain boundaries. 51

Figure 5. 1 Cu-Fe-S ternary plots of atomic percent compositions of sulphide minerals from the Koperberg Suite and Khurisberg Subgroup. KS: Khurisberg Subgroup, KNb: Koperberg Suite from Nababeep Mine, KNg: Koperberg Suite from Nigramoep Mine, KCr: Koperberg Suite from Carolusberg Mine, KSQ: Koperberg Suite from Sugarloaf Quarry. 56

Figure 5. 2 Constituents of a typical violin plot: rotated (symmetrical) kernel density plots (left) and a box plot (right) (after Marfin et al., 2020). 67

Figure 5. 3 Violin plots for Te and Se concentrations in sulphides in the Koperberg Suite (Nababeep Mine, KNb; Sugarloaf Quarry, KSQ; Nigramoep Mine, KNg; Carolusberg Mine; KCr) and the Khurisberg Subgroup (KS)..... 68

Figure 5. 4 Violin plots for Ag and Bi concentrations in sulphides in the Koperberg Suite (Nababeep Mine, KNb; Sugarloaf Quarry, KSQ; Nigramoep Mine, KNg; Carolusberg Mine; KCr) and the Khurisberg Subgroup (KS)..... 69

Figure 5. 5 Violin plots for Cd and In concentrations in sulphides in the Koperberg Suite (Nababeep Mine, KNb; Sugarloaf Quarry, KSQ; Nigramoep Mine, KNg; Carolusberg Mine; KCr) and the Khurisberg Subgroup (KS)..... 70

Figure 5. 6 Violin plots for Ni and Co concentrations in sulphides in the Koperberg Suite (Nababeep Mine, KNb; Sugarloaf Quarry, KSQ; Nigramoep Mine, KNg; Carolusberg Mine; KCr) and the Khurisberg Subgroup (KS)..... 71

Figure 5. 7 Violin plots for Pb and Zn concentrations in sulphides in the Koperberg Suite (KNb, KSQ, KNg, KCr) and the Khurisberg Subgroup (KS). 72

Figure 5. 8 Violin plots for Sn and Mo concentrations in sulphides in the Koperberg Suite (KNb, KSQ, KNg, KCr) and the Khurisberg Subgroup (KS). 73

Figure 5. 9 Bulk and in-situ S isotope values of sulphides in the Khurisberg Subgroup and Koperberg Suite. Bulk analysis values are denoted by filled symbols, in-situ analysis values are denoted by open symbols. The error bars show the 1σ uncertainties. The range of $\delta^{34}S$ values for the mantle in grey and range of $\delta^{34}S$ values for lower continental crust in light grey. Mantle $\delta^{34}S$ values (Sakai et al., 1984; Peters et al., 2010)**;** lower continental crust (LCC) $\delta^{34}S$ values (Hoefs et al., 1982; Iyer et al., 1992; Hammerli et al., 2017)..... 78

Figure 5. 10 Analysis locations (red circles) and the respective $\delta^{34}S$ values for chalcopyrite in sample 3A-3C (a, b) and 4A-4B (c, d). (a) Analysis points lie near the boundaries of chalcopyrite grains and on uneven sulphide surfaces (blue arrows). (b) Analysis point lies in a small (~50 µm) chalcopyrite grain. (c, d) Analysis points lie in the central parts of the chalcopyrite grain and on relatively smooth sulphide surfaces..... 81

Figure 6. 1 Partition coefficient of trace elements between mss and sulphide melt ($D^{mss/sulphide\ melt}$), and iss and sulphide melt ($D^{iss/sulphide\ melt}$) according to Liu and Brenan (2015). Note that $D^{mss/sulphide\ melt}$ and $D^{iss/sulphide\ melt}$ values of all the elements are less than one indicating that the elements partition into sulphide melt relative to mss and iss..... 85

Figure 6. 2 S/Se variations in bornite, chalcopyrite, pyrrhotite and pyrite from the Koperberg Suite and the Khurisberg Subgroup. Note the increase in the S/Se ratios of bornite and chalcopyrite with increasing basicity of the samples suggesting the association of relatively Se-poor (least fractionated sulphide melts) with the most fractionated silicate melts, and the association of relatively Se-rich (most fractionated sulphide melts) with the least fractionated silicate melts. Analytical uncertainties are insignificant at the scale and not shown. KS: Khurisberg Subgroup, KNb: Koperberg Suite from Nababeep Mine, KNg: Koperberg Suite from Nigramoep Mine, KCr: Koperberg Suite from Carolusberg Mine, KSQ: Koperberg Suite from Sugarloaf Quarry. 87

Figure 6.3 Cu/S vs. S/Se plots for bornite (a) and chalcopyrite (b) from the Koperberg Suite. The mafic members (orthopyroxenite and norite) are characterised by high modal content of bornite, high Cu/S values relative to the ideal value and lower S/Se values compared to their felsic counterparts (leucodiorites). This relationship suggests the crystallisation of bornite from fractionated sulphide melts (enriched in Cu and Se, and depleted in S). Arrows in the legend show

increase in the basicity of the samples. The analytical uncertainties for Cu/S and S/Se ratios for chalcopyrite and bornite were calculated using the law of propagation of uncertainty (see Chapter 3.3.2, and Supplementary Table B1 for calculations). KS: Khurisberg Subgroup, KNb: Koperberg Suite from Nababeep Mine, KNg: Koperberg Suite from Nigramoep Mine, KCr: Koperberg Suite from Carolusberg Mine, KSQ: Koperberg Suite from Sugarloaf Quarry. 89

List of Tables

Table 4. 1 Summary of the mineralogy and petrographic classification of samples used in this study. 38

Table 5. 1 EPMA results for pyrite (FeS_2) compositions (in wt%). 55

Table 5. 2 EPMA results for pyrrhotite (Fe_7S_8) compositions (in wt%). 57

Table 5. 3 EPMA results for chalcopyrite ($CuFeS_2$) compositions (in wt%). 60

Table 5. 4 EPMA results for bornite (Cu_5FeS_4) compositions (in wt%), calculated for 10 ions. 63

Table 5. 5 EPMA results for chalcocite (Cu_2S) compositions (in wt%). 66

Table 5. 6 Trace element concentrations of bornite, chalcopyrite, pyrrhotite and pyrite (in ppm). 75

Table 5. 7 Bulk and in-situ S isotope, and bulk S (in wt%) compositions of rocks from the Khurisberg Subgroup and the Koperberg Suite. 79

1 Introduction

1.1 Background

The late Mesoproterozoic mafic to intermediate intrusions of the Koperberg Suite are present in two areas of the western Namaqua Sector of the Namaqua-Natal Metamorphic Province (NNMP), in the O'okiep and the Kliprand areas (Fig. 1.1). In the O'okiep area, the Koperberg Suite occurs as a swarm of ~1700 irregular diapir-, dyke-, sill-like bodies of anorthositic- to orthopyroxenitic composition (Lombaard et al., 1986). This volumetrically small suite intruded the Bushmanland Domain, a region dominantly constituted of granite-gneiss units interspersed with supracrustal sequences that have undergone multiple cycles of deformation and metamorphism (Cornell et al., 2006). The Koperberg Suite in the Kliprand area (Fig. 1.1), 160 km southeast of Springbok, is a major constituent of the Hondekloof Ni deposits, and occurs as structurally-controlled gabbronorite and enderbite units that are sparsely exposed on the southern margin of the Kliprand Dome (Hamman et al., 1996; Bailie et al., 2019). For purposes of this study the term "Koperberg Suite" is restricted to bodies in the O'okiep area, except where stated otherwise.

At a local scale, the Koperberg Suite bodies commonly occur within "steep structures" that are developed in the granite-gneiss country rocks (Kisters et al., 1996). These unique structures are characterised by rotation of pre-existing subhorizontal or shallow-dipping foliation into subvertical, dyke-parallel attitude, and are interpreted to have developed coevally with granulite-facies metamorphism during the waning stages of the ~1200-1000 Ma Namaquan Orogeny (see Chapter 2.3.3.2 for detailed descriptions; Kisters et al., 1994, 1996; Gibson et al., 1996).

The mafic varieties of the Koperberg Suite intrusions, mainly the orthopyroxenites and norites, and to a lesser extent the diorite members, host copper sulphide mineralisation (McIver et al., 1983). After a long period of artisanal mining in pre-colonial times, the O'okiep Copper District (OCD) attracted exploration and industrial mining activities from as early as 1852, making it the oldest formally proclaimed mining district in South Africa (Gibson and Kisters, 1996; Cairncross, 2004). More than 2 Mt of copper ore with grades of 1.75-14% were produced between 1852 and 2002 (Clifford and Barton, 2012). Since 2016, mineral exploration work involving geological mapping, acquisition of datasets for historical mines, drilling and geophysical surveys has been done in the OCD (Galileo Resources, 2016a; b; Orion Minerals, 2021a; b; c; d).

The OCD has been subject to intensive geological research for over 60 years (Clifford and Barton, 2012, and references therein) and as a result, the geology of the area, particularly its lithostratigraphy and the geochronology, is reasonably well understood (Robb et al., 1999). Some discussion however still exists about the subdivision of magmatic suites and emplacement episodes (Macey et al., 2018).

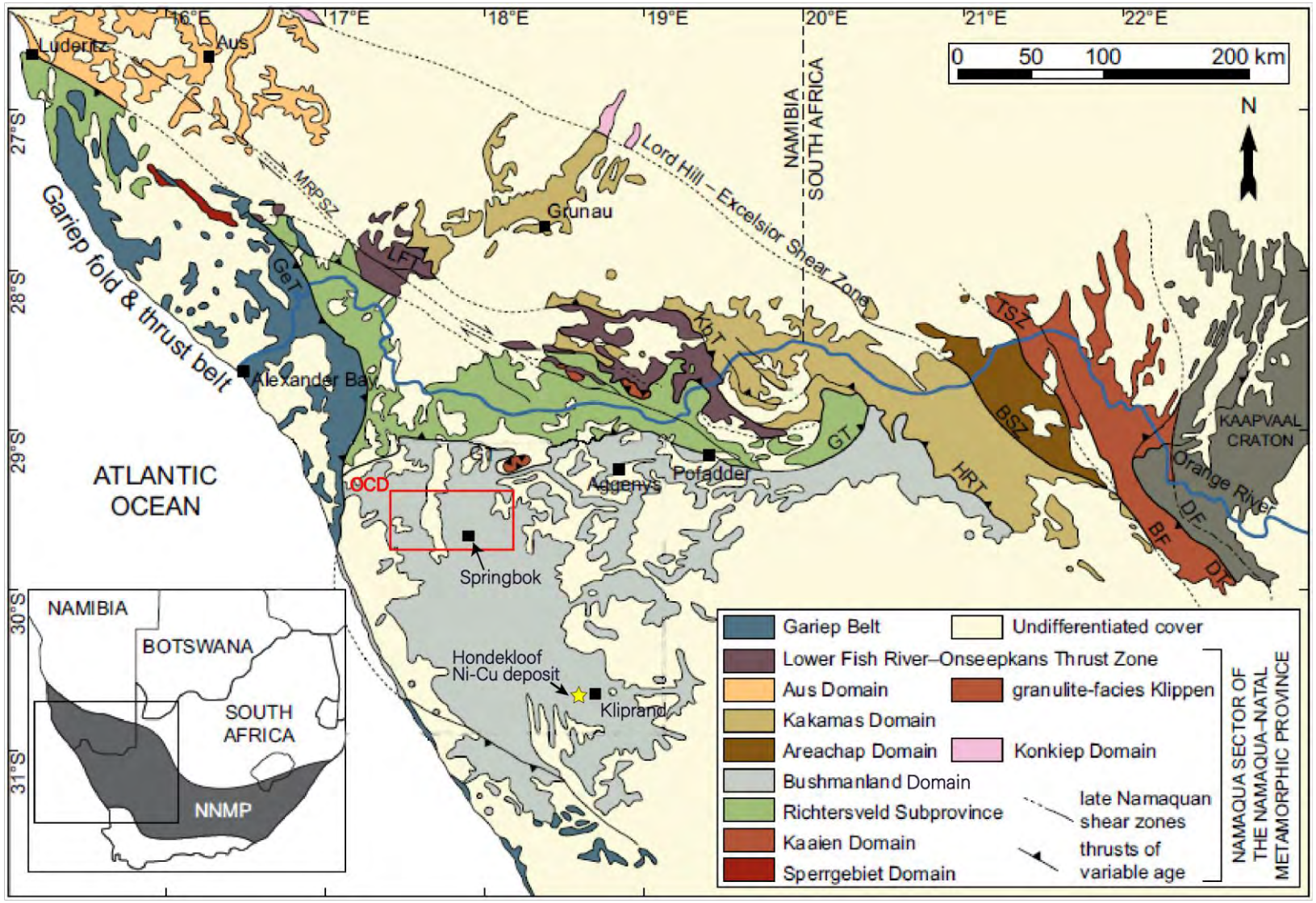

Figure 1. 1 Regional geological setting and the tectonostratigraphic subdivisions of the Namaqua Sector, Namaqua-Natal Metamorphic Province (NNMP). Areal extent of the O'okiep Copper District (OCD) demarcated in red. Insert shows the areal extent of the NNMP. BSZ: Boven Rugzeer Shear Zone, DT: Dabep Thrust, GT: Groothoek Thrust, HRT: Hartbees River Thrust, NSZ: Neusberg Shear Zone, PSZ: Pofadder Shear Zone, MRPSZ: Marshall Rocks-Pofadder Shear Zone, TSZ: Trooilapspan Shear Zone, BF: Brakbosh Fault, DF: Doornberg Fault, GeT: Gemsbokvlei Thrust (GeT) (modified after Macey et al., 2018; Schorn et al., 2020).

The Koperberg Suite deposits are unique in various aspects including: (i) the atypical sulphide assemblage (mainly bornite and chalcopyrite) and geochemical characteristics compared to other magmatic sulphide deposits, such as the unusually high Cu/Ni ratios, high Fe_2O_3/TiO_2 ratios, low S/Se ratios, and low K/Rb ratios for the mafic varieties (Cawthorn and Meyer, 1993; Maier, 2000), (ii) sulphide-silicate textures atypical of magmatic deposits, particularly the granular textures exhibited by sulphides and coexisting silicate minerals (Cawthorn and Meyer, 1993); (iii) the atypical occurrence of Cu mineralisation in anorthosite-bearing complexes (Conradie and Schoch, 1988), (iv) the high REE, U, Th, K, and P concentrations compared to other known mafic rocks (Conradie and Schoch, 1988; Andreoli et al., 2006), and (v) the anorthite and enstatite compositions of coexisting plagioclase and orthopyroxene that are atypical compared to other magmatic deposits (van Zwieten et al., 1996). These are some of the inconsistencies that have sparked a debate on the petrogenesis of the Koperberg Suite, particularly concerning the source of the magmas and mineralisation (e.g., van Zwieten, 1996; Maier et al., 2012).

Different mechanisms have been proposed for the genesis of the Koperberg magmas and related copper mineralisation. These include partial melting of a gabbronoritic granulite in the lower crust containing associated proto-Cu-Fe sulphides (e.g., Clifford et al., 1995, 2004; Duchesne et al., 2007), hybridisation of mantle-derived magmas by granitic crust or granitic anatectic melts (e.g., McIver et al., 1983; Brandriss and Cawthorn, 1996; Van Zwieten et al., 1996), and small degrees of partial melting of the subcontinental lithospheric mantle, differentiation of magmas during ascent, followed by sulphur saturation triggered by the addition of external sulphur and crustal contamination (Maier et al., 2012).

1.2 Key principles of magmatic sulphide deposit formation

Basaltic magmas are produced by partial melting in the upper mantle due to decompression melting in extensional tectonic settings (intracontinental rifts and mid-ocean ridges), anomalous heat input related to plumes, or partial melting related to the addition of volatiles released into the overlying mantle wedge by subducting plates in subduction zones (e.g., Winter, 2014 and references therein). The segregation of a sulphide liquid from such basaltic magmas, the concentration of a sulphide liquid through the coalesce of the segregated sulphide liquid droplets, and the subsequent partitioning of chalcophile elements (e.g., Ni, Cu, PGE) into the sulphide liquid relative to the silicate liquid during partial melting and ascent of mantle-derived magmas are the main processes responsible for the formation of magmatic Ni-Cu-PGE sulphide deposits (Barnes and Lightfoot, 2005; Mungall, 2005; Kiseeva et al., 2017).

Naldrett (2004) noted that the key aspects in the formation of magmatic sulphide deposits are: (1) sulphur saturation which leads to the formation of an immiscible sulphide liquid, (2) concentration of such sulphide liquids in specific parts of magma chambers or conduits, and (3) protracted interaction of the sulphide liquid with magma, which enables continued partitioning of chalcophile

elements within the magma into the sulphide liquid. Immiscible sulphide droplets form in silicate magma when the sulphur concentration exceeds the sulphur solubility in the silicate melt (Shima and Naldrett, 1975). Such sulphur concentration is referred to as the "sulphide concentration at sulphide saturation, or SCSS" (Shima and Naldrett, 1975). The SCSS is controlled by pressure, FeO content of magma, and most importantly, by the addition of externally-derived sulphur and assimilation of felsic country rocks (Wendlandt, 1982; Li and Naldrett, 1993; Mavrogenes and O'Neill, 1999; Ripley and Li, 2013). Assimilation of felsic country rocks during emplacement of basaltic magmas lowers the SCSS and increases the likelihood of forming an early immiscible sulphide liquid in magma. Similarly, the assimilation of externally-derived sulphur can provide the sulphur required in the formation of magmatic sulphides deposits (e.g., Lambert et al., 1998; Ripley et al., 1999, 2002; Ripley and Li, 2013).

The earliest solid sulphide phase to form in an Fe-Ni-Cu-S-O system typical of basaltic magmas associated with Ni-Cu-PGE sulphide deposits is the "monosulphide solid solution" (*mss*), a composite of magmatic pyrrhotite ± pentlandite, which typically coexists with magnetite at temperatures between 1100 and 850 ^{o}C (Mungall, 2005). Iron, Co and IPGE (Ir, Ru, Rh) and in some instances Ni, are preferentially partitioned into *mss*, which coexists with a Cu-rich sulphide liquid enriched in Cu, Au, Ag and PPGE (Pd, Pt) (Naldrett et al., 1997; Mungall et al., 2005). Nickel-IPGE-rich cumulate deposits are attributed to be a product of the *mss* phase (Barnes and Lightfoot, 2005). An intermediate solid solution (*iss*) mainly consisting of magmatic chalcopyrite and pyrrhotite joins *mss* and a fractionated Cu-rich sulphide liquid as the temperature drops below ~900 ^{o}C, which can form Cu-IPGE-rich deposits (Holwell and Mcdonald, 2010; Maier et al., 2012). With temperatures decreasing further to ~600-300 ^{o}C, *mss* decomposes to pyrrhotite and pentlandite, and *iss* decomposes to chalcopyrite and pyrrhotite (Naldrett, 2004; Raghavan, 2004).

1.3 Sulphur isotope and trace element systematics in magmatic sulphide deposits

Sulphur has four stable isotopes which are, in order of decreasing abundance, ^{32}S, ^{34}S, ^{33}S, and ^{36}S (Macnamara and Thode, 1950). The application of S isotope geochemistry in geology is based on fractionation of S isotopes, which due to kinetic and equilibrium effects leads to variations in ^{33}S/^{32}S, ^{34}S/^{32}S and ^{36}S/^{34}S ratios (O'Neil, 1986). Kinetic processes are prevalent in nature and produce large fractionation effects. Such processes are rare in high temperature systems. At lower temperature they involve irreversible and unidirectional processes such as bacterially-mediated sulphate reduction processes, evaporation and diffusion (O'Neil, 1986). These processes produce a number of surface S reservoirs with distinct isotopic signatures (i.e., ^{33}S/^{32}S, ^{34}S/^{32}S, ^{36}S/^{34}S ratios), such as oceans, sedimentary rocks, evaporites.

In Ni-Cu-PGE sulphide deposits, crustal contamination is one of the key processes that leads to attainment of S saturation in mantle-derived magmas (Chapter 1.2; Ripley and Li, 2013). When uncontaminated magmas derived from the mantle interact with a S reservoir or contaminant with

a $\delta^{34}S$ signature atypical of the mantle, the S isotope composition of the contaminated magma are varied and magmas produced by such processes will have $\delta^{34}S$ values outside the range of values for mantle-derived rocks of 0 ± 2‰ (Ohmoto and Rye, 1979; Sakai et al., 1984; Peters et al., 2010). Hence, $\delta^{34}S$ isotopic signatures are used as tracers for the sources of sulphur in magmatic sulphide deposits (Ohmoto, 1986).

Trace element contents in magmatic sulphides are mainly determined by the geological processes and the environment in which they form, the partition coefficients of trace elements in sulphide liquids, and the crystal structure of sulphides (George et al., 2018; Mansur et al., 2021). Trace element ratios for bulk compositions and sulphides in Ni-Cu-PGE deposits have been widely used to determine the involvement of crustal contamination in ore genesis (Smith et al., 2016). However, trace element systematics in magmatic sulphides have much broader applications in ore genesis of magmatic sulphide deposits which include deciphering fractionation of sulphide liquids, and partitioning of trace elements between sulphide liquids (Helmy et al., 2010).

1.4 Previous stable isotope and trace element work

The source of sulphides and the effects of crustal contamination in triggering sulphur saturation in magmatic sulphides deposits can be readily monitored by stable isotopes, particularly oxygen and sulphur isotopes (Smith et al., 2016). A few stable isotope studies have been conducted on the Koperberg Suite, the most recent by Von Gehlen et al. (1990) and Boer et al. (1994). Silicate phases from rocks of the Koperberg Suite exhibit enriched $\delta^{18}O$ values (average $\delta^{18}O$ of 7.4‰; Boer et al., 1994) compared to mantle-derived rocks which have $\delta^{18}O$ values of 5.7 ± 0.3‰ (Kyser et al., 1982; Fig. 1.2).

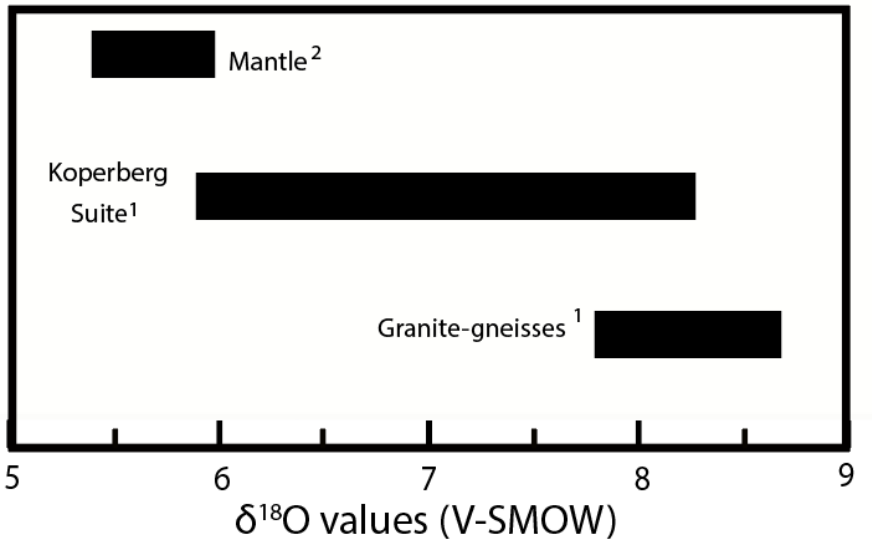

Figure 1. 2 $\delta^{18}O$ values of the granite-gneiss country rocks and the Koperberg Suite in comparison with typical mantle values. [1]Boer et al. (1994), [2]Kyser et al. (1982).

Boer et al. (1994) interpreted these data as pointing to the derivation of the Koperberg magmas from the mantle, and subsequent crustal contamination of mafic magmas by the granite-gneiss country rocks ($\delta^{18}O$ values of +7.8 to +8.7‰) and low-temperature alteration of sulphides.

The Koperberg Suite ores have been grouped into to three groups based on the main sulphide assemblage at specific mines or localities in the OCD which are: (1) the Narrap-type ore characterised by a typical *iss* assemblage (chalcopyrite + pyrrhotite ± pentlandite), (2) the Carolusberg-type ore characterised by a bornite-magnetite (±chalcopyrite) assemblage, and (3) and intermediate Hoist-type ore characterised by a bornite-chalcopyrite assemblage (Clifford, 1985; Clifford et al., 1990). The Narrap-type ores are characterised by lower Cu/S (0.36-0.97; Cawthorn and Meyer, 1993), lower S/Se ratios (13899-21000; Cawthorn and Meyer, 1993), and higher $\delta^{34}S$ values compared to their Carolusberg counterparts (Fig. 1.3; -2.1 to +3.6 ‰, Dechow and Jensen, 1965; +0.9 to +2.1 ‰, Von Gehlen et al., 1990; -1.7 to -2.5 ‰, Boer et al., 1994). These $\delta^{34}S$ values have been interpreted as of typical mantle-derived rocks using the $\delta^{34}S$ values of 0 ± 3‰ (Ohmoto, 1986; Chaussidon and Lorand, 1990). The Carolusberg-type ores are characterised by higher Cu/S (1.68-3.93; Cawthorn and Meyer, 1993), lower S/Se ratios (567-908; Cawthorn and Meyer, 1993) and relatively lower $\delta^{34}S$ values (Fig. 1.3; -1.0 to + 1.0‰; Dechow and Jensen, 1965; -0.1 ± 0.8‰, Von Gehlen et al., 1990; -1.5 to -4.1‰, Boer et al., 1994) compared to the Narrap-type ores, with some $\delta^{34}S$ values extending outside the typical range for mantle-derived rocks (Boer et al., 1994; Fig. 1.3).

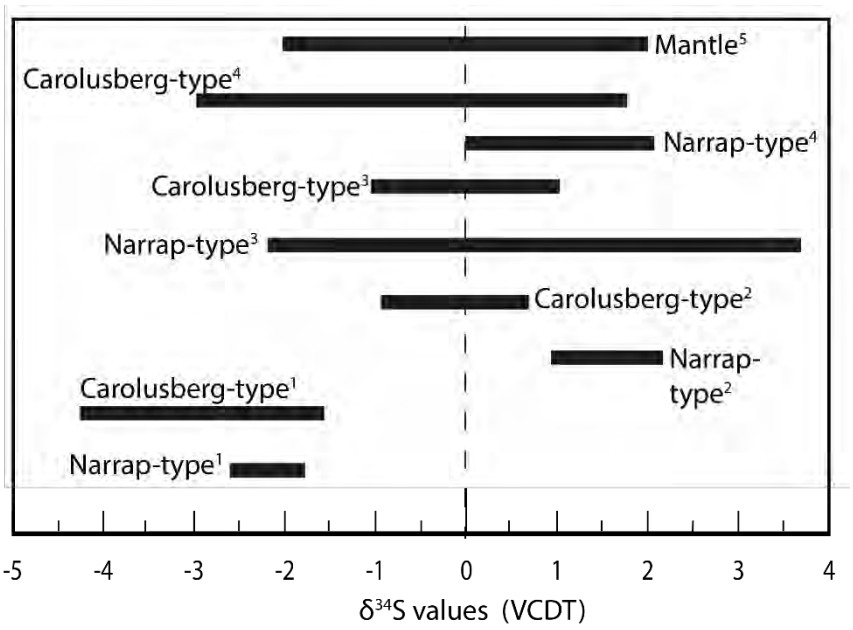

Figure 1. 3 $\delta^{34}S$ values of mantle-derived rocks, Narrap- and Carolusberg-type ores. References: [1] Boer et al. (1994), [2] von Gehlen et al. (1990), [3]Dechow and Jensen (1965), [4]von Gehlen et al. (1983), [5]Ohmoto and Rye (1979), Sakai et al. (1984), Peters et al. (2010).

Based on the low Cu/S and S/Se ratios, and the $\delta^{34}S$ values atypical of the mantle-derived rocks exhibited by the Carolusberg-type ores, the Carolusberg-type ores are interpreted to be a product of the oxidation and sulphur devolatisation of the primary chalcopyrite-pyrrhotite (Narrap-type ore) during the peak granulite-facies metamorphism (Reaction 1; Cawthorn and Meyer, 1993; Boer et al., 1994).

$$5\ CuFeS_2 + 5\ FeS + 6\ H_2O + [8\ O_2] = Cu_5FeS_4 + 3\ Fe_3O_4 + 6\ H_2S + 5\ SO_2 \qquad \textit{(Reaction 1)}$$
Ccp *Po* *Bn* *Mag*

1.5 Research problem and research approach

A phenomenon that has not been investigated is that almost all the sub-economic to economic Koperberg bodies (36 out of 37; Fig. 1.4; Potgieter, 1996) have intruded through the regionally shallow-dipping supracrustal sequences, particularly the metasedimentary rocks of the Khurisberg Subgroup. Past production records as of 1996 (about six years before mining temporarily ceased in the OCD) show that of these sub-economic to economic bodies, 29 occur within or immediately above the Khurisberg Subgroup in stratigraphic regions termed "favourable horizons" due to the higher concentration of ore bodies (Fig. 1.4; Benedict et al., 1964; Potgieter, 1996).

Field evidence in support of assimilation of the Khurisberg Subgroup metasediments by Koperberg magmas (though to a limited extent compared to assimilation of the granitic country rocks) includes the "pinch" geometries (reduction in horizontal thickness) of the Koperberg dykes at the Khurisberg Subgroup/granite-gneiss contact or within the Khurisberg Subgroup, and "swell" geometries (increase in thickness) of the Koperberg bodies within the granite-gneiss country rocks (Fig. 1.5; Kisters et al., 1994). Kisters et al. (1994) interpreted the different geometries as indicative of thermal erosion as a function of contrasts in fusion temperatures of the quartzitic metasedimentary units (~1600 ^{o}C) and country rocks undergoing granulite-facies metamorphism (~800 ^{o}C). Also, elongated xenoliths of the country rocks aligned along the walls of the Koperberg Suite intrusions are common (Lombaard et al., 1986). By implication and in the context of the crustal contamination model, this suggests that the metasedimentary rocks of the Khurisberg Subgroup are an additional potential contaminant and could have been influential in triggering sulphur saturation of the Koperberg magmas. Maier et al. (2012) proposed the addition of external crustal sulphur as an additional mechanism that might have triggered sulphur saturation. Though the authors do not specify the potential contaminant(s), the metasediments of the Khurisberg Subgroup are likely candidates, since these rocks contain pyrrhotite, chalcopyrite and pyrite as accessory phases (Raith and Harley, 1998).

This study places constraints on the role of crustal contamination by supracrustal sequences in triggering sulphur saturation. Potentially this may be the assimilation of Al_2O_3 and SiO_2, or sulphur dissolved from the Khurisberg Subgroup metasedimentary rocks, or a combination of both. The research approach used here aims at comparing sulphur isotope signatures of sulphides hosted in

the Koperberg Suite bodies which intruded through the metasedimentary rocks of the Khurisberg Subgroup versus the sulphur isotope signatures of sulphides in the metasedimentary rocks of the Khurisberg Subgroup, and the sulphides in the Koperberg Suite bodies stratigraphically below the Khurisberg Subgroup (potentially uncontaminated Koperberg Suite bodies). Similarly, the trace element variations of sulphide phases from both the Koperberg Suite (and the Khurisberg Subgroup) are assessed in the context of the evolution of magmas and sulphide melt in magmatic sulphide deposits.

It must be noted that there is an inevitable sampling bias of the uncontaminated Koperberg Suite because there is only one known locality, the Sugarloaf Quarry, where the Koperberg Suite is easily accessible at a stratigraphic level below the Khurisberg Subgroup (K. Beukes, 2019, pers. comm.). No drill core samples were available from the only other alternative locality (the East Okiep Mine).

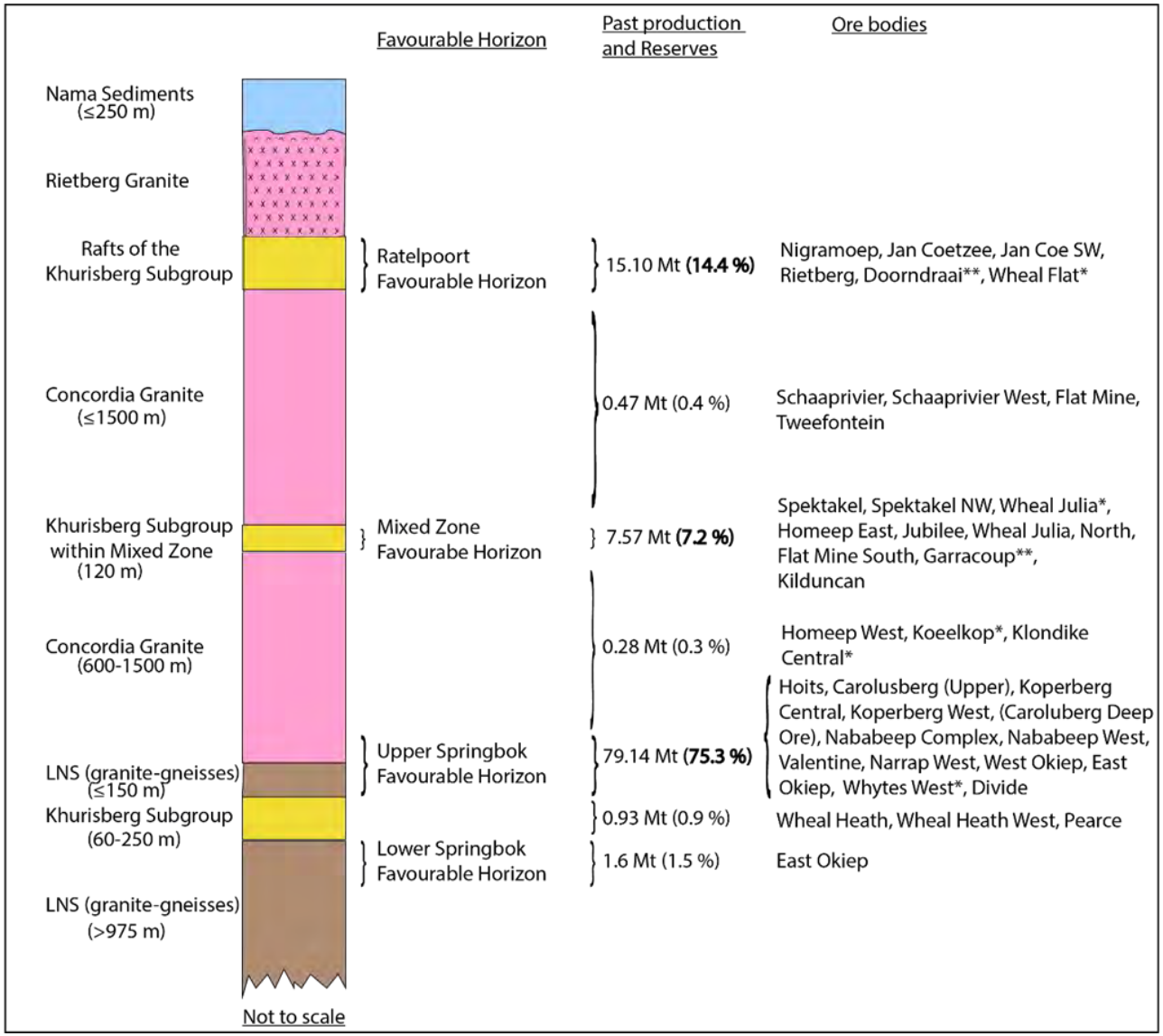

*Figure 1. 4 A stratigraphic column showing the spatial relations of the Khurisberg Subgroup and the Koperberg ore bodies, and past production and orebodies as of 1996. Mixed Zone=Intercalated Nababeep and Concordia Granites. *Subeconomic ore bodies, **uneconomic ore bodies; LNS: Little Namaqualand Suite (modified after Potgieter, 1996).*

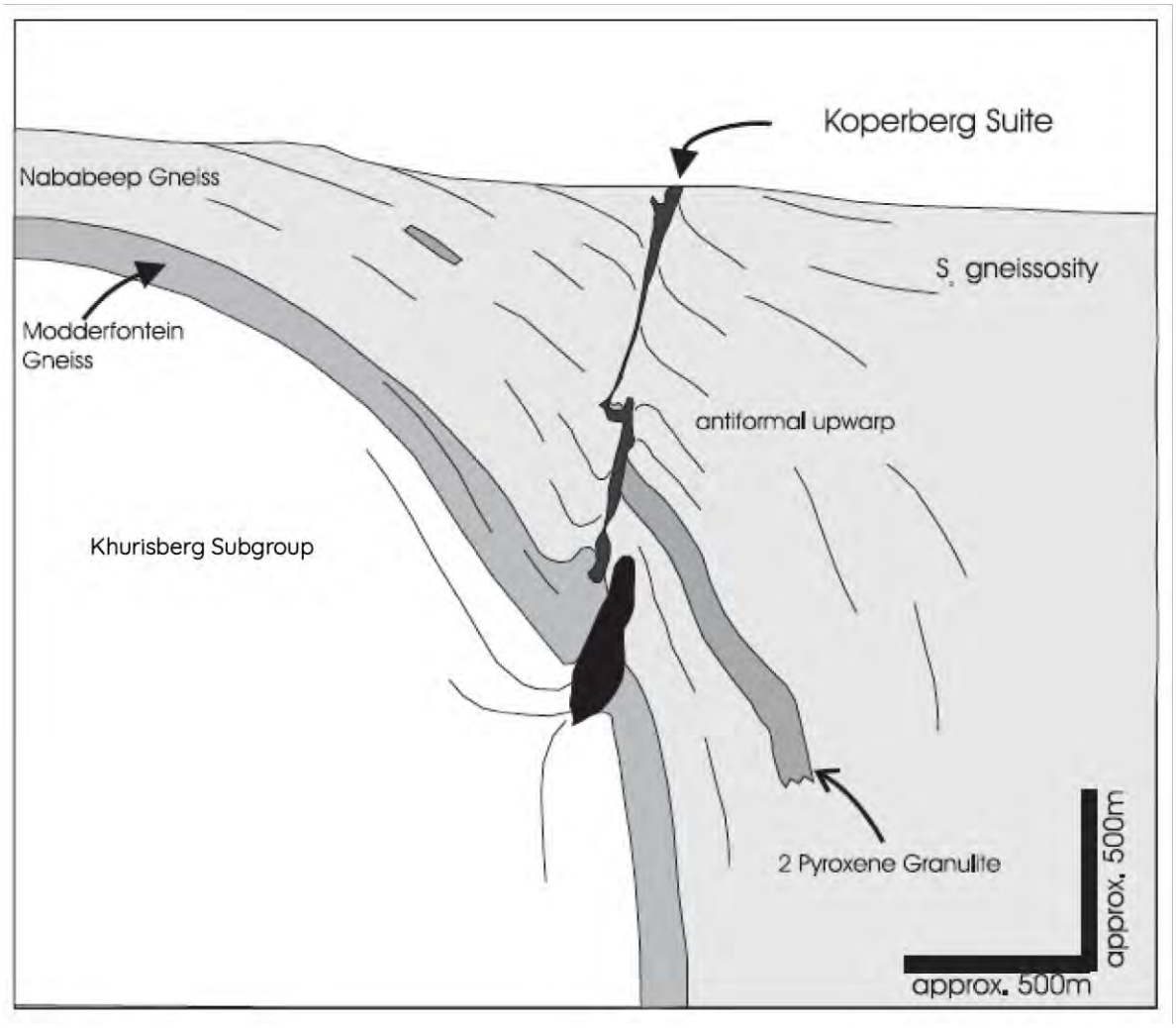

Figure 1. 5 Cross-section showing pinch-and-swell geometries developed in the Koperberg Suite bodies at Koperberg-Carolusberg Mine (modified after Lombaard et al., 1986; Kisters et al., 1994; Maier, 2000).

1.6 Aims and objectives

This thesis aims to test the following hypothesis: If the formation of Koperberg Suite orebodies depends on the provision of additional crustal sulphur from the supracrustal Khurisberg Subgroup, this contamination may be recorded in changing sulphur isotope signatures of sulphides in the orebodies compared to sulphides in the Koperberg Suite below the Khurisberg Subgroup. Similarly, the contamination of Koperberg Suite magmas may be recorded in changing trace element patterns in sulphides in Koperberg Suite rocks below and above the Khurisberg Subgroup supracrustal rocks. Isotopic and trace element variations in the Koperberg Suite below and above the Khurisberg Subgroup should be compatible with isotope and trace element patterns within the Khurisberg Subgroup as the potential contaminant.

Accordingly, the aims and objectives of the study are to:

(1) determine the S isotopic signatures and trace element contents of sulphide phases hosted in the Koperberg Suite orebodies above the Khurisberg Subgroup, the Koperberg Suite bodies below the Khurisberg Subgroup, and the metasedimentary rocks of the Khurisberg Subgroup itself, and assess the role of magma contamination by the metasedimentary rocks in triggering sulphur saturation in the Koperberg Suite magmas,

(2) assess the trace element variations in sulphide phases hosted in the Koperberg Suite in the context of potential processes which produce similar trends in the ore genesis of magmatic sulphide deposits.

2 Geological setting

2.1 Regional geology

2.1.1 The Namaqua Sector of the Namaqua-Natal Metamorphic Province

The Mesoproterozoic Namaqua-Natal Metamorphic Province (NNMP) forms an arcuate orogenic belt that surrounds the southern and western parts of the Archean Kaapvaal Craton (Fig. 1.1 insert). The belt has been interpreted to be part of the Grenville-aged belts formed during assembly of the Rodinia supercontinent (e.g., Hartnady et al., 1985; Hoffman, 1991; Li et al., 2008). The NNMP is broadly constituted of a reworked Paleoproterozoic granitic basement, supracrustal and plutonic rocks, which have undergone polyphase deformation during the ~1210-1000 Ma Namaqua orogenic event, and syn- and post tectonic intrusive granitoids (Cornell et al., 2006). The West Coast Belt in the western parts of the NNMP consists of greenschist- and amphibolite-facies rocks that formed and/or have been variably reworked during the Pan-African tectono-metamorphic event, involving thrusting of the Gariep Belt onto the NNMP (e.g., Joubert, 1986b). In the south and southeast, the Phanerozoic sediments of the Cape and Karoo Supergroups cover the NNMP (Cornell et al., 2006; Fig. 1.1).

Two main tectonic models for the formation of these domains have been proposed: (1) a traditional collisional model which suggests that the Namaqua Sector is a product of ~1.2-1.0 Ga Wilson cycle-related crustal accretion and arc-continent-collision events subsequently superseded by transtensional tectonics on the margins of the Proto-Kalahari Craton (see the review by Miller, 2012), and (2) the more recent model that suggests the evolution of the NNMP by cyclic episodes of extension, tectonic stability and contraction in a continental back-arc mobile belt (Bial et al., 2015a,b; Macey et al., 2018; Bailie et al., 2019). The back-arc mobile belt model has important implications to mafic magmatism in most parts of the NNMP including the Bushmanland Domain, as discussed in the forthcoming sections.

The Bushmanland Domain, which is the largest of all the domains in the Namaqua Sector, is in the north bound by the RMA, in the east by the Kakamas Domain (Fig. 1.1), and in the south by the Saldania Belt (Cornell et al., 2006).

The RMA contains plutonic rocks of the Vioolsdrif Domain and their volcanic equivalents of the Orange River Group, and the amphibolite-facies orthogneisses of the Pella Domain (Macey et al., 2017). Their emplacement ages range between ~1910 and 1860 Ma (Macey et al., 2017). The geochemical characteristics of rocks from both domains point to the development of the RMA in an island-arc setting (Reid, 1997; Macey et al., 2017). The ~2020 Ma Sperrgebiet Domain, a Palaeoproterozoic region that is interpreted as an older tectono-magmatic equivalent of the RMA, forms an inlier within the Pan-African Gariep Belt (Fig. 1.1; Thomas et al., 2016).

The Kakamas Domain to the north and east of the RMA (Fig. 1.1) dominantly comprises amphibolite- and granulite-facies granitoids, granitoid gneisses, metasedimentary rocks, and minor calc-silicate rocks (Cornell and Pettersson, 2007; Cornell et al., 2006). The voluminous S- and A-type granitoids that were emplaced between ~1200 Ma and ~1100 Ma have been interpreted as indicative of high heat flux in a continental back-arc setting (Bial et al., 2015a). The metamorphic host rocks of these granitoids show a long-lasting isobaric high-temperature history between ~1230 and <1100 Ma (Bial et al., 2015b). Further north in the Kakamas Domain of the Aus region in Namibia, the basement underwent a similar high-temperature metamorphic evolution associated with granite emplacement more than 100 Ma later, at ~1065-1045 Ma (Diener et al., 2013), approximately at the same time when the Koperberg Suite was emplaced in the waning stages of high-temperature metamorphism in the neighbouring Bushmanland Domain.

2.1.2 The Bushmanland Domain

The lowermost parts of the domain consist of a Paleoproterozoic granite-gneiss basement complex, the oldest of which is the ~1.82 Ga old Gladkop Suite (e.g., Nke et al., 2020). The Gladkop Suite forms large outcrops in the Steinkopf area north of the OCD, and is more sparsely exposed in the western portions of the OCD (Fig. 2.1; Lombaard et al., 1986; Robb et al., 1999). The basement is overlain by supracrustal sequences consisting of metavolcano-sedimentary rocks of the Bushmanland Group and Okiep Group in the northern parts of the domain, and the Kamiesberg Group in the southern parts of the Bushmanland Domain (Fig. 1.1). The Sm-Nd T_{DM} model ages of the Bushmanland Group (~2.25-2.85 Ga; Bailie et al., 2007) and the Kamiesberg Group (~1.59-2.00 Ga; Yuhara et al., 2002) are similar to the model ages of the RMA (~2.2-2.4 Ga; Macey et al., 2017). The Sm-Nd T_{DM} Macey et al., 2017). The Bushmanland Group is thus interpreted to have been derived from Archean and Paleoproterozoic sources most likely the RMA and Kaapvaal Craton,

whereas the Kamiesberg Group is interpreted to have been derived from the RMA and reworked Paleo- to Mesoproterozoic sources most likely the Little Namaqualand Suite (Bailie et al., 2007, 2019; Cornell et al., 2009).The depositional for the two groups is bracketed between ~1.64 Ga and 1.16 Ga (Raith et al., 2003; Eglington, 2006; Bailie et al., 2007, 2019; Cornell et al., 2009), a period which overlaps the proposed depositional age (~1.13-1.28 Ga) of the Broken Hill-type Pb-Zn-Cu-Ag deposits in Aggneys, about 100 km northeast of Springbok (Cornell et al., 2009). The Khurisberg Subgroup, the potential contaminant of the Koperberg magmas, is part of these supracrustal sequences.

The supracrustal sequences were intruded by granitic and mafic intrusive rocks emplaced during Namaquan Orogeny at ~1200Ma (Cornell et al., 2006; Miller, 2012 and references therein), a period marked by ubiquitous magmatism in other domains of the NNMP as exemplified by the emplacement of S- and A- granites, and ferroan granites in the Kakamas and Areachap Domains, respectively (Cornell et al., 2006; Bial et al., 2015a; Bailie et al., 2017). The magmatism has been interpreted to be linked to thinning of the lithosphere in a back-arc environment (Bial et al., 2016) or to amalgamation of the southern and northern parts of the Bushmanland Domain (Miller, 2012, and references therein). This period is locally referred to as the Okiepian episode (1210-1180 Ma) of the Namaquan Orogeny by Clifford et al. (2004), and Kibaran episode (1220-1170 Ma) by Robb et al. (1999). In contrast to a period of tectonic quiescence and no magmatic activity from this episode until the ~1030 Ma orogenic event (the 1060-1030 Ma Namaquan Orogeny, Robb et al., 1999; the 1040-1020 Ma Klondekian episode, Clifford et al., 2004), more recent research suggests a continuum of magmatic activity during this period in the Bushmanland Domain and other domains in the NNMP (e.g., Bial et al., 2015a,b; Macey et al., 2018; Fig. 2.1). Macey et al. (2018) have redefined the timing of intrusion of the granitic Spektakel Suite which had been traditionally considered as coeval with the intrusion of the Klondekian/Namaquan orogenic event to between 1097 Ma and 1033 Ma. Macey et al. (2018) have therefore suggested the discontinuation of the terms O'okiepian and Klondekian, hence the terms are more applicable in a local OCD context.

The oldest of the granitoids are the pre- to syn-tectonic gneisses of the Little Namaqualand Suite and the post-tectonic gneisses of the Aggeneys Suite emplaced at ~1220−1170 Ma (Robb et al., 1999; Clifford et al., 2004; Cornell et al., 2009) coeval with magmatism in all other domains of the NMC (Pettersson et al., 2007; Cornell et al., 2009; Bial et al., 2015a). The end of this period also marks the initial emplacement of mafic sills dated between 1109 Ma and 1168 Ma, which are interpreted as protoliths of the two-pyroxene granulite unit of the Oorkraal Suite (Clifford et al., 1981; Robb et al., 1999; Raith et al., 2003; Table 2.1). These mafic dykes are the clearest indicator of mantle magma involvement, but also most other granitoid rocks in the Namaqua Sector show strong evidence of mantle contributions in their origins (Bailie et al., 2019; Büttner et al., 2021).

The second magmatic phase is represented by the granitoids of the 1097-1033 Ma late- to post-tectonic Spektakel Suite, abundantly exposed outcrop exposure in the central parts of the

Bushmanland Domain (Macey et al., 2018). The Koperberg Suite in the O'okiep and Kliprand areas were emplaced at ~1030 Ma and ~1048 Ma, respectively (Clifford et al., 2004; Bailie et al., 2019). The final episode of magmatism related to the Mesoproterozoic crustal evolution is the emplacement of the Orange River Pegmatite Belt between ~960 Ma and 1038 Ma (Doggart, 2019).

2.2 Geology of the O'okiep Copper District

2.2.1 Lithostratigraphy and geochronology

The lithostratigraphy of the OCD is subdivided into five main entities: (1) a granitic basement, the oldest being the Gladkop Suite in the northern parts of the OCD (Robb et al., 1999; Fig. 2.1); (2) the Okiep Group, a succession of supracrustal metavolcano-sedimentary rocks; (3) intrusive rocks of the Koperberg Suite; (4) the voluminous pre- to post-tectonic granite-gneisses (Modderfontein Granite Gneiss, Nababeep Granite Gneiss, Concordia Granite, Kweekfontein Granite and Rietberg Granite); and (5) the Neoproterozoic sedimentary rocks of the Nama Group (e.g., Lombaard et al., 1986; Fig. 2.1).

The orthogneisses of the Gladkop Suite are comprised of three units sequentially emplaced at ~1820 Ma, which are the fine-grained granodioritic Steinkopf Gneiss (1816 ± 8 Ma; Nke et al., 2020), which is intruded by the K-feldspar megacrystic Brandewynsbank gneiss (1824 ± 36 Ma, Robb et al., 1999; 1822 ± 36 Ma, Nke et al., 2020), and the Noenoemaasberg gneiss (1822 ± 70, Barton, 1983; 1825 ± 10 Ma, Nke et al., 2020).

The Okiep Group consists of the aluminous metasedimentary rocks of the Khurisberg Subgroup that is overlain by metavolcano-sedimentary rocks of the Lammerhoek Subgroup (Lombaard et al., 1986). Metasediments of the Khurisberg Subgroup record sources of Eburnian ages of ~2000 Ma (Clifford et al., 2004) and deposition ages of between ~1650 Ma and ~1200 Ma, based on correlations with the Bushmanland Group (Eglington, 2006; Bailie et al., 2007).

The Khurisberg Subgroup is subdivided into three main subunits (or formations) which are, from the southern to the northern parts of the OCD, (i) the Springbok Formation, (ii) the Wolfram Schist (or Wolfram Formation), and (iii) Ratelpoort Formation (Benedict et al., 1964; South African Committee for Stratigraphy, 1980; Fig 2.1). The Springbok Formation occurs in the southernmost parts of the OCD and is the structurally deepest subunit of the Khurisberg Subgroup (Benedict et al., 1964). It comprises metaquartzites, quartz-biotite-garnet-sillimanite schists (Benedict et al., 1964; Raith and Harley, 1998) and minor sapphirine-cordierite-orthopyroxene-phlogopite schists (Clifford et al., 1975b). The Wolfram Schist mainly occurs as rafts at the base of the Concordia Granite and is dominated by garnet-biotite-sillimanite schists (Söhnge, 1950). The Wolfram Schist hosts small exogranitic W-Mo deposits hosted in wolframite-bearing quartz veins that have been mined in places like Narrap and Nababeep (Söhnge, 1950; Bowles, 1988; Raith and Prochaska, 1995). The Ratelpoort Formation occurs in the northernmost parts of the OCD and is the structurally

shallowest subunit of the Khurisberg Subgroup. It is dominated by metaquartzites and quartz-biotite-garnet-sillimanite shists with minor quartz conglomerate, banded iron formation, and calc-silicate rocks (Benedict et al., 1964).

The Lammerhoek Subgroup forms part of the Kaip Antiform in the southern parts of the OCD (Fig. 2.1) and consists of quartz-felspar-biotite gneisses and granulites with minor proportions of quartzite, conglomerate, amphibolite and calc-silicates (Lombaard et al., 1986; Clifford et al., 2004).

Mesoproterozoic granitoids and the Koperberg Suite intrude, and hence post-date the Okiep Group. Table 2.1 shows the lithostratigraphic relations and geochronology of the intrusive rocks. The oldest Mesoproterozoic intrusive rocks are the volumetrically most abundant granitic rocks of the Little Namaqualand Suite (Marais and Joubert, 1980), which includes the Nababeep and Modderfontein Granite-Gneisses.

The Nababeep Granite-Gneiss, which commonly occurs as a quartz-feldspar-biotite augen-textured- or well-foliated orthogneiss, is intruded by the quartz-microcline Modderfontein Granite prior to their tectonic overprint (Raith, 1995; Robb et al., 1999). The Nababeep and Modderfontein Granite Gneisses have emplacement ages of ~1200 Ma (Table 2.1, Fig. 2.2). The tectono-metamorphic overprint has been dated as ~1030 Ma, coeval with the emplacement of the Koperberg Suite in the OCD (Table 2.1; Fig. 2.2).

The Little Namaqualand Suite is intruded by the Concordia, Kweekfontein and Rietberg Granites that have been traditionally grouped as the Spektakel Suite (Marais and Joubert, 1980; Lombaard et al., 1986). Recent interpretations however suggest exclusion of the Concordia and Kweekfontein Granite from the Spektakel Suite (Table 2.1; Macey et al., 2018). The emplacement age for the Concordia Granite is still not well constrained (Macey et al., 2018). Emplacement ages of ~1060 Ma, ~1160 Ma and ~1200 Ma have been proposed (Robb et al., 1999; Clifford et al., 2004; Macey et al., 2018; Fig. 2.2; Table 2.1). Either of these ages indicates that the Concordia Granite predates the Koperberg Suite, which is consistent with crosscutting relationships in the field.

The Concordia Granite forms a 1500 m-thick extensive sheet of locally garnetiferous medium- to coarse-grained leucogranite which is strongly foliated at the base and grades into a porphyritic texture in the upper parts (Raith, 1995). The Kweekfontein Granite occurs as irregular sills and dykes which intrude the Concordia Granite (Raith, 1995). The high contents of K, and the peraluminous character of the Concordia and Kweekfontein Granites have been interpreted as pointing to their derivation from anatexis of a pelitic source (Raith, 1995; Duchesne et al., 2007). The Rietberg Granite forms an extensive sheet of porphyritic quartz-microline-biotite granite or biotite syenite (Lombaard et al., 1986). The Rietberg Granite is the youngest of the granitic intrusions and was emplaced contemporaneously with the Koperberg Suite at ~1035 Ma (Table 2.1; Clifford et al., 2004).

The Koperberg Suite, locally referred to as “noritoids or basic bodies” (Stumpfl et al., 1976) hosts Cu-sulphide mineralization in the OCD (see Chapter 2.3.3 for detailed descriptions). The suite was emplaced within the granite-gneisses of the Little Namaqualand Suite or the Concordia Granite and the metasedimentary country rocks as magmatic pulses between 1060 Ma and 1030 Ma (Robb et al., 1999; Clifford et al., 2004; Table 2.1; Fig. 2.2; see section 2.3.3 for detailed descriptions).

The Neoproterozoic Nama Group overlies unconformably the magmatic and metamorphic rocks of the Namaqua basement (Fig. 2.1). It comprises a 400-thick sedimentary sequence of limestone, shale, sandstone, and conglomerate deposited between ~520 and 550 Ma in the foreland basin of the Pan-African Gariep Belt further west (Fig.1.1; Lombaard et al., 1986). These rocks underwent low-grade metamorphism during the late-Pan-African Damaran orogenic phase (Clifford and Barton, 2012, and references therein).

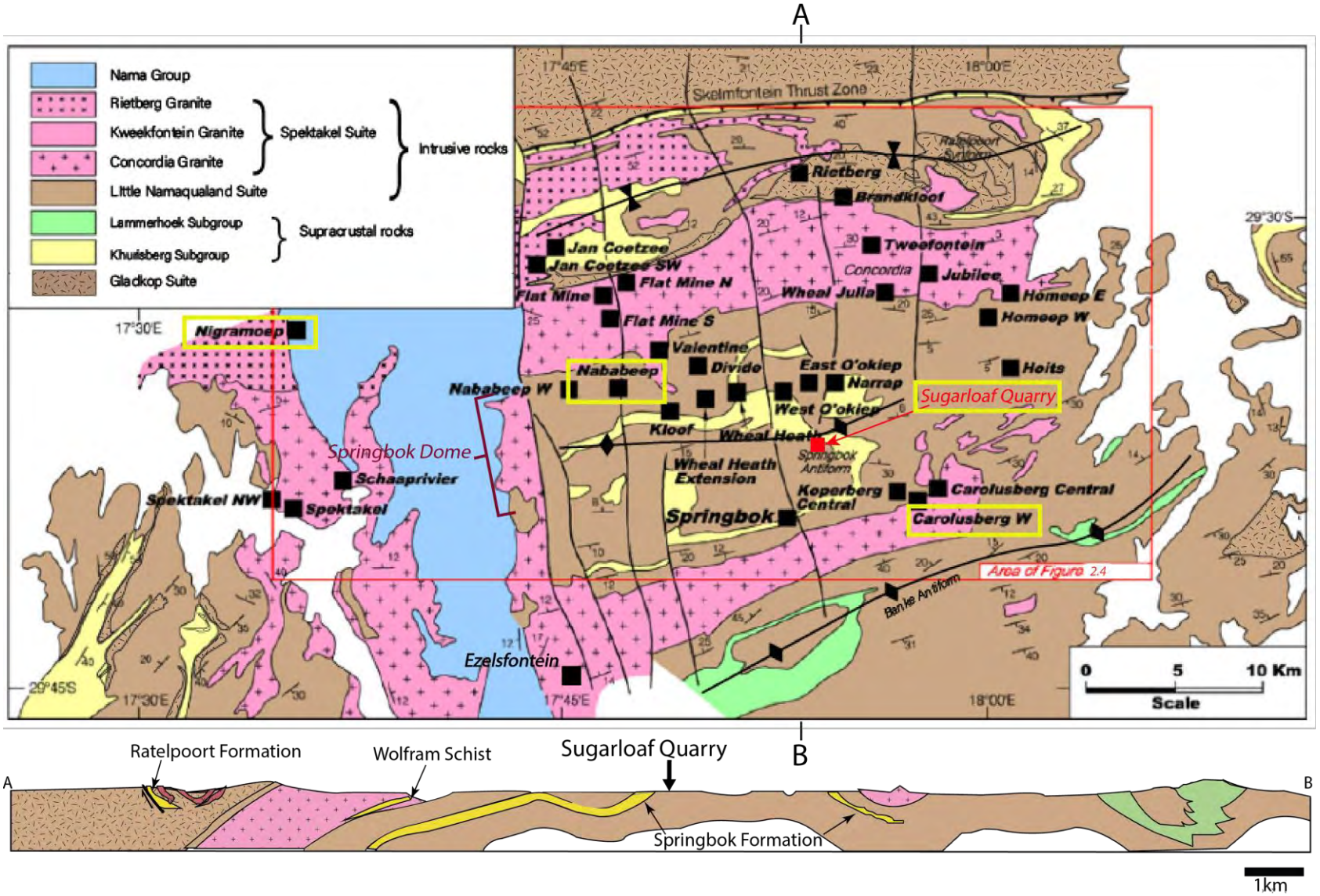

Figure 2. 1 Geological map and cross-section of the O'okiep Copper District. Lithostratigraphic positions of the Khurisberg Subgroup subunits (the Springbok Formation, Wolfram Schist, and Ratelpoort Formation) shown in the cross-section. Locations of historical and operational copper mines depicted as black squares. The location of Sugarloaf Quarry is depicted as red square. Sample localities are highlighted in yellow (modified after Lombaard et al., 1986; Clifford and Barton, 2012).

2.2.2 Structure and metamorphism

The earliest deformation (D_1) in the Bushmanland Domain is recorded as tight intrafolial folds (F_1) within gneissic layering of older gneissic units (e.g., Joubert, 1986b). The second deformation event (D_2 of Clifford et al. (2004); D_1 of Cornell et al. (2009)) is deemed the most pervasive in the Namaqua Sector (Miller, 2012). Macey et al. (2018) have subdivided the D_2 event in the Bushmanland Domain into three stages: (1) the~1200 Ma D_{2a} event characterised by syn-deformational magmatism and metamorphism in all domains in the Namaqua Sector, (2) the D_{2b} event characterised by extension and sediment deposition across most parts of the Namaqua Sector, including the Kakamas and Kaaien Domains in the east, at ~1160 Ma, and subsequently (3) the D_{2c} event characterise by reshuffling of crust and thrusting (D_{2c}) to produce penetrative E-W-striking subhorizontal gneissosity (S_2) at ~1110 Ma (Fig. 2.2). The second deformational event (D_2) or D_{2a} (Raith and Harley, 1998) produced the pervasive subhorizontal gneissosity observed in the Nababeep and Modderfontein Granite Gneises, and the lower parts of the Concordia Granite. D_3 is linked to the formation of large-scale upright folds (F_3) by rotation of pre-existing D_2 fabrics. In the OCD, D_3 resulted in reactivation of the Skelmfontein Thrust (Blignault et al., 1983). The event manifested as regional open folds (e.g., Springbok Dome, Springbok Synform, Ratelpoort Synform; Fig. 2.1, Kisters et al., 1993, 1996), and structures related to the emplacement of the Koperberg Suite locally referred to as "steep structures" (D_{3b} event of Clifford and Barton, 2012; see Chapter 2.3.3.2 for more detail). The D_3 deformation event is also associated with the emplacement of the Spektakel Suite mostly in the central parts of the Bushmanland Domain between 1097 Ma and 1033 Ma (Macey et al., 2018). Dewey et al. (2006) have suggested that D_3 was a transtensional event accompanied by ultra-high temperature metamorphism and intrusion of the Spektakel and Koperberg Suites due to mafic underplating during the Namaquan Orogeny. The last major deformation event (D_4 of Joubert, 1986b; D_5 of Kisters et al., 1996) produced NNW-trending right-lateral normal faults related to the Gariep Orogeny.

The Bushmanland Domain exhibits symmetric metamorphic zonation – upper granulite facies in the central parts of the domain, flanked by lower granulite facies zones, and amphibolite facies zones in the outermost northern and southern parts of the domain (Waters, 1986). The domain has undergone at least two major cycles of metamorphism (M_2 and M_3), after the postulated Paleoproterozoic M_1 event related to the D_1 (e.g., Cornell et al., 2006). The sequencing of the metamorphic events has been interpreted in two ways, leading to the proposition of an anticlockwise and a clockwise pressure-temperature-time path (Raith and Harley, 1998; Clifford et al., 2004; Clifford and Barton, 2012). In the lower granulite facies zone, in which the study area lies, an anticlockwise path is proposed to be characterised by a prograde amphibolite facies stage (>550^{o}C, 3.5 kbar) synchronous with D_2, and a subsequent upper granulite metamorphic peak (750-870^{o}C, 4.5-6 kbar) reached during D_3 between ~1.06 Ga and 1.03 Ga (Waters, 1986, 1989; Robb et al., 1999). In contrast, a clockwise path is proposed as syn-D_2 granulite facies metamorphism (750-870^{o}C, 5-6 kbar; Clifford et al., 1981; Raith and Harley, 1998) related to magmatism at ~1200 Ma,

followed by ~150 Ma of tectonic quiescence and isobaric cooling, and subsequent upper amphibolite facies metamorphism (M_3 of Clifford et al., 2004 or M_{3a} of Raith and Harley, 1998) at PT conditions of 580-660°C/5.8 ± 0.5 kbar (Raith and Harley, 1998). The Koperberg Suite was emplaced during this event at ~1030 Ma (Clifford et al., 2004; Clifford and Barton, 2012).

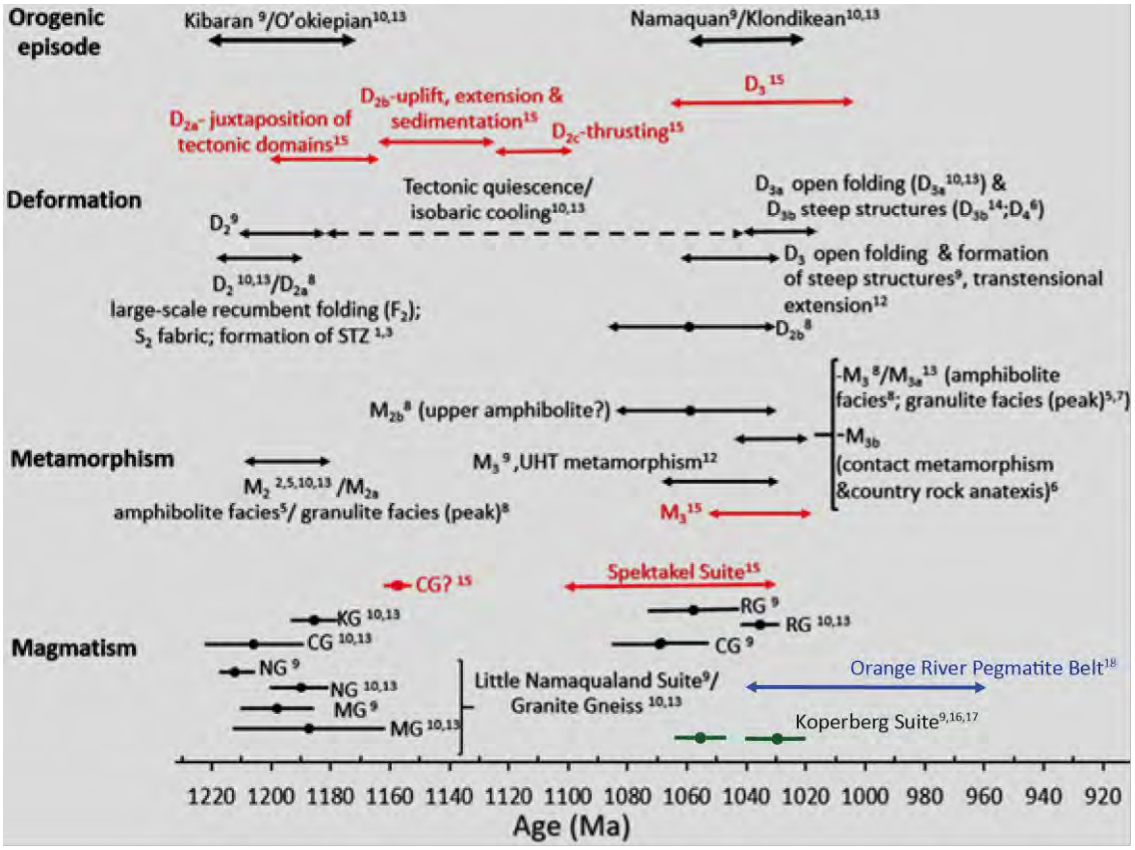

Figure 2. 2 The timing of the main magmatic, metamorphic, deformation and related orogenic events in the Bushmanland Domain and the OCD in the Mesoproterozoic. These episodes overprint the Palaeoproterozoic basement and form new Mesoproterozoic crust. STZ: Skelmfontein Thrust Zone, UHT: Ultra-high temperature, NG: Nababeep Granite, MG: Modderfontein Granite, KG: Kweekfontein Granite, CG: Concordia Granite, RG: Rietberg Granite. Reinterpretation by Macey et al. (2018) depicted in red. References: [1] Joubert, (1986) [2]Clifford et al. (1981), [3] Blignault et al., (1983), [4]Barton (1983), [5]Waters (1989), [6]Kisters et al. (1996), [7]Gibson et al. (1996), [8]Raith and Harley (1998), [9]Clifford et al., (2004), [11]Cornell et al., (2006), [12]Dewey et al., (2006), [13]Clifford and Barton (2012), [14]Macey et al., (2017), [15]Macey et al. (2018), [16]Clifford et al. (2004), [17]Robb et al. (1999), [18]Doggart (2019).

Table 2. 1 A summary of lithostratigraphic relations and geochronology of intrusive rocks in the OCD.

Intrusive member	**Emplacement age (Ma)**	**Metamorphic age (Ma)**	**Suite/Group**	**Mineralogy & petrographic classification**	**Field characteristics & geochemical interpretations**	**Associated orogenic event**
Nababeep Granite Gneiss	1179 ± 28 [4] 1192 ± 9 [2] 1212 ± 11 [1] 1223 ± 48 [3]	1037 ± 12 [2]	Little Namaqualand Suite[6]/Granite Gneiss[12]	- Qz, Kfs, Bt[8] - Augen-textured orthogneiss/coarse-grained granite[8]	-Voluminous sheet-like intrusion[8] -produced by syn-tectonic anatexis of Proterozoic crust [13]	-Kibaran[1]/ O'okiepian[2] - *DUT[7*]
Modderfotein Granite Gneiss	1187 ± 25 [2] 1199 ± 12 [1]	1039 ± 11 [2] 1032 ± 12 [1]	Little Namaqualand Suite[6]/Granite Gneiss[12]	- Qz, Kfs[9] - Augen-textured orthogneiss/coarse-grained granite[8]	-voluminous sheet-like intrusion[8] -produced by syn-tectonic anatexis of Proterozoic crust [13]	Kibaran[1]/ O'okiepian[2] - *DUT[7*]
Kweekfontein Granite	1186 ± 15		Spektakel Suite[6]	- Qz, Kfs, Plag, Bt, Ms [7,8] - leucogranite[7]	-devoid of tectonic fabric[8] -occurs as irregular dyke- or sill-like intrusions[1] - A-type granite[10]	Kibaran[1]/ O'okiepian[2] - *DUT[7*]
Two-pyroxene granulite[11]/ hornblende gneiss[8]	1160 ± 50 [5] 1163 ± 9 [1]	1063 ± 16 [1]	-Little Namaqualand Suite[1] -Lammerhoek Subgroup[8]	-Hyp, Di, Pl, Hbl ± Bt[8,11] -granulite[8,11]	-occurs mainly as up to 60m-thick rafts within the Nababeep Granite Gneiss[8] -intruded as a mafic sill into the Nababeep Granite at ~1163 Ma and underwent granulite-facies metamorphism at ~1063 Ma[1,5]	-Kibaran[1] - *DUT[7*]
Concordia Granite	1060 ± 69 [3] 1064 ± 31 [1] 1161 ± 10 [7] 1206 ± 16 [2]	861 ± 45 [1] 1055 ± 23 [2]	-Spektakel Suite[6] - *DUT[2*]/ **Excl.[7*]	-Kfs, Qz, Pl, Ms ± Grt[9] -leucogranite[9]	-voluminous sheet-like intrusion[8] -parental melts derived from dehydration melting of a pelitic source[9,10] - S-type granite[9,10]	-Namaquan[1]/ O'okiepian[2] - *DUT[7*]

Table 2.1 (continued)

Intrusive member	Emplacement age (Ma)	Metamorphic age (Ma)	Suite/Group	Mineralogy & petrographic classification	Field characteristics & geochemical interpretations	Associated orogenic event
Concordia Granite					-parental melts derived from dehydration melting of a pelitic source[9,10] -occurs as irregular dyke- or sill-like intrusions[8] - S-type granite	
Rietberg Granite	1058 ± 30 [1] 1035 ± 13 [2]	841 ± 23 [1]	-Spektakel Suite[6, 7*] - *DUT[2*]	Kfs, Pl, Bt, Qz[7,9] -Granite[7,9]/ biotite syenite[9]	-porphyritic sheet-like intrusions[9] -post collisional A-type granite[10]	-Namaquan[1]/Klondikean[2] - *DUT[7*]
[#]Orthopyroxene monzonite (jotunite)[2*]	1035 ± 13 [2]		Koperberg Suite[2]	Hyp, Di, Pl, Hbl ± Bt[8,11]	-progenitors of the other members of the Koperberg Suite[10]	
Anorthosite	1029 ± 10 [2]		Koperberg Suite[2]	Pl ± Bt [14]	-early members of the Koperberg Suite [14]	-Namaquan[1]/Klondikean[2] -*DUT[7*]
Diorite	1029 ± 10 [3] 1030 ± 6 [2] 1057 ± 8 [1]		Koperberg Suite[2]	Pl, Hyp ± Bt ± Ap ± Opq [14]	-commonly intrudes anorthosite members of the Koperberg Suite	-Namaquan[1]/Klondikean[2] - *DUT[7*]
Hypersthenite	1035 ± 33 [2] 1037 ± 8 [1]		Koperberg Suite[2]	Hyp ± Bt ± Opq	- commonly intrudes diorite members of the Koperberg Suite	-Namaquan[1]/Klondikean[2] - *DUT[7*]
Breccia granite	1018 ± 20 [2]		Koperberg Suite[2]	-Qz, Kfs, Pl, Bt, Opx ± Grt ± Zrn ± Hbl	-forms granitic matrix (~5-90 % vol.) of megabreccias[8,15] -devoid of tectonic fabric at outcrop scale[15]	-Namaquan[1]/Klondikean[2] - *DUT[7*]

[#]Orthopyroxene monzonite (jotunite) previously regarded as "two-pyroxene granulite"[11] or "hornblende gneiss"[8]. *DUT: Discontinued use of the term for suite or orogenic event accordingly. **Excl.: intrusive member excluded from previously assigned Suite. Mineral abbreviations after (Whitney and Evans, 2010). References: [1]Robb et al. (1999), [2]Clifford et al. (2004), [2*]Reinterpretation by Clifford et al. (2004), [3]Clifford et al. (1995), [4]Barton (1983), [5]Clifford et al. (1981), [6] Marais and Joubert (1980), [7]Macey et al. (2018), [7*] Reinterpretation by Macey et al. (2018), [8]Lombaard et al. (1986), [9]Raith (1995), [10]Duchesne et al. (2007), [11]Clifford et al. (1975), [12]Clifford and Barton (2012), [13]Joubert (1986b), [14]Conradie and Schoch (1986), [15]Kisters et al. (1998).

This implies that the Koperberg Suite was emplaced into hot mid-crustal rocks at upper amphibolite or granulite facies temperatures. The last regional metamorphic event (M_4) is a retrograde greenschist facies overprint (300-400 ^oC) related to the ~500 Ma Pan-African orogeny (e.g., Raith and Prochaska, 1995).

2.2.3 Koperberg Suite

2.2.3.1 Petrology

The Koperberg Suite consists of a range of mafic to felsic rocks which include orthopyroxene monzonite (jotunites), andesine anorthosites, biotite diorites, hypersthene-bearing-leuconorites, norites and melanorites, and hypersthenites (Conradie and Schoch, 1986; Duchesne et al., 2007). The most prevalent rock types are anorthosites, hypersthenites and biotite diorites (McIver et al., 1983; Conradie and Schoch, 1986).

The orthopyroxene monzonites are an enigmatic lithology that has been historically termed the "two-pyroxene granulite" (Clifford et al., 1975; Robb et al., 1999; Table 2.1) or "hornblende gneiss" (Lombaard et al., 1986). These rocks have been interpreted both as xenoliths of the supracrustal Lammerhoek Subgroup within the granite-gneiss country rocks (Lombaard et al., 1986) or as a mafic sill emplaced into the Nababeep Granite Gneiss at ~1163 Ma that underwent granulite-facies metamorphism at ~1063 Ma, coeval with emplacement of the Concordia Granite (Robb et al., 1999). Subsequent work has corroborated earlier interpretations by van Zyl (1978) that the orthopyroxene monzonites are earlier members of the Koperberg Suite, and they have thus been interpreted as parental to anorthosites and other members of the Koperberg Suite (Clifford et al., 2004; Duchesne et al., 2007).

The mineral composition of the Koperberg Suite is relatively simple. The main silicate phases are plagioclase (An_{31-52}), hypersthene (En_{58-68}), biotite-phlogopite and quartz (Stumpfl et al., 1976; Conradie and Schoch, 1986; Cawthorn and Meyer, 1993; van Zwieten et al., 1996). Rounded and tabular apatite is abundant in the mafic varieties of the Koperberg Suite (Conradie and Schoch, 1988). Clinopyroxene, hornblende and zircon are rare (Stumpfl et al., 1976; Lombaard et al., 1986) and monazite is common accessory phase (Stumpfl et al., 1976).

Copper mineralisation in the Koperberg Suite is associated with the more mafic members of the Koperberg Suite (Latsky, 1942; Benedict et al., 1964; van Zyl, 1978). Sulphides occur as individual crystals or as pairs, interstitial to silicate phases, in association with oxide phases or replacing oxides, and along biotite cleavage planes (Conradie and Schoch, 1986; Cawthorn and Meyer, 1993). The principal sulphide phases are bornite and chalcopyrite, with chalcocite occurring as an alteration product of bornite (Stumpfl et al., 1976). Pyrrhotite, chalcopyrite, and minor pentlandite (Narrap-type ore) are a rare assemblage restricted to East Okiep, Narrap, and Wheal Heath mines (Lombaard et al., 1986). Pyrite is a minor phase but common in most of the ore bodies. Sphalerite

and galena have been documented at Okiep and Carolusberg mines but are of no economic significance (Stumpfl et al., 1976). Other trace ore phases include vallerite, linnaite, native copper, molybdenite, niccolite, molenite, sylvanite, and tetradymite (Lombaard et al., 1986).

Magnetite is an ubiquitous phase in the Koperberg Suite, whereas ilmenite is less abundant and mainly occurs as exsolution lamellae in magnetite (Conradie and Schoch, 1986). In some places, hematite with ilmenite and rutile forms as an alteration of magnetite (Stumpfl, 1978). Based on the textural relations and alterations, microscopic studies on the Koperberg Suite have suggested the following sequence of stages in the deposition of the suite as: (1) crystallisation of silicates, (2) hydration of silicates and oxides, and (3) contemporaneous deposition of sulphides, with chalcopyrite being a slightly later phase (Stumpfl et al., 1976; Stumpfl, 1978; McIver et al., 1983).

2.2.3.2 Distribution, field relationships, and emplacement models

Field relationships point to the emplacement of the more felsic members (anorthosites) of the Koperberg Suite followed by intrusion by more mafic members (biotite-diorite and hypersthene-rich rocks) (Conradie and Schoch, 1986; Van Zwieten et al., 1996). The Koperberg Suite generally also exhibits sharp contacts with no discernible chilled margins, consistent with intrusion at granulite facies metamorphic conditions (Lombaard and Schreuder, 1978; Lombaard et al., 1986). Elongated xenoliths of the country rocks aligned along the walls of the Koperberg Suite intrusions are common (Lombaard et al., 1986).

The Koperberg Suite occurs as a swarm of ~1700 irregular E-W-trending dyke-, sill- or plug-like intrusions (McIver et al., 1983). The plug-like intrusion and sills are not common and are restricted to the upper and lower stratigraphic levels of the granite-gneiss country rocks, respectively (Kisters et al., 1994). The Koperberg Suite dykes are commonly >1 km in length and their width is commonly ~60-100 m (Lombaard et al., 1986). These intrusions are mostly hosted within unique structures termed “steep structures” (e.g., Benedict et al., 1964) which are antiformal structures characterised by the rotation of the subhorizontal gneissosity of the granite-gneiss country rocks to subvertical attitudes with increasing proximity towards their central parts of the steep structure or the Koperberg Suite body (Fig. 2.3; Lombaard and Schreuder, 1978; Kisters et al., 1994). The length along strike of the steep structures varies from ~30 m to 7 km, the common range being 500 m to 1 km; and width of ~3-500 m, the common range being ~50-100 m (Fig. 2.4; Lombaard and Schreuder, 1978; Lombaard et al., 1986).

The emplacement of the Koperberg Suite is proposed to have been controlled by pre-existing anisotropies in the granite-gneiss country rocks such as stratigraphic contacts and gneissosity (S_2 and S_3) (Kisters et al., 1994, 1996) or cusp-like folds developed due to large competence contrasts at the interface between a deep-seated magma chamber (source of the Koperberg Suite magmas) and the relatively competent granite-gneiss country rocks during the D_3 event (Watkeys, 1996).

According to Kisters et al. (1994), each of the geometries (sill-, dyke, diapir-like) exhibited by the Koperberg Suite bodies is related to emplacement at specific stratigraphic levels in the granite-gneiss country rocks as a function of composition (and hence viscosity). The authors proposed that the sill-like bodies were emplaced earlier in the deformation history before the pronounced rotation of S_2 foliation as exemplified by development of sills mainly along stratigraphic contacts and along the subhorizontal gneissosity in the granite-gneiss sequence. The mafic members of the Koperberg Suite (norites and hypersthenites) are dominantly dykes and are interpreted to have exploited the subvertical S_3 foliation which crosscuts stratigraphic contacts (Kisters et al., 1994). Diapir-like Koperberg Suite bodies that exhibit tear-drop morphologies are dominantly composed of felsic phases (anorthosites and diorites) and have been predominantly emplaced at higher stratigraphic levels (upper parts of the Concordia Granite and the Rietberg Granite), indicating higher viscosity and hence lower buoyancy of the magmas relative to the country rocks (Kisters et al., 1994).

Watkeys (1996) proposed the following set of events culminating in the emplacement of the Koperberg Suite: (1) drawing in of magma (from the deep-seated magma chamber) into sites of least compressive stress (the cores of the cusp-like folds), (2) decrease in the competence contrasts between emplaced rock bodies of the Koperberg Suite and the granite-gneiss host rocks as the crystallisation of intrusive bodies progressed, leading to subsequent decoupling of intrusive bodies within cusps and their migration to higher stratigraphic levels, (3) cessation of the migration of the bodies due to increasing viscosity with cooling. The migration process was also characterised by lower strain rates which manifested in ductile vertical dragging of the wall rocks undergoing granulite-facies metamorphism (Watkeys, 1996). In line with the interpretation by Watkeys et al. (1996), steep structures might not be related to any deformational event or pre-existing structures but are a product of dragging of foliation of the labile granite-gneisses undergoing granulite-facies metamorphism by the intruding Koperberg Suite bodies (S. Büttner, 2019, pers. comm).

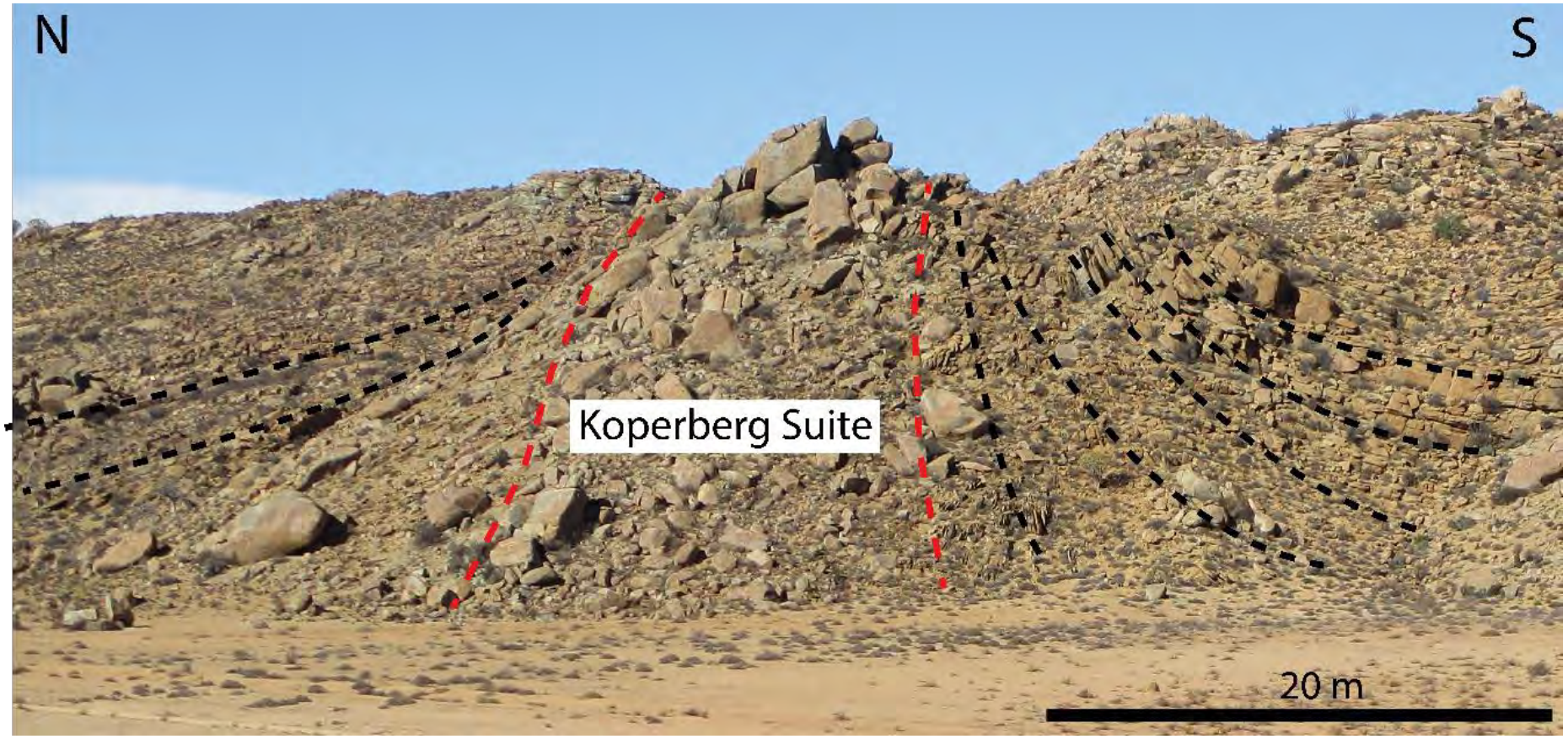

Figure 2. 3 The Klondike East steep structure located ~5 km north of Okiep showing a Koperberg Suite dyke in the central parts of the steep structure (red dashed lines). Note the dragging or the rotation of the subhorizontal foliation of the Nababeep Granite Gneiss (black dashed lines) to subvertical attitude with increasing proximity to the Koperberg Suite dyke in the centre of the steep structure.

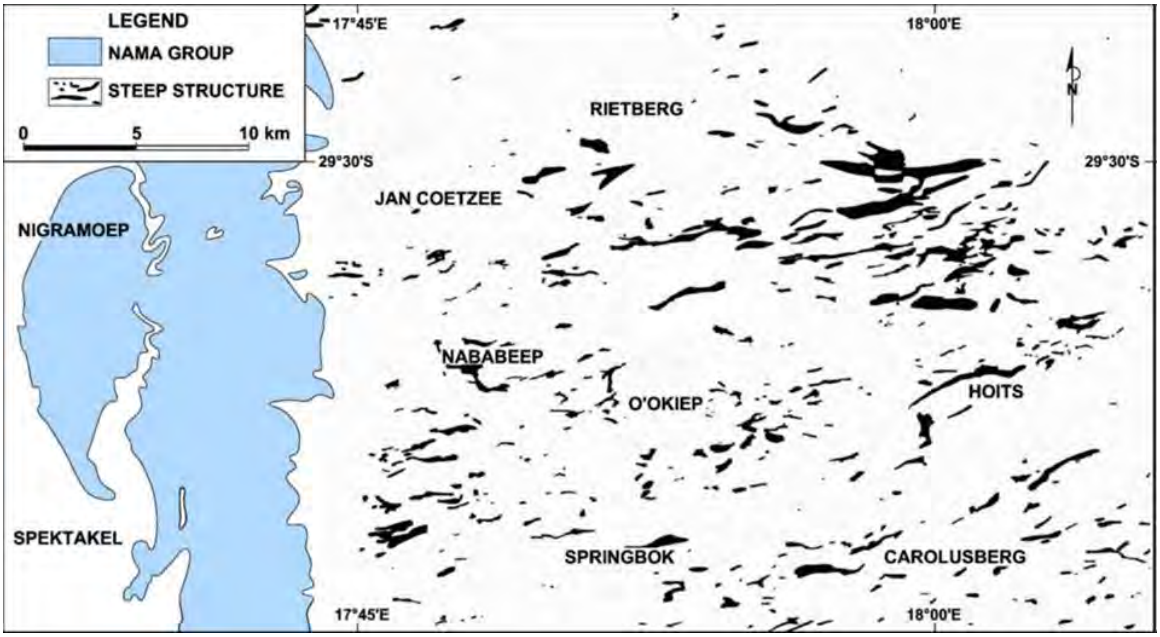

Figure 2. 4 The distribution of steep structures within the O'okiep Copper District (modified after Clifford and Barton, 2012).

2.2.3.3 Proposed petrogenetic models for the Koperberg Suite

The petrogenesis of the Koperberg Suite, particularly the source of magmas has been interpreted in a number of different models (e.g., Maier, 2000; Maier et al., 2012). Since the recognition of the Koperberg Suite as a suite of magmatic intrusions (Lombaard and Schreuder, 1978), four main petrogenetic models have been proposed: (i) differentiation model (Latsky, 1942; van Zyl, 1978; Lombaard et al., 1986), (ii) the contamination model (Schoch and Conradie, 1990; Boer et al., 1994; Brandriss and Cawthorn, 1996; van Zwieten et al., 1996; Geringer et al., 1998), (iii) the crustal melting model (Clifford et al., 1995, 2004; Duchesne et al., 2007), and (iv) the Iron-Oxide-Copper-Gold (IOCG) deposit model (Maier et al., 2012).

Differentiation model

The differentiation model is one of the earliest petrogenetic models proposed (Lombaard et al., 1986). The model is based on the lack of post-intrusive differentiation of the Koperberg Suite bodies and the intrusive relationships of the different phases of the Koperberg Suite (i.e., the intrusion of early felsic members followed by more basic members), a phenomenon which the proponents of the model interpreted as indicative of extensive differentiation of the Koperberg Suite magmas in a deep-seated magma chamber prior to their emplacement (Latsky, 1942; van Zyl, 1978; Lombaard et al., 1986). As such, the Koperberg Suite is interpreted to have been emplaced by tapping off the top of a differentiated magma reservoir and sequential emplacement of progressively more basic fractions.

Contamination model

This model proposes that basaltic mantle magmas were subsequently subjected to crustal contamination in the mid- to lower crust at upper amphibolite- to granulite facies conditions (Schoch and Conradie, 1990; Boer et al., 1994; Brandriss and Cawthorn, 1996; van Zwieten et al., 1996; Geringer et al., 1998).

The crustal contamination model is based on the following observations and lines of evidence:

(1) The high initial $^{87}Sr/^{86}Sr$ values (0.722-0.727) and low anorthite content (An_{31-41}) of the felsic members (leucotonalites and anorthosites), and the low initial $^{87}Sr/^{86}Sr$ values (0.706-0.720) and high anorthite content (An_{39-44}) of the more mafic members (diorites, monzodiorites, leucodiorites and leuconorites). This is deemed indicative of hybridization of two genetically-distinct components, a radiogenic LILE-rich tonalitic-anorthositic (felsic) component with initial $^{87}Sr/^{86}Sr$ values of 0.722-0.727 derived from granitic crust, and a less radiogenic dioritic (mafic) derived from the mantle with initial $^{87}Sr/^{86}Sr$ values of ≤ 0.710 (Brandriss and Cawthorn, 1996). Alternatively, high degrees of contamination of the earlier anorthositic members and minimum degrees of contamination for the more mafic members by granitic contaminant with high initial Sr values may explain the different isotopic signatures (van Zwieten et al., 1996).

(2) The discordance of enstatite (En_{60}) and anorthite (An_{40}) contents of coexisting orthopyroxene and plagioclase (which are normally similar in mafic intrusions) interpreted as indicative of the assimilation of a granitic contaminant (probably the Nababeep Granite-Gneiss) which lowered the Ca/Na ratios and hence lowering the An values of plagioclase in mafic magmas, whereas the En values remained unaffected (van Zwieten et al., 1996).

(3) The abundance of orthopyroxene (coupled with the paucity of olivine), a common phenomenon in anorthositic complexes produced by basaltic melts derived from the mantle below thickened crust that have undergone crustal contamination (Schoch and Conradie, 1990).

(4) The low ε_{Nd} values (-8 to -10) of the Koperberg Suite which could have been produced by an enriched mantle source (ε_{Nd} < -10, ε_{Sr} >700) contaminated by Proterozoic crust (ε_{Nd} -4, ε_{Sr} >700), and extreme differentiation for long periods before the subsequent emplacement of the Koperberg magmas (Geringer et al., 1998).

(5) The enriched $\delta^{18}O$ ratios (5.9-9.6 ‰) for mafic rocks of the Koperberg Suite relative to mantle-derived mafic rocks ratios of 5.5-6.0 ‰ (Boer et al., 1994).

(6) The presence of country rock (granite-gneisses) xenoliths in the Koperberg Suite (Lombaard and Schreuder, 1978; Lombaard et al., 1986).

(7) High Rb contents (13-189 ppm) and hence low K/Rb (~236) for mafic rocks belonging to the Koperberg Suite which are atypical of mantle-derived rocks (Boer et al., 1994) .

Additionally, the relatively light $\delta^{34}S$ values (-1.5 to -4.1 ‰) of sulphide minerals from mafic rocks of the Koperberg Suite relative to ratios for mantle-derived rocks (~0‰) has been interpreted by Boer et al. (1994) as pointing to crustal assimilation, increase in oxygen fugacity or sulphur devolatisation. The inverse correlation between $\delta^{34}S$ values and Cu/S ratio, and modification of chalcopyrite-pyrrhotite ore assemblage (Narrap-type ore) to bornite-magnetite ore assemblage (Carolusberg-type ore) is interpreted by the authors as indicative of oxidation and sulphur devolatisation processes during granulite-facies metamorphism (Reaction 1). The high Fe_2O_3/TiO_2 and low S/Se ratios exhibited by modified assemblage (Carolusberg-type ore) corroborate the evidence for oxidation and sulphur devolatisation processes (Cawthorn and Meyer, 1993).

Based on the low Cu/S and S/Se ratios and the $\delta^{34}S$ values atypical of the mantle-derived rocks exhibited by the Carolusberg-type ores, the Carolusberg-type ores are interpreted to be a product of the oxidation and sulphur devolatisation of the primary chalcopyrite-pyrrhotite (Narrap-type ore) during granulite-facies metamorphism.

$$5\ CuFeS_2 + 5\ FeS + 6\ H_2O + [8\ O_2] = Cu_5FeS_4 + 3\ Fe_3O_4 + 6\ H_2S + 5\ SO_2 \qquad (1)$$

Ccp *Po* *Bn* *Mag*

Crustal Melting model

This model proposes that the source of magmas for the country rocks and the Koperberg Suite is a gabbronoritic lower crustal mafic granulite (Clifford et al., 1995, 2004; Duchesne et al., 2007).

Radiogenic isotopic work on some of the granitoids and the Koperberg Suite yielded ε_{Nd} values of -7 for the Concordia Granite, the high $^{87}Sr/^{86}Sr$ and μ ratios (0.7061-0.7272 and 10.1, respectively) coupled with low ε_{Nd} values of -9 for the Koperberg Suite at 1030 Ma, which have been interpreted as indicative of the presence of an ancient lower crustal source in the lithosphere of the Bushmanland Domain (Clifford et al., 1995, 2004).

Duchesne et al. (2007) proposed that the jotunite members of the Koperberg Suite are likely parental magmas to anorthosites, and hence the suite can be classified as a massif-type (Proterozoic) anorthosite complex. This is corroborated by earlier research which also suggested classification of the Koperberg Suite as a massif-type anorthosite complex based mainly on the anorthositic-noritic character of the rocks (Conradie and Schoch, 1986; Schoch and Conradie, 1990). Duchesne et al. (2007)'s proposition is based on experimental work which has shown that parental melts for jotunites are produced by partial melting of plagioclase + two pyroxene rocks at granulite conditions under pressure ranging from 10-13 kbar and corresponding depths of 40-50 km (Longhi et al., 1999; Longhi, 2005).

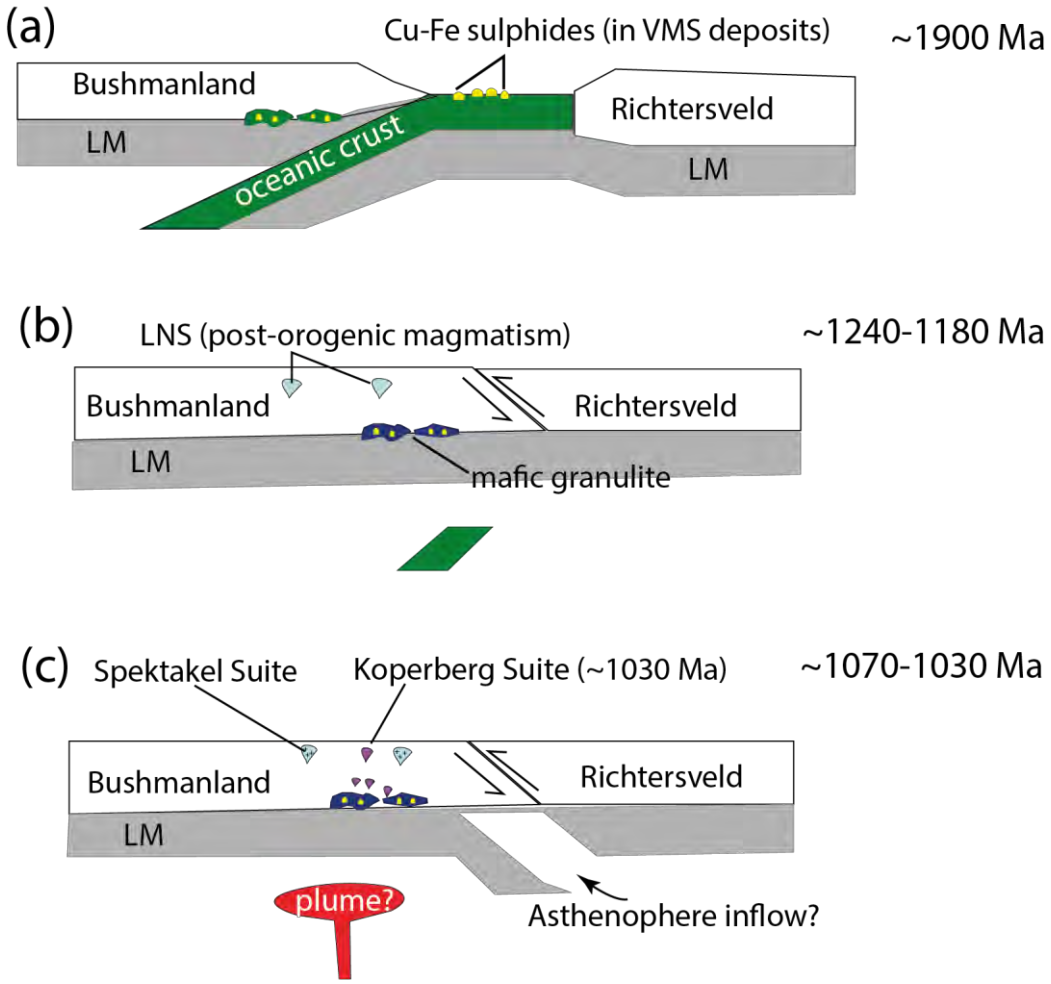

Figure 2. 5 Schematic model of stages leading to the emplacement of the Koperberg Suite according to Duchesne et al. (2007). (a) Incorporation of the oceanic crust with Cu-Fe sulphides into the lower crust at ~1900 Ma. (b) Metamorphism of oceanic crust at granulite facies conditions and the generation of voluminous granitoids related to post-orogenic magmatism between ~1240 and 1180 Ma. (c) Partial melting of crust producing granitoids of the Spektakel Suite and partial melting of the mafic granulites to produce the Koperberg magmas between ~1070 and 1030 Ma. Heat input during the partial melting event related to detachment of subcontinental lithosphere along a major shear zone and asthenosphere inflow or thermal plume beneath the Bushmanland Domain. VMS: volcanogenic massive sulphide, LM: lithospheric mantle, LNS: Little Namaqualand Suite. Not to scale.

To explain the negative ε_{Nd} values (-5 to -11; Clifford et al., 1995; Geringer et al., 1998; Duchesne et al., 2007), the variation in Rb/Sr ratios and initial Sr isotope ratios observed for rocks belonging to the Koperberg Suite at 1030 Ma, Duchesne et al. (2007) proposed the following sequence of events leading to formation of the Koperberg magmas: (1) extraction of magma from the mantle at ~1900 Ma (mean T_{CHUR} and T_{DM} Nd model ages; Clifford et al., 1995) and subsequent formation of LREE-enriched (likely E-MORB) oceanic crust consanguineous with generation of the Richtersveld magmatic arc (cf., Macey et al., 2017), (2) hydrothermal alteration of oceanic crust to yield variation in Rb/Sr ratios, a process possibly accompanied by formation of TAG hydrothermal mound-type massive Cu-Fe sulphide deposits, (3) subduction of oceanic crust and its subsequent incorporation into the lower crust, and metamorphism under granulite facies conditions yielding a mafic granulite (Fig. 2.5 a, b), (4)

emplacement of voluminous granitic material triggered by melting in a post-collisional setting during the O'okiepian episode at ~1190 Ma (Fig. 2.5b), and (5) emplacement of Koperberg magmas triggered by melting of lower crustal mafic granulites under granulite facies conditions at pressures of 10-13 kbar, a process accompanied by remobilization of Cu-Fe sulphide mineralisation to form Koperberg deposits (Fig. 2.5c). Duchesne et al. (2007) also proposed that the inherited LREE-enriched distribution of oceanic crust explain the low ε_{Nd} values (-8.6 ± 1.6; Clifford et al., 1995; Geringer et al., 1998; Duchesne et al., 2007) observed in rocks of the Koperberg Suite.

The temperature rise during the Klondikean episode of the Namaqua Orogeny (~1040 - 1020 Ma; Clifford and Barton, 2012; Clifford et al., 1995) is attributed to a thermal plume or temperature increase at the base of the crust by linear delamination of subcontinental lithospheric mantle along a mega-shear zone (Fig. 2.5c; Lachenbruch et al., 1985; Teyssier and Tikoff, 1998). Thickened crust as a result of intracontinental subduction, that is, Ampferer-type subduction (Clifford et al., 2004) or "crustal tongue" mechanism (underthrusting of lower crust) (Duchesne et al., 1999) has been proposed by Duchesne et al. (2007) to account for the high pressure (10-13 kbar) values.

Iron Oxide Copper-Gold (IOCG) deposit model

The Iron Oxide Copper-Gold (IOCG) deposit model is a composite model proposed by Maier et al. (2012). It is based on a geochemical study of Cu-rich O'okiep deposits (Fig. 2.1), intermediately enriched Eezelsfontein deposits (Fig. 2.1) and Ni-rich Hondekloof deposits near the Kliprand area (Fig. 1.1). Maier et al. (2012) presented a refined petrogenetic model that considers most of the characteristics of the two endmember deposits at O'okiep and Hondekloof.

As with Cawthorn and Meyer (1993), Maier et al. (2012) pointed out that the O'okiep deposits share a number of commonalities with the Caraiba deposits in Brazil, which include high Cu/Ni and Se/S ratios, abundance of bornite and magnetite as main ore minerals, high phlogopite (glimmerites) and apatite contents. Key findings from Maier et al.'s (2012) contribution include the high Au/PGE ratios (similar to those of the subcontinental lithospheric mantle, SCLM) and progressively decreasing Pd/Ir ratios for sulphide-bearing rocks from the O'okiep, Eezelsfontein, and Hondekloof deposits, respectively. Due to the high contents of REE, Th and U exhibited by rocks from O'okiep, Caraiba and Phalaborwa deposits the authors proposed melting of metasomised (fertile) mantle to have led to production of alkaline and volatile-rich source melts for these deposits. Though the O'okiep, Caraiba and Phalaborwa deposits cannot be classified as hydrothermal deposits, the deposits exhibit some of the common characteristics of Iron Oxide Copper-Gold (IOCG) group of deposits which include the occurrence of Cu and/or Au as major economic minerals, abundance of Fe-Ti oxides, and enrichment in LREE, U, Th and P. Hence it has been proposed that the deposits are likely magmatic endmembers of IOCG deposits (Groves and Vielreicher, 2001; Maier et al., 2012). Maier et al. (2012) also noted the occurrence of other unique deposits on or close to the Kaapvaal Craton and the Damara Belt, like the alkali complex-hosted Otjisuzubin copper deposit (Damara Belt), the fayalite-magnetite-fluorite-rich

Vergenoeg Pipe (Kaapvaal Craton) and the Messina copper deposit (Limpopo Mobile Belt). The presence of such deposits was interpreted by the authors as indicative of the presence of fertile sub-continental lithospheric mantle (SCLM) underneath southern Africa.

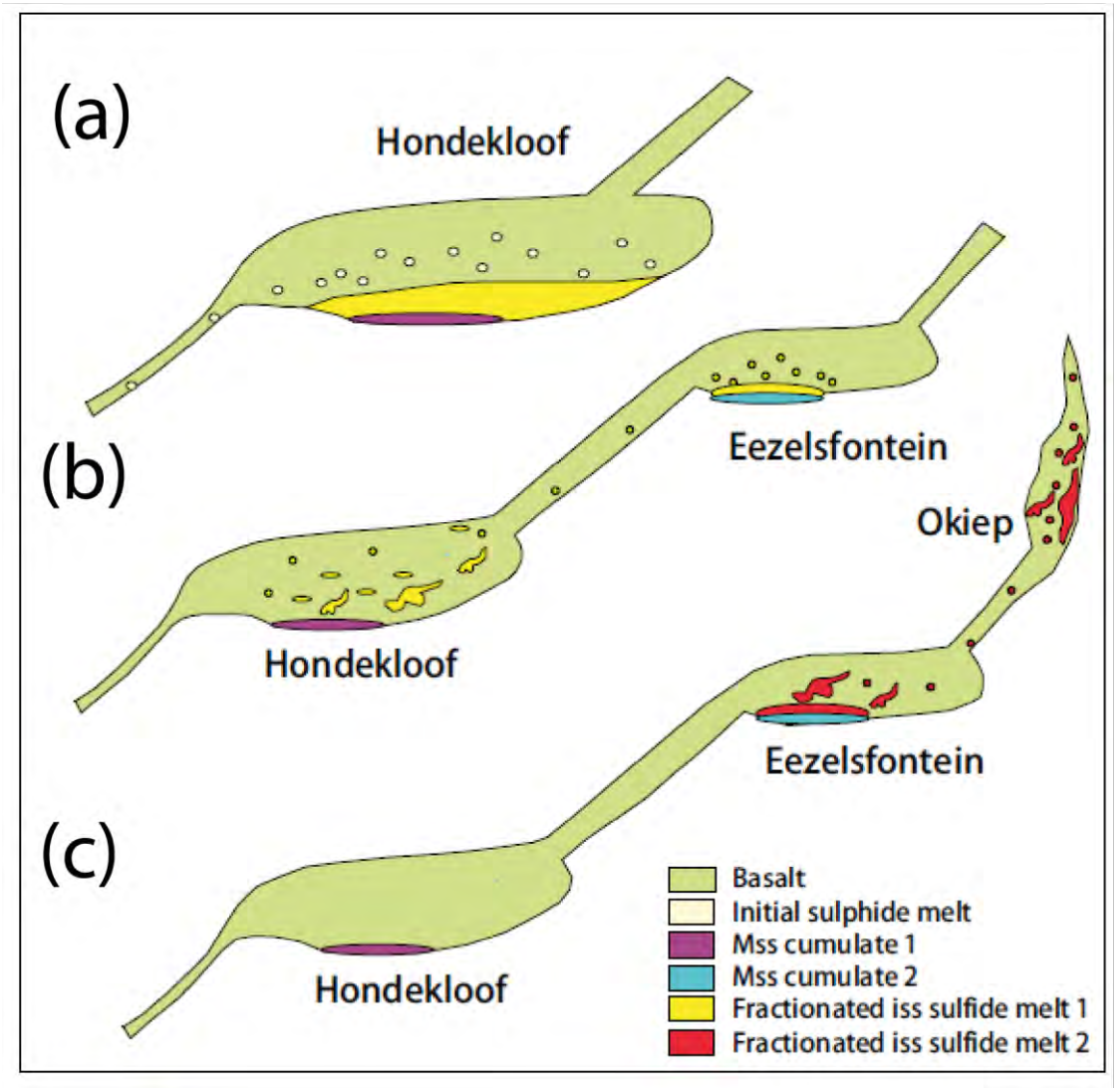

Figure 2. 6 IOCG model for the formation of Hondekloof (Fig. 1.1), Eezelsfontein and O'okiep deposits (Fig. 2.1) according to Maier et al. (2012). (a) Segregation of sulphide liquid from basaltic magma, and fractionation of the sulphide liquid to form a Ni-rich sulphide residue (forming the Hondekloof Ni deposits) and a Cu-rich iss sulphide liquid at deeper crustal levels. (b) Entrainment of the Cu-rich sulphide liquid by magma and redeposition at relatively shallower crustal levels, followed by the fractionation of the sulphide liquid producing a Ni-rich sulphide liquid and a Cu-rich iss sulphide liquid (forming the Eezelsfontein deposits). (c) Entrainment of the Cu-rich iss sulphide liquid by magma to the shallowest crustal levels producing the O'okiep Cu deposits.

Taking into consideration the likely links to IOCG deposits and geochemical characteristics of the O'okiep and Hondekloof deposits, Maier et al. (2012) envisaged the following sequence of events in their IOCG model (Fig. 2.6): (1) magmatism triggered by crustal extension likely linked to radiogenic heat production at mid- to lower crustal depths, (2) small-degree partial melting of the SCLM yielding volatile-LILE-HFS-Au-Cu-P-rich and PGE-depleted magmas, (3) rapid ascend of these oxygenated

magmas to levels where sulphur was stable as sulphate, thereby inhibiting early saturation of sulphide and enrichment of Cu and Au in the melt, (4) S saturation triggered by crustal contamination, (5) fractionation of sulphide liquid in magma conduits leading to formation of Ni-rich cumulates (e.g., Hondekloof ores) by monosulphide solution (*mss*) fractionation at greater depth (Fig. 2.6a), and (6) progressive fractionation, entrainment and re-deposition of *mss* liquid producing Ni-rich cumulates and Cu-rich cumulates (e.g., Eezelsfontein ores), and finally further ascent and deposition of Cu-rich *iss* sulphide melt (e.g., Okiep ores) at shallower depths (Fig. 2.6b-c).

3 Methods

3.1 Sampling and sample preparation

Samples used in this study were obtained from the Khurisberg Subgroup (Khurisberg Subgroup) and the Koperberg Suite lithostratigraphic units at Nababeep, Nigramoep and Carolusberg mines, and Sugarloaf Quarry. A total of six drill core samples were obtained from the mines (Table 4.1). One bulk surface sample was obtained from the Koperberg Suite stratigraphically below the Khurisberg Subgroup at Sugarloaf Quarry (refer to Fig. 2.1 for location and stratigraphic relations). Details of the mineralogy of the samples are given in Chapter 4.

A total of 30 polished thin samples were prepared and 25 samples were selected for use in the study based on the presence of sulphides. Twelve of these thin sections were used for EDS analysis. Two sets of five 1-inch epoxy round blocks each with two samples mounted on it were used for EPMA, LA-ICP-MS and SIMS analysis.

3.2 Petrography

Petrography was conducted at Rhodes University at hand specimen- and thin section scale to document the mineralogy of silicate and sulphide phases, their textural relationships and modal abundance estimations. Modal abundances of major phases were also estimated using a combination of petrography estimations and estimations obtained on backscattered electron images using ImageJ software (version 1.46R).

The rocks from the Koperberg Suite preserve igneous textures although they were emplaced under granulite facies metamorphic conditions. Thus, this study follows the classification based International Union of Geological Sciences (IUGS) Subcommission on the Systematics of Igneous Rocks (Le Maitre et al., 2002) for classification of these rocks. A summary of the petrographic information acquired is presented in Table 4.1. The mineral abbreviations used in the forthcoming sections are after Whitney and Evans (2010).

3.3 Analytical techniques and data processing

3.3.1 Energy Dispersive Spectroscopy (EDS)

EDS analysis was conducted at the Electron Beam Laboratory at Rhodes University using an Oxford Instrument INCA Energy Pentefet-x3 Si(Li) EDS detector attached to a TESCAN Vega TS 5136LM SEM. A cobalt standard was used for peak calibration. The analyses were conducted at an acceleration potential of 15 kV, process time of ~4-5 seconds and a dead time of ~50-55% for the detector. The data acquisition time for point analyses was set at 60 net seconds.

All the EDS analyses were normalised to 100 wt% oxide totals for silicates and phosphates (Table A1-A10, Appendix 1). Volatile content (H_2O and/or F, Cl) was not analysed. The updated version 4.3 of the Rock Maker software (Büttner, 2012) was used to calculate the number of cations per specified number of oxygen atoms and the proportion of ferric to ferrous Fe for silicate and oxide mineral analyses, and the number of ions per given total ions for sulphides (Table A1-A10, Appendix 1; Table 5.2-5.5).

For micas, volatile contents of ~4.0-4.5 wt% were added to achieve 2 (OH+F) anions (Table A4-A5, Appendix 1). Structural site occupation of tetrahedral and octahedral sites in micas was calculated by iteratively modifying the Fe^{2+}/Fe^{3+} ratios until the tetrahedron was occupied by 4 cations, and the octahedron occupied with 2 or 3 cations for muscovite and biotite, respectively (Table A4-A5, Appendix 1).

Similarly, the Fe^{2+}/Fe^{3+} ratios in spinels were varied to obtain 3 cations per 4 oxygen atoms. Spinel endmember compositions were calculated based on the Fe/Mg content and ratios using the spinel calculation sheet in Rock Maker 4.3 (Table A8, Appendix 1).

A volatile estimate of 1.80 wt% for apatite was included in the normalised EDS calculations (Table A9, Appendix 1).

3.3.2 Electron Probe Micro-analysis (EPMA)

Quantitative analyses of sulphides (pyrite, pyrrhotite, chalcopyrite, bornite, and chalcocite) for elements Cu, Fe, S, As, Ni, Pb, and Zn were obtained using four wavelength dispersive spectrometers on a JEOL JXA-8230 electron probe micro-analyser at Rhodes University. The beam was generated by a tungsten cathode, and excited with 20 kV accelerating potential at 20 nA current. A one-µm beam diameter was used. All elements except for As were measured on K-alpha peaks. Arsenic was measured on L-alpha peak. Counting times on peak were 15s, and 7.5s total on background for all elements. Commercial "SPI" standards — Pyrite (S), Sphalerite (Zn), Pentlandite (Ni), Galena (Pb), Chalcopyrite (Fe), Copper (Cu), and Arsenopyrite (As) — were used for intensity calibration. For chalcopyrite and bornite the typical analytical uncertainties for the major elements (Cu, Fe, S) were 0.47- 0.86% (Supplementary Table B1). For pyrite and pyrrhotite the typical analytical uncertanties for the major elements (Fe and S) were 0.37- 0.72% (Supplementary Table B1). The data was collected

using the JEOL software (PC EPMA 1.9.2.0), and its PRZ-XPP matrix algorithm was applied to correct for differential matrix effects.

The cation calculations (Cu, Fe) for sulphides were done using the Rock Maker software based on the ideal total number of ions in the respective sulphides (3 ions for pyrite, 15 for pyrrhotite, 4 for chalcopyrite, and 10 for bornite; Table 5.2-5.5). The analytical uncertainties for major element ratios for chalcopyrite and bornite from the Koperberg Suite (e.g., Cu/S ratios presented in Fig. 6.2) were calculated using the law of propagation of uncertainty (Equation 3.1 and Equation 3.2; Ku, 1966) as follows:

$$\sigma_R = \sqrt{\left(\frac{\partial R}{\partial x}\right)\sigma_x^2 + \left(\frac{\partial R}{\partial y}\right)^2 \sigma_y^2} \qquad \text{(Equation 3.1)}$$

where σ_R is the standard deviation for the ratio $R = \frac{x}{y}$, $\frac{\partial R}{\partial x}$ is the partial derivative of R with respect to *x*, $\frac{\partial R}{\partial y}$ is the partial derivative of R with respect to *y*, σ_x^2 is the variance of *x*, and σ_y^2 is the variance of *y*.

Thus, in the case where R is the ratio of analytical uncertainties of two elements (e.g., Cu and S), *x* and *y* are the analytical uncertainties for element *x* and *y* respectively, and σ_x^2 and σ_y^2 are the variance of analytical uncertainties for element *x* and *y;* the standard deviation of R is

$$\sigma_R = \sqrt{\left(\frac{1}{y}\right)^2 \sigma_x^2 + \left(\frac{x}{y^2}\right)^2 \sigma_y^2} \qquad \text{(Equation 3.2)}$$

The typical analytical uncertainty at 99% confidence level for Cu/S ratio of chalcopyrite and bornite is 0.04 and 0.01, respectively (Supplementary Table B1).

3.3.3 Laser Ablation Inductively Coupled Plasma Mass Spectrometry (LA-ICP-MS)

The trace element analysis for sulphides was conducted at the Central Analytical Facilities (CAF) at Stellenbosch University using a 193 nm Resolution M50-LR Excimer laser ablation system connected to an Agilent 7700 ICP-MS. The LA-ICP-MS analysis was executed by Ms Riana Rossouw from CAF. Quantitative trace element analysis was done on pyrite, pyrrhotite, chalcopyrite and bornite from the Khurisberg Subgroup and Koperberg Suite based on the following isotope concentrations: ^{59}Co, ^{60}Ni, ^{66}Zn, ^{75}As, ^{77}Se, ^{95}Mo, ^{107}Ag, ^{111}Cd, ^{115}In, ^{117}Sn, ^{121}Sb, ^{125}Te, ^{197}Au, ^{208}Pb and ^{209}Bi. The detection limit for the elements analysed are presented in Table 5.6 (Chapter 5). The analyses were performed using an ablation spot size of 26 µm and ablation time of 35 seconds. The laser beam energy and frequency were set at 3.5 J/cm^2 and 8 Hz, respectively. The MASS-1 sulphide standard reference material was used for calibration after analysis of every 15-20 spots. Processing of the data acquired was done using the LADR (version 1.1.06) software.

The detection limit was calculated using the standard deviation of the gas blank (σ), the sensitivity to the mass (S), and the number of time slices investigated in the analysis and gas blank (n_a and n_b respectively) (Equation 3.3; Longerich et al., 1996) as follows:

$$\text{Detection limit} = \frac{3\sigma}{S}\sqrt{\frac{1}{n_b}+\frac{1}{n_a}} \qquad \text{(Equation 3.3)}$$

The analytical uncertainties (2σ) were calculated by the LADR software for each analysis from the scatter in the integrated ablation period of ~40 seconds. The analytical uncertainties for all the analyses are presented in Supplementary Table B1.

3.3.4 Secondary Ion Mass Spectrometry (SIMS)

In-situ triple sulphur isotope (^{32}S, ^{33}S, ^{34}S) ratios were measured on a CAMECA IMS1280 ion microprobe at the Centre for Microscopy Characterisation and Analysis (CMCA) at the University of Western Australia. Half cylinder-shaped rock samples with diameters of 1 cm were embedded in resin mounts and polished flat. The edge of the mounts were trimmed to accommodate the relevant standards and mounted together in a sample holder. The mounts were then cleaned using ethanol and deionised water, and coated with ~20 nm Au coat to prevent charging during analysis. All SIMS analyses were executed by Dr Laure Martin from the CMCA.

A 10 kV Gaussian Cs^+ beam with intensity of ~2.5 nA and total impact energy of 20 keV was sputtered over 10 x 10 µm samples surfaces during analysis. Secondary ions were admitted in the double-focusing mass spectrometer and focussed into the centre of a 3000 µm field aperture (x 130 magnification) with a 60 µm entrance slit. Energy filtering was performed using a 40 eV band pass with a 5 eV gap toward the high-energy side. The S isotopes were simultaneously collected in Faraday cup detectors fitted with 10^{10} Ω (L'2, ^{32}S) and 10^{11} Ω (L1, ^{33}S and H1, ^{34}S) resistors, operating at a mass resolution of ~2500. The hydrite interference on $^{32}S^1H$ and ^{33}S peaks are not completely resolved under these conditions. Thus, the magnetic field was offset slightly to the low-mass side to avoid interference from $^{32}S^1H$ on the ^{33}S peak. The magnetic field was regulated using NMR control. Sample surfaces were bombarded with low energy electrons from a normal incidence electron flood gun for charge compensation. Each analysis includes a pre-sputtering over a 15 x 15 µm area during 30s and the automatic centring of the secondary ions in the field aperture, contrast aperture and entrance slit. Each analysis then consists of a 20 four-second cycles acquisition. The analytical session was monitored in terms of drift using two bracketing standards every 5 sample analyses. Instrumental mass fractionation (IMF) was corrected using a matrix-matched reference material (LaFlamme et al., 2016). IMF correction follows procedure described in Kita et al. (2009).

The relative variation in S isotope compositions are expressed in the delta notation (McKinney et al., 1950) defined as:

$$\delta^{x}S = \left[\frac{\left({}^{x}S/{}^{32}S\right)_{sample} - \left({}^{x}S/{}^{32}S\right)_{reference}}{\left({}^{x}S/{}^{32}S\right)_{reference}} \right] x1000$$

where *x* = 33, 34, or 36. The unit of $\delta^{x}S$ is parts per mil (‰). By convention, the standard reference material for reporting sulphur isotope data is the Vienna-Cañon Diablo Troilite (VCDT) scale defined relative to Ag_2S IAEA-S-1 reference material with an assigned value of -0.3‰ (Coplen and Krouse, 1998). All the S isotope data presented in the forthcoming sections are relative to VCDT.

Only pyrite and chalcopyrite were analysed using SIMS because CMCA did not have reference material for bornite available at the time of analysis. The average reproducibility of the Nifty-b standard (chalcopyrite) and Sierra standard (pyrite) were 0.23‰ (2σ) and 0.24‰ (2σ) respectively (Supplementary Table B1). The analytical uncertainty for all samples analysed was 0.06-0.20‰ (Supplementary Table B1).

3.3.5 Isotope Ratio Mass Spectrometry (IRMS)

Bulk S isotope (^{32}S, ^{34}S) analyses were conducted by Mr Paul Middlestead at the Ján Veizer Stable Isotope Laboratory at University of Ottawa. Sample material is first flash-combusted at 1800°C in an Elemental Analyser Isotope Cube. The gaseous products released are carried by ultra-pure He through the Elemental Analyser Isotope Cube where SO_2 is separated from other gaseous products (water, CO_2, N_2) by chemical absorption method. The SO_2 is then carried into the Thermo Finnigan DeltaPlus XP IRMS via a Conflo IV for ^{34}S analysis. The analytical precision is ± 0.3‰ (2σ).

4 Petrographic descriptions

This section outlines the petrographic descriptions at hand specimen and thin section scale of the samples used in the study. The hand specimen descriptions describe textures and mineral phases observed at such a scale. More comprehensive descriptions which include estimated modal abundance of mineral phases, and their textural relationships are given in the microscopic description sections. Since this study focuses on the geochemistry of sulphides, the petrographic descriptions place more emphasis on sulphide phases and their textural relationships with oxide and silicate phases.

4.1 Khurisberg Subgroup

4.1.1 Sample 039T-1A (Garnet-biotite-sillimanite gneiss, Khurisberg Subgroup, Nababeep Mine)

Hand specimen description

The sample is a garnet-biotite-sillimanite gneiss with gneissosity defined by melanocratic domains (garnet-biotite-sillimanite domains) characterised by relatively high abundance of pink-brown garnet, dark brown biotite and grey acicular sillimanite crystals; and leucocratic domains characterised by relatively higher abundance of quartz and K-feldspar (Fig. 4.1). Garnet occurs as isolated grains or near-oval clusters of crystals ranging from 2 to 40 mm in size (Fig. 4.1). Sulphides, mainly pyrite and pyrrhotite, are spatially associated with the garnet-biotite-sillimanite domains, particularly on or close to biotite.

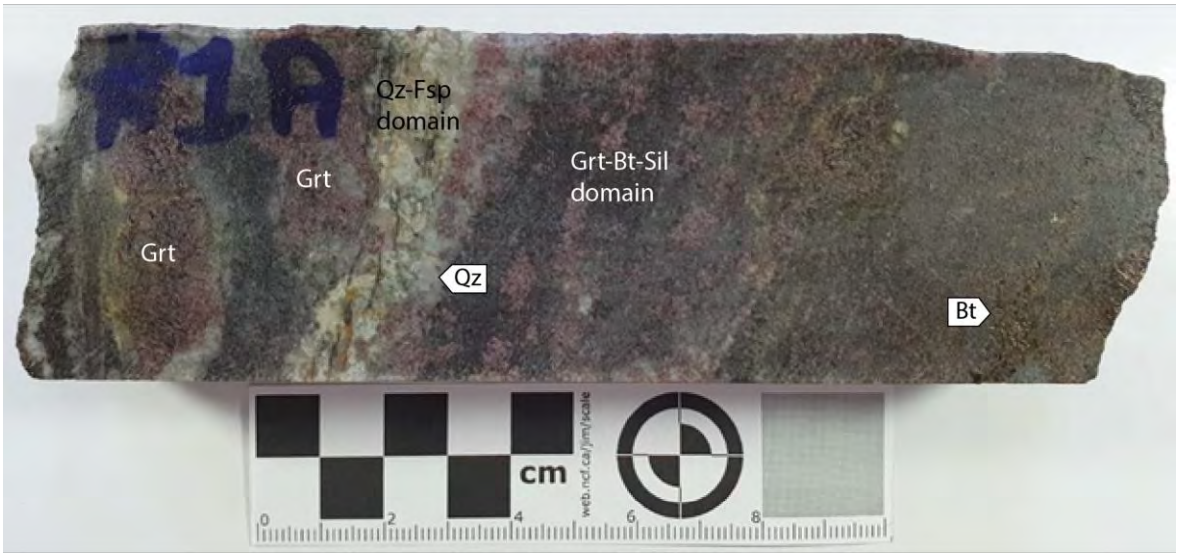

Figure 4. 1 Specimen of sample 039T-1A (Nababeep Mine) exhibiting banding defined garnet-biotite-sillimanite domains and quartz-feldspar domains.

Microscopic description

Garnet constitutes ~25% of the modal volume and occurs as allotriomorphic poikiloblasts with sizes ranging from 4 to 8 mm in the garnet-biotite-sillimanite domain and as isolated poikiloblasts of sizes

of ~1 mm in the quartz-feldspar domain (Fig. 4.2a). The inclusions hosted in garnet are commonly <300 µm rounded quartz, biotite, pyrite, pyrrhotite, spinel, ilmenite and magnetite (Fig. 4c).

Biotite accounts for ~9% of the modal composition. It occurs as ~50-150 µm rounded to elongated inclusions in garnet and quartz, as individual grains in the quartz-feldspar domain or as 0.5-2 mm clusters associated with garnet, sulphides and oxide phases (Fig. 4a-c). The biotite in garnet in some places shows patches with intergrowths of biotite and chlorite.

Table 4. 1 Summary of the mineralogy and petrographic classification of samples used in this study.

Sample	Epoxy round blocks ID	Lithological unit	Sample type & depth; Locality	Mineralogy	Petrographic description and average An content
039T-1A	1A3-1B3	Khurisberg Subgroup (Khurisberg Subgroup)	Core (75.5 m); Nababeep Mine	Grt, Qz, Kfs, Bt, Sil, Ms, Mag, Ilm, Py, Po, Spl Accessories: Mnz, Ap, Ccp, Crd, Rt, Chl	Garnet-biotite-sillimanite gneiss
039T-1B		Khurisberg Subgroup (Khurisberg Subgroup)	Core (144.5 m); Nababeep Mine	Grt, Kfs, Qz, Bt, Sil, Ms, Ilm, Py, Po, Qz Accessories: Mnz, Ap, Pl, Ccp, Pn, Mag	Garnet- biotite-sillimanite gneiss
016T-3	3A-3C	Koperberg Suite	Core (229.2 m); Nababeep Mine	Pl, Qz, Opx, Mag, Ilm, Ccp, Bn, Bt Accessories: Ap	Leucodiorite
039T-4	4A-4B	Koperberg Suite	Core (246.5 m); Nababeep Mine	Pl, Bt, Opx, Ccp, Bn, Mag, Ilm Accessories: Mnz, Ap	Diorite
DSQ	3B2-3D1	Koperberg Suite (stratigraphically below the Khurisberg Subgroup)	Bulk rock chip (surface); Sugarloaf Quarry	Pl, Opx, Ccp, Bn, Mag, Ilm, Bt Accessories: Ap, Kfs	Leuconorite
KNU 477	KNU-CD	Koperberg Suite	Core (396.6 m); Nigramoep Mine	Opx, Pl, Qz, Bt, Ccp, Bn, Ilm, Mag, Usp, Rt	Norite
CD 01		Koperberg Suite	Core (Deep ores >1380 m); Carolusberg Mine	Opx, Bn, Mag, Cct	Orthopyroxenite

Quartz and K-feldspar with minor plagioclase account for ~55% of the modal composition and besides occurring as inclusions in garnet, commonly exhibit interlobate and granoblastic textures with grain sizes of ~0.3-4 mm (Fig. 4.4b). Sillimanite constitutes ~3% of the modal composition and is commonly found as 200-400 µm acicular crystals along grain boundaries of K-feldspar, biotite, garnet grains (Fig. 4.4b). Other accessory phases (<1%) are cordierite, apatite, monazite and zircon.

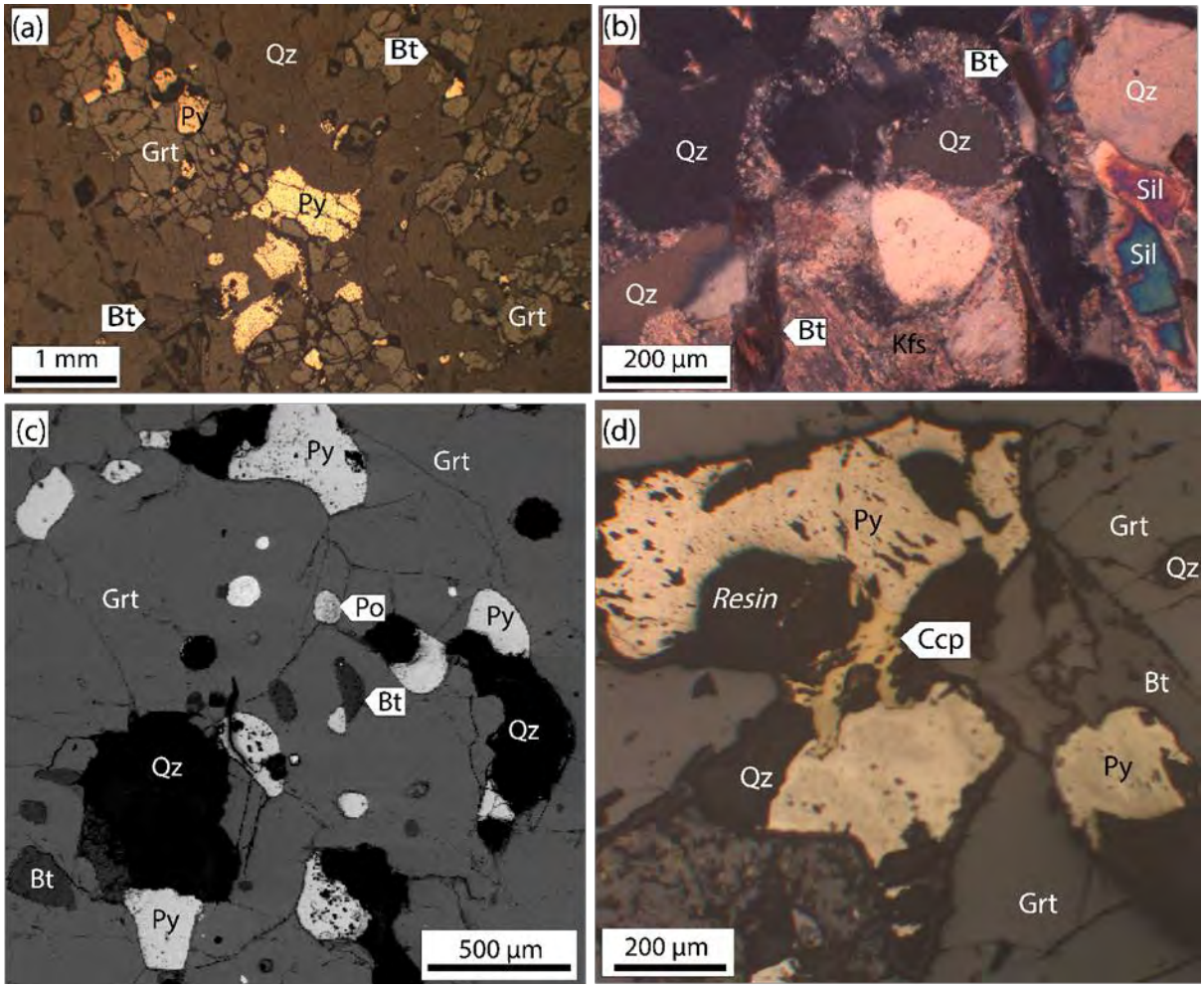

Figure 4. 2 Photomicrographs of typical parts of thin sections from sample 039T-1A (Nababeep Mine) under reflected light (a,d) and cross-polarised (b) and in backscattered electron (BSE) mode (c). (a) Photomicrograph showing close association of pyrite to the garnet-biotite-sillimanite domain and the difference in the size of pyrite crystals in the garnet-biotite-sillimanite and quartz-feldspar domains. (b) Sillimanite and biotite forming along quartz and K-feldspar grain boundaries. (c) Quartz, biotite, pyrite and pyrrhotite inclusions in garnet. (d) Pyrite-chalcopyrite intergrowth hosted in garnet.

The sulphides (pyrite, pyrrhotite and minor chalcopyrite) constitute ~2% of the modal composition. Pyrite and pyrrhotite occur in a ratio of ~9:1 (Fig. 4.4a,c,d), and ~80% of these sulphides are hosted within garnet. Minor chalcopyrite is intergrown with pyrite or pyrrhotite (Fig. 4.4d). The oxides (magnetite and minor ilmenite and rutile) constitute ~2% of the modal composition. The sulphides and oxides exhibit a wide range of habits and sizes, from subhedral to rounded and 200 µm to 1mm in size, respectively. In addition to existence as inclusions in garnet, sulphides and oxides also occur along biotite and garnet grain boundaries, along biotite cleavage planes, in sericitised zones in K-

feldspar, or interstitial to K-feldspar and quartz (Fig. 4a, d). These phases are usually relatively larger in garnet-biotite domains (200-1000 µm) compared to the quartz-rich domain (Fig. 4.2a).

4.1.2 Sample 039T-1B (Garnet-biotite-sillimanite gneiss, Khurisberg Subgroup, Nababeep Mine)

Hand specimen description

The sample is a garnet-biotite-sillimanite gneiss exhibiting banding defined by 20-55 mm bands characterised by higher modal proportions of garnet, biotite and sillimanite (garnet-biotite-sillimanite domains) and leucocratic quartz-feldspar domains characterised by higher modal proportions of quartz and K-feldspar (quartz-feldspar domains) (Fig. 4.3). Pink-brown garnet occurs as ~1-2 mm disseminated anhedral grains within quartz-feldspar domains or as relatively larger (5-7 mm) aggregates of grains within biotite-sillimanite domains (Fig. 4.3). The main sulphides (pyrite and pyrrhotite) are spatially associated with the garnet-biotite-sillimanite domains.

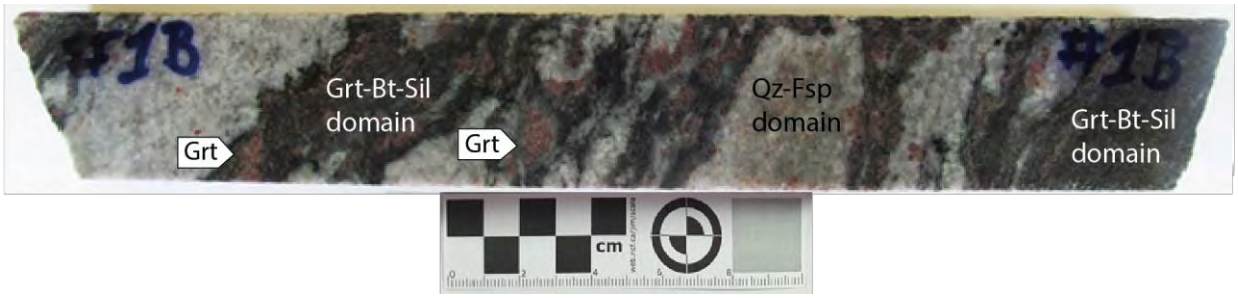

Figure 4. 3 Specimen of sample 039T-1B (Khurisberg Subgroup, Nababeep Mine) exhibiting banding defined garnet-biotite-sillimanite domains and quartz-feldspar domains.

Microscopic description

The garnet in this sample constitutes ~15 vol.% and invariably occurs as subhedral to rounded poikiloblastic grains of sizes 0.5-4 mm (Fig. 4.4a). Inclusions in garnet are quartz, K-feldspar, sillimanite, biotite, ilmenite, spinel, pyrite, pyrrhotite and chalcopyrite (Fig. 4.4b-d). Quartz inclusions in garnet are the most abundant and are commonly rounded with sizes ranging from 100-500 µm (Fig. 4.4a). Spinel is exclusively hosted in garnet and forms elongated to rounded ~150-300 µm inclusions rimmed with fine-grained 50-100 µm biotite.

Biotite accounts for ~8% of the modal composition and occurs as ~60-250 µm rounded to elongated inclusions in garnet, along the margin of sulphides (Fig. 4.4c), along garnet grain boundaries (Fig. 4.4a), and as ~250 µm elongate grains along quartz and/or K-feldspar grain boundaries which define spaced schistosity in some zones of the quartz-feldspar domain. Biotite inclusions in garnet commonly coexist with quartz.

Quartz and feldspar (mostly K-feldspar with minor plagioclase) account for ~70% of the modal composition and exhibit an interlobate texture with grain sizes of ~1-4 mm in the garnet-biotite-sillimanite domains, granoblastic textures with grain sizes of 100-400 µm in some zones of the quartz-feldspar domain, or less commonly as myrmekitic intergrowths. Sillimanite constitutes ~3% of the modal composition and is commonly found along grain boundaries of K-feldspar or garnet grains (Fig. 4.4a). Accessory phases (<1%) are monazite and zircon.

The main sulphides present are pyrrhotite and pyrite and occur in the ratio 3:7. They constitute ~2% of the modal composition. Besides occurring as inclusions in garnet, sulphides commonly occur in association with oxides, as independent grains within or interstitial to silicate phases (Fig. 4.4b-d). Minor chalcopyrite and pentlandite are found in some places intergrown with pyrite or pyrrhotite (Fig. 4.4b, d). The oxides (ilmenite with minor magnetite and rutile) constitute ~1% of the modal composition. Rutile commonly forms as exsolution in ilmenite. The sulphides and oxides exhibit a wide range of habits and sizes, from subhedral to rounded and up to 400 µm, respectively. In some places, sulphide minerals are commonly surrounded by a sericite or biotite rims (Fig. 4.4c).

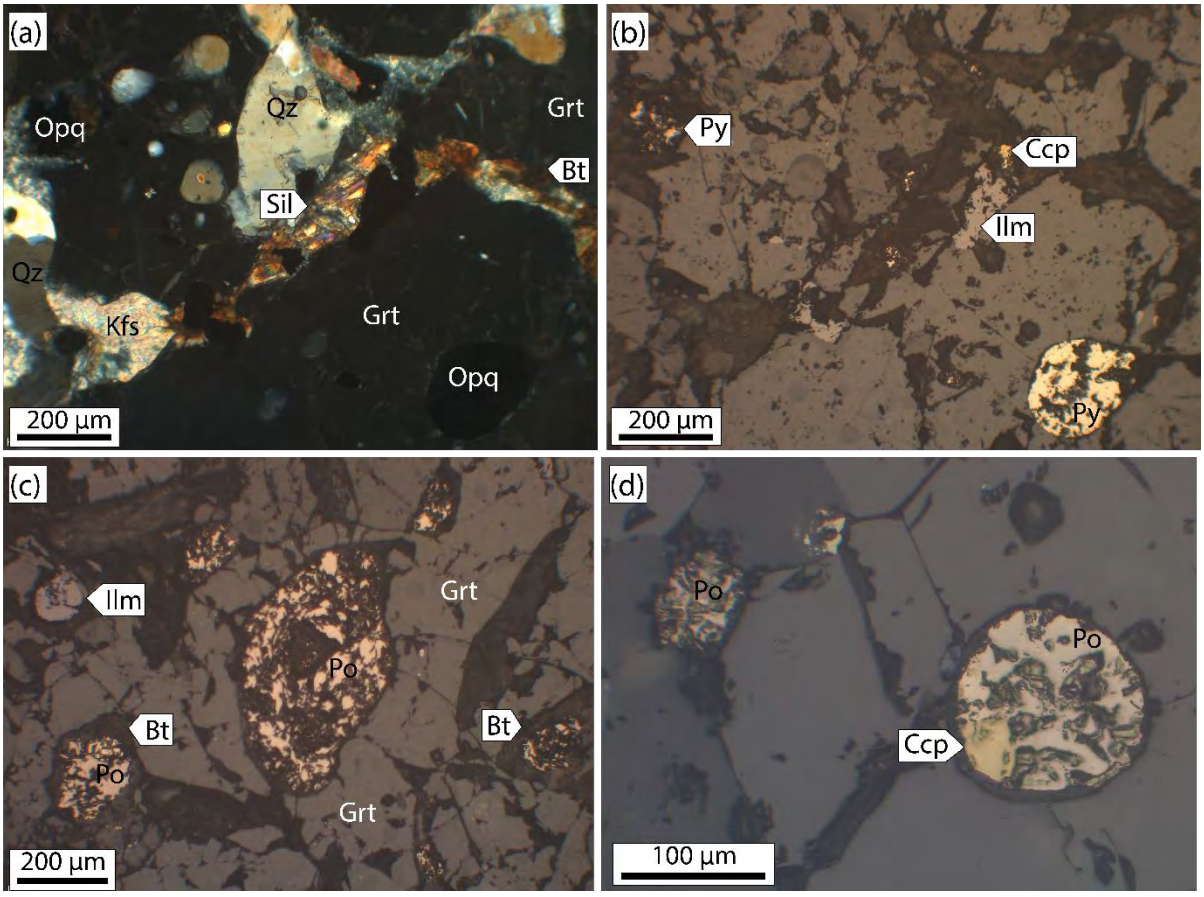

Figure 4. 4 Photomicrographs of typical parts of sample 039T-1B (Nababeep Mine) in cross-polarised light (a) and under reflected light (b-d). Photomicrograph (b) is the corresponding reflected light image for (a). (a) Quartz, K-feldspar, sillimanite, biotite and opaque phases inclusions in garnet. (b-d) Sulphide phases occurring as independent grains or in close association with oxide phases; biotite forms around some of the sulphide grains. (d) Pyrrhotite-chalcopyrite intergrowth in garnet.

4.2 Koperberg Suite

4.2.1 Sample 039T-4 (Diorite, Nababeep Mine)

Hand specimen description

The sample is a mesocratic diorite with green-grey clusters composed of biotite, orthopyroxene and/or oxide phases within a plagioclase-rich matrix, giving the rock a spotty appearance (Fig. 4.5). The main sulphide mineral present is chalcopyrite which occurs as brassy yellow anhedral grains disseminated in both the plagioclase-quartz matrix and biotite-orthopyroxene clusters (Fig. 4.5). The size and abundance of chalcopyrite varies from abundant and relatively larger sizes (>1 mm) within or close to the biotite-orthopyroxene clusters, to fewer and smaller (<1 mm) sizes in the plagioclase-quartz matrix (Fig. 4.5).

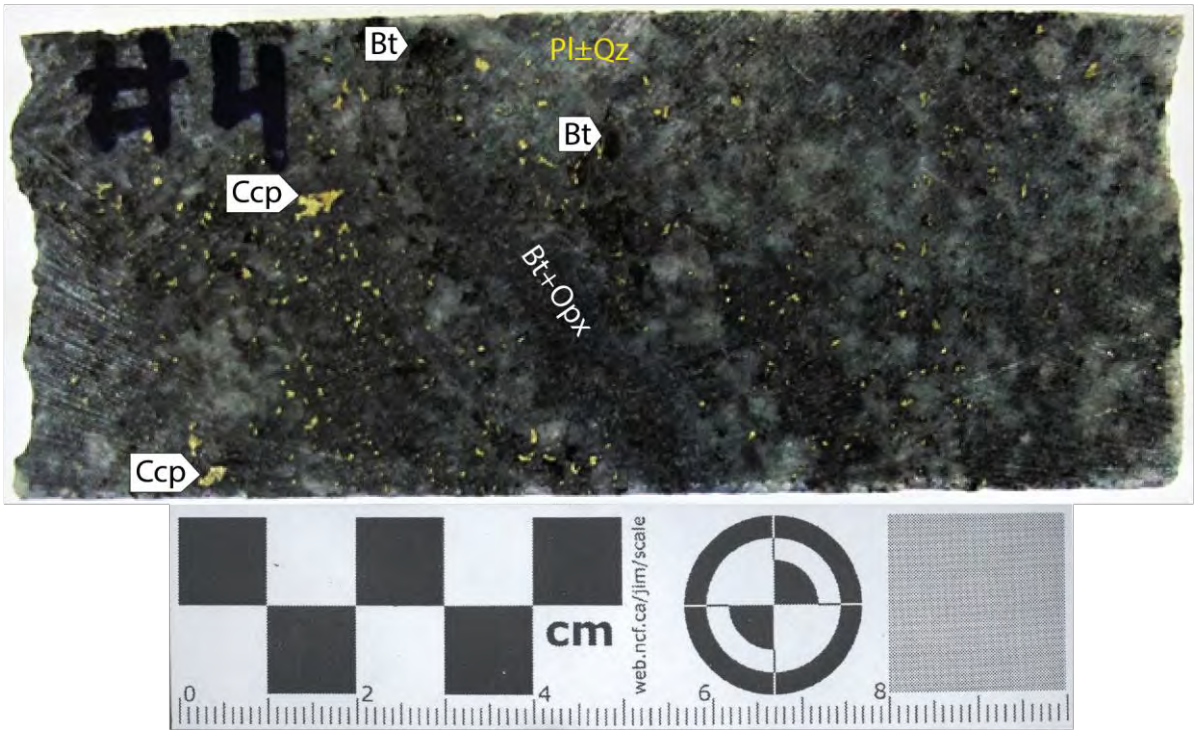

Figure 4. 5 Specimen of mesocratic diorite sample 039T-4 (Nababeep Mine) showing clusters consisting of biotite and orthopyroxene in a plagioclase-quartz matrix. Larger chalcopyrite grains are spatially associated with biotite-orthopyroxene clusters.

Microscopic description

Plagioclase constitutes ~66% of the modal volume and typically forms anhedral 2-4 mm interlocking crystals with minor quartz (Fig. 4.6a, c). Plagioclase commonly shows twinning and muscovite is a common phase along the contacts between plagioclase and oxide and/or sulphide phases (Fig 4.6a).

Biotite and orthopyroxene constitute ~20% and 7% of the modal volume, respectively. Dark brown to greenish-brown biotite and/or pink orthopyroxene commonly form >3mm clusters which host sulphide phases (chalcopyrite and bornite) and oxide phases (magnetite and ilmenite). Other accessory phases (<1%) are monazite and apatite.

Sulphides and oxides are mostly anhedral and constitute ~2% and ~4% of the modal volume, respectively. Chalcopyrite is the dominant sulphide phase (~1.9%), whereas bornite is a minor phase (~0.1%). Ilmenite and magnetite occur in equal proportion. The sulphides invariably exhibit feathered margins, whereas oxide phases exhibit smooth and rounded grain boundaries (Fig. 4.6a-d). The sulphides and oxide phases commonly form interstitial to plagioclase, abut cleavage planes and grain boundaries of biotite or within cracks of orthopyroxene (Fig. 4.6a-d). They also occur both as independent grains and as chalcopyrite-bornite and magnetite-ilmenite intergrowths of sizes ranging from 40 to 900 µm (Fig. 4.6a, b, d).

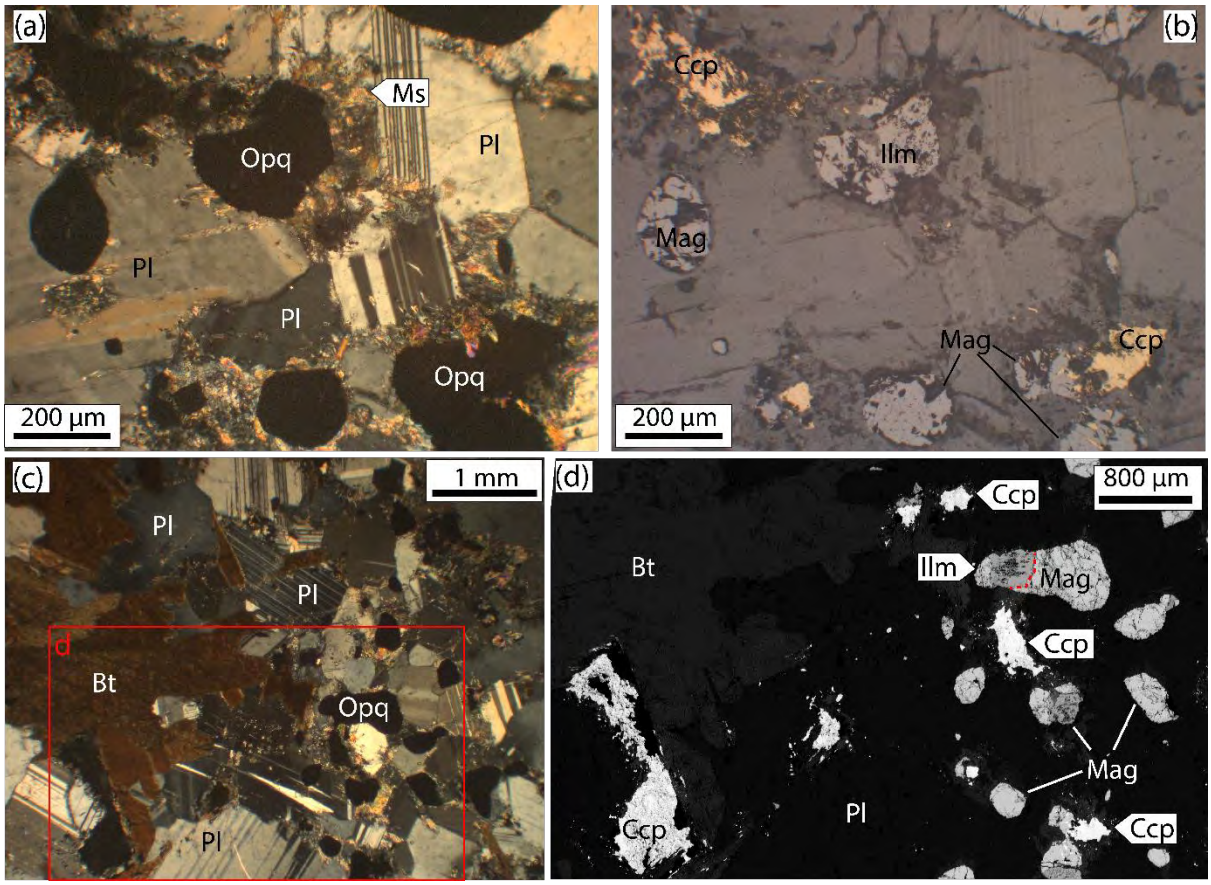

Figure 4. 6 Photomicrographs of typical parts of diorite sample 039T-4 (Nababeep Mine) in cross polarised light (a,c), reflected light (b) and backscattered electron mode (d). Image (b) shows the corresponding area shown in (a) in reflected light. (a) Opaque phases (oxides and sulphides) occur along or close to the grain boundaries of plagioclase. (a-b,d) Sulphide phases are characterised by feathered margins, whereas oxide phases have smooth and rounded grain boundaries. (c) Opaque phases occur along or close to the grain boundaries of plagioclase and along biotite grain boundaries. The position of image (d) is demarcated in red. (d) Chalcopyrite in close spatial association with magnetite and magnetite-ilmenite intergrowths.

4.2.2 Sample 016T-3 (Leucodiorite, Nababeep Mine)

Hand specimen description

The sample is an equigranular leucodiorite consisting of dark green biotite, grey-black orthopyroxene and grey magnetite. Biotite, orthopyroxene and magnetite occur as clusters made up of some or all these minerals, or as individual grains in a plagioclase-quartz matrix (Fig. 4.7). Sulphides form individual crystals in the plagioclase-quartz matrix or in close spatial association with the biotite-orthopyroxene-oxide clusters.

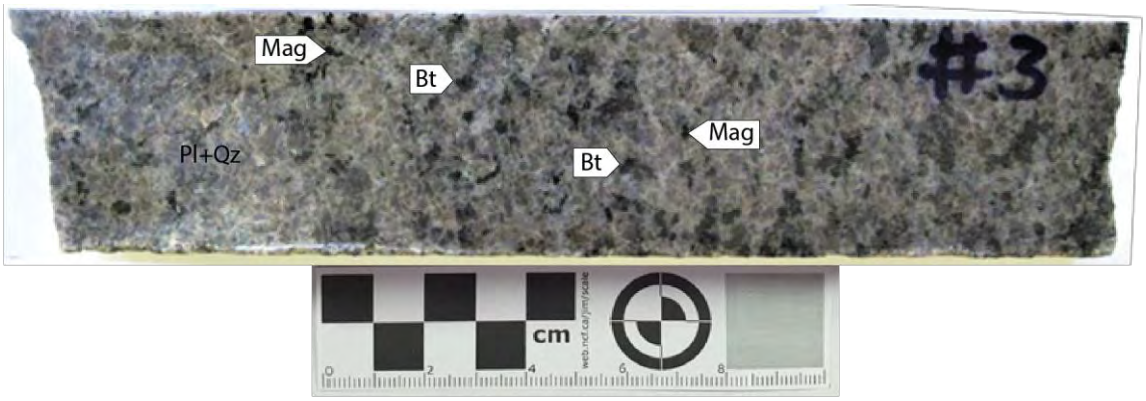

Figure 4. 7 Hand specimen for leucodiorite sample 016T-3 (Nababeep Mine) showing clusters consisting of biotite and/or magnetite in a plagioclase-quartz matrix.

Microscopic description

The sample is modally composed of plagioclase (~75%), quartz (~5%), orthopyroxene (~5%), biotite (~10%) magnetite and ilmenite (~3%), chalcopyrite and bornite (~1%).

Plagioclase and quartz form the matrix characterised by 2-5 mm interlocking grains giving an interlobate texture (Fig. 4.8a). Biotite commonly forms as 2-5 mm clusters within the plagioclase-quartz matrix and as <1 mm acicular crystals in close spatial association with 250-500 µm subhedral to euhedral orthopyroxene grains (Fig. 4.8a-c, e). Accessory phases are apatite, monazite, zircon, muscovite, and K-feldspar.

The sulphides and oxides exhibit a close spatial relationship, and commonly occur as chalcopyrite-bornite and magnetite-ilmenite intergrowths interstitial to plagioclase, as chadacrysts in the plagioclase, as independent grains within biotite-orthopyroxene clusters, or abut biotite cleavage planes and grain boundaries (Fig. 4.8c-e). Where the sulphides and oxides occur within plagioclase, muscovite commonly forms ~100 µm zones between the sulphides and plagioclase (Fig. 4.8e). The sulphides in some places exhibit feathered margins, whereas oxides exhibit smooth and rounded grain boundaries (Fig. 4.8e. Chalcopyrite is the dominant sulphide (~0.8%) compared to bornite (~0.2%), whereas magnetite is the dominant oxide phase (~2%) compared to ilmenite (~0.6%).

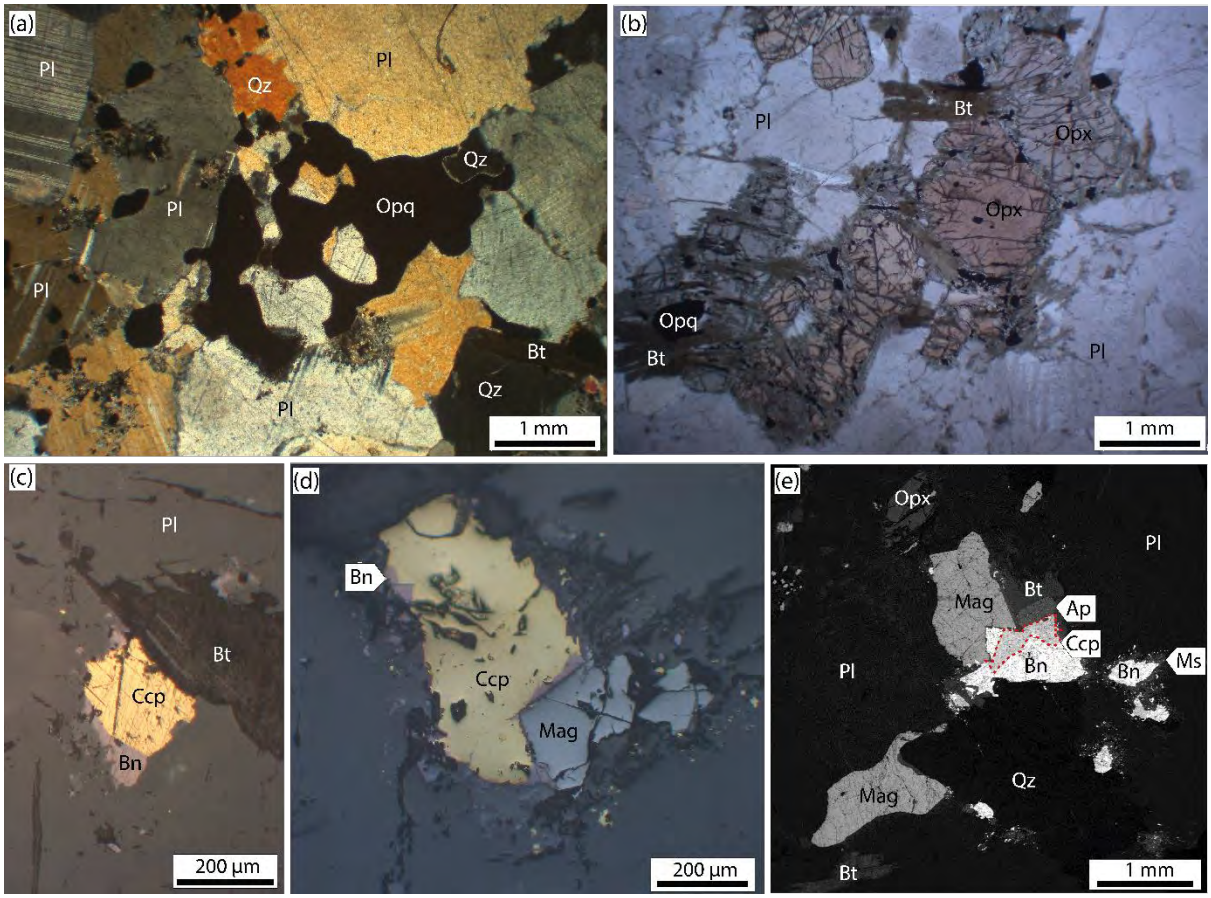

Figure 4. 8 Photomicrographs of typical parts of sample 016-3 (Nababeep Mine) in cross polarised light (a), in plane polarised light (b), under reflected light (c,d) and backscattered electron mode (e). (a,c,e) Opaque phases (oxide and sulphide phases) form along plagioclase grain boundaries or as chadacrysts to plagioclase. (b) Biotite associated with orthopyroxene. (c) Chalcopyrite-bornite intergrowth abuts biotite grain boundaries. (d-e) Chalcopyrite-bornite intergrowth in close association with magnetite. Muscovite commonly forms around bornite.

4.2.3 Sample KNU 477 (Norite, Nigramoep Mine)

Hand specimen description

The sample is a norite from Nigramoep Mine, comprising orthopyroxene, plagioclase, biotite, chalcopyrite and magnetite. Orthopyroxene forms 3-4 mm dark greyish black crystals commonly in close spatial association with dark brown biotite and silver-grey magnetite (Fig. 4.9). Grey plagioclase and aggregates of plagioclase grains of sizes up to 5 mm occur within the orthopyroxene-biotite rich zones (Fig. 4.9). Chalcopyrite grains are associated with orthopyroxene-biotite rich areas (Fig. 4.9).

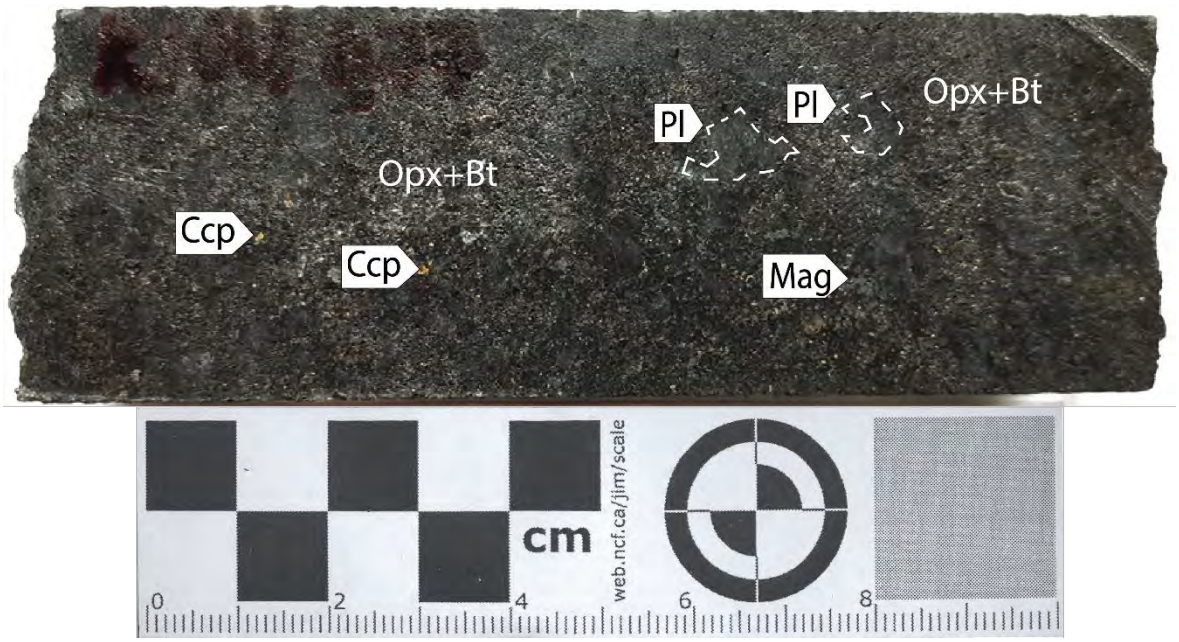

Figure 4. 9 Hand specimen for norite sample KNU 477 (Nigramoep Mine) showing plagioclase within orthopyroxene-biotite rich parts. Dashed white lines demarcate boundaries of some of the plagioclase or clusters of plagioclase grains. Chalcopyrite and magnetite grains are spatially associated with the orthopyroxene-biotite rich parts.

Microscopic description

The sample is modally composed of orthopyroxene (~45%), plagioclase (~35%), biotite (~8%), magnetite, ilmenite and rutile (~5%), chalcopyrite and bornite (~5%).

Plagioclase occurs as 1-5 mm anhedral crystals with its interstitial spaces occupied by clusters consisting of ~1-4 mm orthopyroxene, ~1.0-1.5 mm tabular biotite or in some places <1 mm partly resorbed biotite, and <1 mm opaques phases (oxides and sulphides). The clusters also occur as chadacrysts to- or close to its grain boundaries with plagioclase (Fig. 4.10a). Accessory phases are monazite, apatite and quartz.

The sulphides and oxides are mostly anhedral and grain sizes vary from 0.1 mm to 1mm. The phases commonly exist as pairs interstitial to plagioclase and along cleavage planes or grain boundaries of the mafic silicate phases (Fig. 4.10a-c). The common sulphide and oxide pairs are chalcopyrite-bornite, magnetite-ilmenite, ilmenite-ulvöspinel, and ilmenite-rutile (Fig. 4.10b, c). Magnetite and ilmenite are the main oxide phases and constitute ~80% of the oxides. Chalcopyrite and bornite are found in proportions 20% to 80%.

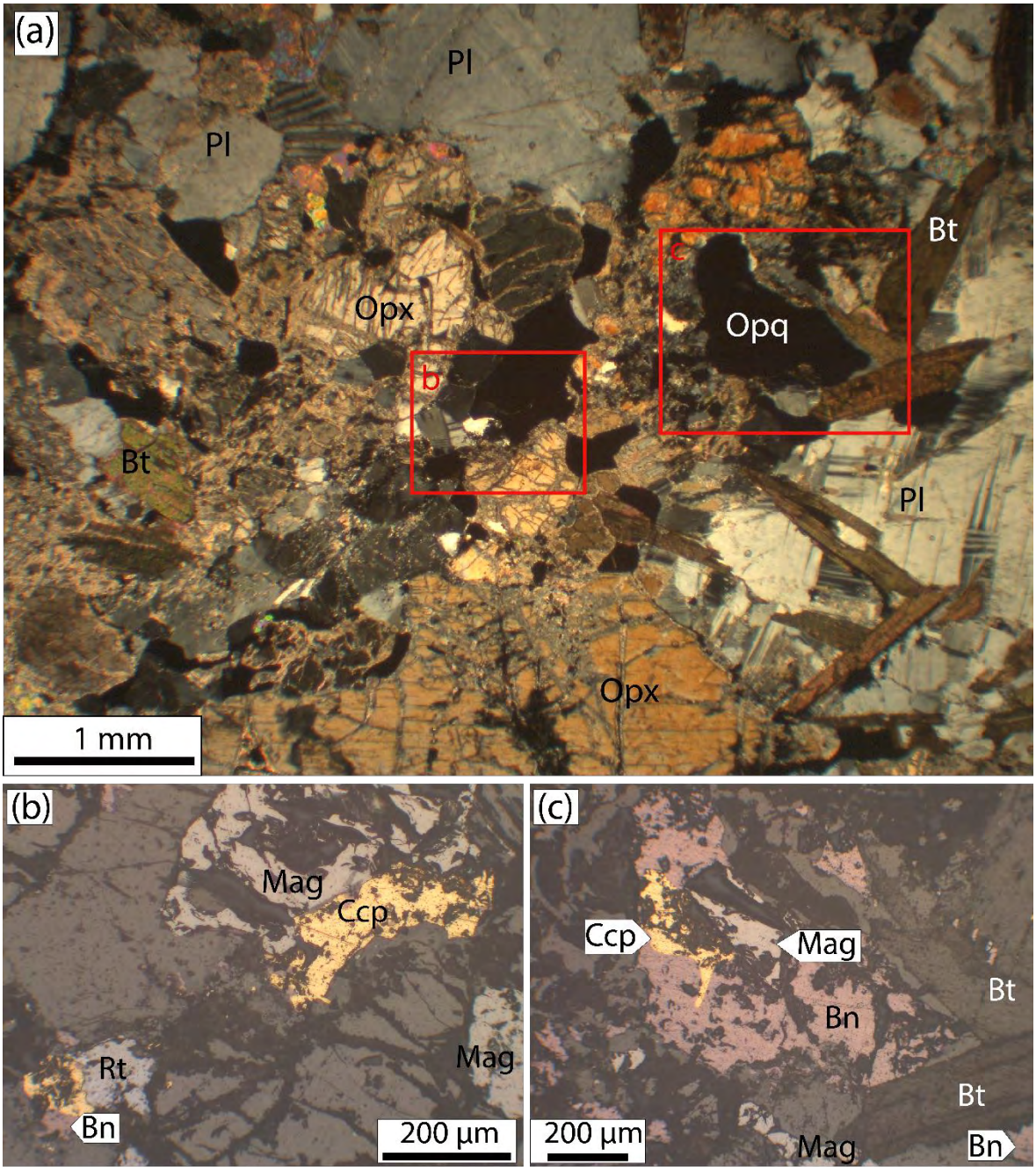

Figure 4. 10 Photomicrographs of typical parts of norite sample KNU 477 (Nigramoep Mine) in cross polarised light (a) and reflected light (b,c). (a) Opaque phases forming within or on grain boundaries of orthopyroxene and biotite. Plagioclase forms chadacrysts to these orthopyroxene-biotite-oxide rich zones. The positions of (b) and (c) are demarcated in red. (b-c) Oxide and sulphide phases showing a close spatial relationship.

4.2.4 Sample CD 01 (Orthopyroxenite, Carolusberg Mine)

Hand specimen description

Sample CD 01 is an orthopyroxenite composed of silver-grey magnetite and with pinkish bornite grains set in a grey-black orthopyroxene matrix (Fig. 4.11). Much of the textural relationships cannot be

deciphered at hand specimen scale since the sample has a high content of dark orthopyroxene.

Figure 4. 11 Hand specimen for orthopyroxenite sample CD 01 (Carolusberg Mine) showing bornite and magnetite within an orthopyroxene matrix.

Microscopic description

The sample contains orthopyroxene (~83%), magnetite (~9%), bornite (~7%), and minor chalcocite. Orthopyroxene exhibits a pinkish colour and forms 0.3–2mm grains which are mostly altered at the margins (Fig. 4.12 a,b). Bornite coexisting with magnetite occurs interstitially to orthopyroxene (Fig. 4.12b). Chalcocite in some places forms as <10 µm exsolutions in bornite (Fig. 4.12c; cf. Chapter 5.1.3.4; Fig.5.1d).

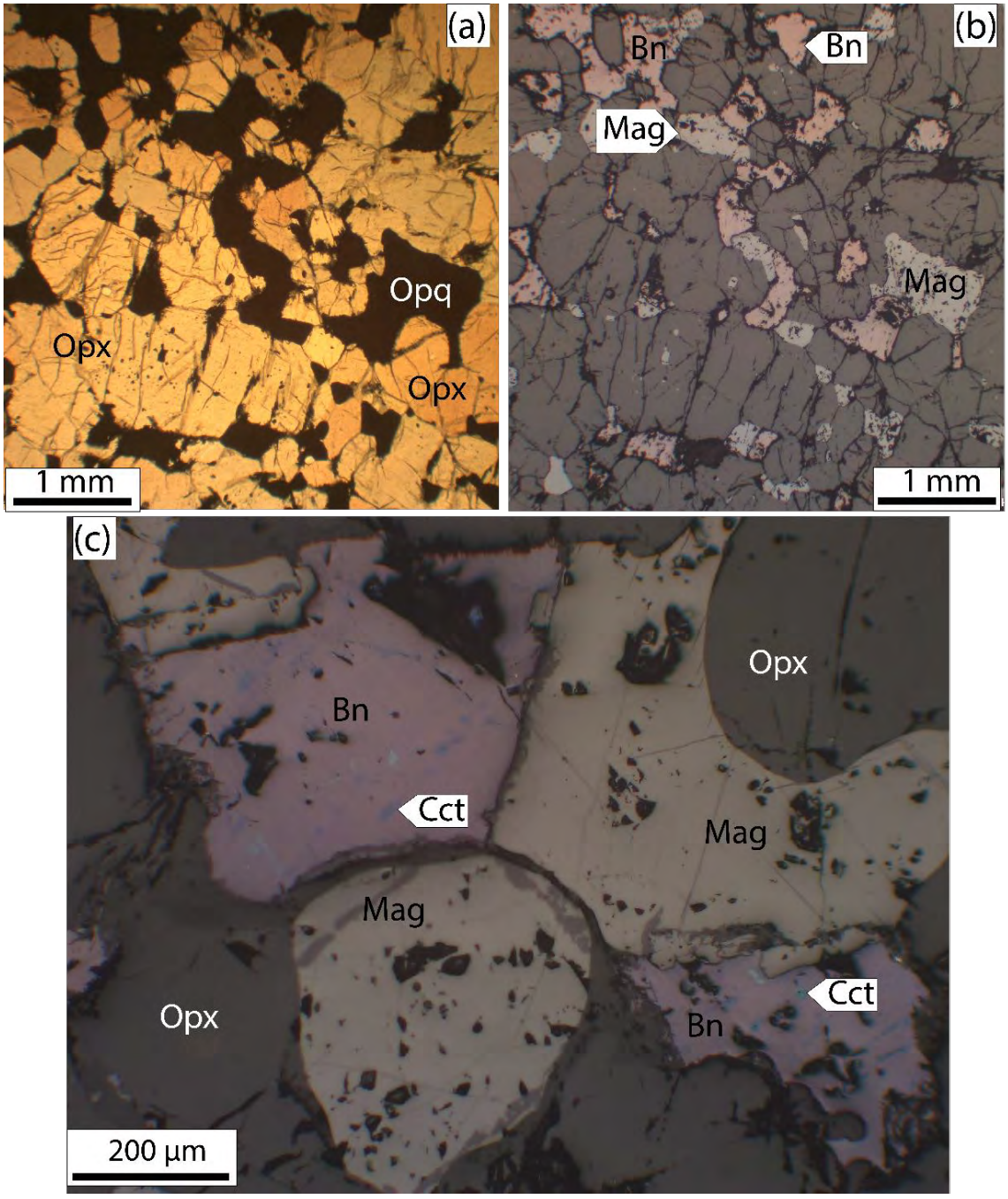

Figure 4. 12 Photomicrographs in plane polarised light (a) and in reflected light (b,c) for the representative parts of orthopyroxenite sample CD 01 (Carolusberg Mine). The corresponding area in (a) is shown in (b). (a-c) Bornite and magnetite coexisting interstitially to orthopyroxene. (c) Chalcocite exsolutions in bornite. Note the inverse or negative grain shapes of bornite (i.e., interstitial) relative to magnetite.

4.3 Koperberg Suite below the Khurisberg Subgroup (Sugarloaf Quarry)

4.3.1 Sample DSQ (Leuconorite, Sugarloaf Quarry)

Hand specimen description

The sample is a leuconorite composed of plagioclase, orthopyroxene, biotite, sulphide phases (chalcopyrite and bornite) and oxide phases. Greyish-pink plagioclase with minor quartz form an equigranular (2-4mm) groundmass in which ~2 mm orthopyroxene grains are evenly disseminated (Fig. 4.13). Sparse ~1-2 mm greenish-brown biotite and smaller (<1mm) sulphides and oxides occur close to orthopyroxene and to a lesser extent in the plagioclase matrix.

Figure 4. 13 Typical hand specimen for leuconorite sample DSQ 3 (Sugarloaf Quarry) showing orthopyroxene evenly disseminated in an equigranular plagioclase-rich matrix.

Microscopic description

The sample modally consists of plagioclase (~80%), orthopyroxene (~10%), oxide phases (magnetite, ilmenite; ~2%), sulphides (chalcopyrite, bornite; ~3.5%) and biotite (~4%). Accessory phases are apatite, monazite and K-feldspar.

Orthopyroxene and biotite commonly form 2-5 mm clusters within the plagioclase matrix (Fig. 4.14 a, c). Bornite and chalcopyrite form 30 – 800 µm intergrowths in close spatial association with biotite and orthopyroxene, as independent grains in sericitised zones in plagioclase, and at the intersection or along grain boundaries of plagioclase grains (Fig. 4.14a-d). A similar spatial relationship as the sulphides is exhibited by oxides. Magnetite constitutes ~70% of the total oxide phases, whereas

bornite constitutes ~75% of the total sulphide phases. Sulphides are invariably anhedral and exhibit feathered grain boundaries probably due to their formation in <100 µm plagioclase alteration zones around them, whereas magnetite and ilmenite are commonly subhedral and exhibit smooth grain boundaries (Fig. 4.14a-d).

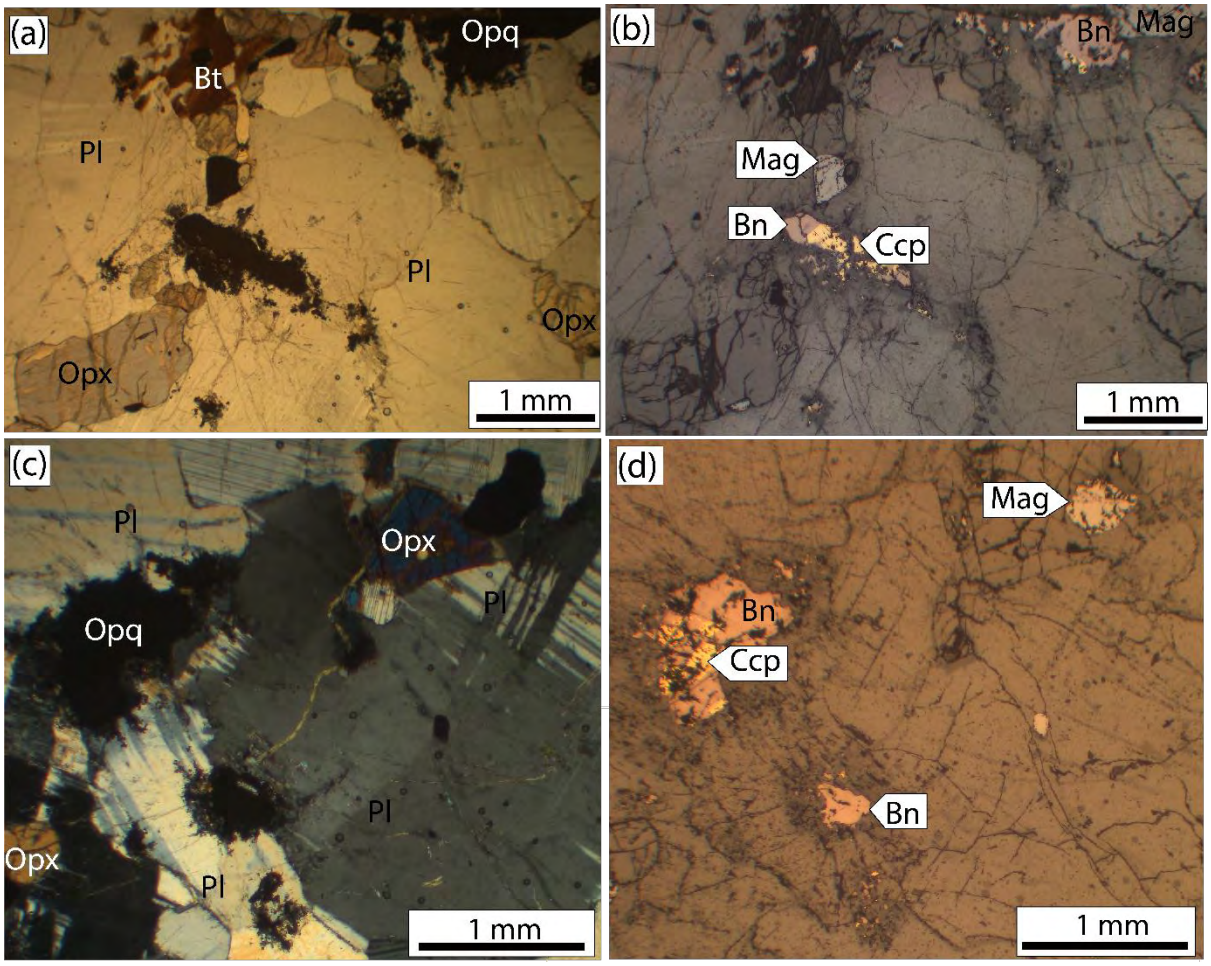

Figure 4. 14 Photomicrographs of leuconorite DSQ 3 (Sugarloaf Quarry) in plane polarised light (a), cross polarised light (c) and reflected light (b,d). The corresponding reflected light images for (a) and (c) are (b) and (d), respectively. (a-d) Sulphide and oxide phases commonly occur within orthopyroxene-biotite clusters, along grain boundaries of mafic silicate phases (biotite and orthopyroxene) and plagioclase. Sulphides exhibit feathered grain boundaries whereas oxides have smooth grain boundaries.

5 Mineral chemistry

5.1 Major element chemistry

The major element compositions of the main phases from the Khurisberg Subgroup and the Koperberg Suite were determined using the EDS and EPMA techniques. EPMA was used to determine the composition of sulphide phases only. The compositions of the silicates, oxide and phosphates were determined using EDS.

The analytical results presented in this section are for the sulphide phases. Results for main oxide and silicate phases (garnet, K-feldspar, plagioclase, biotite, muscovite, orthopyroxene, ilmenite and spinels), and common accessory phases (zircon, monazite, rutile and apatite) are presented in Table A1-A10 (Appendix 1).

The analyses in the tables have been grouped according to the lithological unit and/or locality. The following abbreviations have been used: KS (Khurisberg Subgroup), KNb (Koperberg Suite from Nababeep Mine), KNg (Koperberg Suite from Nigramoep Mine), KCr (Koperberg Suite from Carolusberg Mine), and KSQ (Koperberg Suite from Sugarloaf Quarry).

5.1.1 Silicates

5.1.1.1 Garnet

The garnet in the Khurisberg Subgroup samples is generally almandine-rich (X_{Alm}=0.65-0.80, X_{Prp}=0.16-0.27; Table A1; Appendix 1) and is characterised by low grossular and spessartine content (X_{Grs}=0.01-0.03, X_{Sps}=0.01-0.06; Table A1; Appendix 1). The andradite component is ≤0.02 moles in most analyses (Table A1; Appendix 1).

5.1.1.2 K-feldspar

The K-feldspar has X_{Or} values of 0.79-0.98. The K-feldspar analyses are presented in Table A2 (Appendix 1). K-feldspar in the Khurisberg Subgroup has relatively lower X_{Or} values (0.79-0.90) compared to samples from the Koperberg Suite with values 0.95-0.98. All K-feldspars contain minor contents (≤0.52 wt %) of CaO and TiO_2.

5.1.1.3 Plagioclase

The plagioclase compositions lie within the andesine to labradorite range (An=0.35-0.59) and contain ≤0.03 moles of the orthoclase component. The plagioclase analyses are presented in Table A3 (Appendix 1). Plagioclase in the Khurisberg Subgroup samples has lower An values (0.35-0.36), whereas Koperberg Suite samples are characterised by higher An values (0.43-0.59). All samples are characterised by minor contents of K_2O (≤0.5 wt %).

5.1.1.4 Biotite

The biotite in all the samples is phlogopitic (X_{Mg}=0.51-0.75; Tischendorf et al., 2007) and Ti-bearing (0.11-0.33 cations per formula unit (pfu) for 0.00-0.25 cations of Al^{IV}). The biotite analyses are presented in Table A4 (Appendix 1). Chromium, Mn, and Ni content is <1 oxide wt% and contribute

≤0.02 cations pfu. A few samples with low TiO_2 content (≤0.7 wt%; Analyses 10-12) are characterised by higher Al^{IV} (1.03 moles per 11 O) and Cr_2O_3 contents (~1 wt%).

5.1.1.5 Muscovite

The samples contain Mg-Fe-rich and Fe-rich varieties of muscovite ($X_{Fe(tot)}$=0.2-0.5, and $X_{Fe(tot)}$=0.2-1.0, respectively; Tischendorf et al., 2007). The muscovite analyses show significant amounts of MgO and FeO (up to ~8 wt% combined; Table A5, Appendix 1), which would require confirmation with EPMA. The Ba, Cr, Mn, Ni, and Ti contents are low (≤0.16 oxide wt%) in all samples.

5.1.1.6 Orthopyroxene

The orthopyroxene has enstatite (En) contents ranging from $En_{59.3}$ to $En_{65.6}$ (Table A6; Appendix 1). The orthopyroxene in the leuconorite samples is characterised by slightly lower enstatite contents due to higher Fe^{2+} ($En_{0.70-0.74}$) compared to the orthopyroxene found in the rest of the samples (Table A6; Appendix 1). Calcium, Cr and Mn contents are mostly ≤0.7 wt% and account for 0.01-0.02 cations per 6 O of the total metal cation content (Table A6; Appendix 1).

5.1.2 Oxides

5.1.2.1 Ilmenite

The ilmenite in the Khurisberg Subgroup samples has uniformly higher X_{Ilm} values (≥0.97) and lower X_{Pph} values (≤0.02) compared to the Koperberg Suite samples with X_{Ilm} values of 0.84-0.95 and X_{Pph} values ≥0.04 (Table A7; Appendix 1). All the samples have a small geikielite component (≤0.02 mol%; Table A7, Appendix 1). The Khurisberg Subgroup samples invariably contain lower but uniform Fe^{3+} contents (0.03-0.06 cations), whereas some of the Koperberg Suite samples show higher Fe^{3+} contents (0.07-0.13 cations; Table A7, Appendix 1). All samples contain minor (≤1.0 oxide wt%) V, Zr, Cr and Ti contents and these elements contribute 0.01-0.02 cation per formula unit.

5.1.2.2 Spinel

Magnetite is present in all samples. It shows limited variability in Fe^{2+} content (1.99-1.01 cations pfu; Table A8, Appendix 1) and a larger variability in Fe^{3+} content (1.87-1.97 cations pfu). The orthopyroxenite samples from Carolusberg Mine and some of the norite samples from Nigramoep Mine have magnetite with lower Fe^{3+} content compared to the rest of the samples (<1.90 cations pfu) which is somewhat compensated by higher Cr content (0.07-0.08 cations pfu). The magnetite from the leuconorite samples exhibits slightly higher V content (0.03 cations pfu) compared to the rest of the samples with 0.01-0.02 cations pfu. All samples contain minor contents (≤1 oxide wt%) of Mg, Mn, Zn and Ni. The chemical composition of the magnetite, therefore, falls within a solid solution series comprising magnetite (91.9-98.5 mol%), chromite (up to 3.9 mol%), hercynite (2.5 mol%), and coulsonite (up to 1.7 mol%).

Hercynitic spinel is present in the garnet-biotite-sillimanite gneiss sample (039T-1B3) from the Khurisberg Subgroup at Nababeep Mine. It shows limited variability in its Fe^{2+} and Al content (0.59 and 1.88 cations per formula unit, respectively). Representative results for hercynite compositions

and endmember compositions are presented in Table A8 (Analyses 1-3). The major divalent substituents in hercynite are Mg and Zn (0.1-0.3 cations) whereas Fe and Cr are the major trivalent substituents (0.04-0.09 cations). Vanadium, Mn, Ni and Ti contents are minor (<0.5 oxide wt%). The hercynitic spinel is thus a solid solution containing hercynite (~55 mol%), spinel (~20-28 mol%), and gahnite (~11-18 mol%).

Ulvöspinel is present in norite sample (KNU 477) from the Nigramoep Mine and forms exsolutions in magnetite and ilmenite. The Fe^{2+} and Ti content in ulvöspinel is variable (1.4-1.9 and 0.4-0.9 cations pfu). The results for ulvöspinel are presented in Table A8 (Analyses 24-26). Lower contents of Fe^{2+} in ulvöspinel are compensated by higher Fe^{3+} and Cr content, making these elements the main trivalent substituents. The ulvöspinel is thus a solid solution made up of magnetite (~12-50 mol%) and ulvöspinel (~42-85 mol%).

5.1.3 Sulphides

5.1.3.1 Pyrite

Pyrite (FeS_2) is present in the Khurisberg Subgroup (KS) samples 039T-1A and 039T-1B3. It occurs as a matrix phase and as inclusions in garnet (Fig. 4.2a). Compositionally both varieties are indistinguishable. The S/Fe ratios of pyrite are 1.81-1.93 with an average of 1.89 (*n=15*; Table 5.1), slightly below the ideal S/Fe ratio of 2.00. Sulphur is slightly depleted and Fe slightly enriched (average of 1.96 and 1.04 ions pfu, respectively; Table 5.1). The slight shift of data points towards the Fe corner in the Cu-Fe-S ternary diagram depicts this relationship (Fig. 5.1a). The main minor base metal is Ni, which contributes ~0.01 ions pfu (~0.1-0.3 wt%; Table 5.1). Arsenic, Cu, Zn, and Pb contents are low (<0.09 wt %; Table 5.1) and mostly below the detection limit of EPMA (0.04 wt%, 0.02 wt%, 0.14 wt%, 0.05 wt%, respectively; Table A11, Appendix 2).

5.1.3.2 Pyrrhotite

Pyrrhotite (Fe_7S_8) is present in the Khurisberg Subgroup (KS) samples 039T-1A and 039T-1B3. Pyrrhotite is non-stoichiometric and exists as various monoclinic or hexagonal polytypes with variable S and Fe contents. The S/Fe ratios of pyrrhotite are 1.08-1.13 with an average of 1.10 (*n=34*; Table 5.2). Most of these values fall within the S/Fe range for the common hexagonal pyrrhotite varieties of 1.09-1.11 (Fe_9S_{10}, $Fe_{10}S_{11}$, and $Fe_{11}S_{12}$; Wang and Salveson, 2005), as depicted in the Cu-Fe-S ternary diagram in (Fig. 5.1a). The main minor element is Ni and it contributes ~0.05 cations pfu (~0.50 wt%; Table 5.2). Arsenic, Cu, Zn, and Pb contents are low (<0.15 wt %; Table 5.2) and mostly below the EPMA detection limit (0.05 wt%, 0.03 wt%, 0.15 wt%, 0.05 wt%, respectively; Table A11, Appendix 2).

Table 5. 1 EPMA results for pyrite (FeS_2) compositions (in wt%).

Sample	**1A3**	**1A3**	**1A3**	**1A3**	**1A3**	**1A3**	**1A3**	**1A3**	**1A3**	**1A3**	**1A3**	**1A3**	**1A3**	**1A3**	**1A3**
Analysis	**1 (KS)**	**2 (KS)**	**3 (KS)**	**4 (KS)**	**5 (KS)**	**6 (KS)**	**7 (KS)**	**8 (KS)**	**9 (KS)**	**10 (KS)**	**11 (KS)**	**12 (KS)**	**13 (KS)**	**14 (KS)**	**15 (KS)**
S	52.63	52.71	52.51	52.40	52.61	50.52	52.63	52.56	53.05	52.48	52.91	52.55	52.54	53.10	53.49
Fe	48.23	48.42	48.46	48.44	48.26	48.70	47.96	48.18	48.35	48.50	48.61	48.53	48.43	48.16	48.26
As	-	-	0.04	0.05	-	0.04	-	0.06	0.04	0.05	0.08	0.05	-	-	0.09
Cu	-	-	-	-	-	-	-	-	-	-	-	-	-	-	-
Zn	-	-	-	-	-	-	-	-	-	-	-	-	-	-	-
Pb	-	-	-	-	-	-	-	-	-	-	-	-	-	-	-
Ni	0.09	0.12	0.12	-	0.13	0.30	0.28	0.35	-	0.12	-	-	-	0.14	-
Total	100.96	101.25	101.13	100.89	101.00	99.56	100.87	101.15	101.44	101.14	101.60	101.13	100.97	101.41	101.84
Ions															
S	1.96	1.96	1.96	1.96	1.96	1.93	1.97	1.96	1.97	1.96	1.96	1.96	1.96	1.97	1.97
Fe	1.03	1.04	1.04	1.04	1.03	1.07	1.03	1.03	1.03	1.04	1.04	1.04	1.04	1.03	1.02
As	-	-	-	-	-	-	-	-	-	-	-	-	-	-	-
Cu	-	-	-	-	-	-	-	-	-	-	-	-	--	-	-
Zn	-	-	-	-	-	-	-	-	-	-	-	-	-	-	-
Pb	-	-	-	-	-	-	-	-	-	-	-	-	-	-	-
Ni	-	-	-	-	-	0.01	0.01	0.01	-	-	-	-	-	-	-
Total	3.00	3.00	3.00	3.00	3.00	3.00	3.00	3.00	3.00	3.00	3.00	3.00	3.00	3.00	3.00
S/Fe	1.90	1.90	1.89	1.88	1.90	1.81	1.91	1.90	1.91	1.88	1.90	1.89	1.89	1.92	1.93

KS: Khurisberg Subgroup. '–' below detection limit

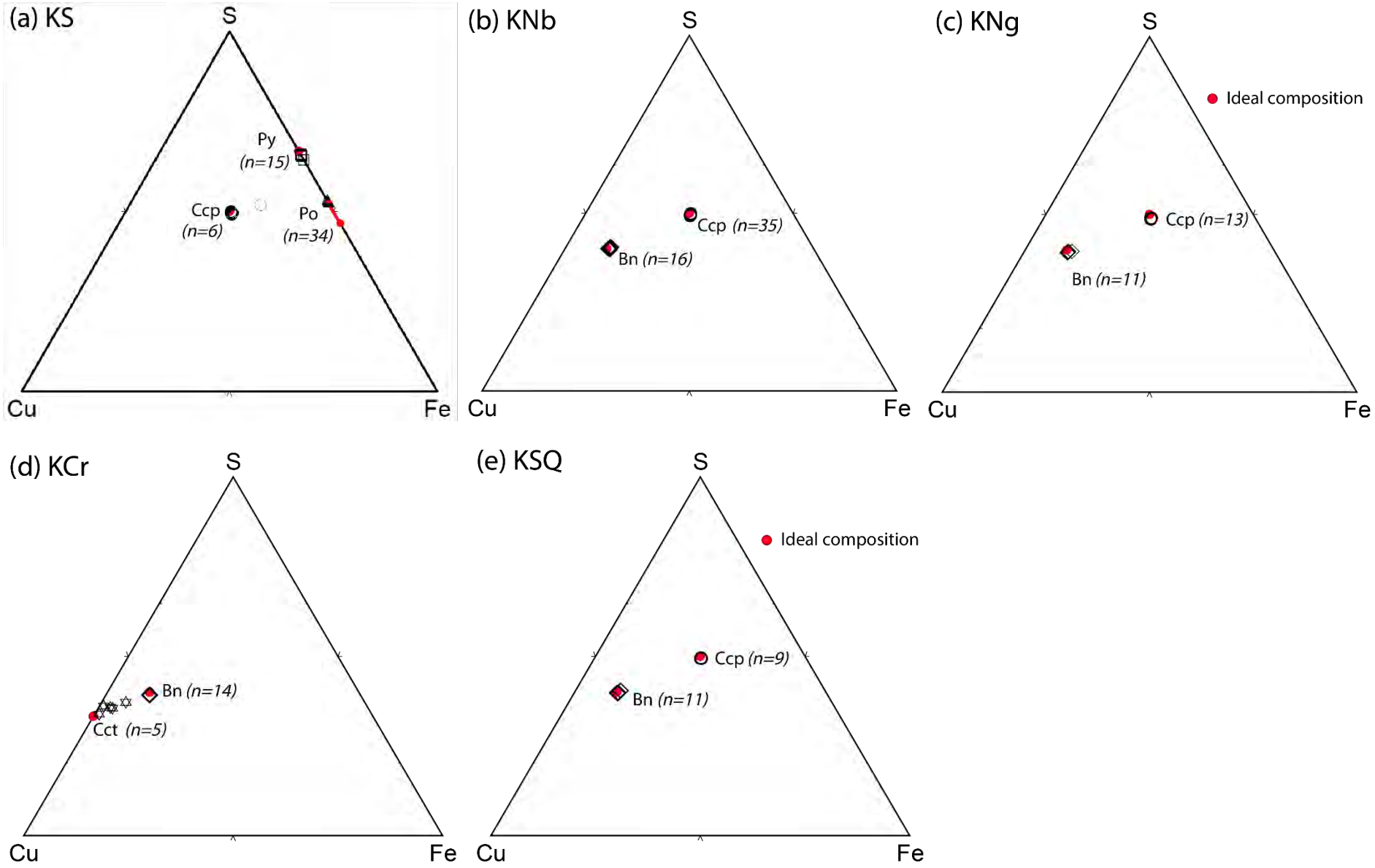

Figure 5. 1 Cu-Fe-S ternary plots of atomic percent compositions of sulphide minerals from the Koperberg Suite and Khurisberg Subgroup. KS: Khurisberg Subgroup, KNb: Koperberg Suite from Nababeep Mine, KNg: Koperberg Suite from Nigramoep Mine, KCr: Koperberg Suite from Carolusberg Mine, KSQ: Koperberg Suite from Sugarloaf Quarry.

Table 5. 2 EPMA results for pyrrhotite (Fe_7S_8) compositions (in wt%).

Sample	**1A3**	**1A3**	**1A3**	**1A3**	**1A3**	**1A3**	**1A3**	**1A3**	**1B3**	**1B3**	**1B3**	**1B3**	**1B3**	**1B3**	**1B3**	**1B3**	**1B3**
Analysis	**1 (KS)**	**2 (KS)**	**3 (KS)**	**4 (KS)**	**5 (KS)**	**6 (KS)**	**7 (KS)**	**8 (KS)**	**9 (KS)**	**10 (KS)**	**11 (KS)**	**12 (KS)**	**13 (KS)**	**14 (KS)**	**15 (KS)**	**16 (KS)**	**17 (KS)**
S	39.24	38.71	39.49	39.54	38.93	39.37	39.64	39.23	38.72	38.59	38.33	38.70	38.67	38.70	38.49	38.51	38.42
Fe	61.22	61.81	61.21	61.28	61.54	61.02	61.18	61.01	61.49	61.56	61.57	61.51	61.93	61.68	61.56	61.45	61.04
As	0.07	0.13	0.03	0.08	0.07	0.06	0.05	0.07	0.11	0.10	-	0.08	0.05	0.11	0.05	0.12	0.12
Cu	-	-	-	-	-	-	-	-	-	-	-	-	-	-	-	-	-
Zn	-	-	-	-	-	-	-	-	-	-	-	-	-	-	-	-	-
Pb	-	-	-	-	0.06	-	-	-	-	-	-	-	-	-	-	-	0.05
Ni	0.13	0.24	0.09	0.11	0.20	0.20	0.17	0.12	0.50	0.56	0.42	0.55	0.43	0.27	0.43	0.53	0.42
Total	100.66	100.89	100.82	101.01	100.81	100.65	101.05	100.43	100.82	100.81	100.32	100.83	101.08	100.77	100.53	100.60	100.06
Ions																	
S	7.90	7.81	7.93	7.93	7.85	7.92	7.94	7.91	7.81	7.79	7.78	7.81	7.79	7.81	7.79	7.79	7.81
Fe	7.08	7.16	7.06	7.05	7.12	7.06	7.04	7.07	7.12	7.14	7.17	7.12	7.16	7.15	7.16	7.14	7.13
As	0.01	0.01	-	0.01	0.01	-	-	0.01	0.01	0.01	-	0.01	-	0.01	-	0.01	0.01
Cu	-	-	-	-	-	-	-	-	-	-	-	-	-	-	-	-	-
Zn	-	-	-	-	-	-	-	-	-	-	-	-	-	-	-	-	-
Pb	-	-	-	-	-	-	-	-	-	-	-	-	-	-	-	-	-
Ni	0.01	0.03	0.01	0.01	0.02	0.02	0.02	0.01	0.06	0.06	0.05	0.06	0.05	0.03	0.05	0.06	0.05
Total	15.00	15.00	15.00	15.00	15.00	15.00	15.00	15.00	15.00	15.00	15.00	15.00	15.00	15.00	15.00	15.00	15.00
S/Fe	1.12	1.09	1.12	1.12	1.10	1.12	1.13	1.12	1.10	1.09	1.08	1.10	1.09	1.09	1.09	1.09	1.10

Table 5. 2 *(continued)*

Sample	**1B3**	**1B3**	**1B3**	**1B3**	**1B3**	**1B3**	**1B3**	**1B3**	**1B3**	**1B3**	**1B3**	**1B3**	**1B3**	**1B3**	**1B3**	**1B3**	**1B3**
Analysis	**18 (KS)**	**19 (KS)**	**20 (KS)**	**21 (KS)**	**22 (KS)**	**23 (KS)**	**24 (KS)**	**25 (KS)**	**26 (KS)**	**27 (KS)**	**28 (KS)**	**29 (KS)**	**30 (KS)**	**31 (KS)**	**32 (KS)**	**33 (KS)**	**34 (KS)**
S	38.69	38.83	38.82	39.13	38.75	38.54	38.63	38.61	38.59	38.54	38.58	38.78	38.71	38.96	38.40	38.56	38.94
Fe	61.59	61.73	61.66	61.65	61.52	61.96	61.35	61.45	61.34	61.32	61.29	61.69	61.17	61.18	61.55	61.33	61.65
As	-	-	0.05	0.08	0.08	0.11	0.05	0.05	-	-	-	0.11	0.07	0.05	0.09	0.11	0.12
Cu	-	-	-	-	-	-	-	-	-	-	-	-	-	-	-	-	-
Zn	-	0.15	-	-	-	-	-	-	-	-	-	-	-	-	-	-	-
Pb	-	-	-	-	-	-	-	-	-	-	-	-	-	-	-	-	-
Ni	0.51	0.46	0.66	0.47	0.49	0.48	0.45	0.52	0.49	0.39	0.48	0.46	0.50	0.51	0.58	0.49	0.42
Total	100.83	101.16	101.19	101.33	100.84	101.09	100.47	100.63	100.42	100.25	100.36	101.03	100.45	100.71	100.63	100.49	101.12
Ions																	
S	7.81	7.81	7.81	7.85	7.82	7.77	7.82	7.81	7.81	7.82	7.81	7.81	7.83	7.86	7.77	7.81	7.83
Fe	7.13	7.13	7.12	7.10	7.12	7.17	7.13	7.13	7.13	7.14	7.13	7.13	7.11	7.08	7.15	7.13	7.12
As	-	-	-	0.01	0.01	0.01	-	-	-	-	-	0.01	0.01	-	0.01	0.01	0.01
Cu	-	-	-	-	-	-	-	-	-	-	-	-	-	-	-	-	-
Zn	-	0.01	-	-	-	-	-	-	-	-	-	-	-	-	-	-	-
Pb	-	-	-	-	-	-	-	-	-	-	-	-	-	-	-	-	-
Ni	0.06	0.05	0.07	0.05	0.05	0.05	0.05	0.06	0.05	0.04	0.05	0.05	0.05	0.06	0.06	0.05	0.05
Total	15.00	15.00	15.00	15.00	15.00	15.00	15.00	15.00	15.00	15.00	15.00	15.00	15.00	15.00	15.00	15.00	15.00
S/Fe	1.09	1.10	1.10	1.11	1.10	1.08	1.10	1.09	1.10	1.09	1.10	1.09	1.10	1.11	1.09	1.10	1.10

KS: Khurisberg Subgroup. '–': below detection limit

5.1.3.3 Chalcopyrite

Chalcopyrite ($CuFeS_2$) has been analysed in samples from all localities except for Carolusberg Mine (KCr). Irrespective of sample or lithology, chalcopyrite compositions are close to the ideal endmember ($CuFeS_2$). The Cu/S ratios of analysed chalcopyrite are in the range of 0.49 to 0.52 (*n=63*; Table 5.3) with an average ratio of 0.51, close to the ideal value of 0.50. The chalcopyrite shows limited variability in Cu content (0.99-1.01 cations pfu) and the average Cu cation contribution is the same as the ideal composition (1.00; Table 5.3). The chalcopyrite however shows slight enrichment in Fe (1.01-1.04 ions pfu, average=1.03) and depletion in S compared to ideal chalcopyrite as indicated by the slight shift of compositions towards the Cu-Fe axis in Cu-Fe-S space (Fig. 5.1a-c,e). Arsenic, Zn, Ni and Pb contents are low (≤0.18 wt %; Table 5.3) and mostly below the EPMA detection limit (0.05 wt%, 0.16 wt%, 0.09 wt%, 0.05 wt%, respectively; Table A11, Appendix 2).

5.1.3.4 Bornite and chalcocite

Bornite (Cu_5FeS_4) is present in samples from the Koperberg Suite. The observed Cu/S ratios of bornite are 1.20-1.30. The average Cu/S ratio of 1.26 (*n=52*) is close to the ideal value of 1.25. The bornite compositions are presented in Table 5.4. All samples show slight enrichment in Fe (1.03-1.16 cations pfu, average=1.06). The bornite in the norite and orthopyroxenite from Nigramoep (KNg) and Carolusberg (KCr) mines have higher Cu/S ratios (>1.27) consistent with slight enrichment in Cu relative to S, a relationship depicted by the shift of compositions towards the Cu-Fe axis in Figures 5.1c and 5.1d. Conversely, the bornite in samples from Nababeep Mine (KNb) and Sugarloaf Quarry (KSQ) have close to- or slightly below the ideal Cu/S value (<1.26) consistent with slight enrichment in S relative to Cu clustering around the ideal mineral composition or showing a slight shift towards the S corner in the Cu-Fe-S ternary diagrams (Fig. 5.1b, e). Arsenic, Zn, Ni and Pb contents are low (≤0.01 wt; Table 5.4) and commonly below the EPMA detection limit (0.05 wt%, 0.17 wt%, 0.09 wt%, 0.05 wt%, respectively; Table A11, Appendix 2).

Chalcocite (Cu_2S) is present only in the orthopyroxenite sample from Carolusberg Mine (KCr), where it forms <10 µm µm thin exsolution lamellae (Fig. 4.12c). It has variable Cu and Fe content and lower Cu/S ratios (1.54-1.92, average=1.73; *n=5*) compared to the ideal value of 2.0, pointing to enrichment in S relative to Cu (Table 5.5). It also contains small amounts of Fe (~0.08 cations pfu). Chalcocite compositions form a linear trend between ideal chalcocite and bornite in Cu-Fe-S space (Fig. 5.1d). This is consistent with chalcocite exsolution from bornite (Fig. 4.12c) or could be a result of minor contamination by the host bornite during EPMA analysis.

Table 5. 3 EPMA results for chalcopyrite ($CuFeS_2$) compositions (in wt%).

Sample	**1A3**	**1A3**	**1A3**	**1A3**	**1A3**	**1B3**	**4A**	**4A**	**4A**	**4B**	**4B**	**4B**	**4B**	**4B**	**4B**	**4B**	**4B**	**4B**	**4B**	**4B**
Analysis	**1 (KS)**	**2 (KS)**	**3 (KS)**	**4 (KS)**	**5 (KS)**	**6 (KS)**	**7 (KNb)**	**8 (KNb)**	**9 (KNb)**	**10 (KNb)**	**11 (KNb)**	**12 (KNb)**	**13 (KNb)**	**14 (KNb)**	**15 (KNb)**	**16 (KNb)**	**17 (KNb)**	**18 (KNb)**	**19 (KNb)**	**20 (KNb)**	**21 (KNb)**
S	34.22	34.75	34.80	34.52	34.97	34.73	34.50	34.27	34.21	34.45	34.43	34.40	34.50	34.44	34.60	34.60	34.35	34.62	34.44	34.47	34.31
Fe	31.36	31.31	31.50	31.51	31.05	31.18	30.95	30.95	31.10	31.12	31.05	31.23	31.22	31.22	30.98	31.37	31.21	31.09	30.91	31.02	31.13
As	0.08	0.05	-	0.13	0.08	-	-	0.11	0.08	-	0.10	0.08	0.05	0.13	-	-	-	0.09	-	0.05	-
Cu	34.15	34.46	34.09	34.23	34.25	34.11	34.53	34.53	34.48	34.43	34.49	34.49	34.58	34.63	34.54	34.40	34.61	34.33	34.47	34.55	34.36
Zn	-	-	-	-	-	-	-	-	-	-	-	-	-	-	-	-	-	-	-	-	-
Pb	-	-	-	-	-	-	-	-	0.05	-	-	-	-	-	-	-	-	-	-	-	-
Ni	-	-	-	-	-	-	-	-	-	-	-	-	-	-	-	-	-	-	-	-	-
Total	99.81	100.57	100.39	100.39	100.35	100.02	99.98	99.86	99.92	100.00	100.07	100.20	100.35	100.42	100.12	100.37	100.17	100.13	99.82	100.09	99.80
Ions																					
S	1.97	1.98	1.99	1.97	2.00	1.99	1.98	1.97	1.97	1.98	1.98	1.97	1.97	1.97	1.98	1.98	1.97	1.98	1.98	1.98	1.97
Fe	1.04	1.03	1.03	1.03	1.02	1.03	1.02	1.02	1.03	1.03	1.02	1.03	1.03	1.03	1.02	1.03	1.03	1.02	1.02	1.02	1.03
As	-	-	-	-	-	-	-	-	-	-	-	-	-	-	-	-	-	-	-	-	-
Cu	0.99	0.99	0.98	0.99	0.99	0.99	1.00	1.00	1.00	1.00	1.00	1.00	1.00	1.00	1.00	0.99	1.00	0.99	1.00	1.00	1.00
Zn	-	-	-	-	-	-	-	-	-	-	-	-	-	-	-	-	-	-	-	-	-
Pb	-	-	-	-	-	-	-	-	-	-	-	-	-	-	-	-	-	-	-	-	-
Ni	-	-	-	-	-	-	-	-	-	-	-	-	-	-	-	-	-	-	-	-	-
Total	4.00	4.00	4.00	4.00	4.00	4.00	4.00	4.00	4.00	4.00	4.00	4.00	4.00	4.00	4.00	4.00	4.00	4.00	4.00	4.00	4.00
Cu/S	0.50	0.50	0.49	0.50	0.49	0.50	0.50	0.51	0.51	0.50	0.51	0.51	0.51	0.51	0.50	0.50	0.51	0.50	0.50	0.51	0.51

Table 5.3 *(continued)*

Sample	**4B**	**4A**	**4A**	**4A**	**4A**	**4A**	**4A**	**4A**	**4A**	**4A**	**3C**	**3A**	**3A**	**3A**	**3A**	**3A**	**3A**	**3A**	**3A**	**3C**	**KNU**
Analysis	**22 (KNb)**	**23 (KNb)**	**24 (KNb)**	**25 (KNb)**	**26 (KNb)**	**27 (KNb)**	**28 (KNb)**	**29 (KNb)**	**30 (KNb)**	**31 (KNb)**	**32 (KNb)**	**33 (KNb)**	**34 (KNb)**	**35 (KNb)**	**36 (KNb)**	**37 (KNb)**	**38 (KNb)**	**39 (KNb)**	**40 (KNb)**	**41 (KNb)**	**42 (KNg)**
S	34.37	35.28	34.43	34.69	34.64	34.54	34.78	34.77	34.50	34.52	34.56	34.28	34.45	34.83	34.97	34.82	34.69	34.43	33.70	33.85	33.51
Fe	31.24	31.20	31.28	31.24	31.06	31.20	31.30	31.28	31.19	31.29	30.90	31.02	30.71	31.18	30.83	31.15	30.87	30.90	30.69	30.57	31.15
As	0.05	-	-	-	-	-	0.06	-	0.12	-	0.06	-	-	0.05	-	-	0.08	-	-	0.09	-
Cu	34.73	34.57	34.54	34.44	34.39	34.61	34.62	34.58	34.60	34.45	34.62	34.38	34.68	34.26	34.24	34.37	34.52	34.39	34.29	34.18	34.30
Zn	-	-	-	-	-	-	-	-	-	-	-	-	-	-	-	-	-	-	-	-	-
Pb	-	-	-	-	-	-	-	-	-	-	-	-	-	-	-	-	-	-	-	0.07	-
Ni	-	-	-	-	-	-	-	-	-	-	-	-	-	-	-	-	-	-	-	-	-
Total	100.39	101.05	100.25	100.37	100.09	100.35	100.76	100.63	100.41	100.26	100.14	99.68	99.84	100.32	100.04	100.34	100.16	99.72	98.68	98.76	98.96
Ions																					
S	1.97	2.00	1.97	1.98	1.98	1.98	1.98	1.98	1.97	1.97	1.98	1.97	1.98	1.99	2.00	1.99	1.99	1.98	1.96	1.97	1.95
Fe	1.03	1.01	1.03	1.02	1.02	1.02	1.02	1.02	1.02	1.03	1.02	1.03	1.01	1.02	1.01	1.02	1.01	1.02	1.03	1.02	1.04
As	-	-	-	-	-	-	-	-	-	-	-	-	-	-	-	-	-	-	-	-	-
Cu	1.00	0.99	1.00	0.99	0.99	1.00	0.99	0.99	1.00	0.99	1.00	1.00	1.01	0.99	0.99	0.99	1.00	1.00	1.01	1.00	1.01
Zn	-	-	-	-	-	-	-	-	-	-	-	-	-	-	-	-	-	-	-	-	-
Pb	-	-	-	-	-	-	-	-	-	-	-	-	-	-	-	-	-	-	-	-	-
Ni	-	-	-	-	-	-	-	-	-	-	-	-	-	-	-	-	-	-	-	-	-
Total	4.00	4.00	4.00	4.00	4.00	4.00	4.00	4.00	4.00	4.00	4.00	4.00	4.00	4.00	4.00	4.00	4.00	4.00	4.00	4.00	4.00
Cu/S	0.51	0.49	0.51	0.50	0.50	0.51	0.50	0.50	0.51	0.50	0.51	0.51	0.51	0.50	0.49	0.50	0.50	0.50	0.51	0.51	0.52

Table 5.3 *(continued)*

Sample	**KNU**	**KNU**	**KNU**	**KNU**	**KNU**	**KNU**	**KNU**	**KNU**	**KNU**	**KNU**	**KNU**	**KNU**	**3B2**	**3B2**	**3B2**	**3D1**	**3D1**	**3D1**	**3D1**	**3D1**	**3D1**
Analysis	**43 (KNg)**	**44 (KNg)**	**45 (KNg)**	**46 (KNg)**	**47 (KNg)**	**48 (KNg)**	**49 (KNg)**	**50 (KNg)**	**51 (KNg)**	**52 (KNg)**	**53 (KNg)**	**54 (KNg)**	**55 (KSQ)**	**56 (KSQ)**	**57 (KSQ)**	**58 (KSQ)**	**59 (KSQ)**	**60 (KSQ)**	**61 (KSQ)**	**62 (KSQ)**	**63 (KSQ)**
S	33.72	33.72	33.53	33.33	33.73	33.48	33.50	33.74	33.56	33.55	33.70	33.75	34.54	34.76	34.26	34.20	34.28	34.19	34.05	34.04	34.13
Fe	31.14	31.18	31.15	30.93	30.93	30.80	30.95	31.05	30.81	30.88	31.02	30.97	30.81	30.99	30.62	30.84	30.89	30.87	30.82	30.36	30.54
As	-	-	0.10	0.05	-	0.15	-	-	-	-	0.06	-	0.07	-	-	-	0.07	-	0.07	-	-
Cu	34.17	34.24	34.44	34.47	34.23	34.40	34.57	34.57	34.24	34.28	34.57	34.44	34.47	34.57	34.91	34.43	34.46	34.23	34.30	34.12	34.27
Zn	-	-	-	-	0.16	-	-	-	-	0.18	-	-	-	-	-	-	-	-	-	-	-
Pb	-	-	-	-	-	-	-	-	-	-	-	-	-	-	-	-	-	-	-	-	-
Ni	-	-	-	-	-	-	-	-	-	-	-	-	-	-	-	-	-	-	-	-	-
Total	99.03	99.14	99.22	98.78	99.05	98.83	99.02	99.36	98.61	98.89	99.35	99.16	99.89	100.32	99.79	99.47	99.70	99.29	99.24	98.52	98.94
Ions																					
S	1.96	1.96	1.95	1.95	1.96	1.95	1.95	1.95	1.96	1.95	1.95	1.96	1.98	1.99	1.97	1.97	1.97	1.97	1.97	1.98	1.98
Fe	1.04	1.04	1.04	1.04	1.03	1.03	1.03	1.03	1.03	1.03	1.03	1.03	1.02	1.02	1.01	1.02	1.02	1.02	1.02	1.02	1.02
As	-	-	-	-	-	-	-	-	-	-	-	-	-	-	-	-	-	-	-	-	-
Cu	1.00	1.00	1.01	1.02	1.00	1.01	1.01	1.01	1.01	1.01	1.01	1.01	1.00	1.00	1.01	1.00	1.00	1.00	1.00	1.00	1.00
Zn	-	-	-	-	-	-	-	-	-	-	-	-	-	-	-	-	-	-	-	-	-
Pb	-	-	-	-	-	-	-	-	-	-	-	-	-	-	-	-	-	-	-	-	-
Ni	-	-	-	-	-	-	-	-	-	-	-	-	-	-	-	-	-	-	-	-	-
Total	4.00	4.00	4.00	4.00	4.00	4.00	4.00	4.00	4.00	4.00	4.00	4.00	4.00	4.00	4.00	4.00	4.00	4.00	4.00	4.00	4.00
Cu/S	0.51	0.51	0.52	0.52	0.51	0.52	0.52	0.52	0.51	0.52	0.52	0.51	0.50	0.50	0.51	0.51	0.51	0.51	0.51	0.51	0.51

KS: Khurisberg Subgroup, KNb: Koperberg Suite from Nababeep Mine, KNg: Koperberg Suite from Nigramoep Mine, KCr: Koperberg Suite from Carolusberg Mine, KSQ: Koperberg Suite from Sugarloaf Quarry. "–": below detection limit.

Table 5. 4 EPMA results for bornite (Cu_5FeS_4) compositions (in wt%), calculated for 10 ions.

Sample	**4A**	**4A**	**4A**	**4A**	**4B**	**4B**	**4B**	**4A**	**4A**	**4A**	**4A**	**4A**	**3C**	**3A**	**3A**	**3A**	**KNU**
Analysis	**1 (KNb)**	**2 (KNb)**	**3 (KNb)**	**4 (KNb)**	**5 (KNb)**	**6 (KNb)**	**7 (KNb)**	**8 (KNb)**	**9 (KNb)**	**10 (KNb)**	**11 (KNb)**	**12 (KNb)**	**13 (KNb)**	**14 (KNb)**	**15 (KNb)**	**16 (KNb)**	**17 (KNg)**
S	25.39	25.39	25.43	25.82	25.91	25.60	26.00	25.85	25.95	25.77	25.80	25.53	25.63	25.34	25.45	25.51	25.12
Fe	12.17	12.04	11.92	11.90	11.79	12.06	12.55	11.86	12.08	11.76	11.77	11.80	11.63	11.55	11.49	11.48	12.81
As	0.08	0.07	-	0.09	-	-	-	-	-	-	-	0.12	0.11	0.06	-	0.05	-
Cu	62.33	62.36	62.18	61.89	61.40	61.98	61.92	62.51	61.81	62.43	62.38	62.62	62.39	62.35	62.64	62.75	61.57
Zn	-	-	-	-	-	-	-	-	-	-	-	-	-	-	-	-	-
Pb	-	-	-	-	-	-	-	-	0.06	-	-	-	-	-	-	-	-
Ni	-	-	-	-	-	-	-	-	-	-	-	-	-	-	-	-	-
Total	99.97	99.86	99.53	99.70	99.10	99.64	100.47	100.22	99.90	99.96	99.95	100.07	99.76	99.30	99.58	99.79	99.50
Ions																	
S	3.98	3.98	3.99	4.04	4.07	4.01	4.03	4.03	4.05	4.02	4.03	3.99	4.01	3.99	4.00	4.00	3.95
Fe	1.09	1.08	1.07	1.07	1.06	1.08	1.12	1.06	1.08	1.05	1.05	1.06	1.05	1.04	1.04	1.03	1.16
As	0.01	-	-	0.01	-	-	-	-	-	-	-	0.01	0.01	-	-	-	-
Cu	4.92	4.93	4.93	4.89	4.87	4.90	4.85	4.91	4.87	4.92	4.91	4.94	4.93	4.96	4.96	4.96	4.89
Zn	-	-	-	-	-	0.01	-	-	-	-	-	-	-	-	-	-	-
Pb	-	-	-	-	-	-	-	-	-	-	-	-	-	-	-	-	-
Ni	-	-	-	-	-	-	-	-	-	-	-	-	-	-	-	0.01	-
Total	10.00	10.00	10.00	10.00	10.00	10.00	10.00	10.00	10.00	10.00	10.00	10.00	10.00	10.00	10.00	10.00	10.00
Cu/S	1.24	1.24	1.23	1.21	1.20	1.22	1.20	1.22	1.20	1.22	1.22	1.24	1.23	1.24	1.24	1.24	1.24

Table 5.4 *(continued)*

Sample	**KNU**	**KNU**	**KNU**	**KNU**	**KNU**	**KNU**	**KNU**	**KNU**	**KNU**	**KNU**	**CD**	**CD**	**CD**	**CD**	**CD**	**CD**	**CD**
Analysis	**18 (KNg)**	**19 (KNg)**	**20 (KNg)**	**21 (KNg)**	**22 (KNg)**	**23 (KNg)**	**24 (KNg)**	**25 (KNg)**	**26 (KNg)**	**27 (KNg)**	**28 (KCr)**	**29 (KCr)**	**30 (KCr)**	**31 (KCr)**	**32 (KCr)**	**33 (KCr)**	**34 (KCr)**
S	24.70	24.82	24.61	24.71	24.83	25.04	24.64	24.69	24.67	24.84	24.66	24.66	24.82	24.85	24.67	24.54	24.81
Fe	11.68	11.70	11.63	11.58	11.68	11.69	11.68	11.46	11.59	11.49	11.34	11.47	11.45	11.56	11.64	11.49	11.46
As	-	-	-	-	0.06	-	-	-	0.12	-	0.11	-	-	-	-	-	0.13
Cu	62.47	62.00	62.57	62.73	62.49	62.51	62.78	62.44	62.79	62.66	63.16	63.08	63.13	63.09	62.65	63.11	63.06
Zn	-	-	-	-	-	-	-	-	-	-	-	-	-	-	-	-	-
Pb	0.05	-	-	-	-	-	-	-	-	-	-	-	-	-	-	-	-
Ni	-	-	-	-	-	-	-	-	-	-	-	-	-	-	-	-	-
Total	98.90	98.52	98.81	99.02	99.06	99.24	99.10	98.59	99.17	98.99	99.27	99.21	99.40	99.50	98.96	99.14	99.46
Ions																	
S	3.92	3.95	3.92	3.92	3.94	3.96	3.91	3.93	3.91	3.94	3.91	3.91	3.92	3.92	3.92	3.89	3.92
Fe	1.07	1.07	1.06	1.06	1.06	1.06	1.06	1.05	1.05	1.05	1.03	1.04	1.04	1.05	1.06	1.05	1.04
As	-	-	-	-	-	-	-	-	0.01	-	0.01	-	-	-	-	-	0.01
Cu	5.01	4.98	5.02	5.02	5.00	4.98	5.03	5.02	5.02	5.01	5.05	5.05	5.04	5.02	5.02	5.05	5.03
Zn	-	-	-	-	-	-	-	-	-	-	-	-	-	0.01	-	0.01	-
Pb	-	-	-	-	-	-	-	-	-	-	-	-	-	-	-	-	-
Ni	-	-	-	-	-	-	-	-	-	-	0.01	-	-	-	-	-	-
Total	10.00	10.00	10.00	10.00	10.00	10.00	10.00	10.00	10.00	10.00	10.00	10.00	10.00	10.00	10.00	10.00	10.00
Cu/S	1.28	1.26	1.28	1.28	1.27	1.26	1.29	1.28	1.28	1.27	1.29	1.29	1.28	1.28	1.28	1.30	1.28

Table 5.4 *(continued)*

Sample	**CD**	**CD**	**CD**	**CD**	**CD**	**CD**	**CD**	**3B2**	**3B2**	**3B2**	**3B2**	**3D1**	**3D1**	**3D1**	**3D1**	**3D1**	**3D1**	**3D1**
Analysis	**35 (KCr)**	**36 (KCr)**	**37 (KCr)**	**38 (KCr)**	**39 (KCr)**	**40 (KCr)**	**41 (KCr)**	**42 (KSQ)**	**43 (KSQ)**	**44 (KSQ)**	**45 (KSQ)**	**46 (KSQ)**	**47 (KSQ)**	**48 (KSQ)**	**49 (KSQ)**	**50 (KSQ)**	**51 (KSQ)**	**52 (KSQ)**
S	24.66	24.72	24.69	24.87	24.90	24.49	24.74	25.18	25.57	25.35	25.27	24.93	25.20	25.90	25.18	25.76	25.18	25.25
Fe	11.45	11.39	11.53	11.42	11.45	11.53	11.56	11.60	11.63	11.56	11.55	11.39	11.54	11.88	11.66	12.09	11.46	11.57
As	-	0.06	-	-	-	0.10	-	0.05	0.07	0.09	-	0.06	-	-	-	-	0.09	-
Cu	63.02	62.91	62.98	62.95	62.92	63.03	62.93	62.56	62.71	62.61	62.87	62.46	62.72	62.04	62.83	61.47	62.94	63.22
Zn	-	-	-	-	-	-	-	-	-	-	-	-	-	-	-	-	-	-
Pb	-	-	-	-	-	-	-	-	-	-	-	-	-	-	-	-	-	-
Ni	-	-	-	-	-	-	-	-	-	-	-	-	-	-	-	-	-	-
Total	99.13	99.08	99.20	99.24	99.27	99.15	99.23	99.39	99.98	99.61	99.69	98.84	99.46	99.82	99.67	99.32	99.67	100.04
Ions																		
S	3.91	3.92	3.91	3.94	3.94	3.89	3.92	3.97	4.00	3.98	3.97	3.96	3.97	4.04	3.96	4.04	3.96	3.96
Fe	1.04	1.04	1.05	1.04	1.04	1.05	1.05	1.05	1.04	1.04	1.04	1.04	1.04	1.06	1.05	1.09	1.04	1.04
As	-	-	-	-	-	0.01	-	-	-	0.01	-	-	-	-	-	-	0.01	-
Cu	5.04	5.04	5.04	5.03	5.02	5.05	5.03	4.98	4.95	4.96	4.98	5.00	4.98	4.89	4.98	4.87	5.00	5.00
Zn	-	-	-	-	-	0.01	-	-	-	-	-	-	-	-	-	-	-	-
Pb	-	-	-	-	-	-	-	-	-	-	-	-	-	-	-	-	-	-
Ni	-	-	-	-	-	-	-	-	-	-	-	-	-	-	-	-	-	-
Total	10.00	10.00	10.00	10.00	10.00	10.00	10.00	10.00	10.00	10.00	10.00	10.00	10.00	10.00	10.00	10.00	10.00	10.00
Cu/S	1.29	1.28	1.29	1.28	1.27	1.30	1.28	1.25	1.24	1.25	1.26	1.26	1.26	1.21	1.26	1.20	1.26	1.26

KS: Khurisberg Subgroup, KNb: Koperberg Suite from Nababeep Mine, KNg: Koperberg Suite from Nigramoep Mine, KCr: Koperberg Suite from Carolusberg Mine, KSQ: Koperberg Suite from Sugarloaf Quarry. "–": below detection limit

Table 5. 5 EPMA results for chalcocite (Cu_2S) compositions (in wt%).

Sample	**CD**	**CD**	**CD**	**CD**	**CD**
Analysis	**1 (KCr)**	**2 (KCr)**	**3 (KCr)**	**4 (KCr)**	**5 (KCr)**
S	21.90	21.73	21.18	23.00	20.46
Fe	2.91	3.66	1.12	6.20	1.02
As	-	0.09	-	-	-
Cu	74.79	74.13	72.93	69.98	77.72
Zn	-	-	-	-	-
Pb	-	-	0.04	-	-
Ni	-	-	-	-	-
Total	99.60	99.61	95.27	99.32	99.20
Ions					
S	1.07	1.06	1.08	1.11	1.02
Fe	0.08	0.10	0.03	0.17	0.03
As	-	-	-	-	-
Cu	1.85	1.83	1.88	1.71	1.95
Zn	-	-	-	-	-
Pb	-	-	-	-	-
Ni	-	-	-	-	-
Total	3.00	3.00	3.00	3.00	3.00
Cu/S	1.72	1.72	1.74	1.54	1.92

KCr: Koperberg Suite from Carolusberg Mine. "–": below detection limit

5.2 Trace element chemistry

Quantitative trace element analysis was done on pyrite, pyrrhotite, chalcopyrite and bornite from the Khurisberg Subgroup and Koperberg Suite. The analytical data are presented in Table 5.6 and illustrated in form of violin diagrams (Figs. 5.3-5.8). Violin plots are constituted of two superimposed components: (i) symmetrical non-parametric kernel density plots (or curves), which show peaks where data points are highly concentrated (thus allowing easy visualisation of the distribution of data points), and (ii) box plots. Figure 5.2 shows the components of a typical violin diagram. In the following descriptions, trace elements have been grouped according to their association in specific sulphide phases.

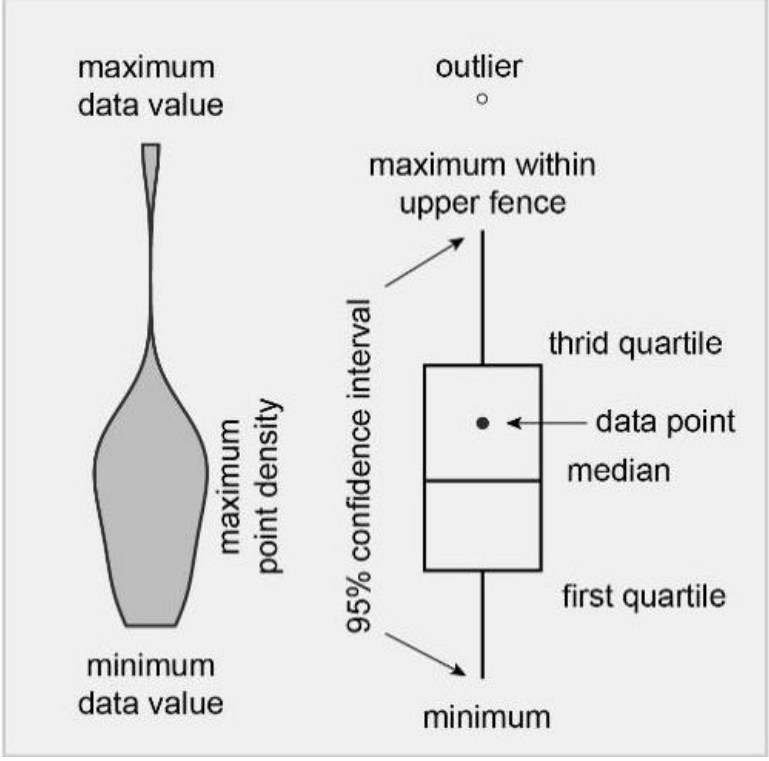

Figure 5. 2 Constituents of a typical violin plot: rotated (symmetrical) kernel density plots (left) and a box plot (right) (*after Marfin et al., 2020*).

Se and Te

Bornite in the Koperberg Suite samples (KCr, KNg, KNb) is enriched in Te and Se (up to ~380 ppm for both the elements; Table 5.6; Fig. 5.3a, b) compared to chalcopyrite (up to ~130 ppm; Table 5.6; Fig. 5.3a,b). The highest contents of Te and Se are recorded by bornite in the most basic Koperberg Suite host rocks (orthopyroxenite from Carolusberg Mine (KCr) and norite from Nigramoep Mine (KNg)) (Table 5.6; Fig. 5.3a, b). Bornite hosted in the less basic Koperberg Suite rocks (leucodiorites and diorites from Nababeep Mine (KNb)) show lower Te and Se contents (<5 ppm, <160 ppm, respectively; Table 5.6; Fig. 5.3a, b). Selenium contents for chalcopyrite hosted in the Koperberg Suite samples follows the same trends as bornite, that is, enrichment in the more basic rocks (KNg) (up to ~130 ppm, Table 5.6; Fig. 5.3a, b) compared to less basic rocks (KNb) (<75 ppm; Table 5.6; Fig. 5.3a, b). The Te trends for chalcopyrite hosted in the Koperberg Suite are antithetic to those of Se, that is, enrichment (~2-12 ppm; Table 5.6; Fig. 5.3a, b) in the less basic rocks (KNb) and relative depletion (~<2 ppm; Table 5.6; Fig. 5.3a,b) in the basic rocks (KNg).

The Se content of pyrrhotite overlaps with chalcopyrite from Nababeep Mine (KNb), whereas pyrite shows overlap in Se content with chalcopyrite from the Khurisberg Subgroup (KS) (Fig. 5.3a, b). The Te content of both pyrrhotite and pyrite from the Khurisberg Subgroup (KS) is < 1ppm (Table 5.6; Fig. 5.3a, b) and does not overlap with the bornite and chalcopyrite composition (Fig. 5.3a, b).

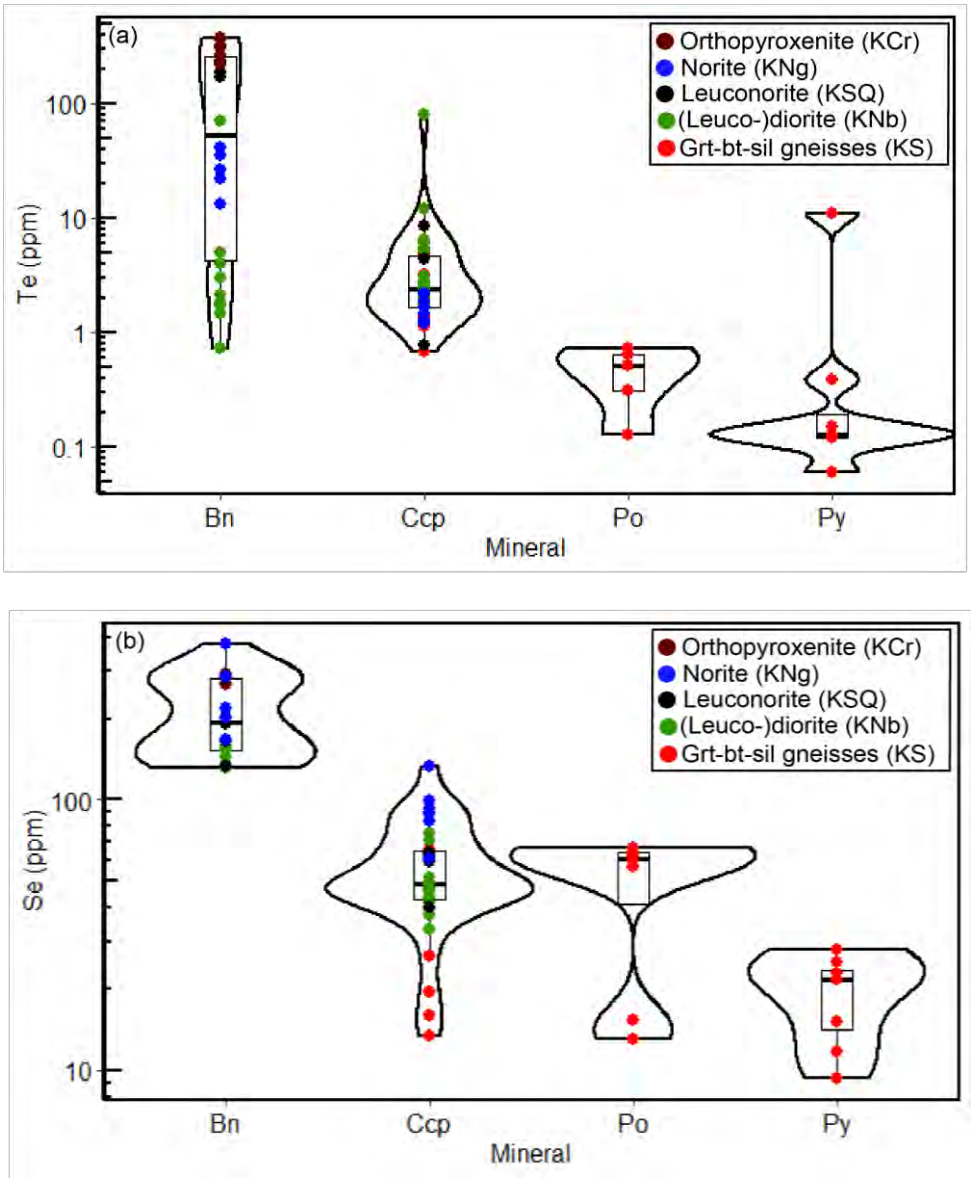

Figure 5. 3 Violin plots for Te and Se concentrations in sulphides in the Koperberg Suite (Nababeep Mine, KNb; Sugarloaf Quarry, KSQ; Nigramoep Mine, KNg; Carolusberg Mine; KCr) and the Khurisberg Subgroup (KS).

Ag and Bi

Bornite shows higher concentrations of Ag and Bi (up to ~190 ppm and ~2100 ppm, respectively; Table 5.6; Fig. 5.4a, b) compared to chalcopyrite (up to ~40 ppm and ~14 ppm, respectively; Table 5.6; Fig. 5.4a, b). Both Ag and Bi show significant variability (over two orders of magnitude). Similar to Se, there is minor overlap in the Bi content of bornite and chalcopyrite (Fig. 5.4a, b). Bornite in the Carolusberg Mine sample (KCr) records the lowest Bi among the Koperberg Suite samples (Fig. 5.4a, b). The Nababeep Mine samples (KNb) show the highest Ag content in chalcopyrite (up to ~3 ppm; Table 5.6; Fig. 5.4a), and Bi content in bornite and chalcopyrite (up to ~2.5 ppm in chalcopyrite, up to ~2100 ppm in bornite; Table 5.6; Fig. 5.4b). The Ag contents of pyrrhotite and pyrite from the Khurisberg Subgroup (KS) are <1 ppm or below detection limit (Table 5.6; Fig. 5.4a). Pyrrhotite and pyrite are also

characterised by low Bi content (mostly <0.7 ppm), overlapping with Bi contents in the chalcopyrite from the Koperberg Suite, but not with the much higher Bi contents in bornite (Table 5.6; Fig. 5.4b).

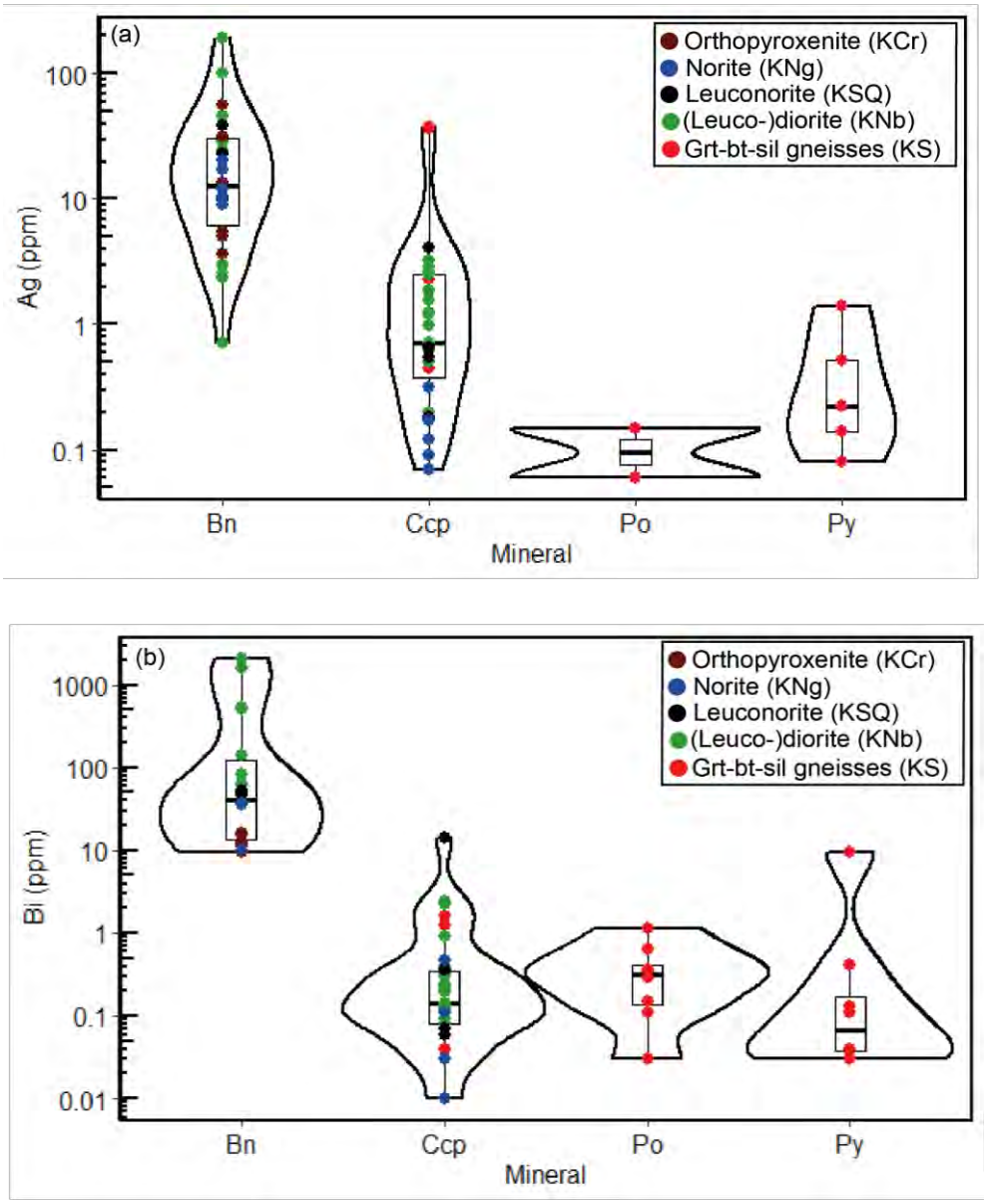

Figure 5. 4 Violin plots for Ag and Bi concentrations in sulphides in the Koperberg Suite (Nababeep Mine, KNb; Sugarloaf Quarry, KSQ; Nigramoep Mine, KNg; Carolusberg Mine; KCr) and the Khurisberg Subgroup (KS).

In and Cd

Cadmium and In contents are low (<10 ppm) in all analysed sulphide phases and samples (Tabel 5.6; Fig. 5.5a). In rocks where bornite and chalcopyrite are present, bornite generally contains higher Cd contents than chalcopyrite (Fig. 5.5a). An exception are samples from Nababeep Mine (KNb), where Cd contents in bornite and chalcopyrite overlap, due to a large spread of Cd contents in bornite. In the Khurisberg Subgroups (KS) the Cd contents in pyrrhotite and pyrite are low (<0.1 ppm; Table 5.6; Fig. 5.5a) or below detection limit. Minor chalcopyrite in Khurisberg Subgroup (KS) shows Cd

contents (~0.2-5 ppm), overlapping with chalcopyrite from Nababeep (KNb) and higher than in chalcopyrite from Nigramoep (KNg) (Table 5.6; Fig. 5.5a).

Indium is mainly hosted in chalcopyrite and bornite (Table 5.6; Fig. 5.5b). Chalcopyrite hosts more In compared to bornite, and the chalcopyrite from Khurisberg Subgroup has the highest content (~10 ppm; Table 5.6; Fig. 5.5b). There is no strong systematic distribution in concentrations based on localities as seen in other trace elements described above. One analysis in pyrite from the Khurisberg Subgroup (KS) shows In concentrations of less than 0.1 ppm (Fig. 5.5b).

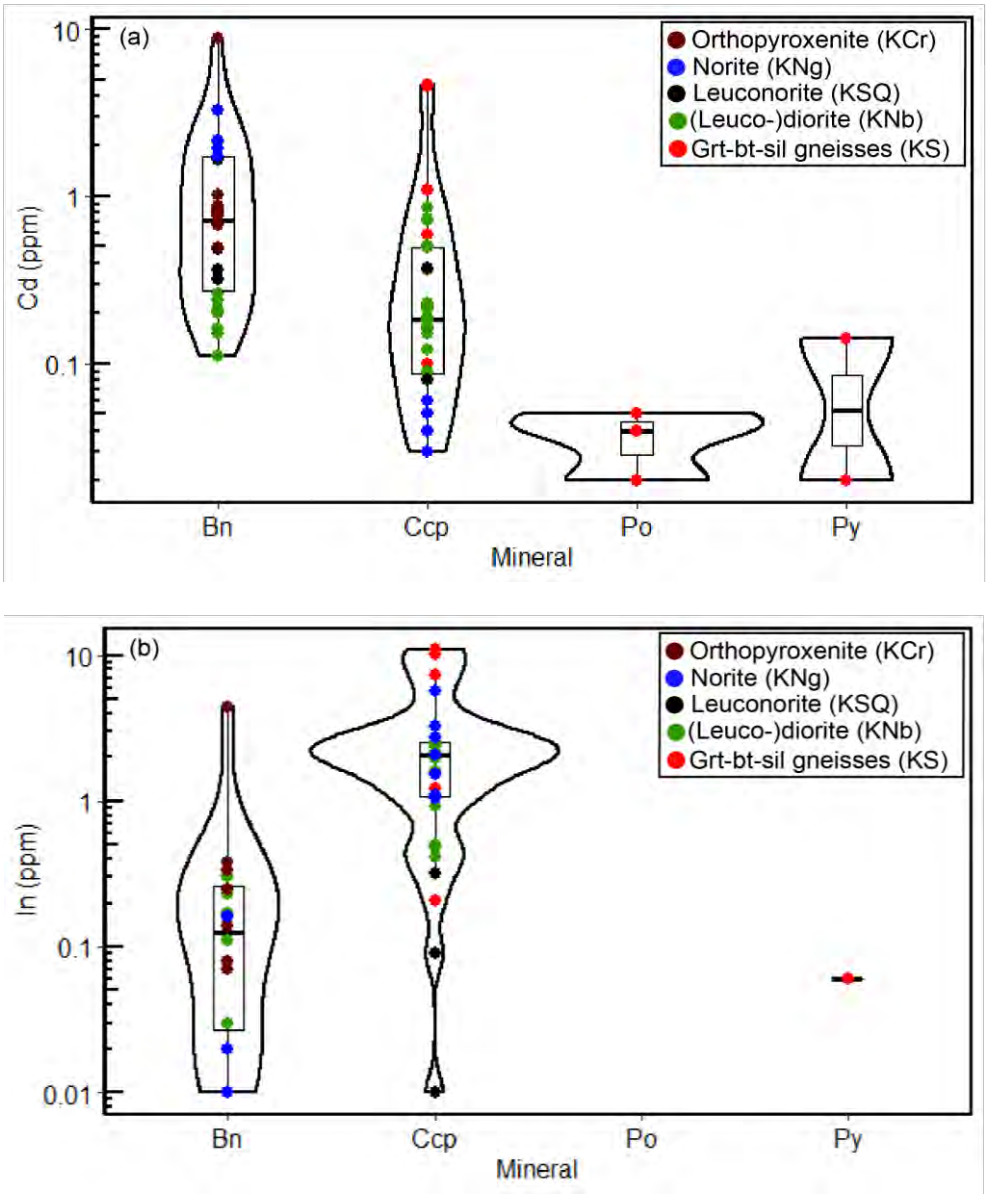

Figure 5. 5 Violin plots for Cd and In concentrations in sulphides in the Koperberg Suite (Nababeep Mine, KNb; Sugarloaf Quarry, KSQ; Nigramoep Mine, KNg; Carolusberg Mine; KCr) and the Khurisberg Subgroup (KS).

Ni and Co

Nickel and Co are principally hosted in pyrrhotite and pyrite of the Khurisberg Subgroup (KS: ~930-5400 ppm Ni and 200-1200 ppm Co; Table 5.6; Figs. 5.6a, b). The minor chalcopyrite in the Khurisberg Subgroup (KS) contains less of these elements (2-180 ppm Ni; <30 ppm Co; Table 5.6; Fig. 5.6a, b).

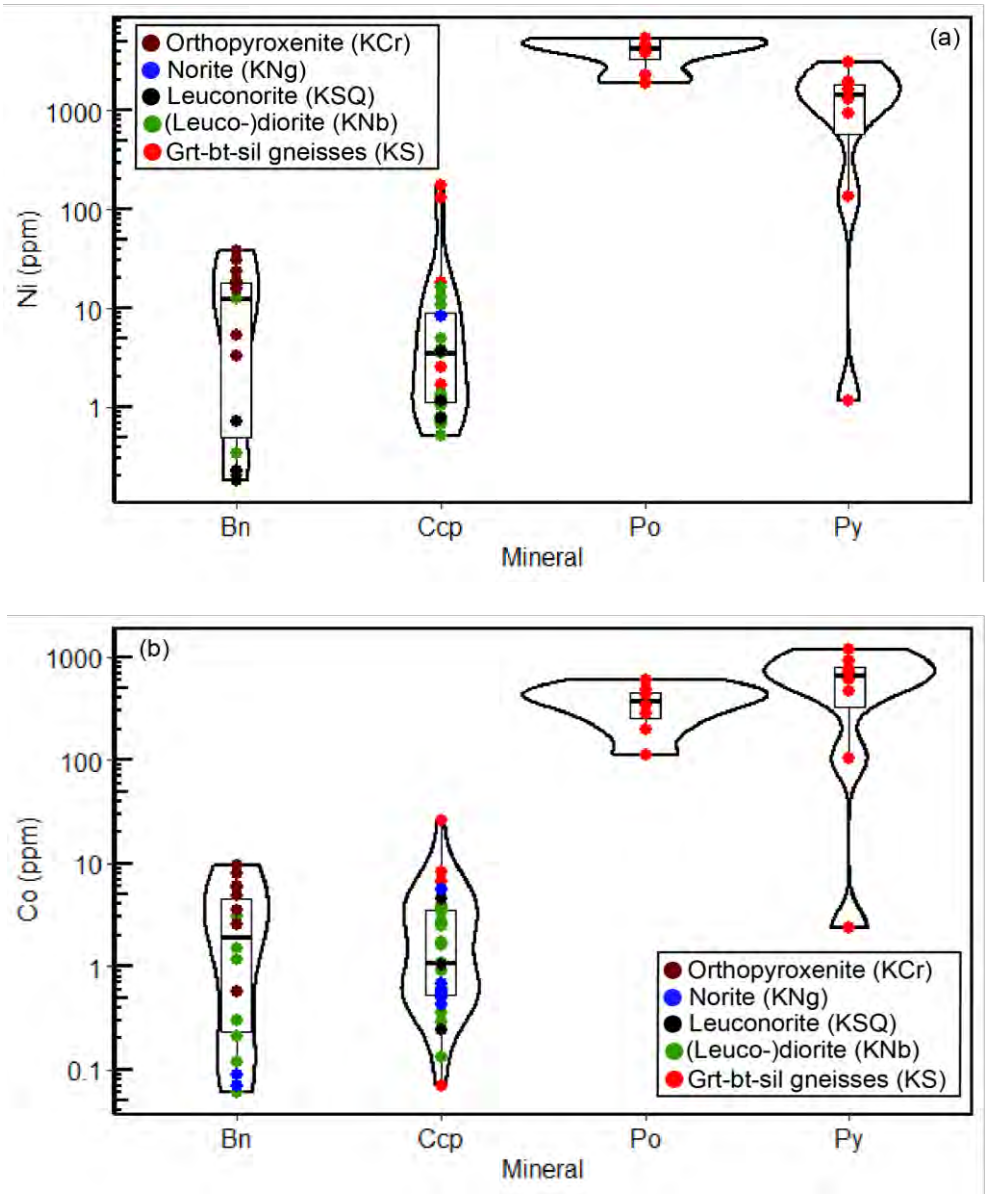

Figure 5. 6 Violin plots for Ni and Co concentrations in sulphides in the Koperberg Suite (Nababeep Mine, KNb; Sugarloaf Quarry, KSQ; Nigramoep Mine, KNg; Carolusberg Mine; KCr) and the Khurisberg Subgroup (KS).

The sulphides of the Koperberg Suite rocks (KCr, KNg, KNb) nowhere exceed ~40 ppm Ni and 10 ppm Co (Table 5.6; Fig. 5.6a, b), and typically show concentrations that are significantly lower than of sulphides hosted in the Wolfram Schist (KS). Amongst the Koperberg rocks, bornite from Carolusberg Mine (KCr) has the highest Ni and Co contents (up to ~40 ppm and up to ~10 ppm, respectively; Table 5.6; Fig. 5.6a, b). Bornite from other mines has low concentrations (0.06-1 ppm) or concentrations

below the detection limit (Table 5.6; Figs. 5.6a, b). The Ni and Co contents of chalcopyrite from the Koperberg Suite and Khurisberg Subgroup are in the same range as for bornite (Figs. 5.6a, b).

Pb and Zn

Lead is mainly hosted in bornite and chalcopyrite, but varies in abundance by two to three orders of magnitude (Table 5.6; Fig. 5.7a). Bornite shows larger variability (~0.1-235 ppm) compared to chalcopyrite (~0.4-20 ppm; Table 5.6; Fig. 5.7a). Bornite from Carolusberg Mine (KCr) and Sugarloaf Quarry (KSQ) has the highest Pb concentration, whereas bornite, and also chalcopyrite, from other localities are show Pb contents of <10 ppm (Table 5.6; Fig. 5.7a). Pyrite and pyrrhotite in the Khurisberg Subgroups (KS) show Pb concentrations of mostly <1 ppm, with a few outliers (up to ~80 ppm) in pyrrhotite (Table 5.6; Fig. 5.7a).

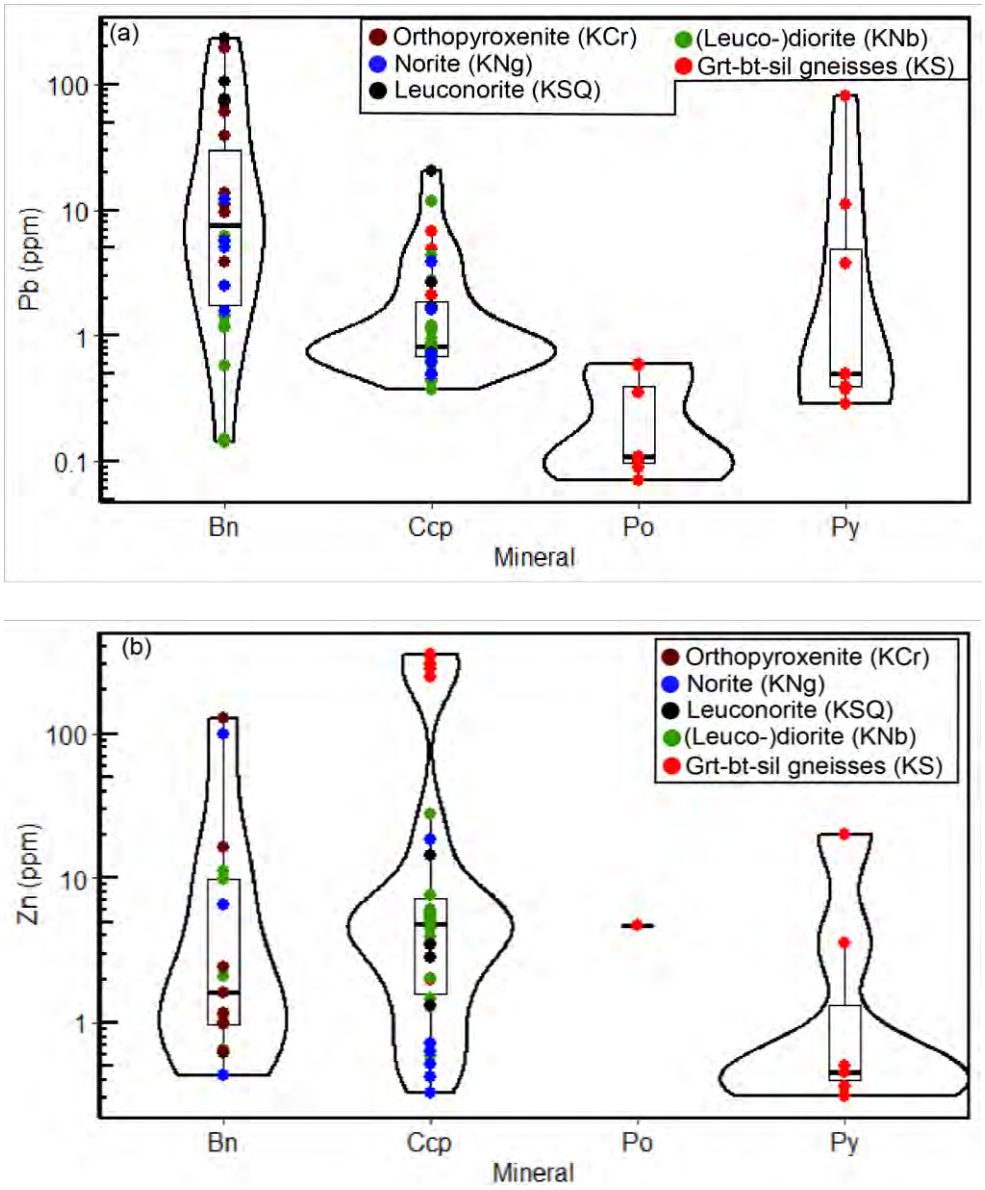

Figure 5. 7 Violin plots for Pb and Zn concentrations in sulphides in the Koperberg Suite (KNb, KSQ, KNg, KCr) and the Khurisberg Subgroup (KS).

Zinc is mainly hosted in chalcopyrite, bornite, and pyrite, and exhibits large variability in concentration (~0.3-350 ppm; Table 5.6; Fig. 5.7b). The chalcopyrite from Khurisberg Subgroup (KS) hosts high concentrations of Zn (240-350 ppm; Table 5.6; Fig. 5.7b) compared to chalcopyrite from the Koperberg Suite (mostly <10 ppm; Table 5.6; Fig 5.7b), but also compared to pyrite from the same Khurisberg Subgroup (KS) samples (mostly <1ppm; Table 5.6; Fig 5.7b). Bornite from Koperberg Suite rocks commonly shows Zn concentrations below the detection limit (Table 5.6b) but may variably range between 0.05 ppm and just over 100 ppm in most samples (Table 5.6; Fig 5.7b). In the Khurisberg Subgroup (KS), Zn content in pyrrhotite is mostly below the detection limit and the Zn concentrations for pyrite are mostly below 1 ppm (Table 5.6; Fig. 5.7b).

Sn and Mo

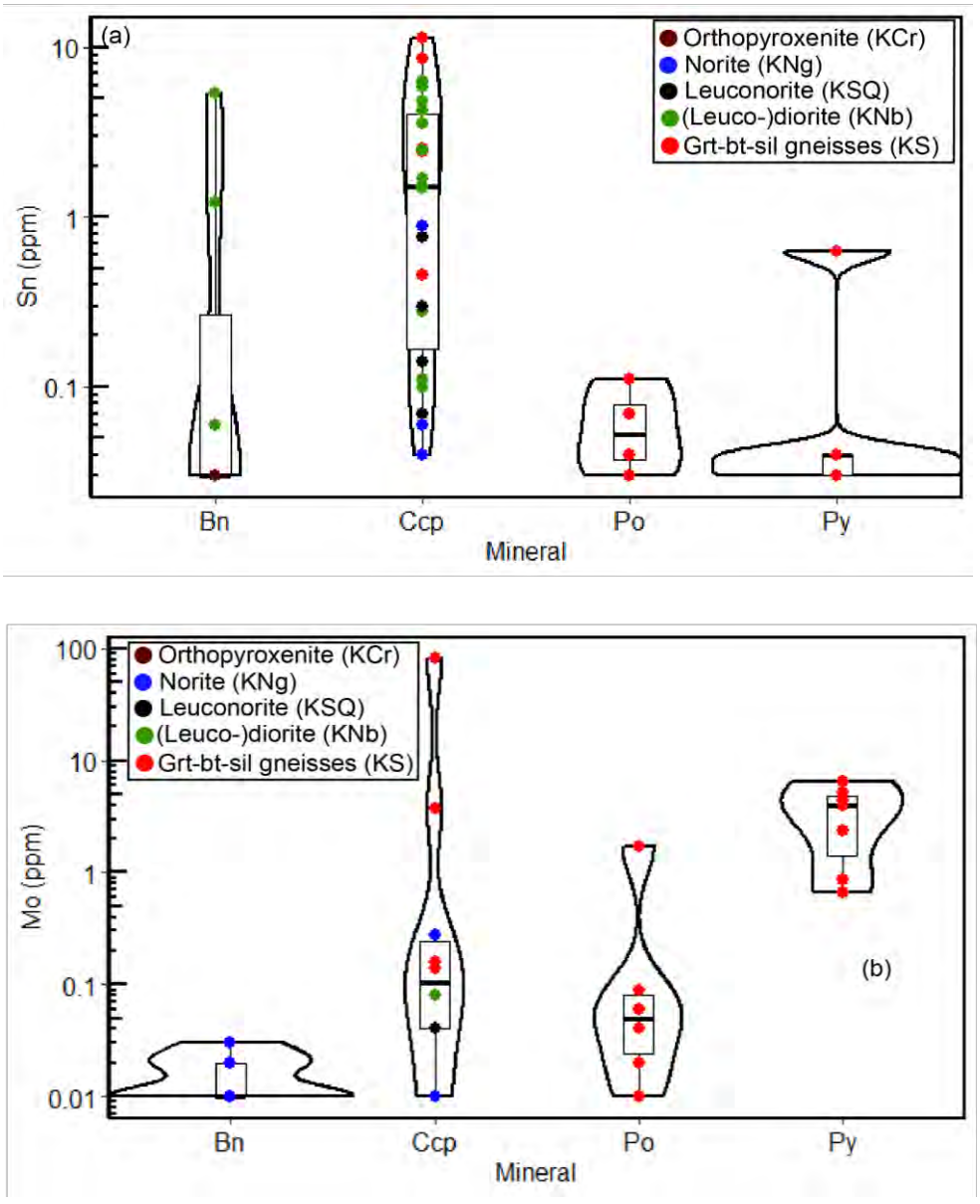

Figure 5. 8 Violin plots for Sn and Mo concentrations in sulphides in the Koperberg Suite (KNb, KSQ, KNg, KCr) and the Khurisberg Subgroup (KS).

Tin is mainly hosted in chalcopyrite where the concentration varies from ~0.06 to 11 ppm (Table 5.6; Fig. 5.8a). The Sn concentrations in the other sulphide phases are mostly <0.1 ppm or below the detection limit, with some exceptions in bornite from the Nababeep Mine (KNb; Fig. 5.8a). Also, pyrrhotite and pyrite in the Khurisberg Subgroups (KS) contain typically <0.1 ppm Sn.

Molybdenum is quantifiable in all sulphide phases but most abundant in pyrite (KS: ~1-10 ppm; Table 5.6; Fig. 5.8b). Also, some analyses of pyrrhotite and chalcopyrite from the Khurisberg Subgroup (KS) contain significant Mo. The Mo concentration in chalcopyrite and bornite from the Koperberg Suite are <0.3 ppm or below the detection limit (Table 5.6; Fig. 5.8b).

As, Sb and Au

The As, Sb, and Au concentrations for sulphides from all localities are mostly below the detection limit (Table 5.6).

Table 5. 6 Trace element concentrations of bornite, chalcopyrite, pyrrhotite and pyrite (in ppm).

Sample	Lith. Unit	Mineral	Te	Ag	Au	Se	Ni	Bi	Cd	Pb	Co	Sn	In	As	Sb	Mo	Zn
LOD	**-**	**-**	**0.05**	**0.05**	**0.05**	**0.62**	**0.23**	**0.01**	**0.02**	**0.01**	**0.04**	**0.03**	**0.006**	**0.11**	**0.040**	**0.006**	**0.29**
1A3	KS	Ccp	1.12	0.45	-	26.3	13.0	0.32	0.59	2.07	8.26	2.42	7.33	-	-	0.14	245
1A3	KS	Ccp	6.34	3.26	-	19.6	178	1.61	1.10	4.88	25.6	2.53	0.21	-	-	82.7	341
1A3	KS	Ccp	3.21	37.9	-	13.4	2.50	0.14	4.59	0.71	2.56	8.56	10.2	-	-	3.74	302
1A3	KS	Ccp	4.91	36.0	-	16.0	1.69	0.13	4.56	0.74	3.46	11.4	10.1	-	-	0.16	355
1A3	KS	Ccp	0.69	2.30	0.10	66.0	130	1.26	0.21	6.72	6.75	0.46	11.1	-	-	-	278
3A	KNb	Ccp	1.38	-	-	48.6	18.1	0.04	0.10	0.45	0.07	-	1.23	-	-	-	1.99
3A	KNb	Ccp	79.5	0.72	0.06	71.3	16.1	0.19	0.73	4.34	0.29	-	0.48	-	-	0.08	4.42
3A	KNb	Ccp	2.16	-	0.05	49.9	8.34	0.32	0.05	1.09	0.36	-	0.41	-	-	0.04	1.29
3A	KNb	Ccp	1.95	0.55	-	41.8	12.9	2.43	0.21	11.8	5.50	0.28	0.92	-	-	-	28.1
3A	KNb	Ccp	12.1	0.98	-	39.4	10.7	2.18	0.12	0.80	0.13	-	0.50	-	-	-	1.46
3C	KNb	Ccp	2.01	-	-	74.9	3.66	0.12	0.09	0.43	0.53	-	3.24	-	-	-	0.58
4A	KNb	Ccp	5.57	3.29	-	49.3	1.21	0.22	0.17	0.78	1.60	3.56	2.33	-	-	-	4.91
4A	KNb	Ccp	6.38	2.66	-	47.0	1.33	0.08	0.49	1.21	2.71	5.85	2.45	-	-	-	5.64
4A	KNb	Ccp	1.64	0.50	-	44.1	1.31	0.14	0.22	0.81	3.62	2.49	2.53	-	-	-	5.08
4A	KNb	Ccp	6.01	2.47	-	47.1	3.66	0.24	0.71	0.79	3.91	6.37	2.43	-	-	-	6.12
4A	KNb	Ccp	1.77	0.62	-	45.8	3.52	0.92	0.15	2.69	2.42	1.70	2.46	-	-	0.01	5.51
4A	KNb	Ccp	2.80	1.58	-	47.3	3.85	0.20	0.50	0.64	2.65	4.82	2.47	-	-	-	5.88
4B	KNb	Ccp	3.15	1.87	-	48.9	0.71	0.11	0.18	0.82	1.74	1.48	1.62	-	-	-	3.91
4B	KNb	Ccp	2.43	0.55	-	47.2	0.76	0.39	0.09	1.09	1.07	0.11	1.56	-	-	-	2.05
4B	KNb	Ccp	4.39	2.90	-	52.0	0.67	0.09	0.36	0.88	3.36	4.20	2.01	-	-	-	5.17
4B	KNb	Ccp	2.55	1.25	-	49.7	0.79	0.30	0.23	0.96	0.90	0.11	1.98	-	-	-	3.52
4B	KNb	Ccp	5.23	2.50	-	43.6	1.05	0.08	0.86	1.18	5.59	6.22	2.18	-	-	-	7.67
4B	KNb	Ccp	2.52	0.20	1.84	37.5	0.52	0.13	0.16	0.37	1.06	0.10	2.04	-	-	-	4.88
4B	KNb	Ccp	2.63	1.22	-	33.4	5.02	0.08	0.19	0.59	0.61	1.52	2.16	-	-	-	4.88
3B2	KSQ	Ccp	4.44	0.18	-	63.6	-	0.36	-	1.70	0.24	0.77	-	-	-	-	1.32
3D1	KSQ	Ccp	1.29	0.55	0.06	62.6	0.76	0.06	0.03	0.74	0.50	0.14	0.01	-	-	-	2.80
3D1	KSQ	Ccp	0.78	0.65	-	59.3	1.15	0.07	0.08	2.65	1.04	0.07	0.09	-	-	-	3.43
3D1	KSQ	Ccp	8.47	4.13	-	40.2	3.66	13.9	0.37	20.7	4.50	0.30	0.32	-	-	0.04	14.5

Table 5.6 *(continued)*

Sample	Lith. Unit	Mineral	Te	Ag	Au	Se	Ni	Bi	Cd	Pb	Co	Sn	In	As	Sb	Mo	Zn
KNU	KNg	Ccp	1.67	0.32	-	132	8.41	0.47	0.04	3.90	5.68	0.88	2.71	-	-	-	18.6
KNU	KNg	Ccp	1.19	0.17	-	87.6	-	0.11	-	1.63	0.53	-	1.06	-	-	-	-
KNU	KNg	Ccp	2.18	0.17	-	92.7	-	0.03	0.06	0.70	0.68	0.04	1.09	-	-	-	0.63
KNU	KNg	Ccp	1.48	0.07	-	83.9	-	0.03	-	0.61	0.43	-	2.05	-	-	-	0.51
KNU	KNg	Ccp	1.89	0.09	0.07	89.1	-	0.01	0.05	0.50	0.60	0.06	5.76	-	-	0.28	0.42
KNU	KNg	Ccp	1.64	-	-	60.6	-	0.01	0.03	0.48	0.51	-	3.24	1.63	-	-	0.33
1A3	KS	Py	0.12	0.08	-	21.7	1630	0.11	-	0.50	718	0.03	-	-	-	3.98	0.50
1A3	KS	Py	0.39	0.52	-	23.0	3040	0.41	0.02	3.72	1196	0.03	-	-	-	4.44	3.52
1A3	KS	Py	0.15	0.22	-	25.3	1804	0.03	-	0.49	782	-	-	-	-	0.67	-
1A3	KS	Py	0.13	0.14	-	28.1	1324	0.13	-	0.37	600	-	-	-	-	0.85	0.36
1A3	KS	Py	0.12	-	-	21.7	1979	0.04	-	0.29	908	0.04	-	-	-	6.40	0.45
1A3	KS	Py	0.06	-	-	9.33	937	0.04	-	0.40	471	-	-	-	-	5.20	0.31
1A3	KS	Py	0.13	-	-	11.8	1.18	0.03	-	11.1	2.36	0.04	-	-	0.07		0.46
1A3	KS	Py	11.2	1.39	0.08	15.1	136	9.60	0.14	82.0	105	0.63	0.06	2.92	0.14	2.34	20.2
1A3	KS	Po	0.65	0.15	-	13.0	1873	0.11	-	0.35	603	0.04	-	-	-	0.04	-
1A3	KS	Po	0.73	0.06	-	15.3	2297	0.03	-	0.11	432	0.03	-	-	-	1.73	-
1B3	KS	Po	0.13	-	-	64.1	5381	0.29	0.04	0.09	486	-	-	-	-	0.06	-
1B3	KS	Po	0.31	-	-	64.3	5418	0.15	-	0.07	440	0.11	-	-	-	-	-
1B3	KS	Po	-	-	-	62.2	3781	0.35	-	0.10	198	-	-	-	-	0.02	-
1B3	KS	Po	-	-	-	59.4	4689	1.14	0.05	0.60	112	0.07	-	-	-	0.09	4.65
1B3	KS	Po	0.51	-	-	56.9	5365	0.36	-	0.11	341	-	-	-	-	-	-
1B3	KS	Po	-	-	-	66.3	3968	0.64	0.02	0.58	284	-	-	-	-	0.01	-
3A	KNb	Bn	1.8	28.6	-	158	0.20	142	0.15	0.15	0.06	-	-	-	-	0.02	-
3A	KNb	Bn	69.6	46.4	-	130	12.7	82.3	0.26	0.14	0.12	-	0.01	-	-	-	-
3C	KNb	Bn	0.73	24.5	-	153	-	64.6	0.32	11.2	-	-	-	-	-	0.01	-
4A	KNb	Bn	1.46	0.72	-	133	12.3	1566	0.16	0.57	3.02	-	0.03	-	-	-	11.2
4A	KNb	Bn	4.03	2.33	-	158	-	2114	0.20	1.44	2.55	-	0.03	-	-	-	9.87
4A	KNb	Bn	2.13	2.97	-	143	0.34	1581	0.11	1.19	1.48	0.06	0.17	-	-	0.01	0.65

Table 5.6 *(continued)*

Sample	Lith. Unit	Mineral	Te	Ag	Au	Se	Ni	Bi	Cd	Pb	Co	Sn	In	As	Sb	Mo	Zn
4B	KNb	Bn	5.03	193	-	135	-	503	0.21	6.11	0.30	1.21	0.23	-	-	0.01	2.10
4B	KNb	Bn	3.03	101	-	151	-	518	2.11	11.0	0.21	5.32	0.30	-	-	-	1.14
3B2	KSQ	Bn	173	10.3	-	193	0.18	50.7	1.67	77.2	-	-	-	-	-	0.02	-
3D1	KSQ	Bn	324	31.7	0.08	192	0.72	53.8	0.48	234	-	0.03	-	--	-	0.01	0.62
3D1	KSQ	Bn	233	22.8	-	165	-	50.0	0.36	72.8	-	-	-	-	-	0.02	-
3D1	KSQ	Bn	189	38.8	-	133	0.23	46.7	0.32	105	-	-	-	-	-	-	-
KNU	KNg	Bn	26.6	20.3	-	286	-	36.5	1.93	4.99	-	-	0.01	-	-	0.03	-
KNU	KNg	Bn	13.3	12.1	0.06	379	-	36.7	1.91	2.48	-	-	0.01	-	0.08	0.01	98.2
KNU	KNg	Bn	22.3	17.0	-	201	-	9.97	2.16	5.63	-	-	0.16	0.49	-	0.01	-
KNU	KNg	Bn	41.8	8.87	-	217	-	36.9	3.24	12.1	0.09	-	0.02	-	0.13	-	0.43
KNU	KNg	Bn	35.8	10.1	-	167	-	36.7	1.73	1.56	0.07	-	0.02	-	-	0.02	6.60
CD	KCr	Bn	219	4.97	-	294	3.24	13.2	0.67	11.2	0.57	-	0.34	-	-	-	16.5
CD	KCr	Bn	370	9.93	-	267	31.0	9.56	8.83	5.60	5.87	0.03	4.45	-	-	0.03	128
CD	KCr	Bn	380	13.4	-	292	17.3	9.51	0.49	3.85	2.59	0.03	0.08	-	-	-	2.42
CD	KCr	Bn	309	5.51	0.06	293	15.7	12.3	0.84	13.5	3.58	-	0.14	-	-	-	1.16
CD	KCr	Bn	369	31.6	0.16	282	38.7	16.1	0.80	60.8	9.55	-	0.25	-	0.04	-	0.98
CD	KCr	Bn	217	55.6	0.06	270	5.27	12.4	0.76	192	4.84	-	0.38	-	-	0.01	1.63
CD	KCr	Bn	263	10.1	-	290	18.8	15.5	1.01	38.6	6.01	0.03	0.38	-	-	-	0.99
CD	KCr	Bn	312	3.69	-	283	23.4	11.4	0.88	9.64	8.13	-	0.07	-	-	-	0.63

KS: Khurisberg Subgroup, KNb: Koperberg Suite from Nababeep Mine, KNg: Koperberg Suite from Nigramoep Mine, KCr: Koperberg Suite from Carolusberg Mine, KSQ: Koperberg Suite from Sugarloaf Quarry. "–": below detection limit.

5.3 Sulphur Isotopes

5.3.1 Sulphur isotope results

This section presents isotope results from *in-situ* SIMS and bulk S analysis. The results are listed in Table 5.7 and graphically shown in Figure 5.9. Figure 5.10 shows textural relationships of some of the sulphides analysed with SIMS. For samples from the Carolusberg Mine (KCr), Sugarloaf Quarry (KSQ), and one of the Khurisberg Subgroup samples (1B3) only bulk S isotope analyses could be obtained. For other samples, complementary bulk and in-situ data are available, allowing the comparison of results obtained from different methods. This study is based on the assumption that the Khurisberg Subgroup is a contaminant and the Koperberg Suite stratigraphically below the Khurisberg Subgroup (Koperberg Suite at Sugarloaf Quarry) represents the uncontaminated Koperberg Suite.

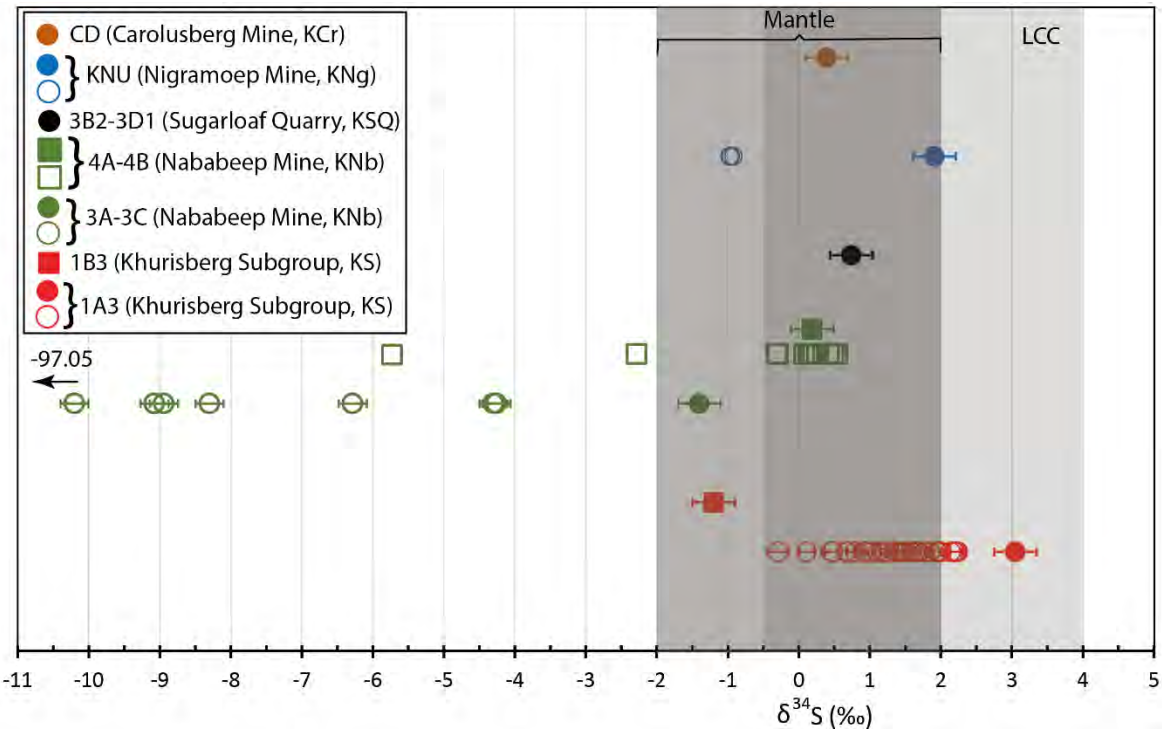

Figure 5. 9 Bulk and in-situ S isotope values of sulphides in the Khurisberg Subgroup and Koperberg Suite. Bulk analysis values are denoted by filled symbols, in-situ analysis values are denoted by open symbols. The error bars show the 1σ uncertainties. The range of $\delta^{34}S$ values for the mantle in grey and range of $\delta^{34}S$ values for lower continental crust in light grey. Mantle $\delta^{34}S$ values (Sakai et al., 1984; Peters et al., 2010); lower continental crust (LCC) $\delta^{34}S$ values (Hoefs et al., 1982; Iyer et al., 1992; Hammerli et al., 2017).

The samples from the Khurisberg Subgroup (1A3 and 1B3) register bulk $\delta^{34}S$ values of -1.2 and +3.05 (Table 5.7; Fig. 5.9). *In-situ* $\delta^{34}S$ values for pyrite hosted in sample 1A3 range from -0.29 to +2.24 (average: +1.36 ± 0.13‰ (1σ); Table 5.7). No chalcopyrite from the Khurisberg Subgroup could be analysed with SIMS, because of SIMS beam sizes exceeded the chalcopyrite grain sizes.

Table 5. 7 Bulk and in-situ S isotope, and bulk S (in wt%) compositions of rocks from the Khurisberg Subgroup and the Koperberg Suite.

Sample(s)	Lithological unit	Analysis type	(Bulk S content, wt%)/Mineral	$\delta^{34}S$ (‰)	1σ (‰)
1A3	Khurisberg Subgroup	Bulk	(1.48)	+3.05	0.3
1B3	Khurisberg Subgroup	Bulk	(0.07)	-1.2	0.3
3A-3C	Koperberg Suite	Bulk	(0.12)	-1.4	0.3
4A-4B	Koperberg Suite	Bulk	(1.18)	+0.19	0.3
3B2-3D1	Koperberg Suite	Bulk	(0.02)	+0.74	0.3
KNU	Koperberg Suite	Bulk	(1.44)	+1.91	0.3
CD	Koperberg Suite	Bulk	(2.83)	+0.39	0.3
1A3-1B3	Khurisberg Subgroup	*In-situ*	Py	-0.29	0.15
1A3-1B3	Khurisberg Subgroup	*In-situ*	Py	+0.11	0.11
1A3-1B3	Khurisberg Subgroup	*In-situ*	Py	+0.46	0.15
1A3-1B3	Khurisberg Subgroup	*In-situ*	Py	+0.48	0.11
1A3-1B3	Khurisberg Subgroup	*In-situ*	Py	+0.67	0.11
1A3-1B3	Khurisberg Subgroup	*In-situ*	Py	+0.69	0.11
1A3-1B3	Khurisberg Subgroup	*In-situ*	Py	+0.79	0.11
1A3-1B3	Khurisberg Subgroup	*In-situ*	Py	+0.93	0.15
1A3-1B3	Khurisberg Subgroup	*In-situ*	Py	+0.96	0.11
1A3-1B3	Khurisberg Subgroup	*In-situ*	Py	+1.02	0.15
1A3-1B3	Khurisberg Subgroup	*In-situ*	Py	+1.03	0.11
1A3-1B3	Khurisberg Subgroup	*In-situ*	Py	+1.11	0.15
1A3-1B3	Khurisberg Subgroup	*In-situ*	Py	+1.18	0.15
1A3-1B3	Khurisberg Subgroup	*In-situ*	Py	+1.22	0.15
1A3-1B3	Khurisberg Subgroup	*In-situ*	Py	+1.35	0.11
1A3-1B3	Khurisberg Subgroup	*In-situ*	Py	+1.35	0.15
1A3-1B3	Khurisberg Subgroup	*In-situ*	Py	+1.39	0.11
1A3-1B3	Khurisberg Subgroup	*In-situ*	Py	+1.44	0.15
1A3-1B3	Khurisberg Subgroup	*In-situ*	Py	+1.46	0.11
1A3-1B3	Khurisberg Subgroup	*In-situ*	Py	+1.46	0.15
1A3-1B3	Khurisberg Subgroup	*In-situ*	Py	+1.48	0.15
1A3-1B3	Khurisberg Subgroup	*In-situ*	Py	+1.51	0.11
1A3-1B3	Khurisberg Subgroup	*In-situ*	Py	+1.58	0.11
1A3-1B3	Khurisberg Subgroup	*In-situ*	Py	+1.63	0.15
1A3-1B3	Khurisberg Subgroup	*In-situ*	Py	+1.67	0.15
1A3-1B3	Khurisberg Subgroup	*In-situ*	Py	+1.68	0.11
1A3-1B3	Khurisberg Subgroup	*In-situ*	Py	+1.69	0.15
1A3-1B3	Khurisberg Subgroup	*In-situ*	Py	+1.77	0.11
1A3-1B3	Khurisberg Subgroup	*In-situ*	Py	+1.85	0.15
1A3-1B3	Khurisberg Subgroup	*In-situ*	Py	+1.94	0.15
1A3-1B3	Khurisberg Subgroup	*In-situ*	Py	+1.95	0.15
1A3-1B3	Khurisberg Subgroup	*In-situ*	Py	+1.98	0.11

Table 5.7 *(continued)*

Sample(s)	Lithological unit	Analysis type	Mineral	$\delta^{34}S$ (‰)	1σ (‰)
1A3-1B3	Khurisberg Subgroup	*In-situ*	Py	+2.01	0.11
1A3-1B3	Khurisberg Subgroup	*In-situ*	Py	+2.14	0.15
1A3-1B3	Khurisberg Subgroup	*In-situ*	Py	+2.19	0.15
1A3-1B3	Khurisberg Subgroup	*In-situ*	Py	+2.21	0.15
1A3-1B3	Khurisberg Subgroup	*In-situ*	Py	+2.24	0.11
3A-3C	Koperberg Suite	*In-situ*	Ccp	-97.05	0.20
3A-3C	Koperberg Suite	*In-situ*	Ccp	-10.20	0.20
3A-3C	Koperberg Suite	*In-situ*	Ccp	-9.08	0.20
3A-3C	Koperberg Suite	*In-situ*	Ccp	-8.94	0.20
3A-3C	Koperberg Suite	*In-situ*	Ccp	-8.30	0.20
3A-3C	Koperberg Suite	*In-situ*	Ccp	-6.28	0.20
3A-3C	Koperberg Suite	*In-situ*	Ccp	-4.30	0.20
3A-3C	Koperberg Suite	*In-situ*	Ccp	-4.26	0.20
4A-4B	Koperberg Suite	*In-situ*	Ccp	-5.80	0.05
4A-4B	Koperberg Suite	*In-situ*	Ccp	-2.28	0.15
4A-4B	Koperberg Suite	*In-situ*	Ccp	-0.31	0.05
4A-4B	Koperberg Suite	*In-situ*	Ccp	-0.29	0.05
4A-4B	Koperberg Suite	*In-situ*	Ccp	+0.08	0.05
4A-4B	Koperberg Suite	*In-situ*	Ccp	+0.14	0.05
4A-4B	Koperberg Suite	*In-situ*	Ccp	+0.16	0.05
4A-4B	Koperberg Suite	*In-situ*	Ccp	+0.17	0.05
4A-4B	Koperberg Suite	*In-situ*	Ccp	+0.19	0.05
4A-4B	Koperberg Suite	*In-situ*	Ccp	+0.20	0.05
4A-4B	Koperberg Suite	*In-situ*	Ccp	+0.20	0.05
4A-4B	Koperberg Suite	*In-situ*	Ccp	+0.26	0.05
4A-4B	Koperberg Suite	*In-situ*	Ccp	+0.43	0.05
4A-4B	Koperberg Suite	*In-situ*	Ccp	+0.49	0.05
4A-4B	Koperberg Suite	*In-situ*	Ccp	+0.55	0.05
KNU-CD	Koperberg Suite	*In-situ*	Ccp	-0.97	0.06
KNU-CD	Koperberg Suite	*In-situ*	Ccp	-0.96	0.06
KNU-CD	Koperberg Suite	*In-situ*	Ccp	-0.92	0.06

The Koperberg Suite sample from Nigramoep Mine (KNU) registers bulk $\delta^{34}S$ value of +0.74‰ (Table 5.7; Fig. 5.9). The chalcopyrite gives $\delta^{34}S$ values of -0.92 to -0.97‰ (Table 5.7; Fig. 5.9), with an average of -0.95 ± 0.06‰ (1σ). Since bornite is the only other major S carrier in this sample, the discrepancy in the $\delta^{34}S$ values between the *in-situ* data of chalcopyrite and the bulk signature is likely due to the contribution of isotopically heavy bornite.

The samples from Carolusberg Mine (CD) and Sugarloaf Quarry (3B2-3D1) yield bulk $\delta^{34}S$ values of +0.39‰ and +0.74‰, respectively (Table 5.7; Fig. 5.9).

One of the Koperberg Suite samples from Nababeep mine (4A-4B) has a bulk $\delta^{34}S$ value of +0.19‰ (Table 5.7; Fig. 5.9). The sample shows relatively limited variation in *in-situ* $\delta^{34}S$ values (-5.80 to +0.55‰; Table 5.7; Fig. 5.9) with an average of 0 ± 0.06‰ (1σ), a value similar to the result of the bulk analysis.

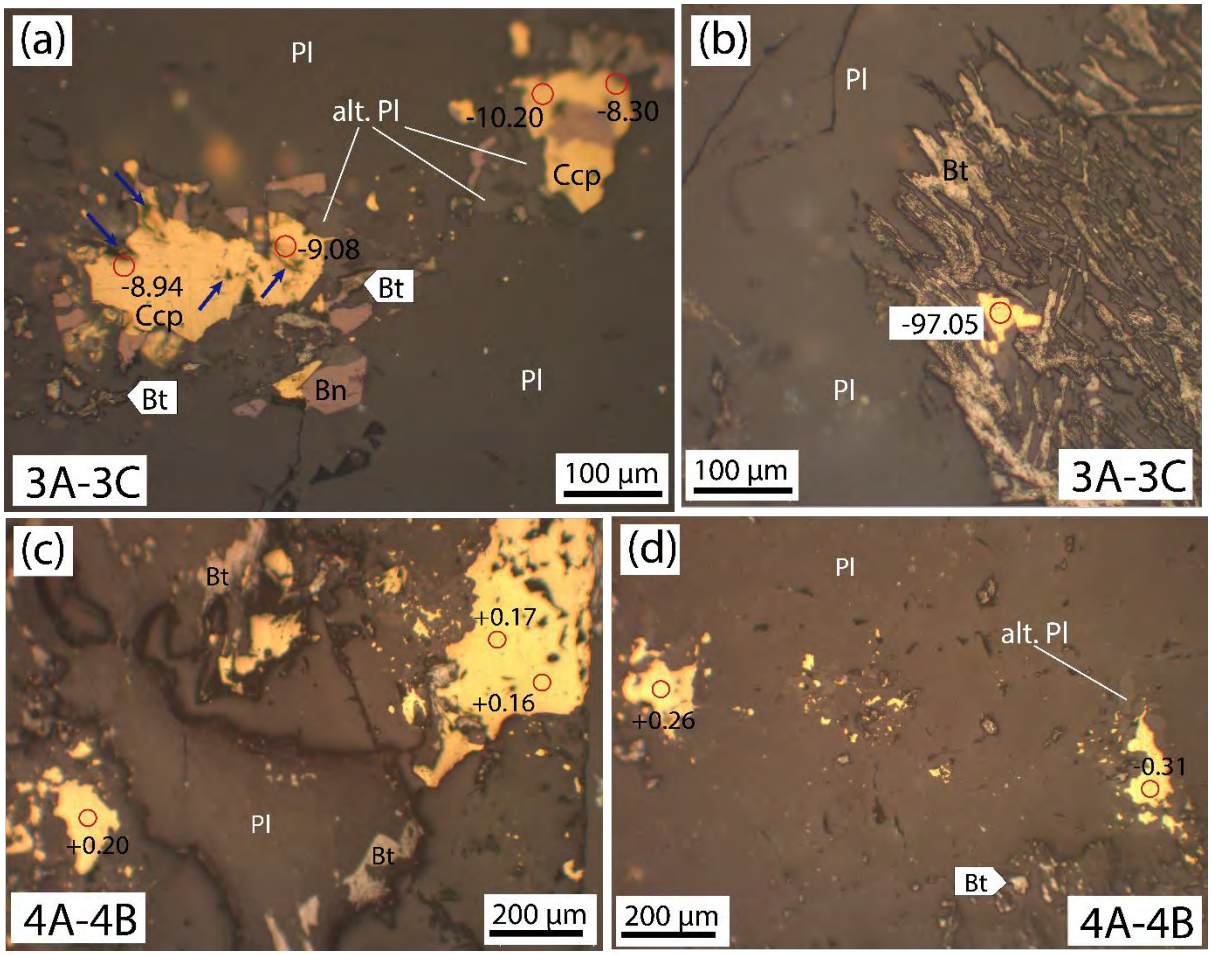

Figure 5. 10 Analysis locations (red circles) and the respective $\delta^{34}S$ values for chalcopyrite in sample 3A-3C (a, b) and 4A-4B (c, d). (a) Analysis points lie near the boundaries of chalcopyrite grains and on uneven *sulphide surfaces (blue arrows). (b) Analysis point lies in a small (~50 µm) chalcopyrite grain. (c, d) Analysis points lie in the central parts of the chalcopyrite grain and on relatively smooth sulphide surfaces.*

The other Koperberg Suite sample from Nababeep Mine (3A-3C) shows relatively large variability in *in-situ* $\delta^{34}S$ values ranging from -4.26‰ to anomalously low values of -97.05 (Table 5.7; Fig. 5.9). Most of the analysed points in this sample lie near the boundaries of chalcopyrite grains (Fig. 5.10a), on relatively small chalcopyrite grains (~50 µm) within altered biotite (Fig. 5.10b) or uneven sulphide surfaces (blue arrows in Fig. 5.10a). The chalcopyrite grains also show high $\delta^{34}S$ intragrain variability (up to ~2‰; Fig. 5.10a). Conversely, analysis spots for other samples (e.g., sample 4A-4B; Fig. 5.10c, d) are located further from alterations, on relatively larger chalcopyrite grains, and on flat and smooth

chalcopyrite surfaces. The location of analysis spots in sample 3A-3C potentially affected the $\delta^{34}S$ values of the chalcopyrite. The *in-situ* $\delta^{34}S$ signatures are therefore excluded in the $\delta^{34}S$ signature interpretations in the coming sections. The bulk S isotope result of -1.4‰ for sample 3A-3C will be included in the data set to be interpreted since the aforementioned factors do not affect bulk analysis.

5.3.2 Synthesis

Considering the average *in-situ* $\delta^{34}S$ value for sample 4A-4B (0 ± 0.06‰) and the bulk $\delta^{34}S$ values for other Koperberg Suites samples, the $\delta^{34}S$ values registered by the Koperberg Suite samples (-1.4 to +1.91‰) lie in the range of mantle-derived rocks 0 ± 2 ‰ (Fig. 5.9; Ohmoto and Rye, 1979; Sakai et al., 1984; Peters et al., 2010). The Khurisberg Subgroup samples register an isotopic signature consistent with the average S isotopic signature of Proterozoic sedimentary rocks of +5 ± 10 ‰ (Canfield and Farquhar, 2009). These $\delta^{34}S$ values overlap with the $\delta^{34}S$ values of the Koperberg Suite and also lie in the range of $\delta^{34}S$ values for the mantle (0 ± 2 ‰; Ohmoto and Rye, 1979; Sakai et al., 1984; Peters et al., 2010).

6 Discussion

This chapter presents the interpretations of trace element and S isotope data presented in Chapter 5. The chapter commences with the presentation of the unusual occurrence of bornite in magmatic sulphide deposits ("the bornite problem") and proposed mechanisms for the formation of bornite in literature. The following subchapter (Chapter 6.2) focusses on the interpretation of trace elements concentrations and S/Se ratios of sulphides hosted in the Koperberg Suite, and the implications of the trace element patterns and the proposed mechanisms for bornite formation on proposed petrogenetic models for the Koperberg Suite. Chapter 6.3 presents interpretation of S isotope results based on the two main sources of the Koperberg Suite magmas (the mantle and the lower crust). At the end, a synopsis of the S isotope and trace element interpretations is given.

6.1 The bornite problem

Pyrrhotite, pentlandite and minor chalcopyrite are the dominant sulphide species in magmatic sulphide deposits (Naldrett, 2004). The bulk Cu/Fe of these sulphides is near unity in accordance with the composition of one of the last sulphide phase to crystallise, *iss* (Yund and Kullerud, 1966). Hence, the occurrence of Cu-rich sulphides with Cu/Fe ratio ≥ 1 (e.g., bornite, Cu_5FeS_4) is atypical of magmatic sulphide deposits (e.g., Le Bras et al., 2021). The enigma of the bornite occurrence in magmatic sulphide deposits is compounded by the lack of studies where Cu-rich sulphides have been synthesised using basaltic magma compositions (Andersen, 2006). Copper-rich sulphides mostly occur in highly fractionated upper layers of igneous layered intrusions (e.g., Holwell et al., 2015). A well-known example is the Cu-rich sulphide occurrence in the Platinova Cu-Au-Pd Reef of the Skaergaard Intrusion in Greenland (Wager et al., 1957).

The mechanisms proposed to explain the occurrences of bornite in magmatic sulphide deposits include: (1) post-magmatic oxidation and de-sulphidation of the primary magmatic sulphide assemblage (pyrrhotite and chalcopyrite) to form bornite and Ti-free magnetite, typically during high-grade metamorphism (upper amphibolite to granulite facies) (Equation 2; Cawthorn and Meyer, 1993; Maier and Barnes, 1996; Andersen, 2006); (2) magmatic oxidation of sulphide melt leading to the preferential oxidation of the FeS (and NiS) components of the sulphide melt to produce magnetite (Equations 3, 4), and the resistance of the Cu_2S component of the sulphide melt to be oxidised to in the process (Wohlgemuth-Ueberwasser et al., 2013). This results in an increase in the Cu/Fe ratio of the sulphide melt and the formation of Cu-rich sulphides.

$$5\ CuFeS_2\ \textit{(Ccp)} + 5\ FeS\ \textit{(Po)} + 6\ H_2O + 8\ O_2 = Cu_5FeS_4\ \textit{(Bn)} + 3\ Fe_3O_4\ \textit{(Mag)} + 6\ H_2S + 5\ SO_2 \qquad \textit{(2)}$$

$$6\ FeS\ \textit{(in melt)} + 4\ O_2 = 2\ FeO{\cdot}Fe_2O_3\ \textit{(Mag)} + 3\ S_2 \qquad \textit{(3)}$$

$$NiS\ \textit{(in melt)} + 1/2\ O_2 = NiO\ \textit{(in Mag)} + 1/2\ S_2 \qquad \textit{(4)}$$

Since S is relatively mobile compared to Se during post-magmatic oxidation and de-sulphidation, the post-magmatic oxidation and de-sulphidation mechanism can therefore explain the low S/Se ratios associated with bornite-bearing ores and the abundance of magnetite in some magmatic sulphide deposits (e.g., Queffurus and Barnes, 2015). However, Queffurus and Barnes (2015) noted that the effect of post-magmatic oxidation and de-sulphidation on S/Se ratios is questionable, because it is only applicable to a limited number of magmatic sulphide deposits and not all deposits subjected to high-grade metamorphism. The post-magmatic oxidation and de-sulphidation model accounts for the S and Se distribution in the sulphides affected by such process but does not account for the enrichment in Cu of the sulphides (i.e., the high Cu/Ni ratios of 50-100) hosted in the Koperberg Suite (Cawthorn and Meyer, 1993; Maier et al., 2012). The model also does not account for the paucity of textures consistent with the replacement of chalcopyrite by magnetite (mantling of chalcopyrite by magnetite), as observed elsewhere, for example in the Platinova Reef of the Skaergaard Intrusion (Fig. 3 in Li, 2017; Fig. 3a in Wernette et al., 2020).

Bornite and chalcopyrite textures in the Koperberg Suite are not consistent with replacement of chalcopyrite by magnetite. The bornite and chalcopyrite in the Koperberg Suite instead form as rims abut magnetite grain boundaries or in close association with magnetite (Figs. 4.6b, 4.8d, e, 4.10b, c; Stumpfl et al., 1976; Conradie and Schoch, 1986; this study), or take inverse or negative grain shapes of sulphides (i.e., interstitial) relative to magnetite (Fig. 4.12c). The inverse or negative grain shapes of sulphides relative to magnetite is consistent with the trapping of sulphide liquid during and/or after crystallisation of magnetite (c.f., Holwell et al., 2015; Georgatou et al., 2018). That is, the textural association of the sulphides and magnetite is consistent with co-crystallisation and/or crystallisation of sulphides after the formation of magnetite. Cawthorn and Meyer (1993) tentatively interpreted the

close association of magnetite with sulphides as indicative of crystallisation of magnetite from a sulphide liquid. Such a hypothesis is in agreement with the magmatic oxidation model (the oxidation of Cu_2S component of the sulphide liquid to produce a Cu-rich sulphide melt and magnetite; Wohlgemuth-Ueberwasser et al., 2013). Georgatou and Chiaradia (2020) have documented the close association of magmatic Cu-rich sulphides with magnetite-rich rocks from various porphyry deposits. Thus, the magmatic oxidation model provides an explanation for the association of higher modal content of magnetite with higher modal contents of Cu-rich sulphides in the most mafic members of the Koperberg Suite (5-9% magnetite for norite and orthopyroxenite samples from Nigramoep and Carolusberg mines; Chapters 4.2.3, 4.2.4).

Ballhaus et al. (2001) noted that S-rich sulphide melts with metal/S ≤1 crystallise in the *iss* stability field (i.e. crystallise to chalcopyrite +pyrrhotite), whereas the oxidation of such sulphide melts (to form S-poor melts with metal/S >1) results in their fractionation past the *iss* stability field, owing to their lower liquidus and solidus temperature. They also noted that the oxidation of sulphide melts will also result in the increase in Ni and Cu content of sulphide melt, and subsequent crystallisation of bornite-digenite-*iss* assemblage or bornite-digenite assemblage instead of *iss*. Thus, the *iss* assemblage (the Narrap-type ores: chalcopyrite + pyrrhotite) and bornite-chalcopyrite (Cu-rich sulphides) hosted in the Koperberg Suite can readily be explained by the oxidation of sulphide melt and depression of its liquidus temperature.

Potential mechanisms that could have led or accompanied oxidation of the Koperberg Suite magmas and the segregated sulphide melt are fractional crystallisation of silicates (e.g., Foden et al., 2015; Zhao et al., 2017), and fractional crystallisation of *mss* (e.g., Doyle and Naldrett, 1986; Keith et al., 2017).

(i) Fractional crystallisation of silicates

Fe^{2+} is more compatible than Fe^{3+} in silicate melts and the fractional crystallisation of Fe^{2+}-dominated silicate phases (e.g., biotite and pyroxene) leads to the increase in the $Fe^{3+}/\Sigma Fe$ ratio of the silicate melt, a proxy to oxygen fugacity (Sossi et al., 2012). Thus, evolved silicate melts are relatively more oxidised and sulphide melt coexisting with such melts becomes oxidised (Zhao et al., 2017, 2019). Such a mechanism applies to the Koperberg Suite where the crystallisation of silicates preceded the deposition of sulphides (Stumpfl et al., 1976; Stumpfl, 1978; McIver et al., 1983).

(ii) Fractional crystallisation of mss

The main constituents of *mss* (pyrrhotite and pentlandite) are Fe^{2+}-dominated phases (e.g., de Villiers, 2009; Xia et al., 2012) and the crystallisation of Ni-rich sulphide melts (segregated from the Cu-rich sulphide melts earlier in the evolution of sulphide melt; Chapter 1.2) to form *mss* results in an increase in the $Fe^{3+}/\Sigma Fe$ ratio of the residual Cu-rich sulphide melt. Such a mechanism is applicable to the

Koperberg Suite where the sulphides are interpreted to have crystallised from a Cu-rich residual sulphide melt (Maier et al., 2012).

A constraint to the magmatic oxidation of sulphide melt mechanism is the relatively higher Ni content expected in magnetite (Equation 4). EDS analysis of magnetite in the Koperberg Suite shows detectable Ni contents (0.05-0.32 wt% NiO). However, since the contents are <1 wt%, the Ni content of magnetite needs to be verified with more robust analysis methods such as EPMA and LA-ICP-MS. On the other hand, this constraint might not be applicable to the Koperberg Suite, where the sulphides are characterised by low Ni contents (Maier et al., 2012; this study; Table 5.6; Fig. 5.6), suggesting that the parental sulphide melt had low Ni contents.

6.2 Trace element chemistry

6.2.1 General trace element trends

The presence of variable quantities of Te, Se, Ag, Bi, Pb, Cd, In, Zn and Sn, and the low Ni and Co contents in the Koperberg Suite sulphides are consistent with a trace element assemblage of Cu-rich sulphide melt fractionated from a Ni-rich *mss* sulphide melt (Zientek et al., 1994; Dare et al., 2011; Caraballo et al., 2020). The trace elements present in Koperberg sulphides are concentrated in the residual Cu-rich sulphide liquid since the partition coefficients between *mss* and the residual Cu-rich sulphide liquid ($D^{mss/sulphide\ melt}$) of these elements are less than 1 (Fig. 6.1; Liu and Brenan, 2015). By contrast, Ni shows a larger partition coefficient up to 1.5 (Mungall et al., 2005). Also, except for Zn, the concentration of these elements should be higher in the sulphide melt relative to the *iss* since their $D^{iss/sulphide\ melt}$ <1 (Fig. 6.1; Liu and Brenan, 2015).

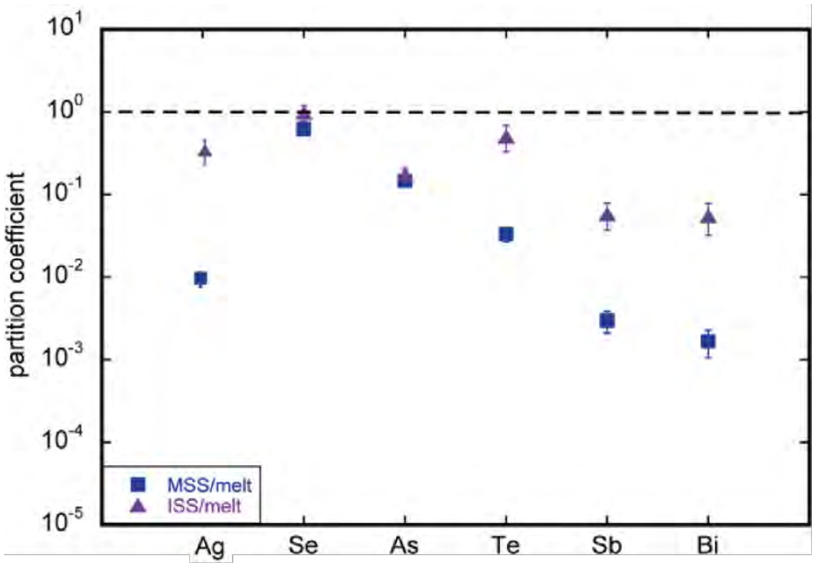

Figure 6. 1 Partition coefficient of trace elements between mss and sulphide melt ($D^{mss/sulphide\ melt}$), and iss and sulphide melt ($D^{iss/sulphide\ melt}$) according to Liu and Brenan (2015). Note that $D^{mss/sulphide\ melt}$ and $D^{iss/sulphide\ melt}$ values of all the elements are less than one indicating that the elements partition into sulphide melt relative to mss and iss.

Nickel and Co partition into *mss* relative to sulphide melt (Barnes and Lightfoot, 2005), hence the Ni content is expected to increase in Cu-rich sulphide melts which segregate from *mss*. The low Ni and Co contents (<40 ppm; Table 5.6; Fig. 5.6) support the generation of the sulphide phases hosted in the Koperberg Suite from such Cu-rich sulphide melts, in line with IOCG model proposed by Maier et al. (2012) (Chapter 2.3.3.3). The $D^{iss/sulphide\ melt}$ of 0.65 of Ni (Table 6.1; Mungall et al., 2005) implies that Ni partitions into sulphide melt relative to *iss*. Thus, the Ni content of sulphide melt is expected to increase with sulphide fractionation. The higher contents of Ni (up to 40 ppm) in bornite hosted in orthopyroxenite from Carolusberg (KCr) is consistent with crystallisation of bornite from a significantly fractionated sulphide melt. The low contents of Ni (<10 ppm) in bornite and chalcopyrite in the more felsic members, such as the leuconorite and diorites from Nababeep Mine (KNb) and Sugarloaf Quarry (KSQ), are consistent with derivation of the bornite and chalcopyrite from a less fractionated sulphide melt.

Chalcogens (Te and Se), which are common substituents for S in sulphides (e.g., Huston et al., 1995; Butler and Nesbitt, 1999), show the highest contents (up to 380 ppm; Fig 5.3a,b) in bornite in orthopyroxenite and norite from Carolusberg (KCr) and Nigramoep (KNg) mines. Since these elements partition into the residual sulphide melt relative to *iss* ($D^{iss/sulphide\ melt}$ <1), such a relationship is consistent with crystallisation of sulphides (at least for bornite) from significantly fractionated sulphide melt. Conversely, the lower contents (<60 ppm Te, <200 ppm Se; Fig. 5.3a, b) of such elements in bornite hosted in the more felsic members, such as the leuconorite and diorites from Nababeep Mine (KNb) and Sugarloaf Quarry (KSQ), are consistent with derivation of these sulphides from less fractionated sulphide melt. Other chalcophile elements (e.g., Bi, Te) do not uniformly show the higher concentrations in bornite or chalcopyrite hosted in the mafic members of the Koperberg Suite. This is probably due to changing oxidation state during the oxidation of sulphide melt which can affect their substitution in sulphides (Fig. 5.3a, 5.4b; Helmy et al., 2010). Lorand and Alard (2010) note that up to 80% Te might not be partitioned into sulphides due to variation of its oxidation state.

6.2.2 S/Se ratios

Because Se strongly fractionates into sulphides (e.g., Lorand and Alard, 2010), Se must be considered as the main substitute for S in sulphides, which should be expressed in systematic S/Se ratio variations. Accordingly, S/Se ratios are commonly used to evaluate provenance and possible contamination in magmatic sulphide deposits (Queffurus and Barnes, 2015; Smith et al., 2016). The contamination of mantle-derived magmas by S-rich crustal rocks is expected to increase the S/Se ratio of mantle-derived magma to ratios above typical mantle values (2850-4350; Eckstrand and Hulbert, 1987; Hattori et al., 2002; Lorand et al., 2003). Additional processes that can modify S/Se values include: (1) loss of S (de-sulphidation) during high-grade metamorphism, leading to lower S/Se values

relative to those of the mantle (e.g., Cawthorn and Meyer, 1993; Maier and Barnes, 1999; Chapter 6.1), (2) fractionation of Se between *iss* and the residual sulphide melts resulting in higher Se content and lower S/Se values in the residual sulphide melt (Keays and Lightfoot, 2004; Mansur et al., 2021), (3) hydrothermal alteration of sulphides which results in lower S/Se values since S is more mobile compared to Se during hydrothermal processes (Yamamoto, 1976).

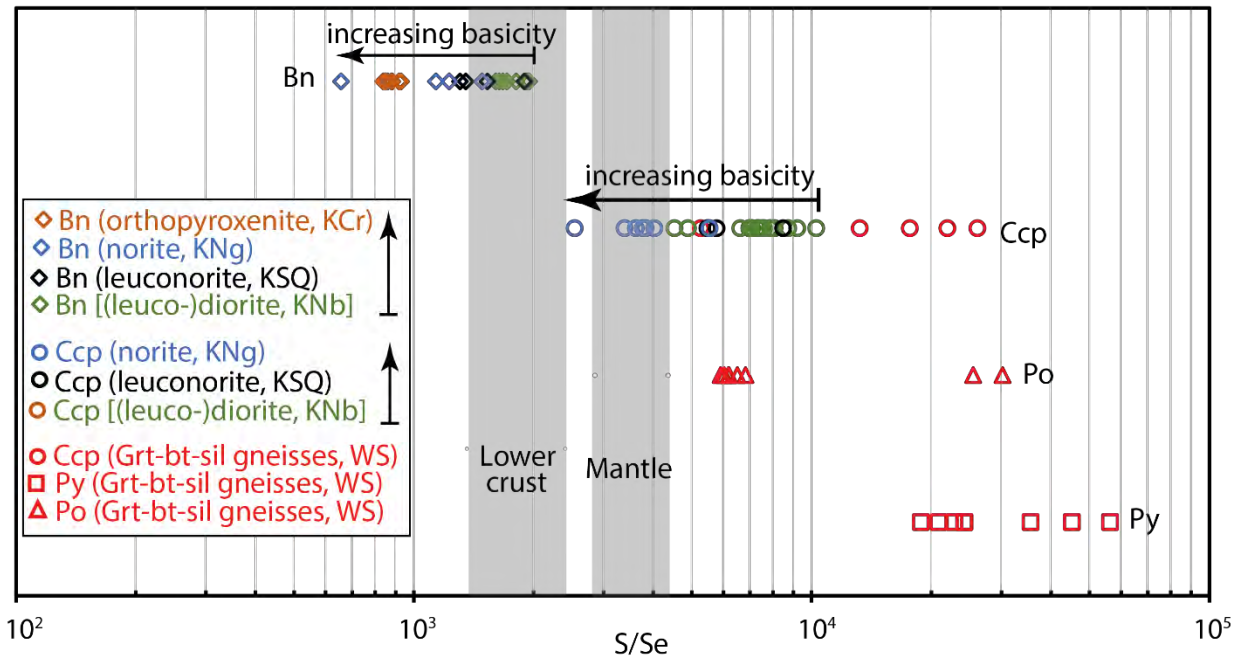

Figure 6. 2 S/Se variations in bornite, chalcopyrite, pyrrhotite and pyrite from the Koperberg Suite and the Khurisberg Subgroup. Note the increase in the S/Se ratios of bornite and chalcopyrite with increasing basicity of the samples suggesting the association of relatively Se-poor (least fractionated sulphide melts) with the most fractionated silicate melts, and the association of relatively Se-rich (most fractionated sulphide melts) with the least fractionated silicate melts. Analytical uncertainties are insignificant at the scale and not shown. KS: Khurisberg Subgroup, KNb: Koperberg Suite from Nababeep Mine, KNg: Koperberg Suite from Nigramoep Mine, KCr: Koperberg Suite from Carolusberg Mine, KSQ: Koperberg Suite from Sugarloaf Quarry.

The S/Se ratios of coexisting bornite and chalcopyrite hosted in the Koperberg Suite (KCr, KNg, KSQ, KNb) do not overlap (Fig. 6.2). Bornite in the Koperberg Suite records lower S/Se ratios (~650-2000; Fig. 6.1) than chalcopyrite in the same samples (~2500-10300; Fig. 6.2), and lower than the typical mantle ratios (2850-4350; Eckstrand and Hulbert, 1987; Hattori et al., 2002; Lorand et al., 2003; Fig. 6.2). The S/Se ratios of chalcopyrite hosted in the Koperberg samples from Nigramoep Mine (KNg) fall within the typical mantle range (Fig. 6.2), whereas the S/Se ratios of bornite in samples from Nababeep Mine (KNb) and some of the samples from Sugarloaf Quarry (KSQ) fall within the range of S/Se ratios typical of the lower crust (~1360-2400; Rudnick and Gao, 2003). The S/Se ratios for pyrrhotite (~5900-30000; Fig. 6.2) in the Khurisberg Subgroup (KS) overlap with chalcopyrite in the Koperberg Suite (KNg, KSQ, KNb; Fig 6.2), whereas chalcopyrite and pyrite hosted in the Khurisberg Subgroup (KS) register higher S/Se ratios (~5300-26000, ~18800-56300, respectively; Fig. 6.2) compared to chalcopyrite and bornite in the Koperberg Suite.

Pyrite in the Khurisberg Subgroup (KS), the main sulphide phase in the proposed contaminant for the Koperberg Suite magmas, registers 10-50 times higher S/Se ratios compared to sulphides in the Koperberg Suite (Fig. 6.2). Pronounced contamination of mantle-derived magmas by a contaminant with high S/Se ratios such as the Khurisberg Subgroup is expected to shift the S/Se ratios of the sulphides in magmatic rocks to higher S/Se ratios compared to those of the mantle (e.g., Smith et al., 2016). Potential processes leading to low S/Se ratios of contaminated magmas are: (i) contamination by a contaminant with low S/Se ratio (e.g., Piña et al., 2008), and (2) no to minimal contamination of magmas (Queffurus and Barnes, 2015). The first factor is clearly not applicable since pyrite, the major sulphide phase in the Khurisberg Subgroup (Chapters 4.1.1 and 4.1.2), shows high S/Se ratios compared to the S/Se ratios typical of the mantle and the sulphides in the Koperberg Suite (Fig. 6.2). Thus, the low S/Se ratios of bornite and chalcopyrite in the Koperberg Suite suggest no to minimal contamination by the Khurisberg Subgroup.

The paucity of textures indicative of the introduction of Cu-S-rich hydrothermal fluids (e.g., sulphide bearing ore fractures), and the minor hydrothermal alteration observed around sulphides in the Koperberg Suite (van Zyl, 1978) rule out the change is in the S/Se ratios of Koperberg sulphides due to hydrothermal alteration. Also, the low a_{H2O} granulite facies conditions existing during emplacement of the Koperberg Suite magmas make the introduction of hydrothermal fluids unlikely (Maier et al., 2012).

The $D_{Se}^{\text{iss/sulphide melt}}$ value of 0.98 (Liu and Brenan, 2015; Fig. 6.1) implies Se slightly partitions into the sulphide melt relative to *iss.* Liu and Brenan (2015) noted that the $D^{\text{iss/sulphide melt}}$ values of elements considered in the study might be lower than the values they presented due to the potential of sulphide melts trapped in *iss.* Hence, the $D_{Se}^{\text{iss/sulphide melt}}$ could be lower than 0.98 (Fig. 6.1), implying that Se may partition more strongly into residual sulphide melts (cf., Keays and Lightfoot, 2004; Mansur et al., 2021).

The Cu content of sulphide melts increases with sulphide fractionation (Naldrett, 2004; Mungall, 2005; Gorbachev, 2006). The high Cu/S and low S/Se ratios of bornite and chalcopyrite in more mafic members of the Koperberg Suite (orthopyroxenite and norite from Carolusberg and Nigramoep mines; KCr, KNg; Figs. 6.2, 6.3a, b) compared to the less mafic members of the Koperberg Suite, such as the leuconorite and (leuco-) diorites from Sugarloaf Quarry and Nababeep Mine (KSQ, KNb; Figs. 6.2, 6.3a, b), can be interpreted as indicative of derivation of the sulphides from a more fractionated sulphide melt. Such an interpretation is consistent with magmatic oxidation of sulphide melt (see Chapter 6.1), where the residual sulphide melt becomes progressively enriched in Cu, resulting in the subsequent crystallisation of a bornite-*iss* assemblage, or bornite instead of *iss*. Indeed, the higher modal

abundance of bornite (4-7%; Fig. 6.3a) in more mafic members of the Koperberg Suite compared to their less mafic counterparts (≤2.5%; Fig. 6.3a) also supports the oxidation of sulphide melt.

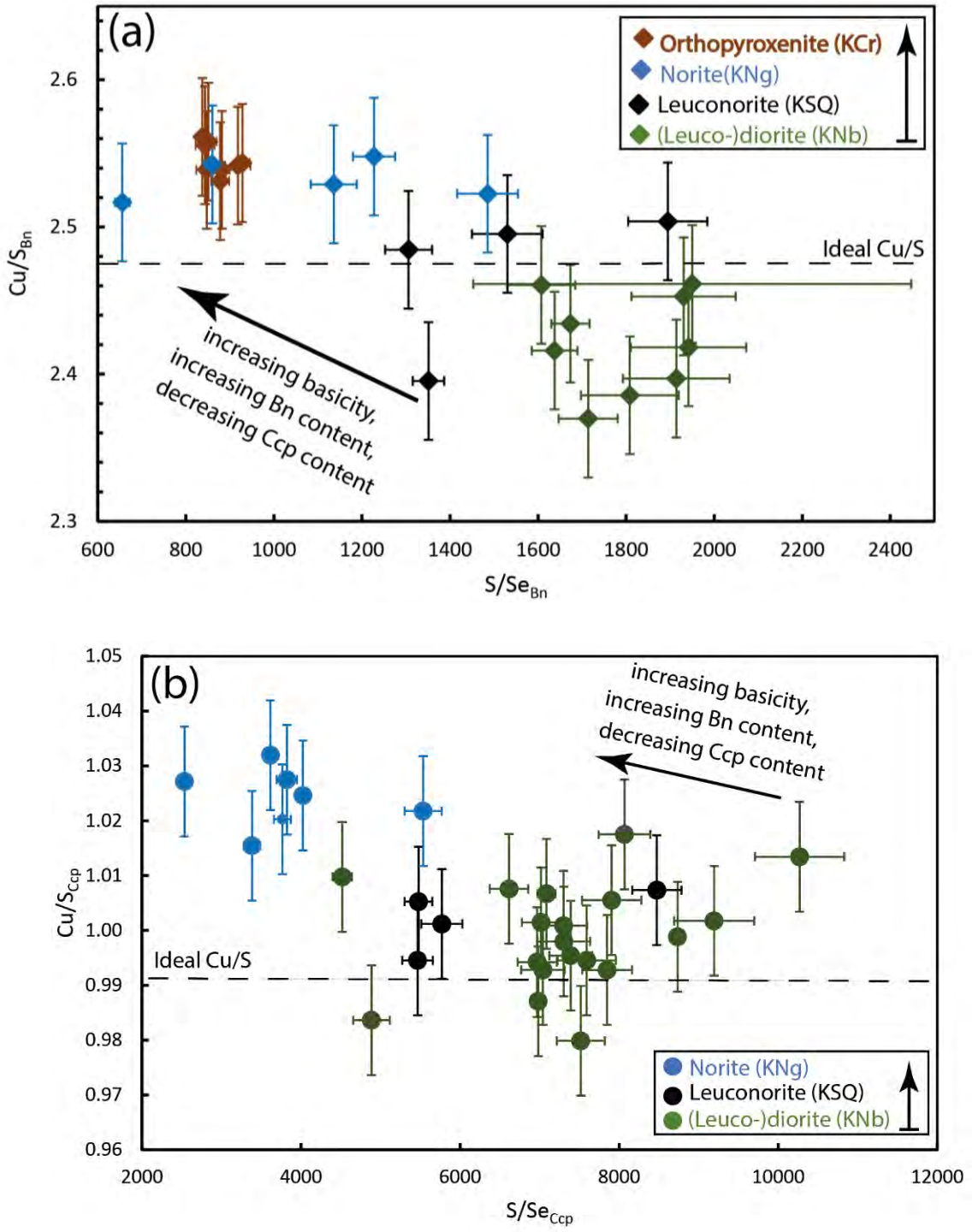

Figure 6.3 Cu/S vs. S/Se plots for bornite (a) and chalcopyrite (b) from the Koperberg Suite. The mafic members (orthopyroxenite and norite) are characterised by high modal content of bornite, high Cu/S values relative to the ideal value and lower S/Se values compared to their felsic counterparts (leucodiorites). This relationship suggests the crystallisation of bornite from fractionated sulphide melts (enriched in Cu and Se, and depleted in S). Arrows in the legend show increase in the basicity of the samples. The analytical uncertainties for Cu/S and S/Se ratios for chalcopyrite and bornite were calculated using the law of propagation of uncertainty (see Chapter 3.3.2, and Supplementary Table B1 for calculations). KS: Khurisberg Subgroup, KNb: Koperberg Suite from Nababeep Mine, KNg:

Koperberg Suite from Nigramoep Mine, KCr: Koperberg Suite from Carolusberg Mine, KSQ: Koperberg Suite from Sugarloaf Quarry.

6.2.3 Implications of S/Se ratios trends for Koperberg Suite petrogenetic model

A petrogenetic model consistent with the trace element trends discussed in the preceding sections (Chapter 6.2.1-6.2.2) is the differentiation model (Chapter 2.3.3.3). The differentiation model proposes that the Koperberg Suite magmas underwent significant differentiation in a deep-seated magma reservoir, and were successively emplaced by tapping off the top of that differentiated magma reservoir, sequentially emplacing progressively more basic fractions (Latsky, 1942; van Zyl, 1978; Lombaard et al., 1986). Such a differentiation process is likely to have promoted simultaneous fractionation of silicate melt and sulphide melt. An example of such coordinated fractionation is documented in the PGE-Cu-Ni deposits hosted in the Khangai Upland massifs in Mongolia (Shapovalova et al., 2020). In these deposits, the least fractionated late intrusions (Mankhan massifs) comprising of gabbro and gabbronorite, host a typical *iss* assemblage (chalcopyrite + pyrrhotite), and the most fractionated late intrusions (Nomgon massifs), comprising of leucogabbroids and anorthosites, host a bornite-cubanite-chalcopyrite assemblage (Mao et al., 2018). The increase in Cu content of the sulphide melt resulting in the replacement of *iss* assemblage during progressive fractionation of the magmas is proposed to be one of the key mechanisms responsible for the formation of the bornite-cubanite-chalcopyrite assemblage (Shapovalova et al., 2020).

In contrast to these Khangai Upland intrusions, the Koperberg Suite shows a reversed relationship between fractionation of the silicate magmas and their sulphide assemblages. The most mafic (least fractionated) members of the Koperberg Suite (e.g., orthopyroxenites) host bornite-dominated ores (bornite, magnetite and minor or no chalcopyrite), whereas the intermediate (moderately) fractionated members (e.g., mica- or orthopyroxene-bearing diorites) host chalcopyrite-dominated ores (chalcopyrite, chalcopyrite and/or bornite; Stumpfl, 1978). The felsic members (most fractionated, e.g., anorthosites) commonly do not host any Cu-sulphide mineralisation (van Zyl, 1978). Field relationships of the Koperberg Suite also show that the felsic members intruded earlier than their mafic counterparts (Conradie and Schoch, 1986; van Zwieten et al., 1996).

This intuitively contradicting relationship between silicate magma and sulphide melt evolution in the Koperberg Suite can be explained considering the following processes: (1) the magmatic oxidation of sulphide melt by fractional crystallisation of Fe^{2+}-dominated silicates and fractional crystallisation of *mss* as a mechanism that yields Cu-enriched sulphide melts, resulting in the subsequent crystallisation of a bornite-*iss* assemblage or the replacement of an *iss* assemblage with bornite (Chapter 6.1; Ballhaus et al., 2001; Wohlgemuth-Ueberwasser et al., 2013); (2) increase in the Se content of, and accordingly the decrease in the S/Se ratio in, the residual sulphide melt with increasing sulphide melt fractionation (Chapter 6.2; Liu and Brenan, 2015; Mansur et al., 2021); (3) the increase in the modal

abundance of bornite coupled with the decrease in the modal abundance of chalcopyrite with increasing basicity of the Koperberg Suite host rocks (Fig. 6.3a, b).

The following set of processes are envisaged to have culminated in the Cu-sulphide mineralisation patterns observed in the Koperberg Suite:

(1) Injection of magma hosting a Cu-rich sulphide melt segregated from a prior *mss* fractionation event in line with the IOCG model (Maier et al., 2012), into a deep-seated magma chamber.
(2) Fractionation of silicate melt (by progressive crystallisation of Fe^{2+}-dominated phases like pyroxene and biotite) accompanied by the oxidation and Cu enrichment of sulphide melt, possibly in a stratified magma chamber, with felsic silicate melts in the upper parts of the magma chamber and mafic melts in the lower parts of the magma chamber. Depending on the size of crystals and sulphide melt droplets in the crystal mush, migration of the denser sulphide melt (~4.5 g/cm^3; Mungall and Su, 2005) in a less dense silicate melt (~2.5 g/cm^3; Lange and Carmichael, 1987) could have accompanied such a process. Migration of sulphide droplets would be less effective with progressive crystallisation and increase in viscosity of the silicate melt (Chung and Mungall, 2009). In such a scenario, the felsic silicate melt in the upper parts of the stratified magma chamber would have contained a small modal proportion of sulphide melt.
(3) Emplacement of the most fractionated but poorly mineralised felsic silicate melt (e.g., anorthosites) along steep structures in the OCD.
(4) Emplacement of silicate magma coexisting with the least fractionated (least oxidised) relatively Cu-poor, S-rich sulphide melt yielding the Narrap-type ores characterised by an *iss* assemblage (chalcopyrite + pyrrhotite) with high bulk S/Se ratios (13800-21000; Cawthorn and Meyer, 1993).
(5) Emplacement of intermediate silicate (dioritic) magma (moderately fractionated) coexisting with the moderately oxidised sulphide melts. Such sulphide melts would be moderately Cu-rich and S-poor, yielding chalcopyrite-dominated ores with variable but typically low bornite contents, characterised by intermediate S/Se ratios. Such ores are represented by the diorite- and leuconorite-hosted Cu-sulphide mineralisation (chalcopyrite + bornite; 1.0-1.9% chalcopyrite and 0.1-2.5% bornite; Fig. 6.3) of Nababeep and the Sugarloaf Quarry (KNb, KSQ). These rocks host sulphides with intermediate S/Se ratios (compared to bulk S/Se ratios of the Narrap-type ores) of ~1300-1950 for bornite and ~4500-10200 for chalcopyrite (Fig. 6.2). The sulphides also show relatively low Cu/S ratios (considering samples used in this study only) of 0.98-1.01 for chalcopyrite and 2.37-2.50 for bornite (Fig. 6.3).
(6) Emplacement of mafic silicate melts coexisting with the most evolved (most oxidised) sulphide melts. Such sulphide melts would be highly Cu-rich and S-poor, yielding bornite-dominated ore (devoid of chalcopyrite or with low chalcopyrite content) characterised by the lowest S/Se ratios. According to this model, these host mafic rocks are expected to contain higher

abundances of sulphides. This is in agreement with a long-known exploration guideline for geologists working in the OCD, that is, the most economic Cu mineralisation is hosted in the more mafic members of the Koperberg Suite (Latsky, 1942; Benedict et al., 1964). The sulphide assemblage produced by such sulphide melts is consistent with the sulphide assemblage observed in the norite (KNg) and orthopyroxenite (KCr) which is characterised by the highest sulphide modal content (4.5-7%; Fig. 6.3), lowest S/Se ratios (~650-1500 for bornite and ~2500-5500 for chalcopyrite; Fig. 6.1), highest Cu/S ratios (1.02-1.03 for chalcopyrite and 2.52-2.56 for bornite; Fig. 6.3).

6.3 Sulphur isotopes

6.3.1 Constraints of S-isotope signatures based on a mantle source

The $\delta^{34}S$ values of the proposed contaminant (Khurisberg Subgroup) overlap with the values of the Koperberg Suite. All data, with some variety in the same rock types, range from -1.4 to +1.91‰ (Table 5.7; Fig. 5.9). A meaningful conclusion about S contamination of intruding magmas from a mantle source would require the deviation of the $\delta^{34}S$ values of the magmatic rocks from the range of $\delta^{34}S$ values for mantle-derived rocks of 0 ± 2 ‰ (Fig. 5.9; Ohmoto and Rye, 1979; Sakai et al., 1984; Peters et al., 2010). However, the similarity between the isotopic signatures in the Koperberg Suite below and above the Khurisberg Subgroup, and in the Khurisberg Subgroup itself, renders the test for crustal contamination inconclusive. If such a contamination exists, it cannot be identified on the basis of S-isotopic signatures.

The proposed uncontaminated Koperberg Suite stratigraphically below the Khurisberg Subgroup (from Sugarloaf Quarry, KSQ) has a $\delta^{34}S$ values +0.74‰, similar to the Koperberg Suite from the Nababeep, Nigramoep and Carolusberg mines, which range mostly from -1.4 to +1.91 (Fig. 5.9, Table 5.7). These values are compatible with mantle signatures of 0 ± 2 ‰ (Fig. 5.9; Ohmoto and Rye, 1979; Sakai et al., 1984; Peters et al., 2010). The sulphides in the Khurisberg Subgroup show similar $\delta^{34}S$ values (-1.2 to +3.05‰), which however may well be a crustal signature because the $\delta^{34}S$ values of Proterozoic sedimentary rocks cover a wide range of $\delta^{34}S$ values (+5 ± 10‰; Canfield and Farquhar, 2009), which include the $\delta^{34}S$ values for mantle-derived rocks of 0 ± 2‰ (Ohmoto and Rye, 1979; Sakai et al., 1984; Peters et al., 2010). The majority of *in-situ* S isotope analyses of pyrite in the paragneisses of the Khurisberg Subgroup was obtained from inclusions in millimetre-sized metamorphic garnet. Garnet growth in the gneisses is associated with the regional metamorphism (~1210-1180 Ma M_2 event; Chapter 2.2.2; Raith and Harley, 1998) prior to the emplacement of the Koperberg Suite at ~1030 Ma. Hence, the pyrite and its S-isotopic signature very likely reflect the original crustal sulphur composition in the paragneisses prior to Koperberg magma emplacement.

The S isotope observed in the Koperberg Suite and the Khurisberg Subgroup results can be explained by limited or no contamination of the Koperberg Suite by the Khurisberg Subgroup, and/or undetectable contamination (based on S isotopes) of Koperberg magmas by the Khurisberg Subgroup.

(i) Limited or no contamination of the Koperberg Suite by the Khurisberg Subgroup

Keays and Lightfoot (2010) note that the contamination of magmas by a source with an insufficient amount of S (e.g., low-S rocks) may not drive magmas to S-saturation. Thus, considering such an assumption, the Koperberg magmas may have not extracted sufficient S from the Khurisberg Subgroup metasedimentary rocks to drive the Koperberg magmas to S-saturation. An implication for such a conclusion is that the Koperberg magmas may have achieved S-saturation at their source or before their interaction with the Khurisberg Subgroup.

(ii) Undetectable contamination of Koperberg magmas by the Khurisberg Subgroup

In this scenario, the Khurisberg Subgroup metasedimentary rocks, with near-neutral S isotope signatures similar to those of the intruding mantle-derived magmas, contaminated the Koperberg magmas significantly, and might have contributed to S-saturation of the magmas. This however would not lead to a detectable change of isotopic signatures of sulphides hosted in the Koperberg Suite orebodies. Accordingly, the S isotopic variation on their own are inconclusive as a test for crustal contamination.

6.3.2 Constraints of S-isotope signatures based on a lower crustal sulphur source

Partial melting of oceanic crust hosting VMS deposits in the lower crust has been proposed as a mechanism for the formation of the Koperberg magmas (cf. the crustal melting petrogenetic model, Chapter 2.3.3.3; Maier, 2000; Duchesne et al., 2007). Duchesne et al. (2007) have proposed underthrusting of oceanic crust beneath the northern parts of the Bushmanland Domain during the ~1.9 Ga Eburnian Orogeny as a mechanism for incorporating oceanic crust into the lower crust (Chapter 2.3.3.3).

The bulk altered oceanic crust and Proterozoic Volcanogenic Massive Sulphide (VMS) deposits are characterised by neutral $\delta^{34}S$ values (~0.9‰ and ~0.‰ , respectively; Alt, 1995; Huston, 1997; Huston et al., 2010), which fall within the range of values of the mantle and lower crust (-2‰ to +4‰). High-grade (granulite facies) metamorphism and partial melting does not affect $\delta^{34}S$ values (e.g., Hammerli et al., 2017). The incorporation of oceanic crust, its subsequent metamorphism at granulite-facies conditions and partial melting is thus expected to yield magmas with $\delta^{34}S$ values within the mantle and lower crust range. Therefore, in the case of the OCD, the S isotope ratios neither provide evidence nor rule out oceanic crust-hosted VMS deposits as a source of Cu and S for the Koperberg Suite magmas.

Interestingly, one of the few known exceptions of Mesoproterozoic volcanogenic massive sulphide (VMS) deposits in which the $\delta^{34}S$ values of sulphides are not close to ~0‰ are deposits hosted in the

Areachap Group of the Areachap Domain, located east of the Bushmanland Domain (Fig. 1.1), close to the border of the Namaqua Sector to the Kaapvaal Craton. Bailie et al. (2010) report $\delta^{34}S$ values of +3.0 to +8.5‰ for sulphides hosted in these rocks. If the incorporated oceanic crust beneath the Bushmanland Domain (according to Duchesne et al., 2007) hosted VMS deposits with sulphides characterised by $\delta^{34}S$ values such as those from the Areachap Group, then VMS-hosted Cu-Fe sulphides could be excluded as a source of Cu and S for the Koperberg Suite magmas.

6.3.3 Synthesis

Because of the similarity in isotopic signatures of the mantle-derived magmas and the potential crustal contaminant, the S isotope data presented in this study neither support nor rule out the contamination of the Koperberg Suite magmas by the Khurisberg Subgroup metasedimentary rocks. For similar reasons, an ancient oceanic crust proposed to be at the base of the crust may or may not have been the source of the magmas.

Trace element systematics argue in favour of the segregation of a Ni-rich sulphide melt extraction at a deeper crustal level, possibly similar to the Hondekloof deposit. This is indicated by the low contents of Ni and Co (<40 ppm; Table 5.6; Fig. 5.6) of the sulphides in the Koperberg Suite, and the high concentrations (up to 1000 ppm) of elements that partition into Cu-rich sulphide melts relative to the Ni-rich *mss* (Table 5.6; Figs 5.3, 5.4, 5.7). An extraction of Ni-rich sulphides at such a deeper level also implies that sulphur saturation already has been reached prior to the emplacement of magmas along the steep structures of the OCD. The addition of sulphur by crustal contamination therefore might not have been required to form the deposits of the OCD.

The crustal signature of the Koperberg Suite (initial Sr ratios of 0.706-0.727, ε_{Nd} ~-9, μ of 10.1; Clifford et al., 1995; van Zwieten et al., 1996) suggests that contamination of the Koperberg magmas by crustal components was probably the main mechanism in the attainment of S saturation for these magmas. However, crustal assimilation of metasedimentary rocks at the emplacement level of the Koperberg magmas by supracrustal rocks of the Khurisberg Subgroup appears unlikely as a key mechanism in the attainment of S saturation for the Koperberg magmas due to: (1) the time interval of emplacement of the Koperberg Suite is proposed to have been short (Lombaard et al., 1986), probably too short for significant reaction between intruding Koperberg magmas and the Khurisberg Subgroup (cf. Calvari et al., 1994; Wooster et al., 1997), (2) the occurrence of sulphides in the Khurisberg Subgroup mainly as inclusions in garnet suggesting garnet remained stable and shielded the contained sulphides from mobilisation (Chapter 4.1.1-4.1.2; Fig. 4.2a,c; Fig. 4.4b,c), (3) the lack of textural evidence consistent with resorption or mobility of matrix sulphides (Chapter 4.1.1-4.1.2; Fig. 4.2c,d; Fig. 4.4c,d). Therefore, the mobilisation and release of S from the Khurisberg Subgroup appears to have been ineffective.

7 Conclusion

The trace element assemblage of Koperberg Suite sulphides, with abundant Ag, Se, Te, Bi, Zn, Pb, In, and Cd, but low Ni and Co contents, are characteristic of sulphides that crystallised from a Cu-rich sulphide melt, which formed after segregating a Ni-rich sulphide component at an earlier stage. This is consistent with the derivation of the Cu-rich OCD sulphide melts from a deeper-seated magma reservoir similar to the Hondekloof deposit in the Kliprand area, about 160 km to the southeast of Springbok. This deposit, formed at a similar time as the OCD (1048 ± 12 Ma; Bailie et al., 2019), is characterised by its Ni- and Co-rich sulphide mineralisation, but low Cu contents (Hamman et al., 1996; Maier et al., 2012).

An alternative mechanism for the formation of bornite in the Koperberg Suite is the magmatic oxidation of sulphide melt, yielding Cu-rich, S-poor sulphide melt that subsequently crystallises to an *iss*-bornite assemblage, or the progressive replacement of *iss* with bornite. This mechanism explains the formation of the two endmember sulphide assemblages observed in the Koperberg Suite: (i) the typical *iss* assemblage (Narrap-type-ores: chalcopyrite + pyrrhotite), and (ii) the bornite-dominated assemblage (Carolusberg-type ores: bornite + magnetite ± chalcopyrite). The fractional crystallisation of *mss* (mainly comprising Fe^{2+}-rich phases) linked to an earlier *mss-iss* segregation event and fractional crystallisation of Fe^{2+}-dominated silicate phases are two likely processes to have led to the increase in oxidation fugacity of the silicate and sulphide melt, and effectuated the magmatic oxidation of sulphide melt. As such, the magmatic oxidation of sulphide melts requires extensive differentiation of the Koperberg magmas in a deep-seated, possibly stratified, magma chamber as suggested in the differentiation model (Latsky, 1942; van Zyl, 1978; Lombaard et al., 1986). The typical chalcopyrite-pyrrhotite assemblage likely formed from the least fractionated Cu-poor, S-rich sulphide melt hosted in the least fractionated silicate melts which likely intruded earlier. These Narrap-type ores record the lowest S/Se ratios in the Koperberg Suite. With increasing fractionation of silicate melt and partitioning of Se into the residual sulphide melt, the more mafic silicate melts in the lower parts of the magma chamber coexisted with the most fractioned Cu-rich, S-poor which subsequently crystallised a bornite-dominated sulphide assemblage. This sulphide assemblage shows the lowest S/Se ratios in the Koperberg Suite.

Sulphides from both the proposed uncontaminated Koperberg Suite and the proposed contaminant (Khurisberg Subgroup) are characterised by near-neutral $\delta^{34}S$ values which are consistent with mantle sources but also may exist in the crust. This makes the determination of crustal contamination of the Koperberg Suite magmas by the Khurisberg Subgroup inconclusive using S isotopes. The possibly limited mobility of sulphur from the Khurisberg Subgroup, may suggest an insignificant contribution of sulphur from the Khurisberg Subgroup.

Accordingly, the Koperberg Suite orebodies are not likely genetically related to the mobilisation of sulphur from the Khurisberg Subgroup. As such, there might be other Koperberg orebodies present below the Khurisberg Subgroup in the structurally deeper parts of the O'okiep area. The different species of sulphides hosted in the Koperberg Suite are likely to be a product of varying oxidation levels of initial sulphide melt.

8 Recommendations for future research

(1) Magmatic oxidation of sulphide melt governs the fractionation of Cu and Fe isotopes during sulphide differentiation (e.g., Zhao et al., 2019) and the oxidation states of these two elements. Cu-Fe sulphides which form from oxidised sulphide melts tend to be enriched in Cu^{2+} and Fe^{3+} relative to Cu^{+} and Fe^{2+}, and are characterised by relatively higher $\delta^{65}Cu$ and lower $\delta^{56}Fe$ values (Zhao et al., 2017). Further Cu and Fe isotope work on sulphides in the Koperberg Suite can thus be used to test the magmatic oxidation of sulphide melt as a mechanism for the formation of the sulphide assemblage observed in the Koperberg Suite as proposed in this study.

(2) The two samples from the Khurisberg Subgroup (1A3 and 1B3) that have been analysed show highly variable bulk S contents of 0.07 and 1.48 wt%, respectively (Table 5.7). A larger sample set of the Khurisberg Subgroup is required to ascertain the S content of these rocks and assess whether the S content was sufficiently high to cause any significant contamination to the Koperberg Suite magmas.

References

Alt, J.C. 1995. Sulfur isotopic profile through the oceanic crust: Sulfur mobility and seawater-crustal sulfur exchange during hydrothermal alteration. Geology, 23, 585–588.

Andersen, J.C.Ø. 2006. Postmagmatic sulphur loss in the Skaergaard Intrusion: Implications for the formation of the Platinova Reef. Lithos, 92, 198–221.

Andreoli, M.A.G., Hart, R.J., Ashwal, L.D. and Coetzee, H. 2006. Correlations between U, Th content and metamorphic grade in the Western Namaqualand belt, South Africa, with Implications for radioactive heating of the crust. Journal of Petrology, 47, 1095–1118.

Bailie, R., Abrahams, G., Bokana, R., van Bever Donker, J., Frei, D. and le Roux, P. 2019. The geochemistry and geochronology of the upper granulite facies Kliprand dome: Comparison of the southern and northern parts of the Bushmanland Domain of the Namaqua Metamorphic Province, southern Africa and clues to its evolution. Precambrian Research, 330, 58–100.

Bailie, R., Armstrong, R. and Reid, D. 2007. The Bushmanland Group supracrustal succession, Aggeneys, Bushmanland, South Africa: Provenance, age of deposition and metamorphism. South African Journal of Geology, 110, 59–86.

Bailie, R., Gutzmer, J., Strauss, H., Stüeken, E. and McClung, C. 2010. Sulfur isotope characteristics of metamorphosed Zn–Cu volcanogenic massive sulfides in the Areachap Group, Northern Cape Province, South Africa. Mineralium Deposita, 45, 481–496.

Bailie, R., Macey, P.H., Nethenzheni, S., Frei, D. and le Roux, P. 2017. The Keimoes Suite redefined: The geochronological and geochemical characteristics of the ferroan granites of the eastern Namaqua Sector, Mesoproterozoic Namaqua-Natal Metamorphic Province, southern Africa. Journal of African Earth Sciences, 134, 737–765.

Ballhaus, C., Tredoux, M. and Späth, A. 2001. Phase relations in the Fe-Ni-Cu-PGE-S system at magmatic temperature and application to massive sulphide ores of the Sudbury Igneous Complex. Journal of Petrology, 42, 1911–1926.

Barnes, S.-J. and Lightfoot, P.C. 2005. Formation of Magmatic Nickel Sulfide Deposits and Processes Affecting Their Copper and Platinum Group Element Contents. In: J.W. Hedenquist, J.F.H. Thompson, R.J. Goldfarb and J.P. Richards (Editors) One Hundredth Anniversary Volume. Society of Economic Geologists, 179–213.

Barton, E.S. 1983. Reconnaissance isotopic investigations in the Namaqua Mobile Belt and implications for Proterozoic crustal evolution—Namaqualand geotraverse. Geological Society of South Africa Special Publication, 10, 45–66.

Benedict, P.C., Wiid, D. de N., Cornelissen, A.K. and Staff 1964. Progress report on the geology of the O' okiep Copper District. In: S.H. Haughton (Editor) The Geology of Some Ore Deposits in Southern Africa, II. Geological Society of South Africa, 239–302.

Bial, J., Büttner, S. and Appel, P. 2016. Timing and conditions of regional metamorphism and crustal shearing in the granulite facies basement of south Namibia: Implications for the crustal evolution of the Namaqualand metamorphic basement in the Mesoproterozoic. Journal of African Earth Sciences, 123, 145–176.

Bial, J., Büttner, S.H. and Frei, D. 2015a. Formation and emplacement of two contrasting late-Mesoproterozoic magma types in the central Namaqua Metamorphic Complex (South Africa, Namibia): Evidence from geochemistry and geochronology. Lithos, 224–225, 272–294.

Bial, J., Büttner, S.H., Schenk, V. and Appel, P. 2015b. The long-term high-temperature history of the central Namaqua Metamorphic Complex: Evidence for a Mesoproterozoic continental back-arc in southern Africa. Precambrian Research, 268, 243–278.

Blignault, H.J., Van Aswegen, G., Van Der Merwe, S.W. and Colliston, W.P. 1983. The Namaqualand Geotraverse and Environs: Part of the Proterozoic Namaqua Mobile Belt. In: B.J.V. Botha (Editor) Namaqualand Metamorphic Complex. Special Publication of the Geological Society of South Africa, 10, 1–29.

Boer, R.H., Meyer, F.M. and Cawthorn, R.G. 1994. Stable isotopic evidence for crustal contamination and desulfidation of the cupriferous Koperberg Suite, Namaqualand, South Africa. Geochimica et Cosmochimica Acta, 58, 2677–2687.

Bowles, M. 1988. Metallogeny of stratabound tungsten mineralization in the Namaqualand Metamorphic Complex, northwest Cape, South Africa - the consanguineous view. South African Journal of Geology, 91, 248–256.

Brandriss, M.E. and Cawthorn, R.G. 1996. Formation of anorthosite and leucotonalite during magma hybridization in the Koperberg Suite of Namaqualand, South Africa. South African Journal of Geology, 99, 135–151.

Le Bras, L.Y., Bolhar, R., Bybee, G.M., Nex, P.A.M., Guy, B.M., Moyana, T. and Lourens, P. 2021. Platinum-group and trace elements in Cu-sulfides from the Loolekop pipe, Phalaborwa: implications for ore-forming processes. Mineralium Deposita, 56, 161–177.

Butler, I.B. and Nesbitt, R.W. 1999. Trace element distributions in the chalcopyrite wall of a black smoker chimney: insights from laser ablation inductively coupled plasma mass spectrometry (LA–ICP–MS). Earth and Planetary Science Letters, 167, 335–345.

Büttner, S.H. 2012. Rock Maker: an MS Excel™ spreadsheet for the calculation of rock compositions from proportional whole rock analyses, mineral compositions, and modal abundance. Mineralogy and Petrology, 104, 129–135.

Büttner, S.H., Prevec, S.A. and Schmeldt, G.A. 2021. Petrogenesis of Mesoproterozoic Granites of the Swartoup Hills Region, Kakamas Domain, Namaqua Belt, South Africa. Frontiers in Earth Science, 8, 615.

Cairncross, B. 2004. History of the Okiep Copper District, Namaqualand, Northern Cape Province, South Africa. Mineralogical Record, 35, 289– 317.

Calvari, S., Coltelli, M., Neri, M., Pimpilo, M. and Scribano, V. 1994. The 1991-1993 Etna eruption: chronology and lava. Acta Vulcanologia, 4, 1–14.

Canfield, D.E. and Farquhar, J. 2009. Animal evolution, bioturbation, and the sulfate concentration of the oceans. Proceedings of the National Academy of Sciences, 106, 8123—8127.

Caraballo, E., Dare, S. and Beaudoin, G. 2020. Variation of trace elements in chalcopyrite from worldwide Ni-Cu sulfide deposits: implications for mineral exploration. In: GeoConvention 2020. Virtual event,.

Cawthorn, R.G. and Meyer, F.M. 1993. Petrochemistry of the Okiep copper district basic intrusive bodies, Northwestern Cape Province, South Africa. Economic Geology, 88, 590–605.

Chaussidon, M. and Lorand, J.P. 1990. Sulphur isotope composition of orogenic spinel lherzolite massifs from Ariege (North-Eastern Pyrenees, France): An ion microprobe study. Geochimica et Cosmochimica Acta, 54, 2835–2846.

Chung, H. and Mungall, J.E. 2009. Physical constraints on the migration of immiscible fluids through

partially molten silicates, with special reference to magmatic sulfide ores. Earth and Planetary Science Letters, 286, 14–22.

Clifford, T. N., Barton, E. S., Stern, R. A., Duchesne, J.-C. 2004. U-Pb Zircon Calendar for Namaquan (Grenville) Crustal Events in the Granulite-facies Terrane of the O'okiep Copper District of South Africa. Journal of Petrology, 45, 669–691.

Clifford, T.N. 1985. O'okiep copper deposits, Namaqualand, South Africa: evidence for partial melting of the Earth's deeper crust in Kibaran (Grenville) times. In: P. Bowden, J.A. Kinnaird and F.D. van Horn (Editors) 13th Colloquium of African Geology. Paris, University of St. Andrews, 59.

Clifford, T.N. and Barton, E.S. 2012. The O'okiep Copper District, Namaqualand, South Africa: A review of the geology with emphasis on the petrogenesis of the cupriferous Koperberg Suite. Mineralium Deposita, 47, 837–857.

Clifford, T.N., Barton, E.S., Retief, E.A. and Rex, D.C. 1990. The Koperberg Suite, Okiep Copper District, Namaqualand, SouthA frica: New isotope data. In: Colloquium of African Geology. Nancy, CIFEG,.

Clifford, T.N., Barton, E.S., Retief, E.A., Rex, D.C. and Fanning, C.M. 1995. A Crustal Progenitor for the Intrusive Anorthosite—Charnockite Kindred of the Cupriferous Koperberg Suite, O'okiep District, Namaqualand, South Africa; New Isotope Data for the Country Rocks and the Intrusives. Journal of Petrology, 36, 231–258.

Clifford, T.N., Barton, E.S., Stern, R.A. and Duchesne, J.-C. 2004. U–Pb Zircon Calendar for Namaquan (Grenville) Crustal Events in the Granulite-facies Terrane of the O'okiep Copper District of South Africa. Journal of Petrology, 45, 669–691.

Clifford, T.N., Gronow, J., Rex, D.C. and Burger, A.J. 1975a. Geochronological and petrogenetic studies of high-grade metamorphic rocks and intrusives in Namaqualand, South Africa. Journal of Petrology, 16, 154–188.

Clifford, T.N., Stumpfl, E.F., Burger, A.J., McCarthy, T.S. and Rex, D.C. 1981. Mineral-chemical and isotopic studies of Namaqualand granulites, South Africa: A Grenville analogue. Contributions to Mineralogy and Petrology, 77, 225–250.

Clifford, T.N., Stumpfl, E.F. and McIver, J.R. 1975b. A sapphirine-cordierite-bronzite-phlogopite paragenesis from Namaqualand, South Africa. Mineralogical Magazine, 40, 347–356.

Conradie, J.A. and Schoch, A.E. 1986. Petrological characteristics of the Koperberg Suite, South Africa - an analogy to massif-type anorthosites? Precambrian Research, 31, 157–188.

Conradie, J.A. and Schoch, A.E. 1988. Rare earth element geochemistry of an anorthosite-diorite suite, Namaqua mobile belt, South Africa. Earth and Planetary Science Letters, 87, 409–422.

Coplen, T.B. and Krouse, H.R. 1998. Sulphur isotope data consistency improved. Nature, 392, 32.

Cornell, D.H., Pettersson, Å., Whitehouse, M.J. and Scherstén, A. 2009. A new chronostratigraphic paradigm for the age and tectonic history of the Mesoproterozoic Bushmanland Ore District, South Africa. Economic Geology, 104, 385–404.

Cornell, D.H., Thomas, R.J., Moen, H.F.G., Reid, D.L., Moore, J.M. and Gibson, R.L. 2006. The Namaqua-Natal Province. In: M.R. Johnson, C.R. Anhaeusser and R.J. Thomas (Editors) Geology of South Africa. Pretoria : Council for Geoscience ; Johannesburg : Geological Society of South Africa, 325–379.

Dare, S.A.S., Barnes, S.-J., Prichard, H.M. and Fisher, P.C. 2011. Chalcophile and platinum-group

element (PGE) concentrations in the sulfide minerals from the McCreedy East deposit, Sudbury, Canada, and the origin of PGE in pyrite. Mineralium Deposita, 46, 381–407.

Dewey, J.F., Robb, L. and Van Schalkwyk, L. 2006. Did Bushmanland extensionally unroof Namaqualand? Precambrian Research, 150, 173–182.

Diener, J.F.A., White, R.W., Link, K., Dreyer, T.S. and Moodley, A. 2013. Clockwise, low-P metamorphism of the Aus granulite terrain, southern Namibia, during the Mesoproterozoic Namaqua Orogeny. Precambrian Research, 224, 629–652.

Doggart, S.W. 2019. Geochronology and isotopic characterisation of LCT pegmatites from the Orange River Pegmatite Province. Stellenbosch University, 37pp.

Doyle, C.D. and Naldrett, A.J. 1986. Ideal mixing of divalent cations in mafic magma and its effect on the solution of ferrous oxide. Geochimica et Cosmochimica Acta, 50, 435–443.

Duchesne, J.C., Auwera, J. Vander, Liégeois, J.P., Barton, E.S. and Clifford, T.N. 2007. Geochemical constraints of the petrogenesis of the O'okiep Koperberg Suite and granitic plutons in Namaqualand, South Africa: A crustal source in Namaquan (Grenville) times. Precambrian Research, 153, 116–142.

Eckstrand, O.R. and Hulbert, L.J. 1987. Selenium and the source of sulfur in magmatic nickel and platinum deposits. In: Geological Association of Canada–Mineralogical Association Canada Program. 40.

Eglington, B.M. 2006. Evolution of the Namaqua-Natal Belt, southern Africa - A geochronological and isotope geochemical review. Journal of African Earth Sciences, 46, 93–111.

Foden, J., Sossi, P.A. and Wawryk, C.M. 2015. Fe isotopes and the contrasting petrogenesis of A-, I- and S-type granite. Lithos, 212–215, 32–44.

Galileo Resources. 2016a. Update on Concordia copper mineralisation. https://galileoresources.com/wp-content/uploads/Concordia-Copper-Mineralisation.pdf

Galileo Resources 2016b. Conclusion of Concordia JV Agreement. https://galileoresources.com/wp-content/uploads/Conclusion-of-Concordia-JV-Agreement.pdf

von Gehlen, K., Nielsen, H., Rozendaal, A. and Jensen, M.L. 1990. Sulphur isotopes indicate a homogeneous, probably mantle source of the Okiep copper ores, Namaqualand. In: Abstract Geocongress '90. Cape Town, Geological Society of South Africa, 582–585.

Georgatou, A.A. and Chiaradia, M. 2020. Magmatic sulfides in high-potassium calc-alkaline to shoshonitic and alkaline rocks. Solid Earth, 11, 1–21.

Georgatou, A., Chiaradia, M., Rezeau, H. and Wälle, M. 2018. Magmatic sulphides in Quaternary Ecuadorian arc magmas. Lithos, 296–299, 580–599.

George, L.L., Cook, N.J., Crowe, B.B.P. and Ciobanu, C.L. 2018. Trace elements in hydrothermal chalcopyrite. Mineralogical Magazine, 82, 59–88.

Geringer, G.J., Schoch, A.E., Sukhanov, M. and Zhuravlev, D. 1998. Geochemical and isotopic characteristics of different types of anorthosite in the Namaqua mobile belt, South Africa. Chemical Geology, 145, 17–46.

Gibson, R.L. and Kisters, A.F.M. 1996. The geology and mineralization of the Okiep Copper District: An overview. South African Journal of Geology, 99, 105–106.

Gibson, R.L., Robb, L.J., Kisters, A.F.M. and Cawthorn, R.G. 1996. Regional setting and geological evolution of the Okiep Copper District, Namaqualand, South Africa. South African Journal of Geology, 99, 107–120.

Gorbachev, N.S. 2006. Mineralogical and geochemical zoning and genesis of massive sulfide ores at the Oktyabr'sky deposit. Geology of Ore Deposits, 48, 473–488.

Groves, D.I. and Vielreicher, N.M. 2001. The Phalabowra (Palabora) carbonatite-hosted magnetite-copper sulfide deposit, South Africa: An end-member of the iron-oxide copper-gold-rare earth element deposit group? Mineralium Deposita, 36, 189–194.

Hamman, J.N., Rozendaal, A. and Jordaan, W. 1996. Gabbro-norite-hosted Ni-Cu-(Co)-sulphide mineralization in southern Namaqualand and its relationship to the cupriferous Koperberg Suite of the Okiep Copper District, South Africa. South African Journal of Geology, 99, 153–167.

Hammerli, J., Kemp, A.I.S., Barrett, N., Wing, B.A., Roberts, M., Arculus, R.J., Boivin, P., Nude, P.M. and Rankenburg, K. 2017. Sulfur isotope signatures in the lower crust: A SIMS study on S-rich scapolite of granulites. Chemical Geology, 454, 54–66.

Hartnady, C., Joubert, P. and Stowe, C. 1985. Proterozoic Crustal Evolution in Southwestern Africa. Episodes, 8, 236–244.

Hattori, K.H., Arai, S. and Clarke Barrie, D.B. 2002. Selenium, tellurium, arsenic and antimony contents of primary mantle sulfides. Canadian Mineralogist, 40, 637–650.

Helmy, H.M., Ballhaus, C., Wohlgemuth-Ueberwasser, C., Fonseca, R.O.C. and Laurenz, V. 2010. Partitioning of Se, As, Sb, Te and Bi between monosulfide solid solution and sulfide melt – Application to magmatic sulfide deposits. Geochimica et Cosmochimica Acta, 74, 6174–6179.

Hoefs, J., Coolen, J.J.M. and Touret, J. 1982. The sulfur and carbon isotope composition of scapolite-rich granulites from southern Tanzania. Contributions to Mineralogy and Petrology, 78, 332–336.

Hoffman, P.F. 1991. Did the breakout of Laurentia turn Gondwanaland inside out? Science, 252, 1409–1412.

Holwell, D.A., Keays, R.R., McDonald, I. and Williams, M.R. 2015. Extreme enrichment of Se, Te, PGE and Au in Cu sulfide microdroplets: evidence from LA-ICP-MS analysis of sulfides in the Skaergaard Intrusion, east Greenland. Contributions to Mineralogy and Petrology, 170, 1–26.

Holwell, D.A. and Mcdonald, I. 2010. A review of the behaviour of platinum group elements within natural magmatic sulfide ore systems. Platinum Metals Review, 54, 26–36.

Huston, D.L. 1997. Stable Isotopes and Their Significance for Understanding the Genesis of Volcanic-Hosted Massive Sulfide Deposits: A Review. Volcanic Associated Massive Sulfide Deposits: Processes and Examples in Modern and Ancient Settings, 8, 0.

Huston, D.L., Pehrsson, S., Eglington, B.M. and Zaw, K. 2010. The Geology and Metallogeny of Volcanic-Hosted Massive Sulfide Deposits: Variations through Geologic Time and with Tectonic Setting. Economic Geology, 105, 571–591.

Huston, D.L., Sie, S.H., Suter, G.F., Cooke, D.R., Both, R.A., Huston, D.L., Sie, S.H. and Suter, G.F. 1995. Trace Elements in Sulfide Minerals from Eastern Australian Volcanic-Hosted Massive Sulfide Deposits: Part I. Proton Microprobe Analyses of Pyrite, Chalcopyrite, and Sphalerite, and Part II. Selenium Levels in Pyrite: Comparison with (5348 Values and Implications for the Source of Sulfur in Volcanogenic Hydrothermal Systems Part I. Proton Microprobe Analyses

of Pyrite, Chalcopyrite, and Sphalerite Introduction and Previous Studies. Economic Geology, 90, 1167–1196.

Iyer, S.S., de Oliveira, M.A.F., Hoefs, J. and Krouse, H.R. 1992. Sulfur and carbon isotopes in scapolite-bearing granulites of the São José do Rio Pardo area, Brazil. Journal of South American Earth Sciences, 6, 59–66.

Joubert, P. 1986a. The Namaqualand Metamorphic Complex-a summary. In: Anhaeusser, C. R. and S. Maske (Editors) Mineral Deposits of Southern Africa, vol. II. Johannesburg, Geological Society of South Africa, 1395–1420.

Joubert, P. 1986b. Namaqualand-a model of proterozoic accretion? Transactions of the Geological Society of South Africa, 89, 79–96.

Keays, R.R. and Lightfoot, P.C. 2004. Formation of Ni–Cu–Platinum Group Element sulfide mineralization in the Sudbury Impact Melt Sheet. Mineralogy and Petrology, 82, 217–258.

Keays, R.R. and Lightfoot, P.C. 2010. Crustal sulfur is required to form magmatic Ni–Cu sulfide deposits: evidence from chalcophile element signatures of Siberian and Deccan Trap basalts. Mineralium Deposita, 45, 241–257.

Keith, M., Haase, K.M., Klemd, R., Schwarz-Schampera, U. and Franke, H. 2017. Systematic variations in magmatic sulphide chemistry from mid-ocean ridges, back-arc basins and island arcs. Chemical Geology, 451, 67–77.

Kiseeva, E.S., Fonseca, R.O.C. and Smythe, D.J. 2017. Chalcophile elements and sulfides in the upper mantle. Elements, 13, 111–116.

Kisters, A.F.M., Charlesworth, E.G., Gibson, R.L. and Anhaeusser, C.R. 1996. Steep structure formation in the Okiep Copper District, South Africa: Bulk inhomogeneous shortening of a high-grade metamorphic granite-gneiss sequence. Journal of Structural Geology, 18, 735–751.

Kisters, A.F.M., Potgieter, J.E., Charlesworth, E.G., Anhaeusser, C.R., Gibson, R.L. and Watkeys, M.K. 1994. Emplacement features of cupriferous noritoids in the Okiep Copper District, Namaqualand, South Africa. Exploration & Mining Geology, 3, 297–310.

Kita, N.T., Ushikubo, T., Fu, B. and Valley, J.W. 2009. High precision SIMS oxygen isotope analysis and the effect of sample topography. Chemical Geology, 264, 43–57.

Ku, H.H. 1966. Notes on the use of propagation of error formulas. Journal of Research of the National Bureau of Standards, Section C: Engineering and Instrumentation, 70C, 263—273.

LaFlamme, C., Martin, L., Jeon, H., Reddy, S.M., Selvaraja, V., Caruso, S., Bui, T.H., Roberts, M.P., Voute, F., Hagemann, S., Wacey, D., Littman, S., Wing, B., Fiorentini, M. and Kilburn, M.R. 2016. In situ multiple sulfur isotope analysis by SIMS of pyrite, chalcopyrite, pyrrhotite, and pentlandite to refine magmatic ore genetic models. Chemical Geology, 444, 1–15.

Lambert, D.D., Foster, J.G., Frick, L.R., Ripley, E.M. and Zientek, M.L. 1998. Geodynamics of magmatic Cu-Ni-PGE sulfide deposits; new insights from the Re-Os isotope system. Economic Geology, 93, 121–136.

Lange, R.A. and Carmichael, I.S.E. 1987. Densities of Na_2O-K_2O-CaO-MgO-FeO-Fe2O3-Al2O3-TiO2-SiO2 liquids: New measurements and derived partial molar properties. Geochimica et Cosmochimica Acta, 51, 2931–2946.

Latsky, R. 1942. The magmatic copper ores of Namaqualand. Transactions of the Geological Society of South Africa, 45, 109–150.

Li, C. 2017. The origin of high Cu/S sulfides in the Skaergaard Intrusion, East Greenland. Duke University, 18pp.

Li, Z.X., Bogdanova, S. V., Collins, A.S., Davidson, A., De Waele, B., Ernst, R.E., Fitzsimons, I.C.W., Fuck, R.A., Gladkochub, D.P., Jacobs, J., Karlstrom, K.E., Lu, S., Natapov, L.M., Pease, V., Pisarevsky, S.A., Thrane, K. and Vernikovsky, V. 2008. Assembly, configuration, and break-up history of Rodinia: A synthesis. Precambrian Research, 160, 179–210.

Li, C. and Naldrett, A.J. 1993. Sulfide capacity of magma; a quantitative model and its application to the formation of sulfide ores at Sudbury, Ontario. Economic Geology, 88, 1253–1260.

Liu, Y. and Brenan, J. 2015. Partitioning of platinum-group elements (PGE) and chalcogens (Se, Te, As, Sb, Bi) between monosulfide-solid solution (MSS), intermediate solid solution (ISS) and sulfide liquid at controlled fO_2–fS_2 conditions. Geochimica et Cosmochimica Acta, 159, 139–161.

Lombaard, A.F., and the Exploration Department staff of the O'okiep Copper Company Limited 1986. Mineral deposits of Southern Africa. Johannesburg, Geological Society of South Africa, 1421–1445pp.

Lombaard, A.F. and Schreuder, F.J.G. 1978. Distribution pattern and general geological features of steep structures, megabreccias and basic rocks in the Okiep Copper District. In: W.J. Verwoerd (Editor) Mineralization in Metamorphic Terranes. Geological Society of South Africa Special Publication, 4, 522–523.

Longerich, H.P., Jackson, S.E. and Günther, D. 1996. Laser Ablation Inductively Coupled Plasma Mass Spectrometric transient signal data acquisition and analyte concentration calculation. Journal of Analytical Atomic Spectrometry, 11, 899–904.

Longhi, J. 2005. A mantle or mafic crustal source for Proterozoic anorthosites? Lithos, 83, 183–198.

Longhi, J., Vander Auwera, J., Fram, M.S. and Duchesne, J.C. 1999. Some phase equilibrium constraints on the origin of Proterozoic (massif) anorthosites and related rocks. Journal of Petrology, 40, 339–362.

Lorand, J.-P. and Alard, O. 2010. Determination of selenium and tellurium concentrations in Pyrenean peridotites (Ariege, France): New insight into S/Se/Te systematics of the upper in mantle samples. Chemical Geology, 278, 120–130.

Lorand, J.-P., Alard, O., Luguet, A. and Keays, R.R. 2003. Sulfur and selenium systematics of the subcontinental lithospheric mantle: Inferences from the Massif Central xenolith suite (France). Geochimica et Cosmochimica Acta, 67, 4137–4151.

Macey, P.H., Bailie, R.H., Miller, J.A., Thomas, R.J., de Beer, C., Frei, D. and le Roux, P.J. 2018. Implications of the distribution, age and origins of the granites of the Mesoproterozoic Spektakel Suite for the timing of the Namaqua Orogeny in the Bushmanland Subprovince of the Namaqua-Natal Metamorphic Province, South Africa. Precambrian Research, 312, 68–98.

Macey, P.H., Thomas, R.J., Minnaar, H.M., Gresse, P.G., Lambert, C.W., Groenewald, C.A., Miller, J.A., Indongo, J., Angombe, M., Shifotoka, G., Frei, D., Diener, J.F.A., Kisters, A.F.M., Dhansay, T., Smith, H., Doggart, S., Le Roux, P., Hartnady, M.I. and Tinguely, C. 2017. Origin and evolution of the ~1.9 Ga Richtersveld Magmatic Arc, SW Africa. Precambrian Research, 292, 417–451.

Macnamara, J. and Thode, H.G. 1950. Comparison of the Isotopic Constitution of Terrestrial and Meteoritic Sulfur. Phys. Rev., 78, 307–308.

Maier, W.D. 2000. Platinum-group elements in Cu-sulphide ores at Carolusberg and East Okiep, Namaqualand, South Africa. Mineralium Deposita, 35, 422–429.

Maier, W.D., Andreoli, M.A.G., Groves, D.I. and Barnes, S.-J. 2012. Petrogenesis of Cu-Ni sulphide ores from O'okiep and Kliprand, Namaqualand, South Africa: Constraints from chalcophile metal contents. South African Journal of Geology, 115, 499–514.

Maier, W.D. and Barnes, S.J. 1996. Unusually high concentrations of magnetite at Caraíba and other Cu-sulfide deposits in the Curaçá Valley, Bahia, Brazil. The Canadian Mineralogist, 34, 717–731.

Maier, W.D. and Barnes, S.J. 1999. The origin of Cu sulfide deposits in the Curaçá Valley, Bahia, Brazil: Evidence from Cu, Ni, Se, and platinum-group element concentrations. Economic Geology, 94, 165–183.

Le Maitre, R.W., Streckeisen, A., Zanettin, B., Le Bas, M.J., Bonin, B. and Bateman, P. (eds.) 2002. Igneous Rocks: A Classification and Glossary of Terms. Cambridge, Cambridge University Press, 3–6, 21–27pp.

Mansur, E.T., Barnes, S.-J. and Duran, C.J. 2021. An overview of chalcophile element contents of pyrrhotite, pentlandite, chalcopyrite, and pyrite from magmatic Ni-Cu-PGE sulfide deposits. Mineralium Deposita, 56, 179–204.

Mao, Y.-J., Dash, B., Qin, K.-Z., Bujinlkham, B. and Tang, D.-M. 2018. Comparisons among the Oortsog, Dulaan, and Nomgon mafic-ultramafic intrusions in central Mongolia and Ni-Cu deposits in NW China: implications for economic Ni-Cu-PGE ore exploration in central Mongolia. Russian Geology and Geophysics, 59, 1–18.

Marais, J.A.H. and Joubert, P. 1980. Little Namaqualand Suite. In: L.E. Kent (Editor) Stratigraphy of South Africa. Geological Survey of South Africa Handbook 8 (Part 1), 294–299.

Marfin, A.E., Ivanov, A. V., Abramova, V.D., Anziferova, T.N., Radomskaya, T.A., Yakich, T.Y. and Bestemianova, K. V. 2020. A trace element classification tree for chalcopyrite from Oktyabrsk deposit, Norilsk–Talnakh Ore District, Russia: LA-ICPMS study. Minerals, 10, 1–15.

Mavrogenes, J.A. and O'Neill, H.S.. 1999. The relative effects of pressure, temperature and oxygen fugacity on the solubility of sulfide in mafic magmas. Geochimica et Cosmochimica Acta, 63, 1173–1180.

McIver, J.R., McCarthy, T.S. and Packham, B. de V. 1983. The copper-bearing basic rocks of Namaqualand, South Africa. Mineralium Deposita, 18, 135–160.

McKinney, C.R., McCrea, J.M., Epstein, S., Allen, H.A. and Urey, H.C. 1950. Improvements in mass spectrometers for the measurement of small differences in isotope abundance ratios. The Review of Scientific Instruments, 21, 724–730.

Miller, R.M. 2012. Review of Mesoproterozoic magmatism, sedimentation and terrane amalgamation in southwestern Africa. South African Journal of Geology, 115, 417–448.

Mungall, J.E. 2005. Magmatic Geochemistry of the PGE. In: J.E. Mungall (Editor) Exploration for Platinum-Group Elements deposits. Mineralogical Association of Canada, Short Course Series, 35, 1–34.

Mungall, J.E., Andrews, D.R.A., Cabri, L.J., Sylvester, P.J. and Tubrett, M. 2005. Partitioning of Cu, Ni, Au, and platinum-group elements between monosulfide solid solution and sulfide melt under controlled oxygen and sulfur fugacities. Geochimica et Cosmochimica Acta, 69, 4349–4360.

Mungall, J.E. and Su, S. 2005. Interfacial tension between magmatic sulfide and silicate liquids: Constraints on kinetics of sulfide liquation and sulfide migration through silicate rocks. 234, 135–149.

Naldrett, A.J. 2004. Magmatic Sulfide Deposits: Geology, Geochemistry and Exploration. Berlin, Heidelberg, Springer Berlin Heidelberg, 17,26,56pp.

Naldrett, A.J., Ebel, D.S., Asif, M., Morrison, G. and Moore, C.M. 1997. Fractional crystallisation of sulfide melts as illustrated at Noril'sk and Sudbury. European Journal of Mineralogy, 9, 365–378.

Nke, A.Y., Bailie, R.H., Macey, P.H., Thomas, R.J., Frei, D., Le Roux, P. and Spencer, C.J. 2020. The 1.8 Ga Gladkop Suite: The youngest Palaeoproterozoic domain in the Namaqua-Natal Metamorphic Province, South Africa. Precambrian Research, 350, 105941.

O'Neil, J.R. 1986. Theoretical and experimental aspects of isotopic fractionation. Reviews in Mineralogy and Geochemistry, 16, 1–40.

Ohmoto, H. 1986. Stable isotope geochemistry of ore deposits. In: J.W. Valley, H.P. Taylor and J.R. O'Neil (Editors) Stable Isotopes in High Temperature Geological Processes. 491–559.

Ohmoto, H. and Rye, R.O. 1979. Carbon and sulfur isotopes. In: A.L. Barnes (Editor) Geochemistry of Hydrothermal Ore Deposits. Wiley-Interscience, 509–567.

Orion Minerals 2021a. Multiple priority EM targets identified from recently completed Airborne Electromagnetic survey at the Okiep Copper Project.

Orion Minerals 2021b. Exploration ramps up at the Okiep Copper Project following exercise of Option to Purchase., 1–28pp.

Orion Minerals 2021c. Orion set to fast-track exploration and evaluation of the Okiep copper district after securing major database., 1–5pp.

Orion Minerals 2021d. Orion identifies four shallow, high-priority drill targets close to existing Mineral Resources at the Okiep Copper Complex.

Peters, M., Strauss, H., Farquhar, J., Ockert, C., Eickmann, B. and Jost, C.L. 2010. Sulfur cycling at the Mid-Atlantic Ridge: A multiple sulfur isotope approach. Chemical Geology, 269, 180–196.

Pettersson, Å., Cornell, D.H., Moen, H.F.G., Reddy, S. and Evans, D. 2007. Ion-probe dating of 1.2 Ga collision and crustal architecture in the Namaqua-Natal Province of southern Africa. Precambrian Research, 158, 79–92.

Piña, R., Gervilla, F., Ortega, L. and Lunar, R. 2008. Mineralogy and geochemistry of platinum-group elements in the Aguablanca Ni-Cu deposit (SW Spain). Mineralogy and Petrology, 92, 259–282.

Potgieter, J.E. 1996. Exploration in the Okiep Copper District, Northern Cape Province, South Africa : an overview. South African Journal of Geology, 99, 209–220.

Queffurus, M. and Barnes, S. 2015. A review of sulfur to selenium ratios in magmatic nickel-copper and platinum-group element deposits. Ore Geology Reviews, 69, 301–324.

Raghavan, V. 2004. Cu-Fe-S (Copper-Iron-Sulfur). Journal of Phase Equilibria & Diffusion, 25, 450–454.

Raith, J.G. 1995. Petrogenesis of the Concordia Granite Gneiss and its relation to W–Mo mineralization in western Namaqualand, South Africa. Precambrian Research, 70, 303–335.

Raith, J.G., Cornell, D.H., Frimmel, H.E. and De Beer, C.H. 2003. New insights into the geology of the Namaqua Tectonic Province, South Africa, from ion probe dating of detrital and metamorphic zircon. Journal of Geology, 111, 347–366.

Raith, J.G. and Harley, S.L. 1998. Low-P/high-T metamorphism in the Okiep Copper District, western Namaqualand, South Africa. Journal of Metamorphic Geology, 16, 281–305.

Raith, J.G. and Prochaska, W. 1995. Tungsten deposits in the Wolfram schist, Namaqualand, South Africa: strata-bound versus granite-related genetic concepts. Economic Geology, 90, 1934–1954.

Reid, D.L. 1997. Sm-Nd age and REE geochemistry of Proterozoic arc-related igneous rocks in the Richtersveld Subprovince, Namaqua Mobile Belt, Southern Africa. Journal of African Earth Sciences, 24, 621–633.

Ripley, E.M. and Li, C. 2013. Sulfide Saturation in Mafic Magmas: Is External Sulfur Required for Magmatic Ni-Cu-(PGE) Ore Genesis? Economic Geology, 108, 45–58.

Ripley, E.M., Li, C. and Shin, D. 2002. Paragneiss assimilation in the genesis of magmatic Ni-Cu-Co sulfide mineralization at Voisey's Bay, Labrador: δ 34S, δ 13C, and Se/S evidence. Economic Geology, 97, 1307–1318.

Ripley, E.M., Park, Y., Li, C. and Naldrett, A.J. 1999. Sulfur and oxygen isotopic evidence of country rock contamination in the Voisey's Bay Ni–Cu–Co deposit, Labrador, Canada. Lithos, 47, 53–68.

Robb, L.J., Armstrong, R.A. and Waters, D.J. 1999. The history of granulite-facies metamorphism and crustal growth from single zircon U-Pb geochronology: Namaqualand, South Africa. Journal of Petrology, 40, 1747–1770.

Rudnick, R.L. and Gao, S. 2003. Composition of the Continental Crust. In: H.D. Holland and K.K. Turekian (Editors) Treatise on Geochemistry. Oxford, Pergamon, 1–64.

Sakai, H., Marais, D.J.D., Ueda, A. and Moore, J.G. 1984. Concentrations and isotope ratios of carbon, nitrogen and sulfur in ocean-floor basalts. Geochimica et Cosmochimica Acta, 48, 2433–2441.

Van Schijndel, V., Cornell, D.H., Anczkiewicz, R. and Scherstén, A. 2020. Evidence for Mesoproterozoic collision, deep burial and rapid exhumation of garbenschiefer in the Namaqua Front, South Africa. Geoscience Frontiers, 11, 511–531.

Schoch, A.E. and Conradie, J.A. 1990. Petrochemical and mineralogical relationships in the Koperberg Suite, Namaqualand, South Africa. American Mineralogist, 75, 27–36.

Shapovalova, M., Tolstykh, N., Shelepaev, R. and Kalugin, V. 2020. PGE-Cu-Ni Mineralization of Mafic-Ultramafic Massifs of the Khangai Upland, Western Mongolia. Minerals, 10, 942.

Shima, H. and Naldrett, A.J. 1975. Solubility of sulfur in an ultramafic melt and the relevance of the system Fe-S-O. Economic Geology, 70, 960–967.

Smith, J.W., Holwell, D.A., McDonald, I. and Boyce, A.J. 2016. The application of S isotopes and S/Se ratios in determining ore-forming processes of magmatic Ni-Cu-PGE sulfide deposits: A cautionary case study from the northern Bushveld Complex. Ore Geology Reviews, 73, 148–174.

Söhnge, P.G. 1950. The Nababeep near West Tungsten Mine, South Africa. American Mineralogist, 35, 931–940.

Sossi, P.A., Foden, J.D. and Halverson, G.P. 2012. Redox-controlled iron isotope fractionation during magmatic differentiation: an example from the Red Hill intrusion, S. Tasmania. Contributions to Mineralogy and Petrology, 164, 757–772.

South African Committee for Stratigraphy 1980. Stratigraphy of South Africa. Pretoria, Republic of South Africa Department of Mineral and Energy Affairs

Stumpfl, E.F. 1978. Variations in silicate, oxide and sulphide mineralogy in the Okiep Copper District. In: W.J. Verwoerd (Editor) Mineralization in Metamorphic Terranes. Pretoria, Geological Society of South Africa Special Publication, 4, 349–350.

Stumpfl, E.F., Clifford, T.N., Burger, A.J. and van Zyl, D. 1976. The copper deposits of the O'okiep District, South Africa: New data and concepts. Mineralium Deposita, 11, 46–70.

Thomas, R.J., Macey, P.H., Spencer, C., Dhansay, T., Diener, J.F.A., Lambert, C.W., Frei, D. and Nguno, A. 2016. The Sperrgebiet Domain, Aurus Mountains, SW Namibia: A ~2020–850 Ma window within the Pan-African Gariep Orogen. Precambrian Research, 286, 35–58.

Tischendorf, G., Förster, H.-J., Gottesmann, B. and Rieder, M. 2007. True and brittle micas: composition and solid-solution series. Mineralogical Magazine, 71, 285–320.

de Villiers, J. 2009. The composition and crystal structures of pyrrhotite: a common but poorly understood mineral. In: A Celebration of Technology. Randburg,.

Wager, L.R., Vincent, E.A. and Smales, A.A. 1957. Sulphides in the Skaergaard intrusion, East Greenland. Economic Geology, 52, 855–903.

Waters, D.J. 1986. Metamorphic zonation and thermal history of pelitic gneisses from western Namaqualand, South Africa. Transactions - Geological Society of South Africa, 89, 97–102.

Waters, D.. J. 1989. Metamorphic evidence for the heating and cooling path of Namaqualand granulites. In: J.S. Daly, R.A. Cliff and W.D. Yardley (Editors) Evolution of Metamorphic Belts. London, Geological Society Special Publication, vol. 43, 357–363.

Watkeys, M.K. 1996. The Klondike steep structure, Okiep Copper District, South Africa. South African Journal of Geology, 99, 169–183.

Wendlandt, R.F. 1982. Sulfide saturation of basalt and andesite melts at high pressures and temperatures. American Mineralogist, 67, 877–855.

Wernette, B., Li, P. and Boudreau, A. 2020. Sulfides, native metals, and associated trace minerals of the Skaergaard intrusion, Greenland: evidence for late hydrothermal fluids. Mineralium Deposita, 55, 1197–1214.

Whitney, D.L. and Evans, B.W. 2010. Abbreviations for names of rock-forming minerals. American Mineralogist, 95, 185–187.

Winter, J.D. 2014. Principles of Igneous and Metamorphic Petrology. New York, Pearson, 195–198pp.

Wohlgemuth-Ueberwasser, C.C., Fonseca, R.O.C., Ballhaus, C. and Berndt, J. 2013. Sulfide oxidation as a process for the formation of copper-rich magmatic sulfides. Mineralium Deposita, 48, 115–127.

Wooster, M.J., Wright, R., Blake, S. and Rothery, D.A. 1997. Cooling mechanisms and an approximate thermal budget for the 1991-1993 Mount Etna lava flow. Geophysical Research Letters, 24, 3277–3280.

Xia, F., Pring, A. and Brugger, J. 2012. Understanding the mechanism and kinetics of pentlandite oxidation in extractive pyrometallurgy of nickel. Minerals Engineering, 27–28, 11–19.

Yamamoto, M. 1976. Relationship between Se/S and sulfur isotope ratios of hydrothermal sulfide minerals. Mineralium Deposita, 11, 197–209.

Yuhara, M., Miyazaki, T., Ishioka, J., Suzuki, S., Kagami, H. and Tsuchiya, N. 2002. Rb-Sr and Sm-Nd Mineral Isochron Ages of the Metamorphic Rocks in the Namaqualand Metamorphic Complex, South Africa. Gondwana Research, 5, 771–779.

Yund, R.A. and Kullerud, G. 1966. Thermal Stability of Assemblages in the Cu—Fe—S System. Journal of Petrology, 7, 454–488.

Zhao, Y., Xue, C., Liu, S.-A., Mathur, R., Zhao, X., Yang, Y., Dai, J., Man, R. and Liu, X. 2019. Redox reactions control Cu and Fe isotope fractionation in a magmatic Ni–Cu mineralization system. Geochimica et Cosmochimica Acta, 249, 42–58.

Zhao, Y., Xue, C., Liu, S.-A., Symons, D.T.A., Zhao, X., Yang, Y. and Ke, J. 2017. Copper isotope fractionation during sulfide-magma differentiation in the Tulaergen magmatic Ni–Cu deposit, NW China. Lithos, 286–287, 206–215.

Zientek, M.L., Likhachev, A.P., Kunilov, V.E., Barnes, S.J., Meier, A.L., Carlson, R.., Briggs, P.H., Fries, T.L. and Adrian, B.M. 1994. Cumulus processes and the composition of magmatic ore deposits: Examples from the Talnakh district, Russia. Ontario Geological Survey Special Publication 5, 373–392.

van Zwieten, A.J.M. 1996. The petrogenesis of the Koperberg Suite in the Jubilee Mine, Namaqualand. University of the Witwatersrand, Johannesburg, 21pp.

van Zwieten, A.J.M., McCarthy, T.S. and Cawthorn, R.G. 1996. A petrogenetic model for the Koperberg Suite: Evidence from the Jubilee Mine, Namaqualand, South Africa. South African Journal of Geology, 99, 121–134.

van Zyl, D. 1978. A petrological approach towards the ore-bearing potentialities of the Okiep basic intrusives in Namaqualand. In: W.J. Verwoed (Editor) Mineralization in Metamorphic Terranes. Geological Society of South Africa, Special Publication 4, 323–329.

Appendix

Appendix 1: EDS analyses for silicates, oxides, and phosphates

Table A1. EDS analyses for garnet compositions and endmember proportions

Sample	039T-1A3	039T-1A3	039T-1A3	039T-1A3	039T-1A4	039T-1A4	039T-1A4	039T-1B1	039T-1B1	039T-1B3	039T-1B3	039T-1B3
Analysis	1 (KS)	2 (KS)	3 (KS)	4 (KS)	5 (KS)	6 (KS)	7 (KS)	8 (KS)	9 (KS)	10 (KS)	11 (KS)	12 (KS)
SiO_2	39.37	39.07	38.98	37.83	38.74	39.09	39.33	40.58	39.89	39.46	40.13	40.01
TiO_2	0.00	0.02	0.03	0.05	0.00	0.00	0.00	0.00	0.00	0.02	0.11	0.01
Al_2O_3	19.65	19.54	20.26	19.61	19.59	19.99	18.80	19.79	19.60	19.95	19.54	19.50
Cr_2O_3	0.00	0.00	0.05	0.08	0.03	0.07	0.00	0.07	0.00	0.00	0.00	0.00
FeO	35.40	35.99	35.02	36.21	34.98	34.67	35.40	29.39	32.06	32.55	32.74	32.49
Fe_2O_3	0.00	0.00	0.00	0.67	0.61	0.00	0.67	0.00	0.00	0.00	0.00	0.00
MgO	4.42	3.95	4.41	4.24	4.70	5.04	4.37	6.81	4.77	5.77	5.20	5.57
CaO	0.87	0.94	0.92	0.89	0.93	0.89	0.97	1.00	0.89	0.90	0.89	0.92
MnO	0.29	0.49	0.33	0.41	0.42	0.24	0.45	2.38	2.79	1.35	1.38	1.49
Total	100.00	100.00	100.00	100.00	100.00	100.00	100.00	100.00	100.00	100.00	100.00	100.00
Cations based on 12 Oxygens												
Si	3.13	3.12	3.10	3.04	3.09	3.10	3.14	3.16	3.16	3.11	3.16	3.15
Ti	0.00	0.00	0.00	0.00	0.00	0.00	0.00	0.00	0.00	0.00	0.01	0.00
Al	1.84	1.84	1.90	1.86	1.84	1.87	1.77	1.82	1.83	1.85	1.82	1.81
Cr	0.00	0.00	0.00	0.01	0.00	0.00	0.00	0.00	0.00	0.00	0.00	0.00
Fe^{2+}	2.36	2.41	2.33	2.44	2.33	2.30	2.37	1.91	2.12	2.15	2.16	2.14
Fe^{3+}	0.00	0.00	0.00	0.04	0.04	0.00	0.04	0.00	0.00	0.00	0.00	0.00
Mg	0.52	0.47	0.52	0.51	0.56	0.60	0.52	0.79	0.56	0.68	0.61	0.65
Ca	0.07	0.08	0.08	0.08	0.08	0.08	0.08	0.08	0.08	0.08	0.08	0.08
Mn	0.02	0.03	0.02	0.03	0.03	0.02	0.03	0.16	0.19	0.09	0.09	0.10
Total	7.95	7.96	7.95	8.00	7.97	7.96	7.95	7.93	7.93	7.96	7.92	7.94
Endmember proportions												
X_{Alm}	0.79	0.80	0.78	0.80	0.78	0.77	0.79	0.65	0.72	0.71	0.72	0.70
X_{Prp}	0.18	0.16	0.18	0.17	0.19	0.20	0.17	0.27	0.19	0.24	0.22	0.23
X_{Grs}	0.02	0.03	0.03	0.00	0.01	0.02	0.01	0.03	0.03	0.03	0.03	0.03
X_{Adr}	0.00	0.00	0.00	0.04	0.02	0.00	0.02	0.00	0.00	0.00	0.00	0.00
X_{Sps}	0.01	0.01	0.01	0.01	0.01	0.01	0.01	0.05	0.06	0.03	0.03	0.04
X_{Uv}	0.00	0.00	0.00	0.00	0.00	0.00	0.00	0.00	0.00	0.00	0.00	0.00

All oxide values are in wt%. KS: Khurisberg Subgroup

Table A2. EDS results for K-feldspar compositions and endmember proportions

Sample	039T-1B1	039T-1B3	039T-1B3	DSQ 3B2	DSQ 3B2	016T-3A	016T-3C
Analysis	1 (KS)	2 (KS)	3 (KS)	4 (KSQ)	5(KSQ)	6 (KNb)	7 (KNb)
SiO_2	67.26	66.83	67.39	65.87	66.38	67.14	67.12
Al_2O_3	17.63	17.67	17.16	17.74	17.37	16.78	17.11
TiO_2	0.15	0.02	0.10	0.16	0.26	0.05	0.16
FeO	0.10	0.12	0.03	0.00	0.03	0.02	0.05
MgO	0.04	0.00	0.00	0.05	0.00	0.06	0.00
MnO	0.00	0.00	0.00	0.00	0.00	0.02	0.00
CaO	0.09	0.13	0.04	0.07	0.52	0.02	0.05
Na_2O	2.14	1.61	0.96	0.44	0.28	0.45	0.25
K_2O	12.60	13.63	14.32	15.67	15.16	15.46	15.26
Total	100.00	100.00	100.00	100.00	100.00	100.00	100.00
Cations based on 8 Oxygens							
Si	3.05	3.05	3.07	3.03	3.05	3.08	3.07
Al	0.94	0.95	0.92	0.96	0.94	0.91	0.92
Ti	0.00	0.00	0.00	0.01	0.01	0.00	0.01
Fe^{2+}	0.00	0.00	0.00	0.00	0.00	0.00	0.00
Mg	0.00	0.00	0.00	0.00	0.00	0.00	0.00
Mn	0.00	0.00	0.00	0.00	0.00	0.00	0.00
Ca	0.00	0.01	0.00	0.00	0.03	0.00	0.00
Na	0.19	0.14	0.09	0.04	0.02	0.04	0.02
K	0.73	0.79	0.83	0.92	0.89	0.90	0.89
Total	4.91	4.94	4.91	4.96	4.94	4.93	4.91
End-members proportions							
Or	0.79	0.84	0.90	0.96	0.95	0.96	0.98
Ab	0.21	0.15	0.10	0.04	0.02	0.04	0.02
An	0.00	0.01	0.00	0.00	0.03	0.00	0.00

All oxide values are in wt%. KS: Khurisberg Subgroup, KNb: Koperberg Suite from Nababeep Mine, KSQ: Koperberg Suite from Sugarloaf Quarry.

Table A3. EDS results for plagioclase compositions and endmember proportions

Sample	039T-1B1	039T-1B1	016T-3A	016T-3A	016T-3A	016T-3C	016T-3C	039T-4A	039T-4A	039T-4A	039T-4A	DSQ 3B2	DSQ 3B2	DSQ 3D1	DSQ 3D1	DSQ 3D1	KNU 477A	KNU 477A
Analysis	1 (KS)	2 (KS)	3 (KNb)	4 (KNb)	5 (KNb)	6 (KNb)	7 (KNb)	8 (KNb)	9 (KNb)	10 (KNb)	11 (KNb)	12 (KSQ)	13 (KSQ)	14 (KSQ)	15 (KSQ)	16 (KSQ)	17 (KNg)	18 (KNg)
SiO_2	62.43	62.68	60.04	58.44	55.74	59.56	60.24	59.59	59.40	59.33	59.26	58.08	56.78	57.57	57.56	57.75	56.32	58.05
Al_2O_3	23.81	23.68	25.13	26.10	27.75	25.72	25.04	25.67	25.95	25.82	25.75	26.77	27.26	26.60	26.80	26.53	28.05	26.03
TiO_2	0.05	0.00	0.01	0.12	0.04	0.04	0.00	0.00	0.00	0.04	0.06	0.00	0.00	0.00	0.02	0.02	0.13	0.00
FeO	0.10	0.03	0.21	0.15	0.07	0.11	0.20	0.00	0.16	0.30	0.09	0.07	0.17	0.18	0.10	0.18	0.14	0.57
MgO	0.00	0.00	0.00	0.00	0.00	0.00	0.00	0.00	0.07	0.08	0.00	0.00	0.00	0.00	0.00	0.00	0.00	0.45
MnO	0.01	0.00	0.06	0.02	0.13	0.00	0.01	0.00	0.00	0.00	0.05	0.05	0.03	0.00	0.03	0.01	0.02	0.00
CaO	6.83	6.70	8.41	9.85	11.76	8.64	8.49	9.30	9.26	9.52	8.99	9.82	10.87	10.43	10.33	10.41	10.58	9.29
Na_2O	6.58	6.72	5.82	5.27	4.42	5.69	5.80	5.33	5.09	4.87	5.72	4.94	4.56	4.88	4.83	4.81	4.66	5.08
K_2O	0.20	0.19	0.32	0.06	0.08	0.25	0.23	0.10	0.07	0.04	0.07	0.26	0.33	0.34	0.33	0.29	0.10	0.53
Total	100.00	100.00	100.00	100.00	100.00	100.00	100.00	100.00	100.00	100.00	100.00	100.00	100.00	100.00	100.00	100.00	100.00	100.00
Cations based on 8 Oxygens																		
Si	2.76	2.77	2.67	2.61	2.51	2.65	2.68	2.65	2.64	2.64	2.64	2.60	2.55	2.58	2.58	2.59	2.53	2.60
Al	1.24	1.23	1.32	1.37	1.47	1.35	1.31	1.35	1.36	1.36	1.35	1.41	1.44	1.41	1.42	1.40	1.48	1.37
Ti	0.00	0.00	0.00	0.00	0.00	0.00	0.00	0.00	0.00	0.00	0.00	0.00	0.00	0.00	0.00	0.00	0.00	0.00
Fe^{2+}	0.00	0.00	0.01	0.01	0.00	0.00	0.01	0.00	0.01	0.01	0.00	0.00	0.01	0.01	0.00	0.01	0.00	0.02
Mg	0.00	0.00	0.00	0.00	0.00	0.00	0.00	0.00	0.00	0.00	0.00	0.00	0.00	0.00	0.00	0.00	0.00	0.03
Mn	0.00	0.00	0.00	0.00	0.00	0.00	0.00	0.00	0.00	0.00	0.00	0.00	0.00	0.00	0.00	0.00	0.00	0.00
Ca	0.32	0.32	0.40	0.47	0.57	0.41	0.40	0.44	0.44	0.45	0.43	0.47	0.52	0.50	0.50	0.50	0.51	0.45
Na	0.56	0.58	0.50	0.46	0.39	0.49	0.50	0.46	0.44	0.42	0.49	0.43	0.40	0.42	0.42	0.42	0.40	0.44
K	0.01	0.01	0.02	0.00	0.00	0.01	0.01	0.01	0.00	0.00	0.00	0.01	0.02	0.02	0.02	0.02	0.01	0.03
Total	4.89	4.91	4.92	4.92	4.94	4.91	4.91	4.91	4.89	4.88	4.91	4.92	4.94	4.94	4.94	4.94	4.93	4.94
End-member proportions																		
An	0.36	0.35	0.43	0.51	0.59	0.45	0.44	0.48	0.50	0.52	0.47	0.52	0.55	0.53	0.53	0.53	0.55	0.49
Ab	0.63	0.64	0.54	0.49	0.41	0.54	0.55	0.51	0.50	0.48	0.53	0.47	0.43	0.45	0.45	0.45	0.43	0.48
Or	0.01	0.01	0.02	0.00	0.00	0.01	0.01	0.01	0.00	0.00	0.00	0.01	0.02	0.02	0.02	0.02	0.01	0.03

All oxide values are in wt%. KS: Khurisberg Subgroup, KNb: Koperberg Suite from Nababeep Mine, KNg: Koperberg Suite from Nigramoep Mine, KSQ: Koperberg Suite from Sugarloaf Quarry.

Table A4. EDS results for biotite compositions

Sample	039T-1A3	039T-1A3	039T-1A4	039T-1A4	039T-1A4	039T-1A4	039T-1B1	039T-1B1	039T-1B1	039T-1B1	039T-1B1	039T-1B1	039T-1B3	039T-1B3
Analysis	**1 (KS)**	**2 (KS)**	**3 (KS)**	**4 (KS)**	**5 (KS)**	**6 (KS)**	**7 (KS)**	**8 (KS)**	**9 (KS)**	**10 (KS)**	**11 (KS)**	**12 (KS)**	**13 (KS)**	**14 (KS)**
SiO_2	38.86	38.62	37.34	37.51	36.98	38.13	39.25	37.66	38.90	42.39	39.17	38.49	38.87	39.67
Al_2O_3	14.61	14.80	14.90	14.35	16.32	14.71	15.30	13.71	14.34	24.64	19.03	19.11	14.66	15.02
Fe_2O_3	0.00	0.00	0.00	0.00	0.59	0.00	0.00	0.00	0.00	0.00	0.00	0.00	0.00	0.00
Cr_2O_3	0.09	0.02	0.10	0.00	0.12	0.00	0.11	0.10	0.05	0.00	0.74	0.95	0.10	0.04
TiO_2	3.84	3.45	3.22	5.81	2.14	4.52	4.29	4.98	4.08	0.15	0.35	0.73	3.24	3.27
FeO	13.88	15.93	18.54	16.95	19.24	18.21	10.87	15.01	14.22	10.75	14.08	15.94	15.02	10.52
MgO	14.11	13.33	12.17	11.79	12.95	10.78	15.62	13.54	13.94	8.47	13.93	11.40	13.73	16.79
MnO	0.00	0.00	0.01	0.06	0.00	0.10	0.03	0.00	0.08	0.13	0.00	0.02	0.00	0.10
CaO	0.01	0.01	0.00	0.00	0.06	0.08	0.09	0.04	0.03	0.07	0.11	0.00	0.06	0.06
NiO	0.07	0.03	0.00	0.00	0.05	0.00	0.00	0.20	0.04	0.00	0.00	0.00	0.02	0.04
Na_2O	0.19	0.30	0.32	0.37	0.33	0.31	0.32	0.26	0.08	0.15	0.16	0.17	0.20	0.31
K_2O	10.01	9.24	9.10	8.82	7.21	9.18	9.99	10.36	10.19	8.89	8.31	9.09	10.05	10.03
BaO	0.25	0.21	0.31	0.32	0.00	0.00	0.02	0.13	0.00	0.09	0.00	0.02	0.00	0.00
H_2O	4.06	4.04	3.98	4.00	4.02	4.00	4.13	4.00	4.05	4.28	4.13	4.07	4.05	4.14
Total	100.00	100.00	100.00	100.00	100.00	100.00	100.00	100.00	100.00	100.00	100.00	100.00	100.00	100.00
Cations based on 11 Oxygens														
Si	2.87	2.87	2.82	2.81	2.76	2.86	2.85	2.82	2.88	2.99	2.85	2.84	2.88	2.88
Al IV	1.13	1.13	1.18	1.19	1.24	1.14	1.15	1.18	1.12	1.01	1.15	1.16	1.12	1.12
Al (VI)	0.15	0.16	0.14	0.07	0.20	0.16	0.17	0.03	0.13	1.03	0.47	0.50	0.16	0.16
Fe^{3+}	0.00	0.00	0.00	0.00	0.03	0.00	0.00	0.00	0.00	0.00	0.00	0.00	0.00	0.00
Cr	0.00	0.00	0.01	0.00	0.01	0.00	0.01	0.01	0.00	0.00	0.04	0.05	0.00	0.00
Ti	0.21	0.19	0.18	0.33	0.12	0.25	0.23	0.28	0.23	0.01	0.02	0.04	0.18	0.18
Fe^{2+}	0.86	0.99	1.17	1.06	1.20	1.14	0.66	0.94	0.88	0.63	0.85	0.98	0.93	0.64
Mg	1.55	1.48	1.37	1.31	1.44	1.21	1.69	1.51	1.54	0.89	1.51	1.25	1.52	1.82
Mn	0.00	0.00	0.00	0.00	0.00	0.01	0.00	0.00	0.00	0.01	0.00	0.00	0.00	0.01
Ca	0.00	0.00	0.00	0.00	0.00	0.01	0.01	0.00	0.00	0.00	0.01	0.00	0.00	0.00
Ni	0.00	0.00	0.00	0.00	0.00	0.00	0.00	0.01	0.00	0.00	0.00	0.00	0.00	0.00
Na	0.03	0.04	0.05	0.05	0.05	0.04	0.04	0.04	0.01	0.02	0.02	0.02	0.03	0.04
K	0.94	0.88	0.88	0.84	0.69	0.88	0.93	0.99	0.96	0.80	0.77	0.86	0.95	0.93
Ba	0.01	0.01	0.01	0.01	0.00	0.00	0.00	0.00	0.00	0.00	0.00	0.00	0.00	0.00
OH	2.00	2.00	2.00	2.00	2.00	2.00	2.00	2.00	2.00	2.00	2.00	2.00	2.00	2.00
Total	9.76	9.75	9.80	9.68	9.75	9.70	9.74	9.80	9.75	9.40	9.69	9.71	9.79	9.79
Anions														
OH/F	2.00	2.00	2.00	2.00	2.00	2.00	2.00	2.00	2.00	2.00	2.00	2.00	2.00	2.00
X_{Mg}	0.64	0.60	0.54	0.55	0.55	0.51	0.72	0.62	0.64	0.58	0.64	0.56	0.62	0.74

Table A4 *(continued)*

Sample	039T-1B3	016T-3A	016T-3C	016T-3C	039T-4A	039T-4A	039T-4A	039T-4B	039T-4B	DSQ 3B2	DSQ 3D1	DSQ 3D1	KNU 477A
Analysis	**15 (KS)**	**16 (KNb)**	**17 (KNb)**	**18 (KNb)**	**19 (KNb)**	**20 (KNb)**	**21 (KNb)**	**22 (KNb)**	**23 (KNb)**	**24 (KSQ)**	**25 (KSQ)**	**26 (KSQ)**	**27 (KNg)**
SiO_2	39.73	38.75	39.35	40.06	39.74	39.78	38.84	39.30	39.19	38.59	38.23	38.68	38.76
Al_2O_3	15.24	15.36	14.58	15.29	13.97	13.40	14.21	13.63	13.46	13.87	13.29	13.27	13.70
Fe_2O_3	0.00	0.00	0.00	0.00	0.00	0.00	0.00	0.00	0.00	0.00	0.00	0.00	0.00
Cr_2O_3	0.09	0.03	0.11	0.07	0.14	0.14	0.05	0.06	0.04	0.08	0.04	0.06	0.19
TiO_2	4.00	3.17	4.40	1.37	2.01	3.23	2.64	3.94	3.17	4.89	5.64	5.07	4.86
FeO	9.69	16.54	14.72	12.14	15.68	12.34	16.46	14.73	16.40	13.37	14.14	14.13	11.18
MgO	16.70	11.34	12.83	17.36	13.96	16.44	14.12	13.87	13.29	15.06	14.05	14.39	15.93
MnO	0.04	0.69	0.29	0.31	0.29	0.09	0.19	0.23	0.15	0.02	0.06	0.07	0.15
CaO	0.02	0.25	0.39	0.10	0.07	0.00	0.08	0.00	0.07	0.14	0.03	0.05	0.05
NiO	0.05	0.05	0.13	0.00	0.00	0.08	0.04	0.00	0.06	0.29	0.16	0.09	0.14
Na_2O	0.39	0.23	0.15	0.18	0.16	0.23	0.21	0.23	0.15	0.01	0.16	0.10	0.19
K_2O	9.90	9.27	8.98	8.97	9.62	9.64	8.69	9.77	9.65	9.52	10.05	10.05	9.27
BaO	0.00	0.31	0.00	0.00	0.34	0.54	0.43	0.21	0.35	0.10	0.11	0.00	1.51
H_2O	4.15	4.01	4.07	4.14	4.03	4.08	4.03	4.04	4.01	4.07	4.03	4.05	4.07
Total	100.00	100.00	100.00	100.00	100.00	100.00	100.00	100.00	100.00	100.00	100.00	100.00	100.00
Cations based on 11 Oxygens													
Si	2.87	2.89	2.90	2.91	2.95	2.92	2.89	2.91	2.93	2.84	2.84	2.87	2.86
Al IV	1.13	1.11	1.10	1.09	1.05	1.08	1.11	1.09	1.07	1.16	1.16	1.13	1.14
Al (VI)	0.17	0.25	0.17	0.22	0.18	0.08	0.14	0.10	0.12	0.05	0.01	0.03	0.05
Fe^{3+}	0.00	0.00	0.00	0.00	0.00	0.00	0.00	0.00	0.00	0.00	0.00	0.00	0.00
Cr	0.00	0.00	0.01	0.00	0.01	0.01	0.00	0.00	0.00	0.00	0.00	0.00	0.01
Ti	0.22	0.18	0.24	0.07	0.11	0.18	0.15	0.22	0.18	0.27	0.31	0.28	0.27
Fe^{2+}	0.58	1.03	0.91	0.74	0.97	0.76	1.02	0.91	1.03	0.82	0.88	0.88	0.69
Mg	1.80	1.26	1.41	1.88	1.55	1.80	1.57	1.53	1.48	1.65	1.56	1.59	1.75
Mn	0.00	0.04	0.02	0.02	0.02	0.00	0.01	0.01	0.01	0.00	0.00	0.00	0.01
Ca	0.00	0.02	0.03	0.01	0.00	0.00	0.01	0.00	0.01	0.01	0.00	0.00	0.00
Ni	0.00	0.00	0.01	0.00	0.00	0.00	0.00	0.00	0.00	0.02	0.01	0.00	0.01
Na	0.05	0.03	0.02	0.03	0.02	0.03	0.03	0.03	0.02	0.00	0.02	0.01	0.03
K	0.91	0.88	0.84	0.83	0.91	0.90	0.83	0.92	0.92	0.90	0.95	0.95	0.87
Ba	0.00	0.01	0.00	0.00	0.01	0.01	0.01	0.01	0.01	0.00	0.00	0.00	0.04
OH	2.00	2.00	2.00	2.00	2.00	2.00	2.00	2.00	2.00	2.00	2.00	2.00	2.00
Total	9.74	9.71	9.65	9.79	9.78	9.78	9.77	9.74	9.77	9.73	9.75	9.75	9.72
Anions													
OH/F	2.00	2.00	2.00	2.00	2.00	2.00	2.00	2.00	2.00	2.00	2.00	2.00	2.00
X_{Mg}	0.75	0.55	0.61	0.72	0.61	0.70	0.60	0.63	0.59	0.67	0.64	0.64	0.72

All oxide values are in wt%. KS: Khurisberg Subgroup, KNb: Koperberg Suite from Nababeep Mine, KNg: Koperberg Suite from Nigramoep Mine, and KSQ: Koperberg Suite from Sugarloaf Quarry.

Table A5. EDS results for muscovite compositions

Sample	039T-1A3	039T-1A3	039T-1B3	039T-1B3	016T-3A
Analysis	**1 (KS)**	**2 (KS)**	**3 (KS)**	**4 (KS)**	**5 (KNb)**
SiO_2	51.11	50.62	46.53	47.34	48.91
Al_2O_3	28.26	27.37	28.99	31.26	29.91
Fe_2O_3	0.43	1.75	4.62	3.60	0.58
Cr_2O_3	0.07	0.04	0.04	0.03	0.07
TiO_2	0.00	0.14	0.00	0.07	0.06
FeO	2.62	2.17	0.00	0.00	2.34
MgO	2.09	2.40	4.30	2.30	1.85
MnO	0.00	0.00	0.00	0.00	0.02
CaO	0.00	0.03	0.00	0.00	0.06
NiO	0.03	0.00	0.02	0.03	0.06
Na_2O	0.22	0.27	0.21	0.24	0.18
K_2O	10.51	10.70	10.71	10.44	11.35
BaO	0.17	0.01	0.12	0.19	0.15
H_2O	4.50	4.49	4.46	4.50	4.46
Total	100.00	100.00	100.00	100.00	100.00
Cations based on 11 Oxygens					
Si	3.41	3.39	3.14	3.17	3.28
Al (IV)	0.59	0.61	0.86	0.83	0.72
Al (VI)	1.63	1.55	1.44	1.63	1.65
Fe^{3+}	0.02	0.09	0.23	0.18	0.03
Cr	0.00	0.00	0.00	0.00	0.00
Ti	0.00	0.01	0.00	0.00	0.00
Fe^{2+}	0.15	0.12	0.00	0.00	0.13
Mg	0.21	0.24	0.43	0.23	0.18
Mn	0.00	0.00	0.00	0.00	0.00
Ca	0.00	0.00	0.00	0.00	0.00
Ni	0.00	0.00	0.00	0.00	0.00
Na	0.03	0.03	0.03	0.03	0.02
K	0.89	0.91	0.92	0.89	0.97
Ba	0.00	0.00	0.00	0.00	0.00
OH	2.00	2.00	2.00	2.00	2.00
Total	8.93	8.96	9.06	8.97	9.01
Anions					
OH	2.00	2.00	2.00	2.00	2.00
X_{Mg}	0.59	0.67	1.00	1.00	0.59
$X_{Fe\ (tot)}$	0.45	0.47	0.35	0.44	0.46

All oxide values are in wt%. KS: Khurisberg Subgroup, KNb: Koperberg Suite from Nababeep Mine

Table A6. EDS results for orthopyroxene compositions and end-member proportions

Sample	016T-3C	DSQ 3B2	DSQ 3B2	DSQ 3B2	DSQ 3D1	DSQ 3D1	KNU 477A	KNU 477A	KNU 477A	CD 01A	CD 01A
Analysis	1 (KNb)	2 (KSQ)	3 (KSQ)	4 (KSQ)	5 (KSQ)	6 (KSQ)	7 (KNg)	8 (KNg)	9 (KNg)	10 (KCr)	11 (KCr)
SiO_2	53.47	53.00	52.95	53.94	53.19	53.01	53.38	53.56	53.55	53.30	53.32
Ti_2O_3	0.02	0.00	0.14	0.15	0.10	0.06	0.03	0.07	0.18	0.05	0.05
Al_2O_3	1.94	2.30	2.02	1.83	1.85	2.00	3.09	2.23	1.80	2.45	2.26
Cr_2O_3	0.02	0.00	0.00	0.00	0.04	0.06	0.12	0.11	0.05	0.07	0.02
Fe_2O_3	0.00	0.00	0.00	0.00	0.00	0.00	0.00	0.00	0.00	0.00	0.00
MgO	20.14	19.86	20.23	20.62	20.21	20.29	21.94	22.22	22.65	22.06	21.67
CaO	0.32	0.38	0.46	0.37	0.40	0.43	0.37	0.32	0.35	0.32	0.34
MnO	1.45	0.57	0.52	0.60	0.53	0.59	0.61	0.57	0.59	0.55	0.45
FeO	22.50	23.83	23.52	22.40	23.63	23.45	20.36	20.77	20.74	21.17	21.72
Na_2O	0.15	0.00	0.13	0.09	0.05	0.08	0.04	0.11	0.06	0.04	0.13
K_2O	0.00	0.05	0.03	0.02	0.00	0.03	0.06	0.04	0.03	0.00	0.03
Total	100.00	100.00	100.00	100.00	100.00	100.00	100.00	100.00	100.00	100.00	100.00
Cations based on 6 Oxygens											
Si	1.99	1.98	1.98	2.00	1.99	1.98	1.96	1.98	1.98	1.97	1.97
Ti	0.00	0.00	0.00	0.00	0.00	0.00	0.00	0.00	0.00	0.00	0.00
Al	0.09	0.10	0.09	0.08	0.08	0.09	0.13	0.10	0.08	0.11	0.10
Cr	0.00	0.00	0.00	0.00	0.00	0.00	0.00	0.00	0.00	0.00	0.00
Fe^{3+}	0.00	0.00	0.00	0.00	0.00	0.00	0.00	0.00	0.00	0.00	0.00
Mg	1.12	1.11	1.13	1.14	1.13	1.13	1.20	1.22	1.25	1.21	1.20
Ca	0.01	0.02	0.02	0.01	0.02	0.02	0.01	0.01	0.01	0.01	0.01
Mn	0.05	0.02	0.02	0.02	0.02	0.02	0.02	0.02	0.02	0.02	0.01
Fe^{2+}	0.70	0.74	0.74	0.70	0.74	0.73	0.63	0.64	0.64	0.65	0.67
Na	0.01	0.00	0.01	0.01	0.00	0.01	0.00	0.01	0.00	0.00	0.01
K	0.00	0.00	0.00	0.00	0.00	0.00	0.00	0.00	0.00	0.00	0.00
Total	3.97	3.97	3.99	3.96	3.98	3.98	3.95	3.98	3.98	3.97	3.97
End-member proportions											
En	61.0	59.3	59.9	61.6	59.9	60.1	65.2	65.2	65.6	64.6	63.5
Fs	38.3	39.9	39.1	37.6	39.3	39.0	34.0	34.2	33.7	34.8	35.7
Wo	0.7	0.8	1.0	0.8	0.9	0.9	0.8	0.7	0.7	0.7	0.7

All oxide values are in wt%. KS: Khurisberg Subgroup, KNb: Koperberg Suite from Nababeep Mine, KNg: Koperberg Suite from Nigramoep Mine, KCr: Koperberg Suite from Carolusberg Mine, and KSQ: Koperberg Suite from Sugarloaf Quarry

Table A7. EDS results for ilmenite compositions and end-member proportions

Sample	039T-1B1	039T-1B1	039T-1B1	039T-1B1	039T-1B3	039T-1B3	039T-1B3	039T-1B3	016T-3C	039T-4A	039T-4A	039T-4A	039T-4B	DSQ 3D1	DSQ 3D1	KNU 477A	KNU 477A	CD 01A
Analysis	**1 (KS)**	**2 (KS)**	**3 (KS)**	**4 (KS)**	**5 (KS)**	**6 (KS)**	**7 (KS)**	**8 (KS)**	**9 (KNb)**	**10 (KNb)**	**11 (KNb)**	**12 (KNb)**	**13 (KNb)**	**14 (KSQ)**	**15 (KSQ)**	**16 (KNg)**	**17 (KNg)**	**18 (KCr)**
SiO_2	0.09	0.10	0.07	0.21	0.30	0.07	0.32	0.15	1.60	2.33	4.85	0.07	0.01	3.15	0.00	0.05	0.15	0.04
Al_2O_3	0.03	1.20	0.06	0.11	0.07	0.17	0.22	1.69	6.77	1.26	0.06	0.06	0.09	0.72	0.15	0.53	0.17	0.04
Fe_2O_3	2.37	1.41	2.43	1.42	2.91	2.18	1.56	2.22	8.84	0.00	0.00	4.41	5.38	0.00	3.52	0.00	0.00	6.59
Cr_2O_3	0.00	0.07	0.00	0.09	0.02	0.00	0.00	0.04	0.20	0.11	0.13	0.07	0.00	0.02	0.02	0.10	0.03	0.04
ZrO_2	0.00	0.00	0.00	0.00	0.00	0.00	0.00	0.08	0.05	0.00	0.00	0.00	0.01	0.07	0.00	0.17	0.03	0.17
V_2O_3	0.63	0.75	0.66	0.92	0.73	0.61	0.67	0.51	0.67	0.04	0.38	0.44	0.46	0.50	0.55	0.66	0.41	0.70
TiO_2	51.24	50.96	51.09	51.41	50.40	51.25	51.17	50.11	42.31	53.98	48.94	50.02	49.87	54.19	50.43	57.46	55.40	48.70
FeO	44.45	44.05	44.38	44.49	44.95	44.84	45.29	44.49	33.93	34.74	38.00	38.71	40.02	35.19	42.07	36.20	36.70	41.88
MgO	0.28	0.18	0.15	0.33	0.10	0.24	0.28	0.12	0.00	0.23	0.18	0.03	0.15	0.43	0.01	0.08	0.06	0.16
MnO	0.81	1.12	1.03	0.82	0.40	0.53	0.42	0.53	5.33	5.69	6.33	6.17	3.74	3.56	3.22	4.52	6.78	1.67
CaO	0.00	0.03	0.00	0.01	0.10	0.04	0.00	0.03	0.10	1.41	1.09	0.01	0.05	2.07	0.03	0.01	0.05	0.00
NiO	0.00	0.06	0.06	0.09	0.02	0.00	0.00	0.02	0.09	0.13	0.00	0.00	0.05	0.09	0.00	0.15	0.05	0.00
Na_2O	0.07	0.08	0.08	0.01	0.00	0.06	0.02	0.02	0.09	0.00	0.01	0.00	0.16	0.01	0.00	0.06	0.14	0.02
K_2O	0.03	0.00	0.00	0.10	0.00	0.01	0.05	0.00	0.01	0.07	0.03	0.00	0.00	0.00	0.01	0.00	0.03	0.00
Total	100.00	100.00	100.00	100.00	100.00	100.00	100.00	100.00	100.00	100.00	100.00	100.00	100.00	100.00	100.00	100.00	100.00	100.00
Cations based on 3 Oxygens																		
Si	0.00	0.00	0.00	0.01	0.01	0.00	0.01	0.00	0.04	0.06	0.12	0.00	0.00	0.08	0.00	0.00	0.00	0.00
Al	0.00	0.04	0.00	0.00	0.00	0.00	0.01	0.05	0.19	0.04	0.00	0.00	0.00	0.02	0.00	0.02	0.00	0.00
Fe^{3+}	0.04	0.03	0.05	0.03	0.06	0.04	0.03	0.04	0.16	0.00	0.00	0.08	0.10	0.00	0.07	0.00	0.00	0.13
Cr	0.00	0.00	0.00	0.00	0.00	0.00	0.00	0.00	0.00	0.00	0.00	0.00	0.00	0.00	0.00	0.00	0.00	0.00
Zr	0.00	0.00	0.00	0.00	0.00	0.00	0.00	0.00	0.00	0.00	0.00	0.00	0.00	0.00	0.00	0.00	0.00	0.00
V	0.01	0.01	0.01	0.02	0.01	0.01	0.01	0.01	0.01	0.00	0.01	0.01	0.01	0.01	0.01	0.01	0.01	0.01
Ti	0.97	0.96	0.97	0.97	0.96	0.97	0.97	0.94	0.78	0.98	0.90	0.95	0.95	0.98	0.96	1.05	1.03	0.93
Fe^{2+}	0.94	0.92	0.94	0.94	0.95	0.94	0.95	0.93	0.69	0.70	0.78	0.82	0.84	0.71	0.89	0.74	0.76	0.89
Mg	0.01	0.01	0.01	0.01	0.00	0.01	0.01	0.00	0.00	0.01	0.01	0.00	0.01	0.02	0.00	0.00	0.00	0.01
Mn	0.02	0.02	0.02	0.02	0.01	0.01	0.01	0.01	0.11	0.12	0.13	0.13	0.08	0.07	0.07	0.09	0.14	0.04
Ca	0.00	0.00	0.00	0.00	0.00	0.00	0.00	0.00	0.00	0.04	0.03	0.00	0.00	0.05	0.00	0.00	0.00	0.00
Ni	0.00	0.00	0.00	0.00	0.00	0.00	0.00	0.00	0.00	0.00	0.00	0.00	0.00	0.00	0.00	0.00	0.00	0.00
Na	0.00	0.00	0.00	0.00	0.00	0.00	0.00	0.00	0.00	0.00	0.00	0.00	0.01	0.00	0.00	0.00	0.01	0.00
K	0.00	0.00	0.00	0.00	0.00	0.00	0.00	0.00	0.00	0.00	0.00	0.00	0.00	0.00	0.00	0.00	0.00	0.00
Total	2.00	2.00	2.00	2.00	2.00	2.00	2.00	2.00	2.00	1.94	1.98	2.00	2.00	1.93	2.00	1.93	1.96	2.00
End-member proportions																		
X_{Ilm}	0.97	0.97	0.97	0.97	0.99	0.98	0.98	0.98	0.86	0.85	0.85	0.86	0.91	0.89	0.93	0.88	0.84	0.95
X_{Pph}	0.02	0.02	0.02	0.02	0.01	0.01	0.01	0.01	0.14	0.14	0.14	0.14	0.09	0.09	0.07	0.11	0.16	0.04
X_{Gk}	0.01	0.01	0.01	0.01	0.00	0.01	0.01	0.00	0.00	0.01	0.01	0.00	0.01	0.02	0.00	0.00	0.00	0.01

All oxide values are in wt%. $X_{Ilm}=Fe^{2+}/(Fe^{2+}+Mg+Mn)$; $X_{Pph}=Mn/(Fe^{2+}+Mg+Mn)$; $X_{Gk}=Mg/(Fe^{2+}+Mg+Mn)$. KS: Khurisberg Subgroup, KNb: Koperberg Suite from Nababeep Mine, KNg: Koperberg Suite from Nigramoep Mine, KCr: Koperberg Suite from Carolusberg Mine, and KSQ: Koperberg Suite from Sugarloaf Quarry

Table A8. EDS results for spinel compositions and end-member proportions

Sample	039T-1B1	039T-1B1	039T-1B1	016T-3C	016T-3C	016T-3C	039T-4A	039T-4B	039T-4B	DSQ 3B2	DSQ 3B2	DSQ 3D1	DSQ 3D1
Analysis	**1 (KS)**	**2 (KS)**	**3 (KS)**	**4 (KNb)**	**5 (KNb)**	**6 (KNb)**	**7 (KNb)**	**8 (KNb)**	**9 (KNb)**	**10 (KSQ)**	**11 (KSQ)**	**12 (KSQ)**	**13 (KSQ)**
SiO_2	0.24	0.21	0.13	0.36	0.18	0.00	0.11	0.08	0.19	0.13	0.07	0.01	0.14
Al_2O_3	55.74	57.02	56.28	0.71	0.83	0.23	0.26	0.22	0.28	0.24	0.41	0.39	0.38
Fe_2O_3	4.06	2.74	2.56	65.50	65.81	67.71	66.02	67.97	67.49	68.05	66.73	66.37	66.36
Cr_2O_3	1.58	1.58	1.55	1.30	0.93	0.61	1.18	0.17	0.28	0.01	0.60	0.77	0.76
V_2O_3	0.41	0.48	0.36	0.61	0.66	0.37	0.77	0.37	0.44	0.11	0.86	1.10	0.99
TiO_2	0.00	0.00	0.04	0.00	0.08	0.00	0.21	0.05	0.01	0.10	0.06	0.12	0.00
FeO	25.01	25.00	24.66	31.06	31.21	30.66	31.32	30.94	31.10	31.20	31.08	30.98	30.94
MgO	6.82	7.16	5.19	0.27	0.01	0.01	0.00	0.10	0.00	0.00	0.02	0.00	0.02
MnO	0.17	0.12	0.09	0.00	0.13	0.23	0.08	0.05	0.09	0.09	0.00	0.17	0.08
ZnO	5.97	5.56	8.97	0.00	0.01	0.00	0.00	0.04	0.06	0.00	0.07	0.05	0.09
NiO	0.02	0.12	0.16	0.19	0.15	0.19	0.04	0.01	0.07	0.08	0.11	0.05	0.23
Total	100.00	100.00	100.00	100.00	100.00	100.00	100.00	100.00	100.00	100.00	100.00	100.00	100.00
Cations based on 4 Oxygens													
Si	0.01	0.01	0.00	0.01	0.01	0.00	0.00	0.00	0.01	0.00	0.00	0.00	0.01
Al	1.86	1.88	1.89	0.03	0.04	0.01	0.01	0.01	0.01	0.01	0.02	0.02	0.02
Fe^{3+}	0.09	0.06	0.05	1.88	1.90	1.96	1.91	1.97	1.95	1.97	1.93	1.92	1.92
Cr	0.04	0.04	0.03	0.04	0.03	0.02	0.04	0.00	0.01	0.00	0.02	0.02	0.02
V	0.01	0.01	0.01	0.02	0.02	0.01	0.02	0.01	0.01	0.00	0.03	0.03	0.03
Ti	0.00	0.00	0.00	0.00	0.00	0.00	0.01	0.00	0.00	0.00	0.00	0.00	0.00
Fe^{2+}	0.59	0.59	0.59	0.99	1.00	0.99	1.01	0.99	1.00	1.00	1.00	1.00	0.99
Mg	0.29	0.30	0.22	0.02	0.00	0.00	0.00	0.01	0.00	0.00	0.00	0.00	0.00
Mn	0.00	0.00	0.00	0.00	0.00	0.01	0.00	0.00	0.00	0.00	0.00	0.01	0.00
Zn	0.12	0.12	0.19	0.00	0.00	0.00	0.00	0.00	0.00	0.00	0.00	0.00	0.00
Ni	0.00	0.00	0.00	0.01	0.00	0.01	0.00	0.00	0.00	0.00	0.00	0.00	0.01
Total	3.00	3.00	3.00	3.00	3.00	3.00	3.00	3.00	3.00	3.00	3.00	3.00	3.00
Endmembers (mol%)													
Ulvöspinel	0.00	0.00	0.06	0.00	0.22	0.00	0.59	0.11	0.00	0.28	0.14	0.34	0.00
Trevorite	0.03	0.27	0.36	0.55	0.45	0.59	0.11	0.00	0.22	0.22	0.34	0.14	0.67
Galaxite	0.37	0.26	0.18	0.00	0.01	0.00	0.00	0.00	0.00	0.00	0.00	0.00	0.00
Jacobsite	0.02	0.01	0.00	0.00	0.38	0.72	0.22	0.17	0.28	0.28	0.00	0.53	0.25
Gahnite	11.81	11.13	18.38	0.00	0.00	0.00	0.00	0.00	0.00	0.00	0.00	0.00	0.00
Franklinite	0.54	0.31	0.46	0.00	0.00	0.00	0.00	0.08	0.14	0.00	0.19	0.14	0.25
Chromite	1.18	1.15	1.26	1.90	1.38	0.91	1.78	0.24	0.42	0.00	0.90	1.15	1.14
Magnesiochromite	0.57	0.59	0.48	0.03	0.00	0.00	0.00	0.00	0.00	0.00	0.00	0.00	0.00
Coulsonite	0.30	0.36	0.30	0.90	1.00	0.56	1.18	0.56	0.67	0.15	1.32	1.69	1.52
Magnesiocoulsonite	0.15	0.18	0.11	0.01	0.00	0.00	0.00	0.00	0.00	0.00	0.00	0.00	0.00
Hercynite	54.71	55.25	55.59	1.58	1.87	0.50	0.59	0.49	0.62	0.55	0.91	0.87	0.84
Magnetite	2.52	1.53	1.39	93.57	94.63	96.66	95.53	97.81	97.66	98.52	96.11	95.14	95.21
Spinel	26.57	28.18	20.90	0.02	0.00	0.00	0.00	0.00	0.00	0.00	0.00	0.00	0.00
Magnesioferrite	1.22	0.78	0.52	1.43	0.05	0.05	0.00	0.53	0.00	0.00	0.08	0.00	0.11

Table A8 *(continued)*

Sample	DSQ 3D1	DSQ 3D1	KNU 477A	KNU 477A	KNU 477A	KNU 477A	CD 01A	CD 01A	CD 01A	KNU 477A	KNU 477A	KNU 477A
Analysis	**15 (KSQ)**	**16 (KSQ)**	**17 (KNg)**	**18 (KNg)**	**19 (KNg)**	**20 (KNg)**	**21 (KCr)**	**22 (KCr)**	**23 (KCr)**	**24 (KNg)**	**25 (KNg)**	**26 (KNg)**
SiO_2	0.11	0.18	0.00	0.16	0.18	0.07	0.10	0.04	0.03	0.00	0.07	0.08
Al_2O_3	0.37	0.41	0.44	0.19	1.13	0.36	0.45	0.46	0.37	0.28	0.42	0.19
Fe_2O_3	66.60	66.19	67.32	67.84	64.51	67.34	65.11	64.86	65.05	37.95	37.36	8.92
Cr_2O_3	0.64	0.60	0.98	0.22	2.35	0.60	2.43	2.60	2.53	0.92	0.74	0.46
V_2O_3	0.85	0.87	0.18	0.31	0.43	0.42	0.57	0.69	0.74	0.94	0.70	0.36
TiO_2	0.08	0.25	0.00	0.00	0.00	0.00	0.02	0.08	0.04	14.93	15.32	30.48
FeO	30.98	30.90	30.74	30.80	31.05	30.95	31.01	30.89	30.91	43.97	44.33	59.34
MgO	0.00	0.20	0.09	0.07	0.13	0.02	0.00	0.01	0.05	0.01	0.12	0.00
MnO	0.15	0.19	0.05	0.02	0.07	0.00	0.11	0.07	0.00	0.96	0.88	0.08
ZnO	0.07	0.02	0.00	0.14	0.00	0.15	0.07	0.00	0.00	0.06	0.01	0.10
NiO	0.14	0.19	0.21	0.24	0.16	0.09	0.12	0.32	0.27	0.00	0.05	0.00
Total	100.00	100.00	100.00	100.00	100.00	100.00	100.00	100.00	100.00	100.00	100.00	100.00
Cations based on 4 Oxygens												
Si	0.00	0.01	0.00	0.01	0.01	0.00	0.00	0.00	0.00	0.00	0.00	0.00
Al	0.02	0.02	0.02	0.01	0.05	0.02	0.02	0.02	0.02	0.01	0.02	0.01
Fe^{3+}	1.93	1.91	1.95	1.96	1.85	1.95	1.88	1.87	1.88	1.08	1.06	0.25
Cr	0.02	0.02	0.03	0.01	0.07	0.02	0.07	0.08	0.08	0.03	0.02	0.01
V	0.03	0.03	0.01	0.01	0.01	0.01	0.02	0.02	0.02	0.03	0.02	0.01
Ti	0.00	0.01	0.00	0.00	0.00	0.00	0.00	0.00	0.00	0.43	0.44	0.86
Fe^{2+}	1.00	0.99	0.99	0.99	0.99	0.99	1.00	0.99	0.99	1.39	1.40	1.85
Mg	0.00	0.01	0.00	0.00	0.01	0.00	0.00	0.00	0.00	0.00	0.01	0.00
Mn	0.00	0.01	0.00	0.00	0.00	0.00	0.00	0.00	0.00	0.03	0.03	0.00
Zn	0.00	0.00	0.00	0.00	0.00	0.00	0.00	0.00	0.00	0.00	0.00	0.00
Ni	0.00	0.01	0.01	0.01	0.00	0.00	0.00	0.01	0.01	0.00	0.00	0.00
Total	3.00	3.00	3.00	3.00	3.00	3.00	3.00	3.00	3.00	3.00	3.00	3.00
Endmembers (mol%)												
Ulvöspinel	0.22	0.70	0.00	0.00	0.00	0.00	0.06	0.20	0.11	42.50	43.41	85.37
Trevorite	0.42	0.56	0.65	0.72	0.48	0.28	0.34	0.98	0.81	0.00	0.14	0.00
Galaxite	0.00	0.01	0.00	0.00	0.01	0.00	0.00	0.00	0.00	0.03	0.05	0.01
Jacobsite	0.47	0.58	0.14	0.06	0.22	0.00	0.36	0.19	0.00	3.01	2.75	0.23
Gahnite	0.00	0.00	0.00	0.00	0.00	0.00	0.00	0.00	0.00	0.00	0.00	0.01
Franklinite	0.19	0.06	0.00	0.36	0.00	0.42	0.19	0.00	0.00	0.14	0.03	0.26
Chromite	0.96	0.88	1.47	0.33	3.50	0.91	3.67	3.92	3.82	1.36	1.08	0.67
Magnesiochromite	0.00	0.01	0.01	0.00	0.03	0.00	0.00	0.00	0.01	0.00	0.01	0.00
Coulsonite	1.30	1.31	0.27	0.47	0.64	0.64	0.87	1.05	1.13	1.42	1.04	0.53
Magnesiocoulsonite	0.00	0.02	0.00	0.00	0.00	0.00	0.00	0.00	0.00	0.00	0.01	0.00
Hercynite	0.83	0.90	0.98	0.42	2.52	0.81	1.01	1.03	0.83	0.57	0.87	0.40
Magnetite	95.60	93.89	96.02	97.24	91.91	96.85	93.49	92.60	93.01	50.92	49.93	12.53
Spinel	0.00	0.01	0.00	0.00	0.02	0.00	0.00	0.00	0.00	0.00	0.01	0.00
Magnesioferrite	0.00	1.08	0.46	0.39	0.68	0.08	0.00	0.03	0.26	0.03	0.65	0.00

All oxide values are in wt%. KS: Khurisberg Subgroup, KNb: Koperberg Suite from Nababeep Mine, KNg: Koperberg Suite from Nigramoep Mine, KCr: Koperberg Suite from Carolusberg Mine, and KSQ: Koperberg Suite from Sugarloaf Quarry.

Table A9. EDS results for apatite compositions (in wt%)

Sample	**016T-3C**	**DSQ 3D1**	**DSQ 3D1**	**KNU 477A**	**KNU 477A**	**KNU 477A**
Analysis	**1 (KNb)**	**2 (KSQ)**	**3 (KSQ)**	**3 (KNg)**	**4 (KNg)**	**5 (KNg)**
SiO_2	0.78	0.29	2.92	0.16	0.23	0.68
TiO_2	0.01	0.05	0.00	0.02	0.06	0.10
Al_2O_3	0.45	0.06	1.43	0.22	0.22	0.08
FeO	0.18	0.21	1.16	1.75	0.14	0.11
MgO	0.00	0.04	0.99	2.78	0.06	0.04
MnO	0.07	0.00	0.00	0.76	0.00	0.10
CaO	53.29	53.67	49.87	53.15	54.07	52.63
Na_2O	0.00	0.00	0.00	0.00	0.00	0.00
K_2O	0.00	0.02	0.09	0.09	0.00	0.06
P_2O_5	43.41	43.86	41.74	39.26	43.41	44.39
Volatiles	1.80	1.80	1.80	1.80	1.80	1.80
Total	100.00	100.00	100.00	100.00	100.00	100.00

*Volatiles = H_2O + F + Cl + CO_2

Table A10. EDS results for monazite compositions (in wt%)

Sample	039T-1B1	039T-1B1	039T-1B3	039T-1B3	039T-4A	KNU 477A	KNU 477A
Analysis	**1 (KS)**	**2 (KS)**	**3 (KS)**	**4 (KS)**	**5 (KNb)**	**6 (KNg)**	**7 (KNg)**
SiO_2	1.57	3.53	0.58	0.95	1.44	0.56	0.22
TiO_2	0.07	0.01	0.11	1.18	0.00	0.00	0.03
Al_2O_3	0.17	0.96	0.10	0.60	0.13	0.30	0.15
FeO	0.47	2.16	0.80	0.75	0.00	0.00	0.00
MgO	0.00	0.21	0.00	0.04	0.00	0.06	0.02
MnO	0.00	0.25	0.20	0.14	0.28	0.00	0.09
CaO	1.26	1.30	0.32	0.13	1.28	1.21	1.07
P_2O_5	31.60	32.74	31.33	26.20	32.14	30.14	28.66
SO_3	0.10	0.00	0.09	0.25	0.79	1.95	1.60
ZrO_2	0.73	0.09	0.75	0.23	0.00	0.00	1.03
La_2O_3	15.77	10.74	16.21	15.40	16.01	18.08	15.84
Ce_2O_3	32.14	28.96	32.03	35.11	32.12	33.63	33.80
Pr_2O_3	2.19	3.14	2.40	2.94	2.74	2.07	3.14
Nd_2O_3	10.62	13.16	10.55	13.53	10.73	10.42	11.98
Sm_2O_3	1.58	1.76	1.95	1.58	1.15	0.63	1.20
Gd_2O_3	1.12	0.58	1.74	0.65	1.11	0.44	0.81
Dy_2O_3	0.32	0.42	0.85	0.20	0.00	0.17	0.35
Yb_2O_3	0.29	0.00	0.00	0.13	0.07	0.33	0.00
Total	100.00	100.00	100.00	100.00	100.00	100.00	100.00

Appendix 2: EPMA detection limits for sulphides

Table A11. EPMA detection limits for sulphides (in ppm)

Element	Pyrite	Pyrrhotite	Chalcopyrite	Bornite	Chalcocite
S	190	186	188	194	212
Fe	174	182	180	186	192
As	444	453	465	485	506
Cu	218	254	234	248	253
Zn	1390	1530	1587	1703	1722
Pb	521	483	469	453	429
Ni	870	891	920	948	1050